ABSTRACT

LIU, YULING. Generation and Reception of Ultrasonic Guided waves in Metallic Plates Induced by Surface Bonded PZT Wafers. (Under the direction of Dr. Fuh-Gwo Yuan).

Massive plate-like structural components are being used in the engineering field, like airplanes, bridges, pipelines, ships, dams, etc. The structural failure of such components will cause accidents to happen, which will result in loss of lives and properties. If the health of structures can be monitored, such accidents can be prevented from happening. This is how the term 'Structural Health Monitoring (SHM)' came into being. One of the most widely used actuators/sensors in SHM is PZT (PZT) actuators/sensors. There has been many studies conducted previously for solving the problem of surface bonded PZT actuators. However, most of them are based on one-dimensional (1-D) actuators. In reality, many PZT actuators are rectangular, which needs to be studied in two-dimension (2-D). However, there has been very few studies for the actuation of rectangular PZT actuators. This thesis is for filling this void. The goal of this thesis is to predict the rectangular PZT sensor output voltage when an input voltage is applied on a rectangular PZT actuator. The whole study is conducted in the frequency domain, the plate on which the actuators and sensors are mounted on is isotropic metallic plate.

The goal of this research is to obtain a theoretical result of output voltage on a rectangular PZT sensor when a voltage is applied on the rectangular PZT actuator. In order to solve this voltage in- voltage out problem, three main problems are solved here. First, with a given voltage on the actuator, the interaction, or the stress distribution between the actuator and the plate needs to be analyzed. Second, the plate wave generated by the stress distribution on the contact surface of the actuator and plate needs to be analyzed. Third, the

voltage output of the sensor needs to be analyzed when the strain distribution between the sensor and the plate is obtained.

For the first problem, the stress on the contact surface of the actuator and plate is expressed in a truncated Chebyshev polynomial form with four unknown coefficients. The equation of motion for the actuator is solved using Gorman's superposition method, which consists of SS, AA, SA, AS vibration modes. The amplitude for each mode is solved using traction free boundary conditions.

For the second problem, the displacement of Lamb wave modes and shear horizontal waves modes on the plate is expressed using carrier wave approach. By means of reciprocity theorem, the amplitudes of each wave mode can be obtained for a point load scenario. When the inter-facial stress is applied on the surface of the plate, the plate displacement can be solved by integrating the displacement under point load case over the entire stress applying area. Using the displacement continuity at the contact surface of the actuator and plate, the unknown coefficients in the assumed contact surface stress expression can be solved using least square method.

For the third problem, considering the open-circuit boundary condition of the PZT sensor, the total charge over the electrode area is zero. Using the constitutive equation of PZT materials, the output voltage can be expressed in a form with the integration of strain on the sensor contact surface with the plate. The effect on plate strain with the existence of sensor is ignored.

The theoretical result is validated by comparing with finite element result in COMSOL. This research can provide a theoretical foundation for damage detection using rectangular PZT actuators and sensors in structural health monitoring.

Generation and Reception of Ultrasonic Guided waves in Metallic Plates Induced by Surface Bonded PZT Wafers

by
Yuling Liu

A dissertation submitted to the Graduate Faculty of
North Carolina State University
in partial fulfillment of the
requirements for the degree of
Doctor of Philosophy

Mechanical Engineering

Raleigh, North Carolina

2016

APPROVED BY:

_____	_____
Dr. Fuh-Gwo Yuan Committee Chair	Dr. Xiaoning Jiang
_____	_____
Dr. Yun Jing	Dr. Gregory Buckner
_____	
Dr. Jing-pu Liu	

DEDICATION

To my beloved parents

and all those who inspired me

BIOGRAPHY

Yuling Liu was born on September 21, 1989 in Tianmen, Hubei province, China. She spent her carefree childhood and teenager years with her beloved parents in the downtown of Tianmen, which is surrounded by many beautiful lakes and rivers. In September 2007, she moved to Beijing to pursue her undergraduate study in Beijing Institute of Technology. In March 2011, she went to Delft University of Technology in Netherlands as an exchange student, where she studied the plasma actuator used to reduce or eliminate tip vortex on airplane wing tip. She obtained her Bachelor degree in July 2011 majoring in Aerospace Engineering. In August 2011, she moved to Raleigh, North Carolina, where she joined the research group of Prof. Fuh-Gwo Yuan in Smart Structures and Materials Laboratory. In May 2013, she completed her Master of Science degree in Mechanical Engineering from North Carolina State University. In her thesis for master degree, she proposed several theorems for locating plane of symmetry and binary, quaternary and trigonal axes of symmetry given the values of piezoelectric tensor in an arbitrary coordinate system, which can be used to determine the material type by solving for normal of plane of symmetry and axis of symmetry. She continued to pursue a Doctor of Philosophy in Mechanical Engineering in the area of Structural Health Monitoring (SHM). Her dissertation is on generation and reception of ultrasonic Lamb waves in metallic plates induced by surface bonded rectangular piezoelectric wafers. She has been supported by China Scholarship Council (CSC) and North Carolina State University.

ACKNOWLEDGMENTS

I would like to express my sincere gratitude to my PhD adviser Dr. Fuh-Gwo Yuan for his unwavering guidance, profound insight, professional attitude and dedication towards his work. You are a model to me in conducting research. Thank you for your support, countless advice and timely response to all my questions. I would not be able to develop my independent research skills and abilities without you.

I would also like to thank my committee members: Dr. Xiaoning Jiang, Dr. Yun Jing, Dr. Gregory Buckner, Dr. Paul (Jingpu) Liu for your time in attending my defense and your advice and help in completing my thesis. I would also thank Dr. Murthy Guddati for your advice in my thesis.

Additionally, I would also like to thank the members, former graduates and visiting scholars in our research group at North Carolina State University: Dr. Shaorui Yang, Dr. Xiang Yan, Dr. Jiaze He, Dr. Rui Zhu, Dr. Mohammad Harb, Dr. Sri Vikram Palagummi, Mr. Chenguang Xu, Mr. Chao Wan, Mr. Che-Yuan Chang, Dr. Juntao Zhu, Ms. Ni Sui, Mr. Abel Fong, Mr. Ningyi Zhang, Mr. Huan-Yu Chang, and Mr. YuSheng Chang, Mr. Howuk Kim, Mr. Patrick Lesser, Mr. Ningyi Zhang, Mr. Andrew Choi, Mr. Karthik Reddy Lyathakula, Mr. Sakib Ashraf Zargar. Thank you for all the helpful talks I had with you about all research topics. My special thanks go to Mr. Abel Fong and Dr. Shaorui Yang. Thank Mr. Abel Fong for generously granting me the access to your workstation for some calculations in my thesis. Thank Dr. Shaorui Yang for answering my theoretical questions in wave propagation field.

I would also like to thank my spiritual guide, Mr. Steve Wang, Mrs. Grace Wang. Thank you for being patterns in faith and love. Thank my good friends and current/previous roommates:

Ms. Juanjuan Gu, Mrs. Si Li, Mrs. Rufina Gilberto, Ms. Rebecca Lim and all the sisters and brothers in the Lord. Thank you for your love, care, prayer, encouragement and companion during my PhD years.

My deepest gratitude goes to my dear parents, who has unconditionally loved and supported me. You are the best I can ask for. Thank you with all my heart.

Jehovah is my Shepherd; I will lack nothing.

He makes me lie down in green pastures; He leads me beside waters of rest.

He restores my soul; He guides me on the paths of righteousness For His name's sake.

Even though I walk Through the valley of the shadow of death, I do not fear evil, For You are with me; Your rod and Your staff, They comfort me.

You spread a table before me In the presence of my adversaries; You anoint my head with oil; My cup runs over.

Surely goodness and loving kindness will follow me All the days of my life, And I will dwell in the house of Jehovah For the length of my days.

(*Psalms 23*)

TABLE OF CONTENTS

LIST OF TABLES

LIST OF FIGURES

CHAPTER 1

Introduction

1.1 Research Motivation

1.1.1 Plate-like structural components

Massive plate-like structural components are being used in the engineering field, like airplanes, bridges, pipelines, ships, dams, etc. The structural failure of such components will cause accidents to happen, which will result in loss of lives and properties. If the health of structures can be monitored, such accidents can be prevented from happening. This is how the term 'Structural Health Monitoring (SHM)' came into being.

1.1.2 Structural Health Monitoring (SHM)

The basic motivations for SHM are: (1) enhancing the safety and prolong structural lifespan; (2) commercial motivation. It was predicated by MarketsandMarkets.com in 2015 November that the SHM will have a continual growing market worth in the next fifteen years.

The way how SHM works can be compared to the function of a human body. If someone touches a hot surface, his hand will quickly draw back. This is because the nerve endings on the hand send the signal to the brain through the spinal cord. Similarly, the smart sensors mounted on the surface of the structures will send the signals containing environmental information or function of the structure to the processing unit through communication bus.

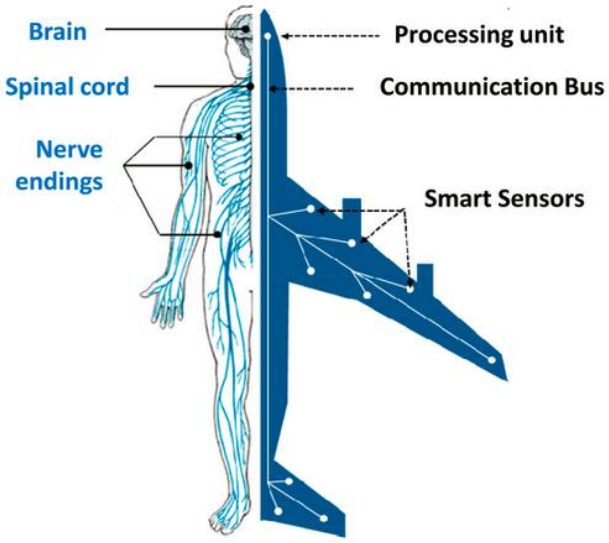

Figure 1.1 Comparison of SHM with human body (Boukabache *et al*., 2014)

One of the most widely used actuators/sensors in SHM is piezoelectric (PZT) actuators/sensors. The way how PZT material works is that when PZT is being used as actuators, the transient/harmonic voltage applied on the top surface of the actuator will result in expansion or shrink in a certain direction, thus generating strain on the contact surface of the substrate material. When PZT material works as sensors, the strain on the contact surface will result in an output voltage of the sensor.

The reasons why PZT materials are widely used in SHM are summarized below:

- Real-time non-destructive inspection
- Light weight (High force-to-weight ratio)
- Lower power consumption

- Easy implementation (integration)
- Large bandwidth (a wide range of actuator frequency)
- Low cost
- Fast response
- Much more sensitive than the strain gage
- Predominantly linear response

1.1.3 Problem statement

There have been many studies conducted previously for solving the problem of surface bonded PZT actuators. However, most of them are based on one-dimensional (1-D) actuators.

The first kind of 1-D actuator is the plane strain case, in which an infinitely long PZT actuator beam is mounted on the surface of a plate. The second kind of 1-D actuator is a circular PZT actuator which is a symmetric case. In both cases the function of actuator is analyzed in 1-D.

In reality, many PZT actuators are rectangular, which needs to be studied in two-dimension (2-D). However, there have been very few studies for the actuation of rectangular PZT actuators. This thesis is for filling this void.

The actuator studied in this thesis has a width of $2a = 4\ mm$ along the x axis, a length of $2b = 8\ mm$ along the y axis and a height of $h_a = 0.2\ mm$ along the z axis. The material

of the actuator is PZT-5A, which is transverse isotropic. The poling direction of the actuator is along the z axis. The plate is aluminum plate with a thickness of $2h$ = 3.2 *mm*. The plate has infinite domain in the $x-y$ plane.

Four things have been solved in this thesis:

- Interaction between rectangular PZT actuator and plate.
- Theoretical solution for rectangular PZT actuator response under prescribed harmonic/transient voltage
- Theoretical solution for 3-D plate wave solution with surface bonded PZT actuator
- Theoretical solution for surface-bonded rectangular PZT sensor response

1.2 Literature Review

1.2.1. Theoretical modeling of PZT actuator bonded on substrate

This section gives a review of the Theoretical approaches in modeling the interaction between PZT actuators and its host structures. The methods include Euler-Bernoulli model using shear-lag theory, pin-force model considering forces on actuator edges and model based on elastic equation of motion. These methods are mainly applied to one dimensional case when the actuator is a plane strain case. Then, in Section 2.3, a review of two dimensional actuator modeling is conducted.

Shear-lag theory

Due to the bonding layer, the PZT actuator is not fully coupled with the host structure. Therefore, the effective PZT actuator size is smaller than the actual size. The reduced PZT actuator size is the so-called "effective PZT size" (di Scalea and Salamone, 2008). Shear-lag model is a commonly used model in consideration of this boning layer effect. The term "shear-lag" was first used by Reissner (1946) for analysis of box beams bending and Troitsky (1976) to analyze the bending of I beam and T beams with wide flanges.

The application of shear-lag theory to analyzing the interaction between PZT actuator and plate can be traced to the work of Crawley and De Luis in 1987. In their model, a shear-lag solution for the inter-facial stress was derived. The actuator was modeled as a beam with only axial stiffness. The beam on which the actuator was attached on was modeled as an Euler-Bernoulli beam. Several enhancements based on Crawley and de Luis's model (1987) were studied later.

Chaudhry and Rogers (1994) modeled the beam and patch actuator as Timoshenko beams, thus the strain distribution in both the actuator and the beam was linear.

The limitations of shear-lag method include: (a) assumption of linear strain distribution across beam thickness can only be applied to scenarios when the product of frequency and thickness are low. (b) It can only be applied to A_0 mode or S_0 mode where the frequencies are the low. As a result, Lamb wave modes with frequencies higher than A_0

mode or S_0 mode are not propagating waves. (c) The thickness and material properties of the bonding layer should be known in advance while they are hard to measure practically.

To resolve the limitations of shear-lag method, Sohn and Lee (2009) developed a theoretical Lamb wave tuning curve (LWTC) model and used Lamb wave mode amplitude adjustment techniques to reduce the discrepancy between the experimental and theoretical LWTCs.

Pin-force model considering forces on actuator edges

It was shown by Crawley and de Luis (1987) and Giurgiutu (2005) that the inter-facial shear stress concentrated on the edges of the actuator when the bonding layer is thin and stiff. For perfect bonding (stiffness of bonding layer is infinite), the shear stress has singularity at the two edges. Based on this assumption, Giurgiutiu (2005) proposed the pin-force model in which the shear stress only existed on the two edges of the actuator in beam case. The resulting harmonic wave on the isotropic plate was then calculated using the Rayleigh-Lamb equations (Rose, 1999).

Raghavan and Cesnik (2005) expanded the pin-force model to a 2-D arbitrary-shaped actuator on elastic plate as in-plane traction of uniform magnitude along its perimeter. The direction of the traction was normal to the free edge of the plate surface. It was assumed that the plate dynamics is uncoupled with the actuator dynamics. The validity of this model of approximation was proved to be appropriate if the product of actuator Young's modulus and thickness is small compared to that of the substrate and the bond layer is thin and stiff.

Rectangular shaped and ring shaped actuators were taken as examples and their harmonic radiation field were calculated.

Lin and Yuan (2001) modeled the actuator as bending moments along the actuator edge. Voltage response of PZT sensor attached to a plate and subject to narrow-band tone-burst excitation from a pair of PZT actuators positioned at opposite side of the plate was modeled. Employing Mindlin plate theory the fundamental antisymmetric A_0 mode below the cut-off frequency of A_1 mode was examined in this study.

Giurgiutiu (2014) explained the pin-force model in the 7th chapter of his book by representing the stiffness of the structure by spring boundary conditions applied at the PZT actuator ends. Since the interaction between the PZT actuator and the substructure is confined at the two ends of the actuator, the stress variation (T_1') along the actuator length is zero. According to the constitutive equation of piezoelectric materials, the strain variation (S_1') is also zero. Therefore, the displacement $u(x)$ is a linear function along x axis.

The limitation of using pin-force model are summarized as (Huang *et al*. ,2010): (a) The model renders good approximation either when the bonding layer is thin and stiff or when Young's modulus and thickness of actuator are small compared to that of the host structure. (b) The resonance effect of PZT actuator is not captured in the model.

Model based on elastic equation of motion

One of the shortcomings of using plate/beam theory is that only the lowest frequency mode can be captured under plate excitation. As for shear-lag solution, it also only applies to

low frequency-thickness product scenarios. However, the approach of elasticity equation based model can overcome this shortcoming. This method was first developed by Wang and Huang (2001, 2003, 2006) and Huang and Sun (2006).

Wang and Meguid (2000) modeled the coupling behavior of a one dimensional thin piezoceramic actuator embedded in or bonded to an elastic medium based upon singular integral equations of the inter-facial shear stress. The singularity of shear stress at the tips of the actuator was modeled by a square root.

Wang and Huang (2001) solved the Rayleigh wave propagation induced by surface-bonded PZT actuators in one-dimensional (1-D) case. Using the constitutive equations for piezoelectric materials and traction free boundary conditions at the two ends of the actuator, the axial strain of the actuator was completely determined. The shear stress on the contact surface, which was expressed as Chebyshev polynomials, was used as the excitation source on the host structure. The Rayleigh wave generated on the plate was obtained by solving the plane strain elastodynamic problem (Achenbach, 1973). The coefficients of the Chebyshev polynomials were determined by continuity of deformation between the actuator and the host structure. Good agreement between the Theoretical result and finite element (FE) result were shown by Wang and Huang (2001). However, this paper fails to include evanescent (non-propagating) wave terms in the near singular field.

Zhang *et al*. (2003a, b) conducted similar analysis for determining the static electromechanical field. For the piezoelectric layer, assumptions that the in-plane axis normal

stress has a linear variation across the thickness and the electric displacement component is a linear function of out-of-plane axis were made.

In Huang and Sun's (2006) work, a one-dimensional actuator model was developed. The inter-facial shear stress is modeled as Chebyshev polynomial expansions involving square-root singularity at the tips of the actuator. This model includes the coupled dynamic interaction between the actuator and host structure (Huang *et al.*, 2010).

1.2.2. FE methods or hybrid methods

(1) FE methods

Commercial FE software such as COMSOL and ANSYS has been convenient tools for the coupling field problem like the elastic wave behavior induced by PZT actuators (Nieuwenhuis *et al.*, 2005, Liu and Giurgiutiu, 2007, Han *et al.* 2009). The disadvantages of using FE methods are summarized by Huang *et al.* (2010) and are quoted as below: (a) FE simulation fails to provide a clear physical explanation of the numerically predicted results. (b) In order to achieve accurate simulation result and achieve numerical convergence, the mesh size needs to be at least one tenth per wavelength. Thus, it was very computational expensive for large three-dimensional models.

(2) Hybrid approaches

Hybrid approaches can overcome the shortcoming of FE method. In hybrid method, the FE method is used to obtain the excitation by modeling the PZT actuator area. Then the plate wave solution was obtained by combining with Theoretical guided wave model.

Moulin *et al*. (1997) showed that the generation of Lamb waves can be achieved by cylindrical piezoelectric transducers embedded in composite plate. In order to identify resonance modes, the electric impedance of the transducer were obtained using finite element method (FEM). It was shown that the radial mode can be used to generate S_0 Lamb mode due to its high coupling coefficient.

Moulin *et al*. (2000) modeled Lamb waves generated by surface bonded or embedded thin piezoelectric transducers on plate-like structures using a hybrid finite element- normal mode expansion modeling technique. The mechanical filed is obtained through FEM and then introduced as a forcing function into the normal modes equations. The normal mode expansion method was used to determine the contribution of each Lamb mode in the generated waveforms as a function of the applied surface and/or volume excitations. This study was valid for lossless materials and harmonic excitation. In 2004, Duquenne *et al*. expanded this method to lossy (viscoelastic) materials and transient excitation. The simplifying assumption was that the effects of attenuation on the local Lamb wave generation process are neglected in their work.

Veidt *et al*. (2001) solved the wavefield excited by surface-bonded rectangular and circular actuators using a hybrid approach. They modeled the actuator as causing normal surface traction. Instead of using FE software, they used the experiment of laser Doppler vibrometer to estimate the magnitude of the normal traction for a given frequency. They then used Mindlin plate theory to obtain plate response. The major disadvantages of Mindlin plate theory are:

(1) Mindlin plate theory can only be used to approximate the lowest antisymmetric A_0 Lamb wave mode.

(2) Mindlin plate theory is valid only when the product of excitation frequency and plate thickness is low enough thus no higher antisymmetric modes are excited.

(3) Mindlin plate theory cannot model symmetric Lamb wave mode or *SH* modes.

Though this approach can reduce computational effort by only simulating the actuator, it still lacks physical explanation of the predicated result.

1.2.3. Two-dimensional (2-D) modeling of surface bonded rectangular actuator

Previous works on guided wave excitation by PZT actuator mainly are 1-D plane strain models which ignore the variation along one direction of the plane. Review of previous attempts in solving interaction of 2-D actuator and plate are listed in this Section.

Modeling 2-D actuator with 2-D shear-lag theory

Giurgiutiu (2008) modeled 2-D PZT actuator as two independent 1-D shear-lag problem under plane strain assumptions. Kapuria and Agrahari (2016) improved Giurgiutiu's work (2008) by solving an accurate 2-D shear-lag solution for thin PZT actuator mounted on plate surface through an adhesive layer. The governing solutions are solved using the mixed field multi-term extended Kantorovich method (MMEKM) which converted bi-variate partial differential equations (PDEs) into two sets of ordinary differential and algebraic equations in two directions.

Modeling 2-D actuator with pin-force model

Raghavan and Cesnik (2007) modeled the interaction of actuator and plate as shear traction of uniform magnitude along its perimeter, in the direction normal to the free edge on the plate surface. The physical dynamics of the actuator was not taken into consideration and the plate dynamics was modeled as uncoupled with the actuator dynamics. Based on this model, examples of ring-shaped actuators and rectangular actuators on plate are modeled. Such modeling is merely an extension of the 1-D pin-force model. Moll *et al*. (2012) also expanded the pin-force model to a complex-shaped actuator with disk-wrapped electrode to conduct a semi-Theoretical 2-D mathematical model.

Modeling 2-D actuator based on equation of motion

Rose and Wang (2004) conducted the 2-D modeling of Lamb wave excited by finite sources. The Theoretical solutions for point forces and bending moments are derived using Mindlin plate theory. The response of plate for circular or rectangular shaped surface sources

can be obtained by spatial integration. In Mindlin plate theory, some characteristics, such as symmetric modes, higher order antisymmetric modes are not properly defined. Besides, the formulation in this paper is moderately delicate to deal with. In search for a simpler approach, Moulin *et al*. (2006) developed a pseudo-3-D numerical model based on 1-D modeling. The prediction of Lamb wave response on plate excited by a rectangular actuator is discussed by separating this problem into two uncoupled problems. The first problem focused on Lamb wave excitation due to the transducer. The second problem dealt with the source diffraction effect on plate. The model is called a pseudo 3-D model due to several assumptions. First, in this model, the rectangular transducer is assumed to have significant difference in length and width sizes, thus the stress distribution on the plate is assumed to be the product of a x-dependent function and a y-dependent function, expressed as $\sigma_0(x,y)=\sigma_0(x)\sigma_0(y)$. Second, when analyzing the displacement on the plate, it is assumed that the location of consideration is far enough from the source of excitation. In this case, far-field asymptotic approximation of Hankel function is adopted. Third, the excitation $\sigma_0(y)$ is considered uniform over the transducer length.

1.2.4. Three dimensional (3-D) wave propagation in plate

The theory of guided wave propagation was first proposed by Lamb (1917) and Gazis (1958) separately based on the theory of elasticity. Their work of the wave propagation used a 2-D plane strain model. Viktorov (1967) proposed extending the 2-D model to 3-D excitation by non-destructive evaluation (NDE) in his book. Santosa and Pao (1989) used normal mode expansion technique to solve a generic 3-D guided wave excitation in an

isotropic plate induced by an impulse point body force. Wilcox (2004) proposed a 3-D elastic model for harmonic GW field on plate generated by surface point load. However, the model was not strictly developed since the extension from 2-D to 3-D was based on some intuitive reasoning.

Raghavan and Cesnik (2004) characterized that Lamb wave excitation using surface bonded infinitely wide actuators or circular actuators. In 2005, Raghavan and Cesnik extended their work to 3-D wave excitation by an arbitrary-shaped PZT actuator. The actuator is modeled as causing in-plane traction of uniform magnitude along its perimeter. In their model, the dynamics of the actuator were neglected and it was assumed that the plate dynamics were uncoupled with actuator dynamics. Though Crawley and de Luis (1987) proved that this is a good assumption given that the product of the actuator Young's modulus and the thickness is small compared to that of the substrate and the bond layer is thin and stiff. However, since the magnitude of the in-plane traction on the actuator perimeter was not yet specified, only the normalized, not the actual plate response amplitude could be given. While solving the 3-D elastic equation of motion of the plate, it was assumed that there body for is equal to 0. However, this intuitive reasoning is not rigorous since the stresses at the contact surface are considered as body forces.

1.2.5. Sensor Response

Constitutive relations for piezoelectric materials are:

converse piezoelectric effect: $\sigma_{ij} = c_{ijkl}^{E}\varepsilon_{kl} - e_{kij}E_k$

direct piezoelectric effect: $D_i = e_{ikl}\varepsilon_{kl} + \epsilon_{ik}^{\varepsilon}E_k$

where $c_{ijkl}^{E}, e_{kij}, \epsilon_{ik}^{\varepsilon}$ are the elastic, piezoelectric and dielectric constants respectively. The superscripts E, ε denote the properties are under conditions of constant elastic field and constant strain respectively.

The converse piezoelectric effect constitutive equation is the actuator equation and the direct piezoelectric effect constitutive equation is the sensor equation. The generated charge is the integration of electric filed over the entire surface:

$$q = \iint D dA$$

where dA is an infinitesimal area normal to the electric displacement D.

Piezoelectric transducers directly convert the mechanical stress and strain energy into electrical energy, thus it can also be used for stress and strain sensing. According to the constitutive equation of piezoelectric material, the resulting voltage is proportional to the strain rate.

(1) Static sensing

An elementary level 1-D sensing functions without the considering of structure and sensor interaction is discussed by Giurgiutiu (2014) in Chapter 7. Four different scenarios are discussed: (1) static stress sensing, (2) static strain sensing, (3) dynamic stress sensing and (4) dynamic strain sensing.

(1.1) 1-D Static stress/strain sensing

For scenarios (1) and (2), the sensor is modeled as a capacitance C_e model, as shown below:

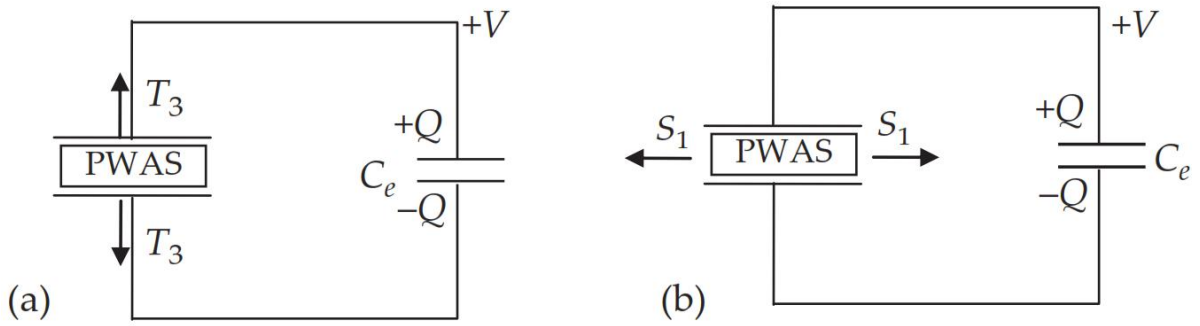

Figure 1.2 A sensor connected to the measuring instrument of capacitance C_e: (a) measuring static out-of-plane stress T_3; (b) measuring static in-plane strain S_1. (Giurgiutiu, 2014)

For scenario (1) static stress sensing, the voltage output can be obtained by combining the constitutive equation

$$D_3 = d_{33}T_3 + \epsilon_{33}^T E_3$$

charge, electric displacement and area relation:

$$Q = D_3 A$$

charge, voltage and capacitance relation:

$$Q = C_e V$$

and the relation between electric filed and voltage:

$$E_3 = -\frac{V}{t_a}$$

The resulting voltage is thus given as

$$V = \frac{Ad_{33}}{C_e + C} T_3$$

For scenario (2) static strain sensing, voltage output in relation to strain can be obtained from constitutive equations as well.

(1.2) 1-D Dynamic stress/strain sensing

For scenarios (3) and (4), the sensor is modeled as an input impedance Z_e and admittance Y_e $(Y_e = 1/Z_e)$ model, as shown below:

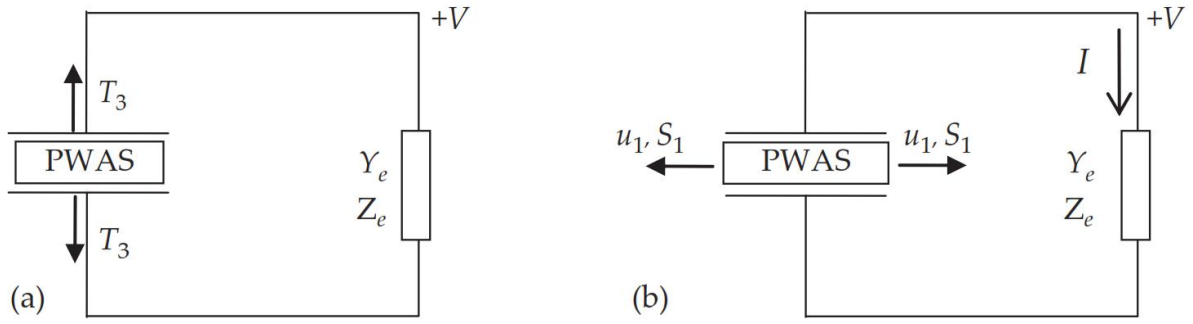

Figure 1.3 A sensor connected to the measuring instrument of input impedance Z_e and admittance Y_e: (a) measuring dynamic out-of-plane stress T_3; (b) measuring dynamic in-plane strain S_1. (Giurgiutiu, 2014)

In these two cases, the voltage outputs are obtained from taking time-derivative of constitutive equations.

(2) Harmonic voltage response for 1-D piezoelectric sensor

Raghavan and Cesnik (2004) gave the voltage response for piezoelectric sensor (PZT sensor) voltage response under the harmonic excitation of infinitely wide PZT actuator and circular surface bonded PZT actuator.

(2.1) PZT sensor voltage response under the harmonic excitation of infinitely wide PZT actuator

The electric displacement is obtained from the constitutive equation of piezoelectric material and the charge accumulated by the sensor is the integration of the electric displacement. By modeling the PZT sensor as a capacitor, the voltage is thus obtained by dividing the charge by the capacitance. By evaluating the variables in the voltage expression, it can be concluded that the following methods can be adopted in order to increase the sensor response (voltage amplitude):

(1) Having smaller sensor length. The smaller the sensor length is, the higher the voltage response will be.

(2) For the sensor, choosing piezoelectric materials with higher piezoelectric constant e_{31}.

(3) For the sensor, choosing piezoelectric materials with higher Young's modulus and sensor thickness. However, it should be noted that this will also increase the local stiffness and thus adversely affect the propagation of Lamb waves on plate.

(4) For the actuator, the optimum length is equal to half wavelength of the traveling wave (say, for A_0 mode or for S_0 mode), at which the actuator will also have minimum power consumption, while ensuring a maximum voltage response.

(2.2) PZT sensor voltage response under the harmonic excitation of circular surface bonded PZT actuator

The voltage response under circular PZT actuator excitation can be obtained in a similar manner as obtaining voltage response under infinitely wide PZT actuator excitation. In this case, in order to increase the sensor response (voltage amplitude), sensors with smaller length should be used. As for the actuator size, since the voltage expression for harmonic response is an oscillating function with a monotonically increasing amplitude envelope, there is no optimal circular actuator size.

In Raghavan and Cesnik's (2004) model, the actuator is modeled as causing two point loads at the two ends of the actuator. However, the amplitude of the point loads is not determined. Thus in their paper, only the normalized sensor response, not the actual sensor response is calculated.

1.2.6. Some related topics studied for applications to structural health monitoring

(1) Response of PZT sensors to plate waves or plane waves

Wang and Huang (2006) conducted a theoretical study of the two dimensional sensor response (modeled as plane strain) to elastic waves on an elastic half-plane. By substituting traction free boundary conditions to the equation of motion of the sensor, the axial strain on the sensor can be expressed as a function of the shear stress. Helmholtz decomposition and spatial Fourier transform were used in calculating the displacement of the homogeneous isotropic elastic host medium. The coupling between the sensor and the host medium was modeled by the continuity of deformation at the contact surface.

di Scalea *et al*. (2007) discussed the fundamental response of surface bonded rectangular piezoelectric sensors to Rayleigh and Lamb ultrasonic waves. Harmonica excitation fields, broadband and narrow-band excitation fields were all being examined. The sensor voltage response is derived by coupling the direct piezoelectric effect to the wave strain field that is averaged over the sensor area. Both general oblique incidence and parallel incidence of the wave were derived.

(2) Tuning of wave mode using PZT actuator

In order to address the detection of specific damage with specific wave modes, it is necessary to tune a particular mode. Giurgiutiu (2005) achieved wave tuning by the maxima and minima of the $\sin(ka)$ where ka is the normalized wave number. It was shown that A_0

mode dominates at low frequencies while S_0 mode can be identified at a certain frequency at the given structural configuration.

Glushkov *et al*. (2010) described selective Lamb wave mode excitation using an omni-directional multi-element transducer. The transducer consisted of several coaxial ring-shaped piezoelectric elements. The excitation signal was n -cycle sinusoidal tone bursts. Through special choice of amplitudes and time delay of input signal on each piezoelectric element, mode selection was achieved.

In 2010, Yu *et al*. used shear-lag method and space-wise Fourier transforms to obtain Theoretical closed-form solution for ideal bonding and not ideal bonding. Lamb wave mode tuning for suppressing or enhancing A_0 mode or S_0 mode were derived based on the solutions.

(3) Evanescent Lamb waves

The solution of wave propagation in structure induced by surface-bonded PZT actuators by Wang and Huang (2001) fails to include evanescent wave terms in the near singular field. In the expression of Lamb wave modes displacement and stress expressions, whether the value of wavenumber k is pure real, pure imaginary or complex determines if the Lamb wave is propagating or evanescent:

- When k is a pure real number, Lamb wave mode displacements are sinusoidal functions with respect to both time and space. Thus Lamb wave modes with real wavenumber are propagating waves.

- When k is a pure imaginary number, the displacement is exponentially decay with respect to the space term. Thus Lamb wave modes with imaginary wave number are evanescent waves.

- When k is a complex number, the displacement is the product of a sinusoidal variation with an exponential decaying function with respect to space term. Thus Lamb wave modes with complex wavenumber are evanescent waves.

For wave modes, the well known Rayleigh-Lamb dispersion relation is represented by

$$\frac{\omega^4}{c_T^4} = 4k^2q^2\left[1-\frac{p}{q}\frac{\tan(ph/2+\gamma)}{\tan(qh/2+\gamma)}\right]$$

where

ω : angular frequency;

$c_T = \sqrt{\mu/\rho} = \sqrt{E/[2(1+\nu)\rho]}$: transverse wave speed;

E : Young's modulus; ν : Poisson's ratio;

$c_L = \sqrt{(\lambda+2\mu)/\rho} = \sqrt{E(1-\nu)/[(1+\nu)(1-2\nu)\rho]}$: longitudinal wave speed;

k : wavenumber;

$p^2 = \frac{\omega^2}{c_L^2} - k^2$, $q^2 = \frac{\omega^2}{c_T^2} - k^2$;

h : plate thickness;

γ : $\gamma = 0$ or $\pi/2$ represents symmetric and antisymmetric modes.

A complex dispersion curve for an isotropic plate with Poisson's ratio 0.33 is shown in the Figure 1.4 below.

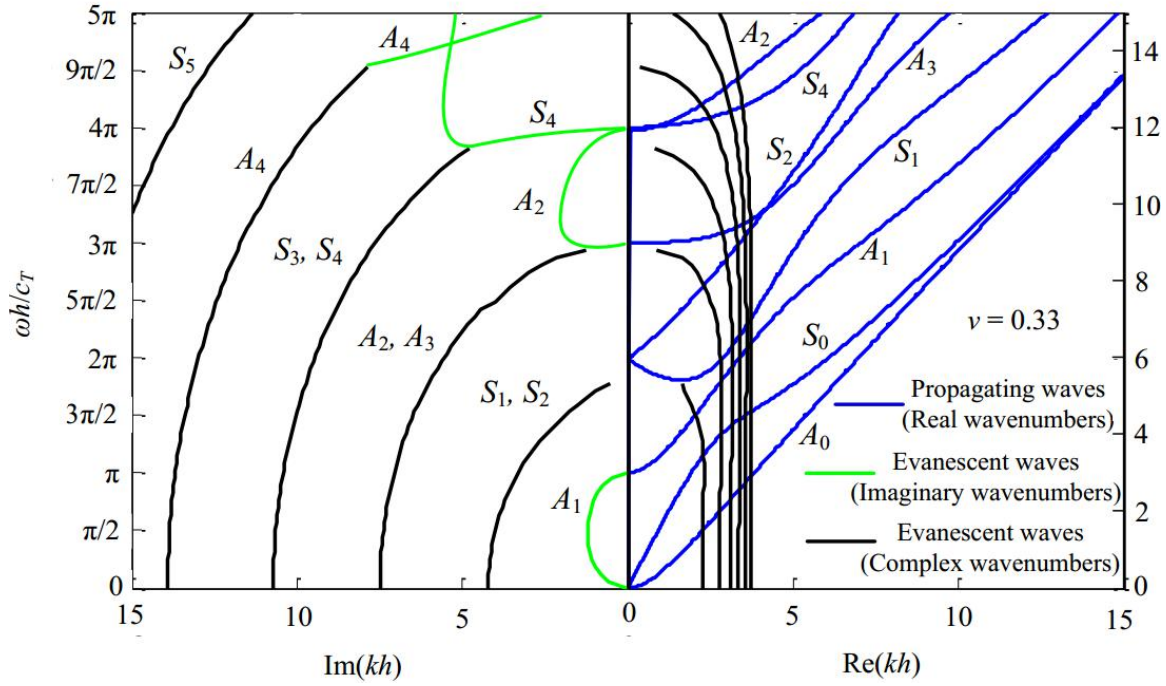

Figure 1.4 Lamb wave dispersion curves including both propagating and evanescent wave modes for an isotropic plate with Poisson's ratio 0.33 (Xiang and Yuan, 2015)

In the figure above, $S_0, S_1, S_2 \cdots$ denote symmetric Lamb wave modes and $A_0, A_1, A_2 \cdots$ denote antisymmetric Lamb wave modes. The wave modes on the left side of the above figure, where kh is imaginary refer to evanescent wave modes; and the wave

modes on the right side where kh is real refer to propagating wave modes. The frequency at which a wave mode transfers between evanescent wave and propagating wave is called the cut-off frequency. Below the cut-off frequency, waves are evanescent and are exponentially decaying with respect to space. The cut-off frequency of a certain mode can be calculated by substituting $k = 0$ to the dispersion equation.

(4) Improvements in the thesis compared to previous work

In all the previous papers concerning 3-D modeling of rectangular actuator attached on plate, none of them discussed the effect of the shear stress distribution over the contact surface on the actuator. The displacement of the actuator and the plate is not matched. Besides, the shear stress distribution over the entire contact surface is either assumed to be uniform stress distribution over the edges, or directly obtained from FEM software. No numerical analysis of the stress distribution has been analyzed.

Compared to existing work, this thesis has the following improvements:

(1) The length to width aspect ratio of the rectangular actuator is not under any constraints. The result in this thesis not only applies to slender actuators, but it also applies to square-like actuators.

(2) The stress distribution on the contact surface is expressed as summation of Chebyshev polynomials, the coefficient of which is determined by matching the displacement on the actuator and the plate.

(3) Not only Lamb waves, but also shear horizontal (*SH*) waves on the plate are taken into consideration.

(4) Near-field evanescent wave is also taken into consideration.

1.3 Objectives and Outline

The objective of this thesis is to provide analytical solutions for the interaction between rectangular PZT actuator/sensor and plate through electro-mechanical coupling. The approaches are threefold:

(1) Obtain analytical solution for rectangular PZT actuator response under prescribed harmonic/transient voltage;

(2) Obtain analytical solution for 3-D Lamb wave solution induced by surface bonded PZT actuator including propagating and evanescent waves;

(3) Obtain analytical solution for surface-bonded rectangular PZT sensor response.

1.4 Assumptions made in this model

The assumptions made in this model are listed below:

(1) Piezoelectric properties are constant over the frequency range of interest. This is verified by Gonzalez and Alemany (1996).

(2) The piezoelectric actuator is assumed to be of plane stress condition. This is true because the thickness of the plate is way larger compared to that of the actuator and the length and width in-plane of the actuator is way larger compared to the thickness of the actuator.

(3) Material damping is neglected. This assumption is based on the fact that, for metals, attenuation from finite excitation sources dominates amplitude decay of the guided wave (Raghavan and Cesnik, 2005).

(4) The existence of PZT sensor does not significantly affect the strain field on plate.

CHAPTER 2

Guided Waves in Plates

2.1 Introduction

In SHM, guided wave (GW) testing has been used widely. Though in many literature, 'guided wave' and 'Lamb wave' are interchangeable, in a more strict sense, Lamb wave only refers to guided waves in a flat, infinite and isotropic plate, while guided wave refers to any kind of waves in structural wave guide (Raghavan and Cesnik, 2005). Guided waves are complex to deal with due to its dispersion relation, which means that the wave velocity is related to propagating frequency. At any given frequency, there are at least two wave modes.

Under the excitation of a PZT transducer, or actuator, there will be shear stress generated at the contact surface of the actuator and the plate resulting from the deformation/strain of the actuator. The shear stress will result in propagating and non-propagating (evanescent) waves in the plate-like structures. Two major different waves are generated: Lamb waves and *SH* waves.

Lamb waves are elastic waves guided by plate-like structures. The reason why Lamb waves have been used for SHM is because it can propagate for long distances and interact with discontinuities (cracks) in the structures. Since Lamb waves can propagate for long distances, only single actuator can monitor the condition of a very wide region. While the incident Lamb wave accouters the damage in the structures, besides the transmitted incident wave, it will also generate damage back scattered waves. The scattering waves, which

contain the information of the damage, can be detected using sensors and being used to interpreter the location and size of the damage.

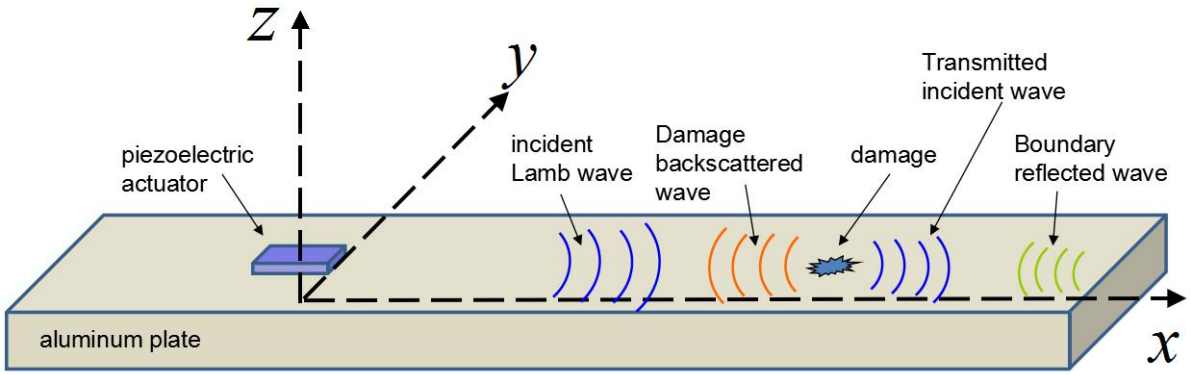

Figure 2.1 Illustration of Lamb waves used in SHM

Lamb waves are dependent on the geometrical and material properties. There are multi-modes of Lamb waves, mainly fall into the categories of symmetric modes (*S*) and antisymmetric modes (*A*).

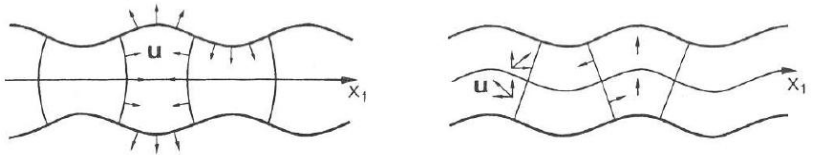

Figure 2.2 Symmetric (left) and antisymmetric (right) Lamb wave modes

For symmetric modes, the longitudinal displacement is symmetric and the transverse displacement is antisymmetric with respect to the mid-plane of the plate. For antisymmetric modes, the transverse displacement is symmetric and the longitudinal displacement is antisymmetric with respect to the mid-plane of the plate.

Lamb waves are also dispersive, which means that the wavenumber of each mode is dependent on frequency. The relation between the wavenumber and the frequency is called the dispersion relation.

Another kind of plate wave is called shear horizontal (*SH*) wave. The difference between Lamb waves and *SH* waves can be illustrated by the figure below.

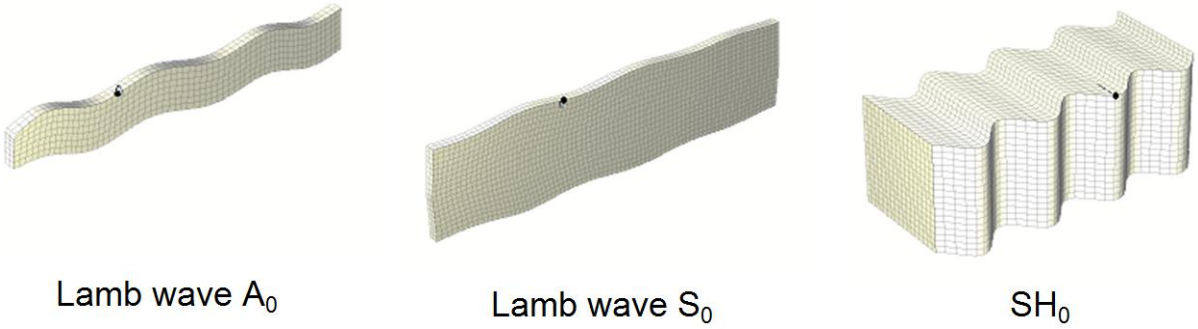

Figure 2.3 2-D Lamb waves and *SH* waves in plates (Figures downloaded from http://nojigon.webs.upv.es/simulations_waves.php)

The left two figures show typical 2-D Lamb wave antisymmetric and symmetric modes, and the Figure 2 on the right shows a typical 2-D *SH* wave mode. For Lamb waves, any particle in the structure moves in the wave propagation direction and the direction which is vertical perpendicular to the wave propagation direction. For *SH* wave mode, particles move in the direction which is horizontally perpendicular to the wave propagation direction.

Same as Lamb waves, *SH* waves are also dependent on geometrical and material properties. It also has multi-modes and it is also dispersive.

In this chapter, the plate waves are discussed in detail. This chapter is organized as follows. In Section 2, the characterization, dispersion relation and propagating/ evanescent

Lamb waves are introduced. In Section 3, the characterization, dispersion relation and propagating/ evanescent *SH* waves are introduced. Finally, some conclusions are drawn in Section 4.

2.2 Bulk waves

The equation of motion (EOM) for waves in a homogeneous, isotropic, linearly elastic medium without body forces is expressed as

$$\mu\nabla^2\mathbf{u} + (\lambda+\mu)\nabla\nabla\cdot\mathbf{u} = \rho\ddot{\mathbf{u}} \tag{2.1}$$

where $\mathbf{u} = (u_1, u_2, u_3)$ is the displacement vector at location $\mathbf{x} = (x_1, x_2, x_3)$ and time t. ρ is the material density; λ is the Lame's constant; μ is the shear modulus.

The displacement can be expressed using Helmholtz decomposition, which is the sum of a the gradient of scalar ϕ and curl of vector $\boldsymbol{\Psi}$.

$$\mathbf{u} = \nabla\phi + \nabla\times\boldsymbol{\psi} \tag{2.2}$$

The scalar potential ϕ has one component and the vector $\boldsymbol{\Psi}$ has three components. $\nabla\cdot\boldsymbol{\psi} = 0$ is an additional constraint in order to determine the three components of $\mathbf{u}$ uniquely. If $\nabla\cdot\boldsymbol{\psi} = 0$ is not used, some other conditions need to be specified in order to determine the three components of $\mathbf{u}$ from the four components of ϕ and $\boldsymbol{\Psi}$.

Substituting Eq. (2.2) into Eq. (2.1) yields

$$\mu\nabla^2[\nabla\phi + \nabla\times\boldsymbol{\psi}] + (\lambda+\mu)\nabla\nabla\cdot[\nabla\phi + \nabla\times\boldsymbol{\psi}] = \rho[\nabla\ddot{\phi} + \nabla\times\ddot{\boldsymbol{\psi}}]$$

Considering that $\nabla\cdot\nabla\phi = \nabla^2\phi$ and $\nabla\cdot\nabla\times\boldsymbol{\psi} = 0$, the above equation can be rewritten as

$$\nabla[(\lambda+2\mu)\nabla^2\phi-\rho\ddot{\phi}]+\nabla\times[\mu\nabla^2\boldsymbol{\psi}-\rho\ddot{\boldsymbol{\psi}}]=0 \tag{2.3}$$

For the EOM to be valid, ϕ and $\boldsymbol{\Psi}$ need to satisfy two wave equations

$$\begin{aligned}\nabla^2\phi-\frac{1}{c_L^2}\frac{\partial^2\phi}{\partial t^2}&=0\\ \nabla^2\boldsymbol{\psi}-\frac{1}{c_T^2}\frac{\partial^2\boldsymbol{\psi}}{\partial t^2}&=0\end{aligned} \tag{2.4}$$

where

$$\begin{aligned}c_L&=\sqrt{(\lambda+2\mu)/\rho}=\sqrt{[E(1-\nu)]/[(1+\nu)(1-2\nu)\rho]}\\ c_T&=\sqrt{\mu/\rho}=\sqrt{E/[2(1+\nu)\rho]}\end{aligned} \tag{2.5}$$

The ratio of c_L and c_T is defined as

$$\alpha=c_L/c_T=\sqrt{(\lambda+2\mu)/\mu}=\sqrt{2(1-\nu)/(1-2\nu)} \tag{2.6}$$

This shows that the scalar potential ϕ represents longitudinal waves traveling with wave speed c_L; vector potential $\boldsymbol{\psi}$ represents transverse waves traveling with wave speed c_T. Eq. (2.4) represents the displacement EOM in a simpler form, thus elastic wave propagation problems are normally addressed using the Helmholtz decomposition in terms of two potentials.

Since both longitudinal waves and transverse waves propagate in the volume (bulk) of a solid, they are both called bulk waves. The longitudinal (*L*) bulk wave is also called P-waves, pressure waves, compressional waves, dilatational waves, or irrotational waves.

Transverse waves are also called shear (S) waves, distorsional waves, equivoluminal waves, or rotational waves.

As can be seen from Eq. (2.5), bulk wave speeds are not related to frequency, which means they are non-dispersive waves. This is strictly true only when the solid is perfectly elastic that there is neither frequency-dependent energy attenuation nor dissipation mechanisms.

Under a source excitation, the stress wavefield can be represented by a plane wave:

$$\boldsymbol{u} = \boldsymbol{a} f(\hat{\boldsymbol{k}} \cdot \boldsymbol{x} / c_p - t) \tag{2.7}$$

In the above expression, $\boldsymbol{a}$ is the vector of the direction of displacement, $\hat{\boldsymbol{k}}$ is the unit vector of wave propagation direction $\boldsymbol{k}$, $\boldsymbol{k} = k\hat{\boldsymbol{k}}$. k is the wavenumber and $\boldsymbol{k}$ is wave vector.

For $\hat{\boldsymbol{k}} \cdot \boldsymbol{x} =$ constant, it describes a plane normal to the unit propagation wave vector $\hat{\boldsymbol{k}}$ and the constant represents the distance of the plane from the origin. For $t > 0$, the plane moves in the direction of $\hat{\boldsymbol{k}}$ with the speed of c_p. At time t, the equation of the plane $\hat{\boldsymbol{k}} \cdot x - c_p t =$ constant, is called the wavefront. Substituting the wavefield in Eq. (2.7) into the equation of motion in Eq. (2.1) yields

$$(\mu - \rho c_p^2)\boldsymbol{a} + (\lambda + \mu)(\hat{\boldsymbol{k}} \cdot \boldsymbol{a})\hat{\boldsymbol{k}} = 0 \tag{2.8}$$

In order for the above equation to be satisfied for two different vectors $\boldsymbol{a}$ and $\hat{\boldsymbol{k}}$, there are two different scenarios for satisfying Eq. (2.8):

$$\boldsymbol{a} /\!/ \hat{\boldsymbol{k}} \quad \text{or} \, \hat{\boldsymbol{k}} \cdot \boldsymbol{a} = 0 \tag{2.9}$$

(1) For $\boldsymbol{a} /\!/ \hat{\boldsymbol{k}}$

In this case, Eq. (2.8) yields

$$c_p = c_L = \sqrt{\frac{\lambda + 2\mu}{\rho}} \tag{2.10}$$

The time-varying displacement is parallel to the direction of propagation and the wave is bulk longitudinal wave.

(2) For $\hat{\boldsymbol{k}} \cdot \boldsymbol{a} = 0$

In this case, Eq. (2.8) yields

$$c_p = c_L = \sqrt{\frac{\mu}{\rho}} \tag{2.11}$$

The time-varying displacement is normal to the direction of propagation and the wave is bulk transverse or shear wave. The displacement can be in any direction in the plane normal to the propagation direction. When the (x_1, x_2) -plane is normal to $\hat{\boldsymbol{k}}$, motions can be either in (x_1, x_2) -plane or along x_3 direction (normal to (x_1, x_2) -plane). These transverse waves are called shear vertical (*SV*) and shear horizontal (*SH*) polarized waves respectively.

Steady-state waves are called harmonic waves; Waves that are not steady-state are called transient waves. In linear elastic materials, transient waves can be obtained by superimposing harmonic wave in Fourier integrals.

A plane harmonic wave propagating in the direction of $\hat{\boldsymbol{k}}$ with phase speed c_p can be represented in the form as

$$\boldsymbol{u} = \boldsymbol{a}\exp[i\omega(\hat{\boldsymbol{k}}\cdot\boldsymbol{x}/c_p - t)] = \boldsymbol{a}\exp[i(\hat{\boldsymbol{k}}\cdot\boldsymbol{x} - \omega t)] \tag{2.12}$$

where $c_p = \omega/k$ and $\boldsymbol{a}$ is a complex vector consisting of amplitude and phase angle. The real part of Eq. (2.12) is

$$Re(\boldsymbol{u}) = Re\left\{\boldsymbol{a}\exp[i\omega(\hat{\boldsymbol{k}}\cdot\boldsymbol{x} - t/c_p)]\right\} = |\boldsymbol{a}|\cos(\hat{\boldsymbol{k}}\cdot\boldsymbol{x} - \omega t + \eta) \tag{2.13}$$

where

$$\eta = \arg\boldsymbol{a}$$

The quantity

$$\theta(x,t) = \hat{\boldsymbol{k}}\cdot\boldsymbol{x} - \omega t \tag{2.14}$$

is called the phase of wave. It gives the relation between $\boldsymbol{x}$ and t. It can be used to determine when $\boldsymbol{u}$ has maximum (wave crest) or minimum (wave trough). In the phase wave equation, phase surfaces $\theta =$ constant are parallel planes. Therefore, Eq. (2.14) represent a plane wave whose planes of constant phases are normal to $\boldsymbol{k}$. The gradient of θ in space is $\boldsymbol{k}$, which is normal to the planes and the magnitude is the average number of crests per 2π units of distance. Similarly, the gradient of θ in time is ω, which is the average number of crests per 2π units of time.

$$\frac{\partial \theta}{\partial \boldsymbol{x}} = -\boldsymbol{k}$$
$$\frac{\partial \theta}{\partial t} = \omega \tag{2.15}$$

ω and $\boldsymbol{k}$ are both related to the period T, frequency f (cycles per second, Hz) and wavelength λ:

$$\omega = 2\pi / T$$
$$\omega = 2\pi f \tag{2.16}$$
$$k = 2\pi / \lambda$$

The relation between wavelength and wavenumber can be compared to that between the period:

$$\left.\begin{matrix}\text{Period} & T \\ \text{Frequency} & \omega\end{matrix}\right\} \omega = 2\pi / T \qquad \left.\begin{matrix}\text{Wavelength} & \lambda \\ \text{Wavenumber} & k\end{matrix}\right\} k = 2\pi / \lambda \tag{2.17}$$

2.3 Lamb Waves

In this Section, two dimensional Lamb waves will be characterized.

2.3.1 Lamb Wave Characterization

For (x_1, x_3) plane strain harmonic wave motion in an elastic plate, the guided wave consists of a standing *SH* wave in the x_2 direction and Lamb waves consisting of standing waves across the thickness and traveling waves in x_1 direction.

Using Helmholtz decomposition, the displacement vectors in x_1, x_3 direction can be represented using a the gradient of scalar ϕ and curl of vector $\boldsymbol{\Psi}$.

$$u_1 = \frac{\partial \phi}{\partial x_1} + \frac{\partial \psi}{\partial x_3}$$
$$u_3 = \frac{\partial \phi}{\partial x_3} - \frac{\partial \psi}{\partial x_1} \tag{2.18}$$

where the ψ in the above equations denotes ψ_2 and the subscript 2 has been omitted for simplicity. The gradient of scalar ϕ and curl of vector $\mathbf{\Psi}$ satisfy wave equations:

$$\frac{\partial^2 \phi}{\partial {x_1}^2} + \frac{\partial^2 \phi}{\partial {x_3}^2} = \frac{1}{c_L^2}\frac{\partial^2 \phi}{\partial t^2}$$
$$\frac{\partial^2 \psi}{\partial {x_1}^2} + \frac{\partial^2 \psi}{\partial {x_3}^2} = \frac{1}{c_T^2}\frac{\partial^2 \psi}{\partial t^2} \tag{2.19}$$

The solution of gradient of scalar ϕ and curl of vector $\mathbf{\Psi}$ can be considered as the form as below:

$$\phi = \Phi(x_3)\exp[i(kx_1 - \omega t)]$$
$$\psi = \Psi(x_3)\exp[i(kx_1 - \omega t)] \tag{2.20}$$

The above functions represent waves traveling in the x_1 direction with the same angular frequency ω and wavenumber k. Substituting Eq. (2.20) to Eq. (2.19) yields

$$\Phi(x_3) = A_1 \sin px_3 + A_2 \cos px_3$$
$$\Psi(x_3) = B_1 \sin qx_3 + B_2 \cos qx_3 \tag{2.21}$$

where

$$p^2 = \frac{\omega^2}{c_L^2} - k^2$$
$$q^2 = \frac{\omega^2}{c_T^2} - k^2 \tag{2.22}$$

Defining the phase velocity as:

$$c_p = \omega / k$$

Thus Eq. (2.22) can be rewritten as

$$p^2 = \omega^2 \left(\frac{1}{c_L^2} - \frac{1}{c_p^2} \right)$$
$$q^2 = \omega^2 \left(\frac{1}{c_T^2} - \frac{1}{c_p^2} \right)$$

In the expressions above, p, q can be real and/or imaginary according to the relation of c_p, c_L, c_T:

(1) $c_p > c_L > c_T$, or $k < \omega / c_L < \omega / c_T$, p, q are both real;

(2) $c_T < c_p < c_L$, or $\omega / c_L < k < \omega / c_T$, q is real and p is imaginary;

(3) $c_p < c_T < c_L$, or $k > \omega / c_T > \omega / c_L$, p, q are both imaginary.

From Eq. (2.18), Eq. (2.20) and Eq. (2.21), it can be seen that the displacement can be divided into symmetric and antisymmetric part.

The stress-displacement relation in tensor form can be expressed as

$$\sigma_{ij} = \lambda \delta_{ij} \varepsilon_{kk} + 2\mu \varepsilon_{ij} \tag{2.23}$$

In plane strain scenario, the stress-displacement relation is

$$\sigma_{11} = \lambda(\frac{\partial u_1}{\partial x_1} + \frac{\partial u_3}{\partial x_3}) + 2\mu \frac{\partial u_1}{\partial x_1}$$
$$\sigma_{33} = \lambda(\frac{\partial u_1}{\partial x_1} + \frac{\partial u_3}{\partial x_3}) + 2\mu \frac{\partial u_3}{\partial x_3} \tag{2.24}$$
$$\tau_{31} = \mu(\frac{\partial u_3}{\partial x_1} + \frac{\partial u_1}{\partial x_3})$$

Substituting Eq. (2.18) into Eq. (2.20) yields

$$\sigma_{11} = \lambda(\frac{\partial^2 \phi}{\partial x_1^2} + \frac{\partial^2 \phi}{\partial x_3^2}) + 2\mu(\frac{\partial^2 \phi}{\partial x_1^2} + \frac{\partial^2 \psi}{\partial x_1 \partial x_3})$$
$$\sigma_{33} = \lambda(\frac{\partial^2 \phi}{\partial x_1^2} + \frac{\partial^2 \phi}{\partial x_3^2}) + 2\mu(\frac{\partial^2 \phi}{\partial x_3^2} + \frac{\partial^2 \psi}{\partial x_1 \partial x_3}) \tag{2.25}$$
$$\tau_{31} = \mu(2\frac{\partial^2 \phi}{\partial x_1 \partial x_3} - \frac{\partial^2 \psi}{\partial x_1^2} + \frac{\partial^2 \psi}{\partial x_3^2})$$

The components for symmetric and antisymmetric modes are listed below:

(a) Symmetric modes:

$$\Phi = A_2 \cos px_3$$
$$\Psi = B_1 \sin qx_3$$
$$u_1 = ikA_2 \cos px_3 + qB_1 \cos qx_3$$
$$u_3 = -pA_2 \sin px_3 - ikB_1 \sin qx_3 \tag{2.26}$$
$$\sigma_{11} = \mu[(2p^2 - k^2 - q^2)A_2 \cos px_3 + 2ikqB_1 \cos qx_3]$$
$$\sigma_{33} = \mu[(k^2 - q^2)A_2 \cos px_3 - 2ikqB_1 \cos qx_3]$$
$$\tau_{31} = \mu[-2ikpA_2 \sin px_3 + (k^2 - q^2)B_1 \sin qx_3]$$

(b) Antisymmetric modes:

$$
\begin{aligned}
\Phi &= A_1 \sin px_3 \\
\Psi &= B_2 \cos qx_3 \\
u_1 &= ikA_1 \sin px_3 - qB_2 \sin qx_3 \\
u_3 &= pA_1 \sin px_3 - ikB_2 \cos qx_3 \\
\sigma_{11} &= \mu[(2p^2 - k^2 - q^2)A_1 \sin px_3 - 2ikqB_2 \sin qx_3] \\
\sigma_{33} &= \mu[(k^2 - q^2)A_1 \sin px_3 + 2ikqB_2 \sin qx_3] \\
\tau_{31} &= \mu[2ikpA_1 \cos px_3 + (k^2 - q^2)B_2 \cos qx_3]
\end{aligned}
\tag{2.27}
$$

2.3.2 Lamb Wave Dispersion Relation

Dispersion relation gives the relationship between wave number and frequency. It is obtained by substituting traction free boundary conditions into the symmetric and antisymmetric wave mode functions given in Eq. (2.26) and Eq. (2.27).

The traction free boundary condition at the two surfaces of the plate is expressed as:

$$\sigma_{33} = \tau_{31} = 0 \tag{2.28}$$

By substituting Eq. (2.26) and Eq. (2.27) into traction free boundary condition in Eq. (2.28), two homogeneous equations about coefficients A, B can be obtained. The only way for the two homogeneous equations to have non-zero solutions is to set the determinant to 0. Setting the determinant for symmetric mode to be zero yields

$$\frac{\tan qh/2}{\tan ph/2} = -\frac{4k^2pq}{(q^2-k^2)^2} \tag{2.29}$$

Setting the determinant for antisymmetric mode to be zero yields

$$\frac{\tan qh/2}{\tan ph/2} = -\frac{(q^2-k^2)^2}{4k^2pq} \tag{2.30}$$

The above two equations can be combined into one

$$\frac{\omega^4}{c_T^4} = 4k^2q^2\left[1 - \frac{p}{q}\frac{\tan(ph/2+\gamma)}{\tan(qh/2+\gamma)}\right] \tag{2.31}$$

In Eq. (2.31), $\gamma = 0$ for symmmetric modes and $\gamma = \pi/2$ for antisymmetric modes.

Eq. (2.31) is known as the Rayleigh-Lamb dispersion relation, which gives the relation between wave number and frequency for an infinite number of Lamb wave modes.

The traction-free boundary conditions gives a relation of coefficients A, B , thus A can be represented by an expression of B . The corresponding displacement components for wave modes are:

$$\begin{aligned} u_1 &= q\left[\cos(qx_3+\gamma)-\frac{2k^2}{k^2-q^2}\frac{\cos(qh/2+\gamma)}{\cos(ph/2+\gamma)}\cos(px_3+\gamma)\right]B \\ u_3 &= -ik\left[\sin(qx_3+\gamma)+\frac{2pq}{k^2-q^2}\frac{\cos(qh/2+\gamma)}{\cos(ph/2+\gamma)}\sin(px_3+\gamma)\right]B \end{aligned} \tag{2.32}$$

The corresponding stress components for wave modes are:

$$\begin{aligned} \sigma_{11} &= 2i\mu kq\left[\frac{2p^2-q^2-k^2}{k^2-q^2}\frac{\cos(qh/2+\gamma)}{\cos(ph/2+\gamma)}\cos(px_3+\gamma)+\cos(qx_3+\gamma)\right]B \\ \sigma_{33} &= 2i\mu kq\left[\frac{\cos(qh/2+\gamma)}{\cos(ph/2+\gamma)}\cos(px_3+\gamma)-\cos(qx_3+\gamma)\right]B \\ \tau_{31} &= \mu\left[\frac{4k^2pq}{k^2-q^2}\frac{\cos(qh/2+\gamma)}{\cos(ph/2+\gamma)}\sin(px_3+\gamma)+(k^2-q^2)\sin(qx_3+\gamma)\right]B \end{aligned} \tag{2.33}$$

2.4 Shear Horizontal (*SH*) Waves

2.4.1 *SH* Wave Characterization

Besides Lamb waves, another type of wave modes in plate is called shear horizontal (*SH*) waves. The main difference between Lamb wave and *SH* wave is the wave propagation direction. For example, if a plane has a surface normal x_3 , Lamb waves would be polarized

in the (x_1, x_3) plane with displacement components u_1, u_3 ; whereas *SH* waves will be polarized in x_2 direction and only have displacement component u_2.

Assuming the displacement is in the form:

$$u_2 = f(x_3)\exp[i(kx_1 - \omega t)] \tag{2.34}$$

The equation of motion is:

$$\frac{\partial^2 u_2}{\partial x_1^2} + \frac{\partial^2 u_2}{\partial x_3^2} = \frac{1}{c_T^2}\frac{\partial^2 u_2}{\partial t^2} \tag{2.35}$$

Substituting the displacement expression in Eq. (2.34) into Eq. (2.35) yields

$$f(x_3) = B_1 \sin qx_3 + B_2 \cos qx_3 \tag{2.36}$$

The traction free boundary condition at the upper and lower surfaces of the plate requires:

$$\tau_{23} = \mu\frac{\partial u_2}{\partial x_3} = 0 \tag{2.37}$$

Substituting Eq. (2.34) and Eq. (2.36) into boundary condition in Eq. (2.37) yields

$$B_1 \cos(qh/2) \pm B_2 \sin(qh/2) = 0 \tag{2.38}$$

The solution of Eq. (2.38) is

$$B_1 = 0, \sin(qh/2) = 0 \tag{2.39}$$

or

$$B_2 = 0, \cos(qh/2) = 0 \tag{2.40}$$

If $B_1 = 0$, the oppression of $f(x_3)$ becomes

$$f(x_3) = B_2 \cos qx_3$$

which is symmetric respect to the mid-plane of the plate.

If $B_2 = 0$, the oppression of $f(x_3)$ becomes

$$f(x_3) = B_1 \sin qx_3$$

which is antisymmetric respect to the mid-plane of the plate.

For both case, there is $qh = n\pi$ and $n = 0, 2, 4, \cdots$ for symmetric modes and $n = 1, 3, 5, \cdots$ for antisymmetric modes.

2.4.2 *SH* Wave Dispersion Relation

Recall the expression of q, the dispersion relation is shown as:

$$\left(\frac{\omega h}{c_T}\right)^2 = (kh)^2 + (n\pi)^2 \tag{2.41}$$

The dispersion relation can be further normalized as:

$$\overline{\omega}^2 = \overline{k}^2 + (n\pi)^2 \tag{2.42}$$

From the dispersion relation, it can be concluded that all *SH* wave modes are dispersive except $n = 0$.

The corresponding displacement for *SH* wave modes is

$$u_2^{\ n} = \begin{cases} B_n \cos\left(\dfrac{n\pi x_3}{h}\right), \text{symmmetric modes} \\ A_n \sin\left(\dfrac{n\pi x_3}{h}\right), \text{antisymmetric modes} \end{cases} \tag{2.43}$$

The corresponding stress for *SH* wave modes is

$$\begin{aligned} \tau_{23}^{\ n} &= \begin{cases} -B_n \mu q_n \sin\left(\dfrac{n\pi x_3}{h}\right), \text{symmmetric modes} \\ A_n \mu q_n \cos\left(\dfrac{n\pi x_3}{h}\right), \text{antisymmetric modes} \end{cases} \\ \tau_{12}^{\ n} &= \begin{cases} ik_n B_n \mu \cos\left(\dfrac{n\pi x_3}{h}\right), \text{symmmetric modes} \\ ik_n A_n \mu \sin\left(\dfrac{n\pi x_3}{h}\right), \text{antisymmetric modes} \end{cases} \end{aligned} \tag{2.44}$$

Noting that among all the expressions above, term $\exp[i(k_n x_1 - \omega t)]$ has been dropped.

2.5 Conclusions

In this chapter, two different kinds of plate waves are introduced: Lamb waves and shear horizontal waves. With the traction-free boundary condition, the dispersion relation for both waves are obtained, which gives the relation between wave-number and frequency for an infinite number of wave modes. The displacement and stresses for each wave modes are also listed.

CHAPTER 3

Theoretical Model for Propagating Plate Waves and Validation

The PZT actuator is bonded on an elastic plate which is infinitely long and infinitely wide. Suppose the *x*-*y* plane is on the mid-plane of the plate with *x* axis parallel to the length of the actuator and *y* parallel to the width of the actuator. The *z* axis crosses the center of the rectangular actuator. Let *u*, *v*, *w* denote the displacement components of the plate in the *x*, *y*, *z* directions respectively, which all depend on time *t*.

3.1 Steady-state time-harmonic wave motions generated by harmonic point forces

The point load F acting either on the surface or in the interior of a plate in an arbitrary direction can be equaled to the summation of the horizontal load Q and vertical load P, while both Q and P can be equaled as summation of symmetric mode and antisymmetric mode, as shown in Figure 3.1 below.

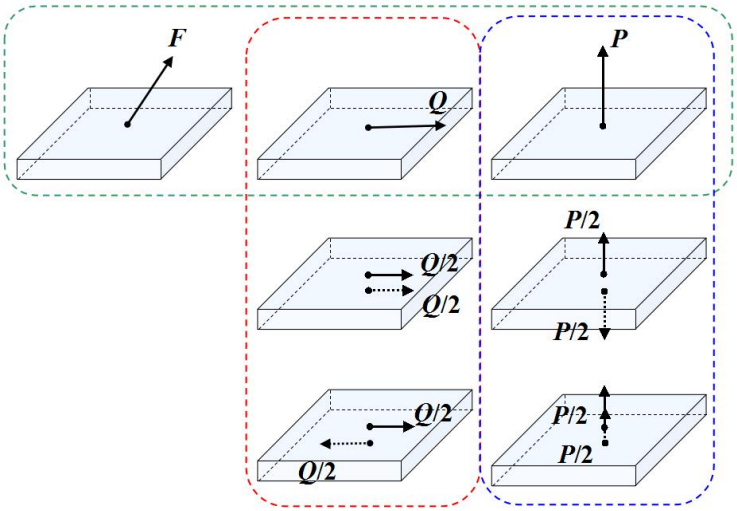

Figure 3.**1** Decomposition of a single point load (Achenbach and Xu, 1999)

The total displacement is the summation of the Lamb wave modes and *SH* modes under the two loadings. First, the solution form is given by carrier wave approach, and then the coefficients are solved by using elastodynamic reciprocity.

3.2 Wave forms given by carrier wave approach

The carrier wave approach proposed by Achenbach (1998) is a method providing steady state time harmonic solutions for general wave forms. In this paper, the time-harmonic waveform is in the form of $e^{-i\omega t}$. Displacement under any transient load can be obtained by the summation of the harmonic load of all the frequencies contained in the transient loading. The plate waveforms are a summation of the Lamb wave modes (symmetric and antisymmetric) and *SH* wave modes (symmetric and antisymmetric).

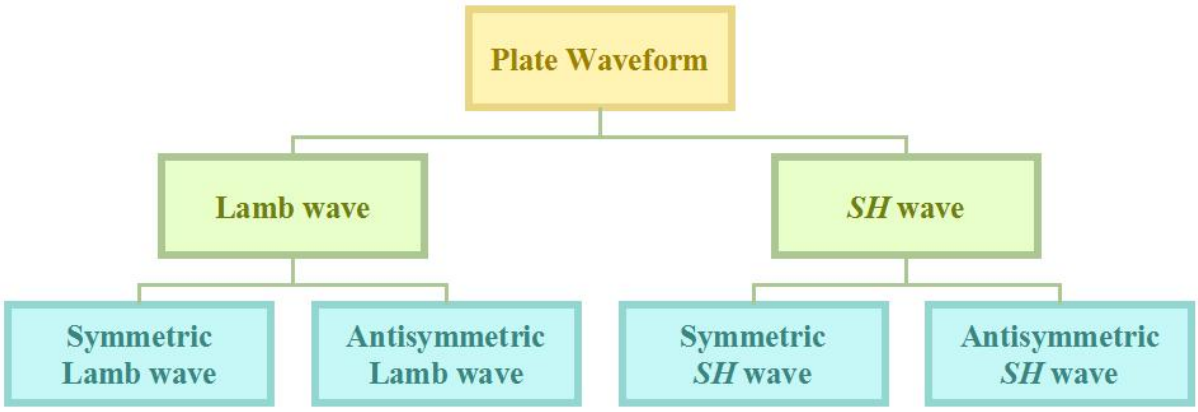

Figure 3.2 Decomposition of a plate waveform

Cylindrical coordinates are used for simplicity of calculation. The quantities in the expression below are normalized by length scale of h (plate thickness). Following this rule, the following variables can be normalized as

$$r^* = r/h, \quad \omega^* = \omega h / c_T, \quad k^* = kh, \quad F^* = F/(\mu h^2)$$

where r is radial distance; ω is the angular frequency of the harmonic wave; k is the wavenumber; F is force; μ is shear modulus. For simplicity, the asterisk will be dropped in the following.

Lamb wave modes

Following carrier wave approach, the displacement caused by a point force applied on the z axis can be expressed as

$$
\begin{aligned}
u_r^n &= \frac{1}{k_n} V^n(z) \frac{\partial \phi}{\partial r}(r,\theta), \\
u_\theta^n &= \frac{1}{k_n} V^n(z) \left[\frac{1}{r} \frac{\partial \phi}{\partial \theta}(r,\theta) \right], \\
u_z^n &= W^n(z) \phi(r,\theta),
\end{aligned}
\tag{3.1}
$$

where n denotes the n^{th} mode; k_n is the normalized wavenumber; V^n and W^n are defined respectively in Appendix; ϕ is the carrier wave function satisfying

$$
\frac{\partial^2 \phi}{\partial r^2} + \frac{1}{r} \frac{\partial \phi}{\partial r} + \frac{1}{r^2} \frac{\partial^2 \phi}{\partial \theta^2} + k_n^2 \phi = 0 \tag{3.2}
$$

The solution of Eq. (3.2) is given by

$$
\phi(r,\theta) = \Phi(k_n r) \cos\theta \tag{3.3}
$$

Substituting Eq. (3.3) back into Eq. (3.2), $\Phi(r)$ is the solution of

$$
\frac{\partial^2 \Phi}{\partial r^2} + \frac{1}{r} \frac{\partial \Phi}{\partial r} + (k_n^2 - \frac{1}{r^2}) \Phi = 0 \tag{3.4}
$$

For outgoing waves,

$$
\Phi(k_n r) = H_1^{(2)}(k_n r) \tag{3.5}
$$

where $H_1^{(2)}$ is Hankel function of the second kind, which is related to Bessel function:

$$
H_1^{(2)}(k_n r) = J_1(k_n r) - i Y_1(k_n r) \tag{3.6}
$$

where J_1 is Bessel function of the first kind and Y_1 is Bessel function of the second kind.

As for Hankel function $H_\alpha^{(2)}(z)$, for large values of z, asymptotic approximations of it are defined as

$$H_\alpha^{(2)}(z) \sim \left(\frac{2}{\pi z}\right)^{1/2} e^{-i(z-\pi/4-\alpha\pi/2)}$$

Substituting Eq. (3.5), Eq. (3.3) into Eq. (3.1) yields the displacement for symmetric modes

$$\begin{aligned} u_r^n &= V_S^n(z)\Phi'(k_n r)\cos\theta, \\ u_\theta^n &= -V_S^n(z)\left(k_n r\right)^{-1}\Phi(k_n r)\sin\theta, \\ u_z^n &= W_S^n(z)\Phi(k_n r)\cos\theta, \end{aligned}$$

where $\Phi'(\xi) = d\Phi / d\xi$. Similarly the displacement for antisymmetric modes can be derived as

$$\begin{aligned} u_r^n &= V_A^n(z)\Phi'(k_n r)\cos\theta, \\ u_\theta^n &= -V_A^n(z)\left(k_n r\right)^{-1}\Phi(k_n r)\sin\theta, \\ u_z^n &= W_A^n(z)\Phi(k_n r)\cos\theta, \end{aligned}$$

The derivative of Hankel function of the second kind is

$$\frac{d}{dx}H_1^{(2)}(x) = H_0^{(2)}(x) - \frac{H_1^{(2)}(x)}{x}$$

SH wave modes

For *SH* wave modes, the displacements only exist in the plane (*i.e.*, horizontal direction)

$$u_r^n = (1/l_n)\cos(n\pi z)\left[(1/r)\frac{\partial \psi}{\partial \theta}(r,\theta)\right],$$
$$u_\theta^n = (1/l_n)\cos(n\pi z)\frac{\partial \psi}{\partial r}(r,\theta). \tag{3.7}$$

where l_n is the wavenumber, ψ is the carrier wave function satisfying Eq. (3.2) and is given by

$$\psi(r,\theta) = \Psi(l_n r)\sin\theta \tag{3.8}$$

in which

$$\Psi(l_n r) = H_1^{(2)}(l_n r) \tag{3.9}$$

Summation of Lamb wave and SH wave modes

The total displacement under point load Q is a summation over the symmetric and antisymmetric modes of both Lamb waves and SH waves

$$\mathbf{u}^Q = \mathbf{u}^{QS} + \mathbf{u}^{QA} \tag{3.10}$$

For waves propagating in the positive r -direction, the symmetric part of the displacement solution is

$$\begin{aligned}
u_r^{QS} &= \cos\theta\left\{\sum_{m=0}^{\infty} A_m^S V_S^n(z)\left[H_0^{(2)}(k_m r) - (k_m r)^{-1}H_1^{(2)}(k_m r)\right] + \sum_{m=0}^{\infty} B_m^S \cos(m\pi z)(l_m r)^{-1}H_1^{(2)}(l_m r)\right\} \\
u_\theta^{QS} &= -\sin\theta\left\{\sum_{m=0}^{\infty} A_m^S V_S^n(z)(k_m r)^{-1}H_1^{(2)}(k_m r) + \sum_{m=0}^{\infty} B_m^S \cos(m\pi z)\left[H_0^{(2)}(l_m r) - (l_m r)^{-1}H_1^{(2)}(l_m r)\right]\right\} \\
u_z^{QS} &= \cos\theta\left[\sum_{m=0}^{\infty} A_m^S W_S^n(z)H_1^{(2)}(k_m r)\right]
\end{aligned} \tag{3.11}$$

where A_m^S and B_m^S (determined in Section 2.3) represent the coefficients for all the symmetric Lamb waves and symmetric SH waves respectively.

Similarly the antisymmetric parts of the displacement solution are given by

$$
\begin{aligned}
u_r^{QA} &= \cos\theta\left\{\sum_{m=0}^{\infty} A_m^A V_S^n(z)\left[H_0^{(2)}(k_m r)-(k_m r)^{-1}H_1^{(2)}(k_m r)\right]+\sum_{m=0}^{\infty} B_m^A \sin(m\pi z)(l_m r)^{-1}H_1^{(2)}(l_m r)\right\} \\
u_\theta^{QA} &= -\sin\theta\left\{\sum_{m=0}^{\infty} A_m^A V_S^n(z)(k_m r)^{-1}H_1^{(2)}(k_m r)+\sum_{m=0}^{\infty} B_m^A \sin(m\pi z)\left[H_0^{(2)}(l_m r)-(l_m r)^{-1}H_1^{(2)}(l_m r)\right]\right\} \\
u_z^{QA} &= \cos\theta\left[\sum_{m=0}^{\infty} A_m^A W_S^n(z)H_1^{(2)}(k_m r)\right]
\end{aligned}
\tag{3.12}
$$

where A_m^A, B_m^A are to be determined in Section 2.3.

Displacement under point load P is the same as Eq. (3.11) and (3.12) by omitting the terms related to B_m.

3.3 Elastodynamic reciprocity for point load along +x direction

The reciprocity (Achenbach, 1998) is a much elegant method in calculating time-harmonic motions than the traditional integral transform techniques. The reciprocity shows the relationship between two elastodynamic states of a same body, which can be mathematically expressed as

$$\int_V [(f_i^A-\rho\ddot{u}_i^A)u_i^B-(f_i^B-\rho\ddot{u}_i^B)u_i^A]dV=\int_S (u_i^A\sigma_{ij}^B-u_i^B\sigma_{ij}^A)n_j dS$$

A, B denotes two distinct states; f_i^A, f_i^B are body forces; V is the region; S is the boundary of region V. For two time-harmonic modes of the same frequency, the reciprocity theorem is simplified to

$$\int_V (f_i^A u_i^B - f_i^B u_i^A) dV = \int_S (u_i^A \sigma_{ij}^B - u_i^B \sigma_{ij}^A) n_j dS \tag{3.13}$$

As can be seen in Figure 3.1, the point load at the surface of the plate can be divided as a sum of symmetric loading and antisymmetric loading, with displacement expressed in Eq. (3.10) and Eq. (3.12) respectively. The corresponding coefficients A_m^S, B_m^S and A_m^A, B_m^A are to be determined respectively by assuming different virtual states in Sections 2.3.1 and 2.3.2.

3.3.1. Determination of coefficients for harmonic vertical point load scenario

The region under consideration is $0 \le r \le b, -h \le z \le h, 0 \le \theta \le 2\pi$. Set state A as load Q applied at $z_0 = 0, r = 0, \theta = 0$ in x axis.

State *B* is set to be a single symmetric Lamb-wave mode comprising the outgoing and converging wave. The displacement in state *B* is expressed as

$$\begin{aligned}
u_r^n &= (1/2) V_S^n(z)[\Phi'(k_n r) + \overline{\Phi}'(k_n r)]\cos\theta, \\
u_\theta^n &= -(1/2) V_S^n(z)(k_n r)^{-1}[\Phi(k_n r) + \overline{\Phi}(k_n r)]\sin\theta, \\
u_z^n &= (1/2) W_S^n(z)[\Phi(k_n r) + \overline{\Phi}(k_n r)]\cos\theta.
\end{aligned}$$

In this scenario, the left hand side of reciprocity theorem becomes $Qu_r^n(0,0,0) = (1/2)QV_S^n(0)$. Substituting the displacement and stress into the right hand side (RHS) of the reciprocity theorem, the coefficient of each wave mode can be determined.

3.3.2. Determination of coefficients for harmonic vertical point load scenario

For loading parallel to the z -direction (or called vertical loading), only Lamb waves exist, thus only the coefficients A_m^S and A_m^A need to be determined. For a distinction from horizontal loading, A_m^S and A_m^A of vertical loading is replaced by C_m^S and C_m^A.

Symmetric Lamb wave modes : *Determination of* C_m^S

Force can be normalized by $F = f/(\mu h^2)$ with μ being the shear modulus and h the length normalization scale. When a normalized vertical point load P (point load along the z direction) is applied on a plate, SH wave will not be present. Thus the displacement form would be as in Eq. (3.10) and Eq. (3.12) without the SH wave terms (the terms with amplitudes B_m). Setting state A as symmetric loading shown in Figure 3.1 with displacements shown in Eq. (3.10) without the SH wave terms. State B (the virtual state) is set to be a single symmetric Lamb-wave mode comprising the outgoing (or diverging) and converging wave. The domain where $0 \le r \le \infty$, $-h \le z \le h, 0 \le \theta \le 2\pi$ is under consideration. From Eq. (3.1) and (3.3), the displacement components for state B are:

$$
\begin{aligned}
u_r^n &= (1/2)V_S^n(z)[\Phi'(k_n r) + \overline{\Phi}'(k_n r)]\cos\theta, \\
u_\theta^n &= -(1/2)V_S^n(z)(k_n r)^{-1}[\Phi(k_n r) + \overline{\Phi}(k_n r)]\sin\theta, \\
u_z^n &= (1/2)W_S^n(z)[\Phi(k_n r) + \overline{\Phi}(k_n r)]\cos\theta.
\end{aligned} \tag{3.14}
$$

Substituting Eq. (3.10) and Eq. (3.14) into the reciprocity theorem in Eq. (3.13) yields

$$
C_m^S = \frac{k_m}{4i}\frac{PW_S^m(\mathrm{z}_0)}{I_{mm}^S} \tag{3.15}
$$

where z_0 is the depth location where force is applied and I_{mm}^S is listed in the Appendix.

Antisymmetric Lamb wave modes: *Determination of* C_m^A

Similarly, the coefficient C_m^S can be obtained by

$$
C_m^S = \frac{k_m}{4i}\frac{PW_S^m(\mathrm{z}_0)}{I_{mm}^S} \tag{3.16}
$$

where I_{mm}^A is listed in the Appendix.

The total displacement under harmonic vertical point load would be the sum of the symmetric Lamb wave and the antisymmetric Lamb wave.

3.3.3 Determination of coefficients for harmonic horizontal point load along +*x* direction

Symmetric Lamb wave modes: *Determination of* A_n^S

When a horizontal load is applied at the position $z = h, r = 0, \theta = 0$, which can be split into a symmetric and antisymmetric loads. State A is thus set to be the symmetric part of the load. State B is set to be a single symmetric Lamb-wave mode comprising the outgoing and converging wave. Substituting Eq. (3.10) and Eq. (3.14) into the reciprocity theorem in Eq. (3.13), yields

$$A_n^S = \frac{k_n}{4i} \frac{QV_S^n(z_0)}{I_{nn}^S} \tag{3.17}$$

Antisymmetric Lamb wave modes: *Determination of* A_n^A

Similarly, the coefficient for antisymmetric Lamb wave modes can be obtained

$$A_n^A = \frac{k_n}{4i} \frac{QV_A^n(z_0)}{I_{nn}^A} \tag{3.18}$$

Symmetric SH wave modes: *Determination of* B_n^S

Set state A as symmetric loading with displacements shown in Figure 3.2 and state B as a single symmetric SH wave consisting of the outgoing and converging waves and using reciprocity, yields

$$B_n^S = \frac{1}{4i}\frac{Q}{J_{nn}} \quad \text{for} \quad n = 0,2,4,\cdots \tag{3.19}$$

where J_{nn} is listed in the Appendix.

Antisymmetric SH wave modes: *Determination of* B_m^A

Set state A as antisymmetric loading with displacements shown in Figure 3.2 and state B as a single antisymmetric SH mode comprising the outgoing and converging waves and using reciprocity, yields

$$B_n^A = \frac{1}{4i}\frac{Q}{J_{nn}} \quad \text{for} \quad n = 1,3,5,\cdots \tag{3.20}$$

3.4 Verification of theoretical model for propagating plate wave under point load along +*x* direction

In order to verify the correctness of the theoretical model of propagating waves in plate, this chapter verifies the solution here with the FEA result obtained in COMSOL. The material properties for the aluminum plate are listed below:

Table 3.1 Material properties and geometry of Al-6061 aluminum plate

Symbol	Description	Value	Unites
ρ	density	2700	kg/m^3
E	Young's modulus	70	GPa
ν	Poisson's ratio	0.33	
h	thickness	3.2	mm

Table 3.2 Wavenumbers of some Lamb wave modes at 100 *kHz*

S_0	S_1 / S_2	S_3 / S_4	
114.84	704.48+1306*i*	970.05+3343.22*i*	
A_0	A_1	A_2 / A_3	A_4 / A_5
391.7	309.3125*i*	865.89+2337.5*i*	1047.8+4340.625*i*

The loading tested are point load, line load and surface load. The result is summarized in Section 3.4, Section 3.5, Section 3.6 respectively.

3.4.1 Theoretical result for propagating plate wave under point load

The following study is conducted at frequency $f = 100\,kHz$, thus the angular frequency $\omega = 2\pi f = 2\times 10^5 \times \pi \;\; rad/\sec$. For Al-6061 aluminum plate, the shear velocity is $c_T = \sqrt{\mu/\rho} = 3171.3 m/s$. Therefore, for a 3.2 mm thick plate, the normalized term $\omega h_{plate} / c_T = 0.634$. For Lamb waves, from the dispersion curve, for it can be seen that there will be S_0 Lamb wave mode and A_0 Lamb wave mode.

The Lamb wave wavenumbers and wavelengths at $f = 100\,kHz$ are listed in the Table 3 below:

Table 3.3 Wavenumber and wavelength of Lamb waves at 100*kHz*

Lamb wave mode	S_0	A_0
wavenumber k	114.84	391.7
wavelength λ (obtained by $\lambda = 2\pi / k$)	0.0547	0.016

For *SH* wave, the dispersion relation is given as

$$\left(\frac{\omega h_{plate}}{c_T}\right)^2 = (kh_{plate})^2 + (n\pi)^2$$

where $n = 0, 2, 4, \cdots$ for symmetric modes, and $n = 1, 3, 5, \cdots$ for antisymmetric modes and h_{plate} is plate thickness. At the given frequency $f = 100\,kHz$, thus the angular frequency $\omega = 2\pi f = 2 \times 10^5 \times \pi \;\; rad/\sec$ and the left hand side of the dispersion relation equals to 0.402. Thus there will only be SH_0 wave. The normalized wavenumber and wavelength are listed below:

Table 3.4 Wavenumber and wavelength of *SH* wave at 100*kHz*

SH wave mode	SH_0
Wavenumber k $(1/meter)$ (obtained from dispersion curve)	198.1358
Wavelength λ (meters) (obtained by $\lambda = 2\pi / k$)	0.0317

To sum up, all the propagating wave modes at $f = 100\;\; kHz$ are listed below:

Table 3.5 Wave number and wavelength of Lamb waves at 100 *kHz*

Lamb wave mode	Lamb S_0	Lamb A_0	SH_0
Wave number k $(1/m)$ (obtained from dispersion relation)	114.8	391.7	198.1
Wavelength λ (mm) (obtained by $\lambda = 2\pi / k$)	54.7	16	31.7
$1/\lambda$ (m^{-1})	18.3	62.5	31.5

It can be seen from the two tables that the minimum wavelength is 16 mm (Lamb wave A_0 mode) and the maximum wavelength is 54.7 mm (Lamb wave S_0 mode). According to our study previously on the PML length, it is chosen to be half of the maximum wavelength, which is 54.7/2=27.35 *mm* For the infinite plate, the size of the rectangular area under observation is set to be 2.2 times of the maximum wavelength, 54.7×2=120.34 *mm*. The thickness of the aluminum plate is 3.2 *mm*.

A point load along the plate upper surface is with amplitude of 10^3 *N*. The *x*-*y* plane is set to be the middle layer of the plate and the *z* axis passes the point load application point. The *x*-axis is set to be in the direction of the point force direction.

The results for displacement elements are calculated in Matlab, as shown below.

Figure 3.3 Theoretical result of (a) displacement *u* (b) displacement *v* (c) displacement *w* under point loading

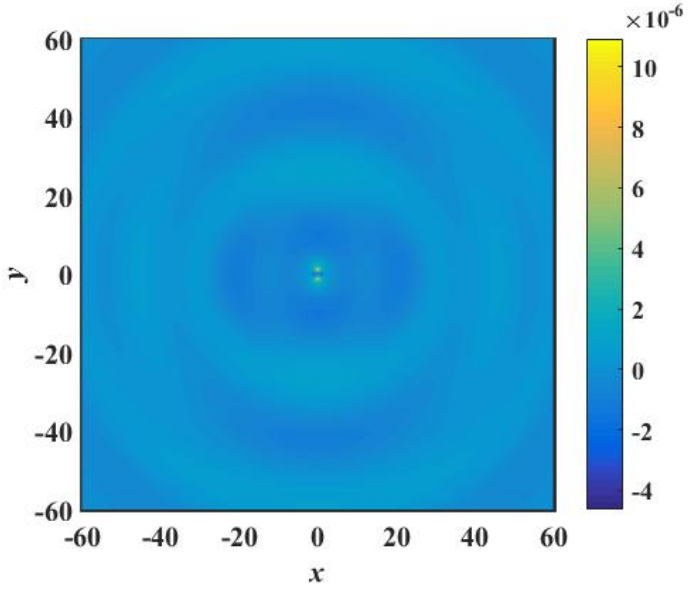

(units for *x*-*y* axis: *mm*)

(a)

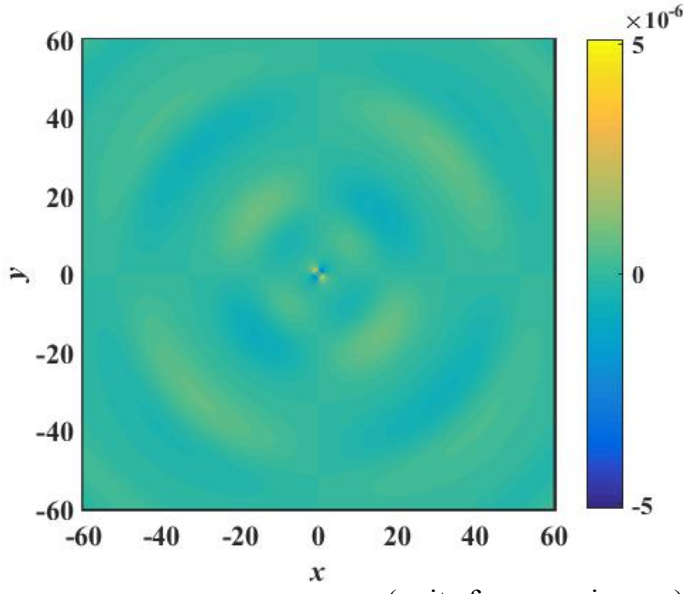

(units for *x*-*y* axis: *mm*)

(b)

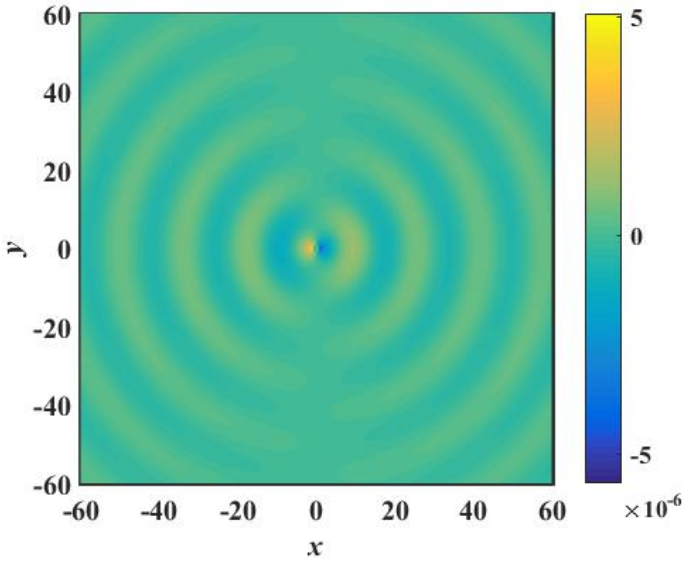

(units for *x*-*y* axis: *mm*)

(c)

In order to verify the theoretical result, FEA is conducted in the software COMSOL.

3.4.2 FEA result for propagating plate wave under point load

First of all, point loads, as well as edge loads in 3-D are singularities, hence are NOT good practice in FEA software, but sometimes you can use the results if you do NOT analyze in detail the local stress concentration. One method to avoid singularities in COSOL is to replace the line load with a surface load of 3-D Gaussian distribution over a square area of $a_w \times a_w$. This results a concentrated load, but no pure singularities, if the Gaussian is larger than a few mesh elements. The plot of a 3-D Gaussian distribution is

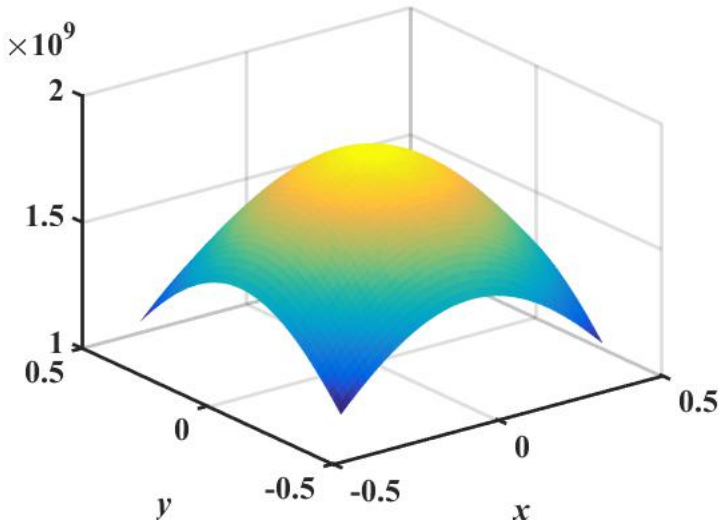

Figure 3.4 Plot of Gaussian load distribution (units for *x*, *y* axis: *mm*, unit for *z* axis: *N*)

In COMSOL, the Gaussian function is applied on the plate upper surface over a small square region. The three-dimensional Gaussian function is defined by

$$Gaussian(x,y) = Ae^{-\frac{x^2}{a_w^2}-\frac{y^2}{a_w^2}}$$

where A is defined as

$$A = \frac{1}{\pi a_w^2 Erf^2[1/2]}$$

And 'Erf' is the error function define as

$$erf(x) = \frac{2}{\sqrt{\pi}}\int_0^x e^{-t^2}dt$$

The value of $Erf^2[1/2]$ can be calculated in Mathematica as 0.27092.

The integration of the Gaussian function over the entire load-applying surface is calculated in Mathematica as 10^3. This indicates the integration of the Gaussian function is 10^3, which means the total force on the area has the amplitude of 10^3.

The size of the plate is 120 *mm* along both x and y axis, which is 2.2 times of the maximum wavelength. The height of the plate is 3.2 *mm*. The width of the perfect matched layer is set to be half of the maximum wavelength.

The maximum size of elements on the plate and PML are 1/20 of the minimum wavelength (minWL), while the element size on the area where Gaussian load is applied is even smaller (1/60 of minimum wavelength) than that of the plate. The load-applying surface size a_w is chosen to be 1/20 of minimum wavelength.

The displacement components when a_w = minWL/20 on plate upper surface are as follows:

Figure 3.5 COMSOL result for (a) displacement *u* (b) displacement *v* (c) displacement *w* for Gaussian point loading on plate upper surface

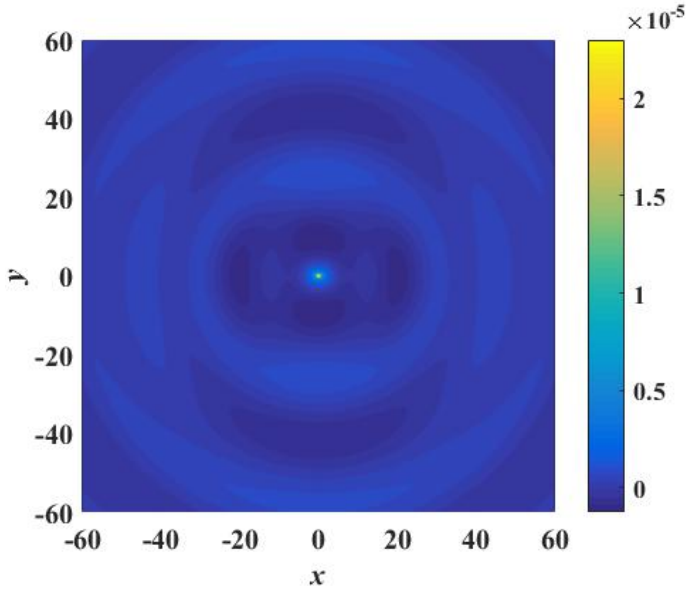

(units for *x*-*y* axis: *mm*)

(a)

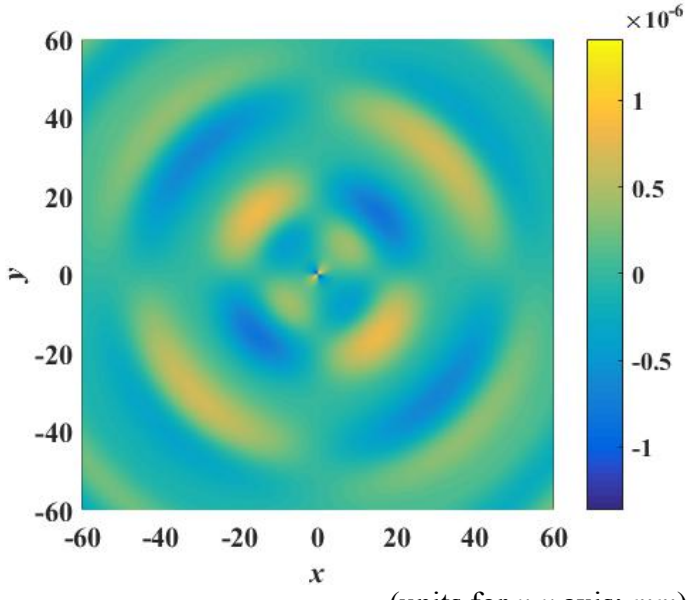

(units for *x*-*y* axis: *mm*)

(b)

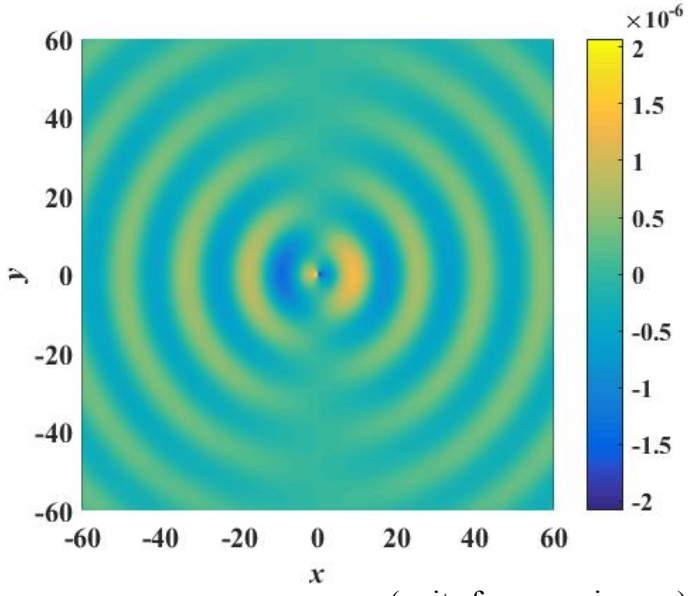

(units for *x*-*y* axis: *mm*)

(c)

From the color bar in the above figure, it can be seen that maximum and minimum value of the displacement is different from the analytical result. This is due to two causes: (1) analytical solution uses actual point loading while in COMSOL point load is replaced by Gaussian surface loading to avoid singularity; (2) the evanescent wave modes near the force applying area is not considered here in the analytical solution. In order to better compare the analytical solution and FEA solution, plate displacements along several monitoring lines are listed in the session below.

4.3.3. Comparing Matlab result with FEA result under Gaussian load

The scenarios of theoretical solution and FEA result when mesh size = minWL/20 are compared in this Section.

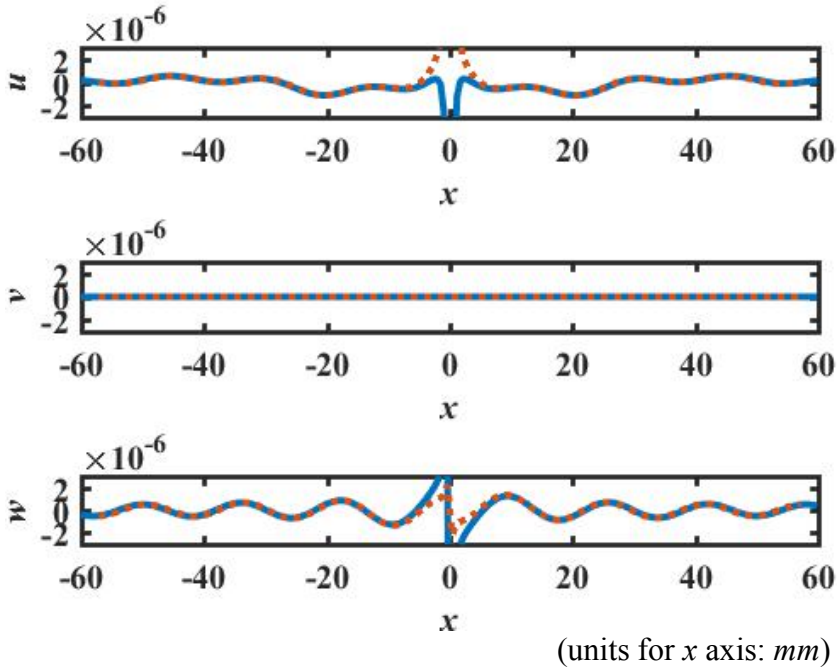

Figure 3.6 Comparing displacement under point load on along 0° (line I) for theoretical solution and FEA solution under Gaussian load. Solid blue line: analytical solution; Dotted red line: COMSOL solution

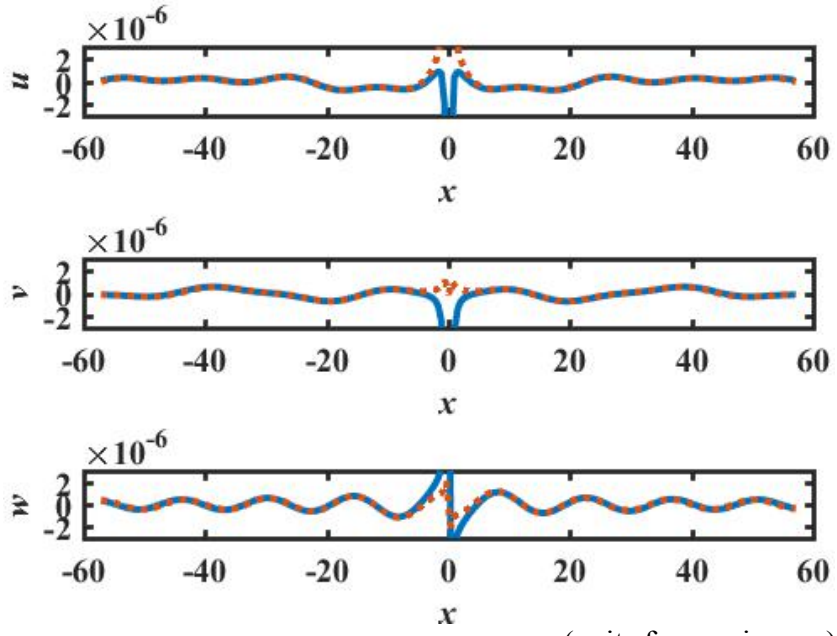

(units for *x* axis: *mm*)

Figure 3.7 Comparing displacement under point load on along atan(1/2) (line II) for theoretical solution and FEA solution under Gaussian load. Solid blue line: analytical solution; Dotted red line: COMSOL solution

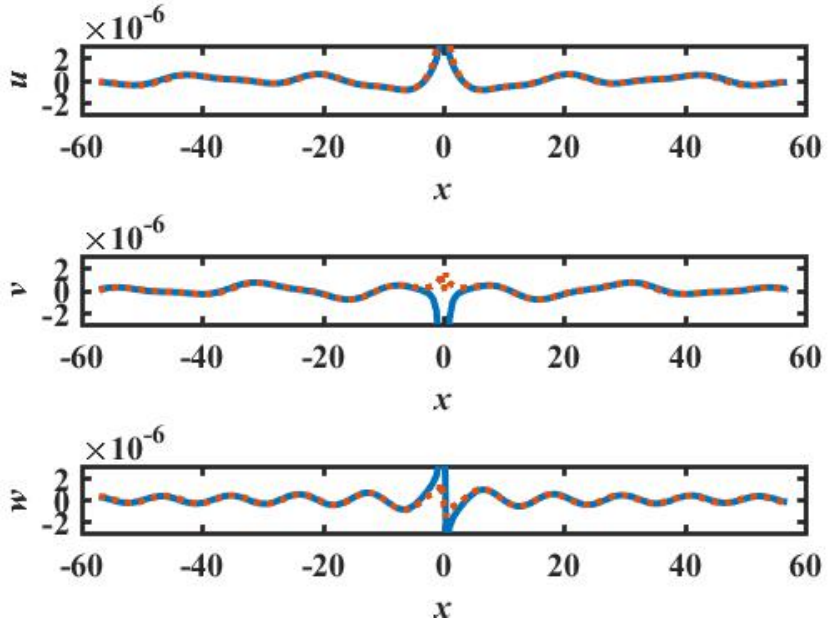

(units for *x* axis: *mm*)

Figure 3.8 Comparing displacement under point load on along 45º (line III) for theoretical solution and FEA solution under Gaussian load. Solid blue line: analytical solution; Dotted red line: COMSOL solution

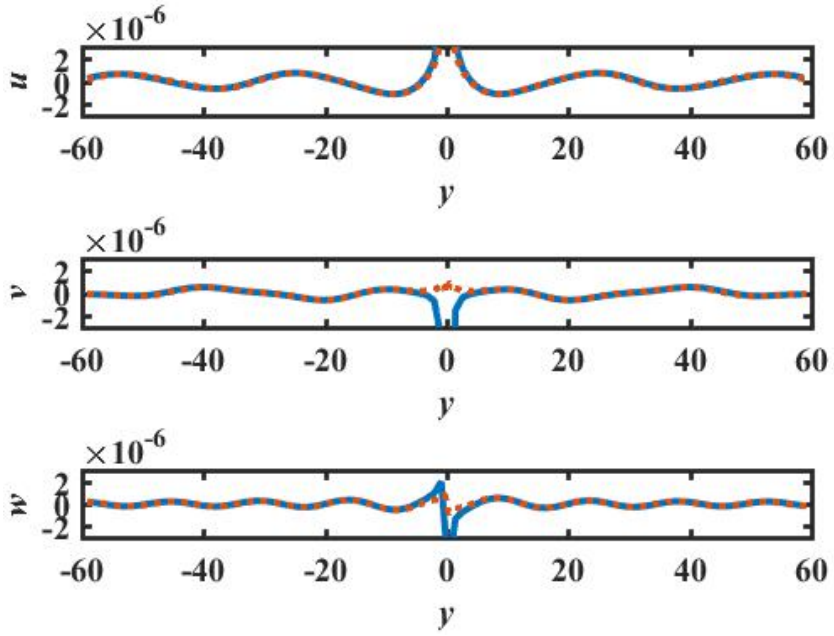

(units for horizontal axis: *mm*)

Figure 3.9 Comparing displacement under point load on along atan(2) (line IV) for theoretical solution and FEA solution under Gaussian load. Solid blue line: analytical solution; Dotted red line: COMSOL solution

It can be seen that displacement match pretty well along these four monitoring lines. The difference mainly resides on the area near the origin, where the force is applied. This is because in the theoretical solution, only propagating waves are concerned, while in the COMSOL results, besides propagating waves, there is also non-propagating waves near the force-applying position.

3.5 Verification of theoretical model for propagating plate wave under line load along +*x* direction

After the verification of the theoretical solution for plate propagating wave under point load., Section 4.5 is going to extend the analytic solution to line load and the solution will be verified by comparing to FEA result obtained in COMSOL.

3.5.1 Theoretical result for propagating plate wave under line load

The following study is conducted at frequency $f = 100\,kHz$. The Lamb wave and *SH* wave wavenumbers and wavelengths at $f = 100\,kHz$ are listed in the Table 3.5.

It can be seen from the two tables that the minimum wavelength is 16 mm (Lamb wave A_0 mode) and the maximum wavelength is 54.7 *mm* (Lamb wave S_0 mode). According to our study previously on the PML length, it is chosen to be half of the maximum wavelength, which is 54.7/2=27.35 *mm* For the infinite plate, the size of the rectangular area

under observation is set to be $p_w \times p_l$, where $p_w = \max WL \cdot 1.6 = 87.52\ mm$ and $p_l = \max WL \cdot 1.6 = 87.52\ mm$. The thickness of the aluminum plate is 3.2 mm.

The *x*-*y* plane is set to be the middle layer of the plate. A single line loads are applied on the plate upper surface:

$$f_x = 10^5\ N/m \quad \text{at} \quad x = p_w/5 = 17.504\ mm, -14.587\ mm = -p_l/6 < y < p_l/6 = 14.587\ mm$$

The results for displacement elements are calculated in Matlab, as shown below.

Figure 3.10 Theoretical result of (a) displacement *u* (b) displacement *v* (c) displacement *w* under line loading

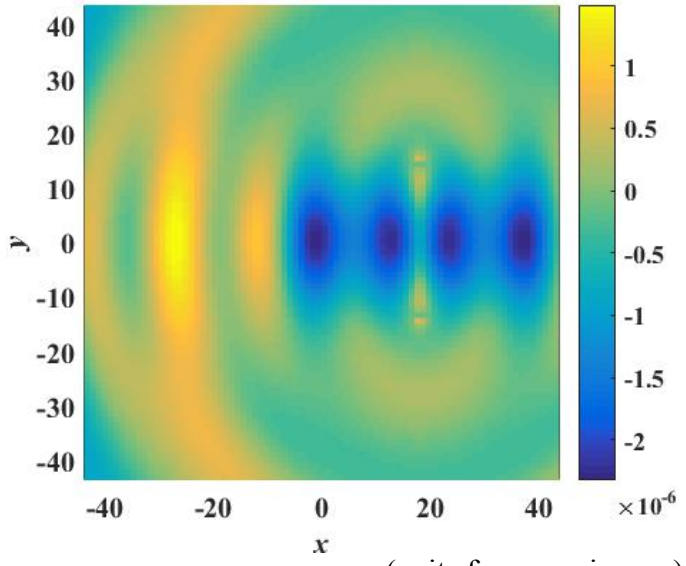

(units for *x*-*y* axis: *mm*)

(a)

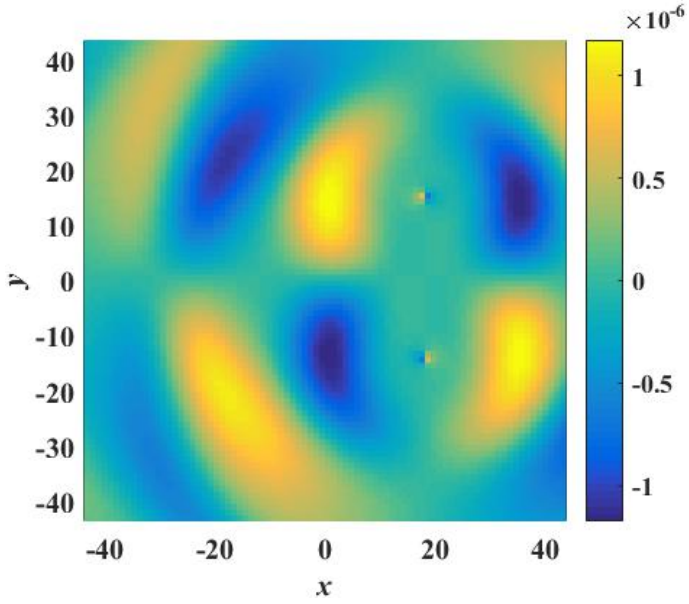

(units for *x*-*y* axis: *mm*)

(b)

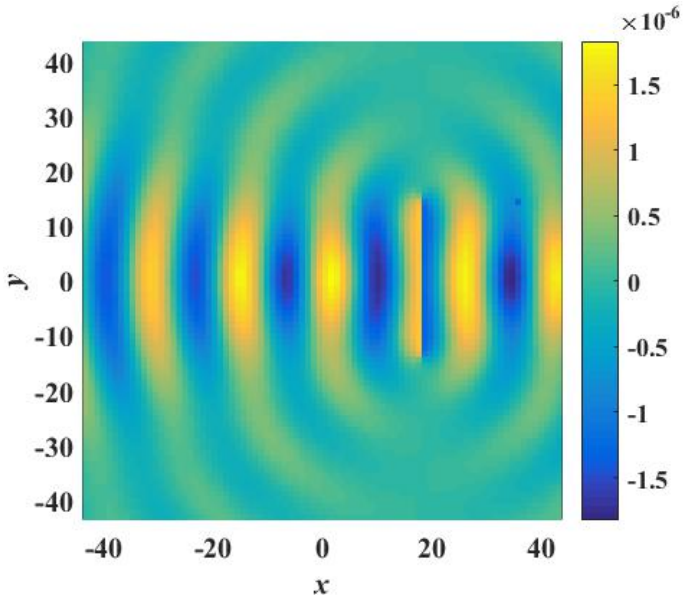

(units for *x*-*y* axis: *mm*)

(c)

In order to verify the theoretical result, FEA is conducted in the software COMSOL.

3.5.2 FEA result for propagating plate wave under line load

Since point loads, as well as edge loads in 3-D are singularities, hence are NOT good practice, but sometimes you can use the results if you do NOT analyze in detail the local stress concentration. One method to avoid singularities in COMSOL is to replace the line load with a surface load of 3-D Gaussian distribution over a rectangular area of $a_w \times a_l$, where $a_w = \text{minWL}/10 = 1.6\,mm$ and $a_l = p_l / 3 = 29.173\,mm$. The center of this rectangular area is located at $(p_w / 5, 0) = (17.504\,mm, 0)$ on the plate upper surface. This results a concentrated load, but no pure singularities, if the Gaussian is larger than a few mesh elements.

In COMSOL, the Gaussian function is applied on the plate upper surface over a small square region. The three-dimensional Gaussian function is defined by

$$Gaussian(x, y) = Ae^{-\frac{x^2}{a_w^2}}$$

In order to have a unit force of 10^5 N/m, there is:

$$\int_{y=-a_l/2}^{a_l/2}\int_{x=-a_w/2}^{-a_w/2} Ae^{-\frac{x^2}{a_w^2}} dxdy = 10^5 a_l$$

Solving the above equation for *A*, yields

$$A = \frac{108394}{a_w}$$

The size of the rectangular area under observation is set to be $p_w \times p_l$, where $p_w = \max WL \cdot 1.6 = 87.52\ mm$ and $p_l = \max WL \cdot 1.6 = 87.52\ mm$. The thickness of the aluminum plate is 3.2 *mm*. The width of the perfect matched layer is set to be half of the maximum wavelength.

The parameters for perfect matched layer (PML) is set to be SF (scaling factor) = 2, SCP (scaling curvature parameter) = 3.

The maximum size of elements on the plate and PML are 1/12 of the minimum wavelength, while the element size on the area where Gaussian load is applied is even smaller (1/40 of minimum wavelength) than that of the plate.

From the previous section of using Gaussian function representing point load, it was concluded that when $a_w = \min WL / 10$, the plate responses is the same as when $a_w = \min WL / 20$. This shows that the Gaussian distribution over a surface result in a converged result and can resemble a point load when $a_w = \min WL / 10$. Therefore, in this line load study, $a_w = \min WL / 10$ is chosen to represent the width of the Gaussian load. The unit line load is $10^5\ N/m$ along $+x$ direction.

The displacement components on plate upper surface are:

Figure 3.11 Displacement component (a) u (b) v (c) w under Gaussian line load in COMSOL

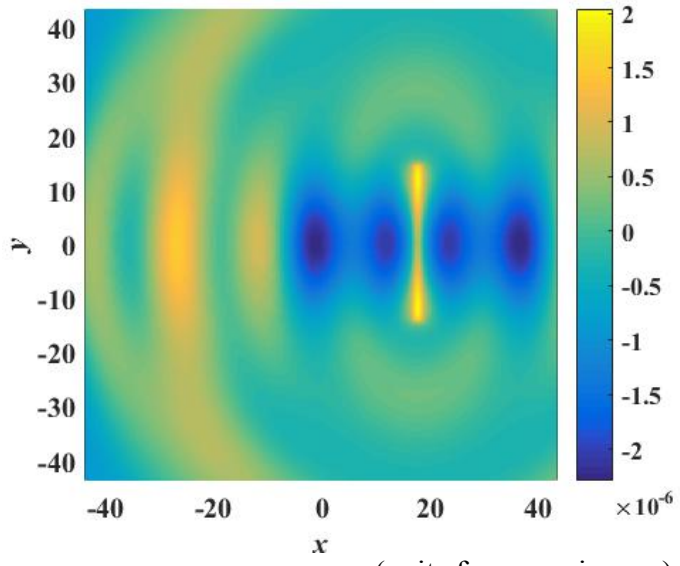

(units for *x*-*y* axis: *mm*)

(a)

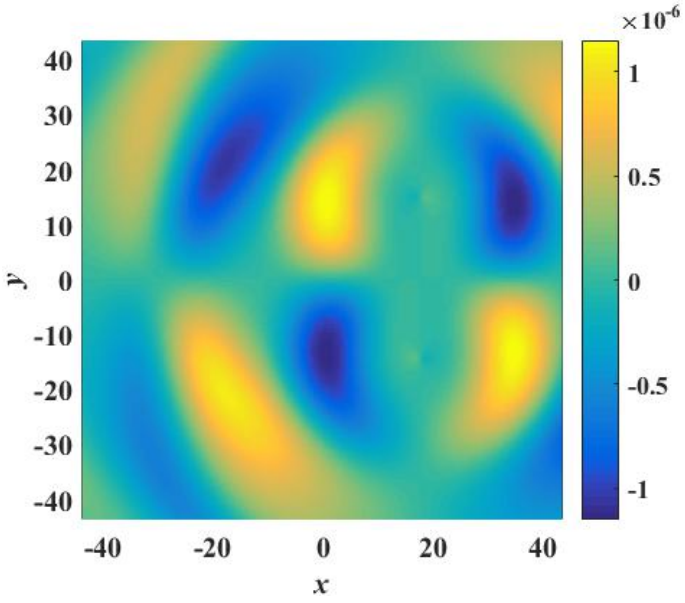

(units for *x*-*y* axis: *mm*)

(b)

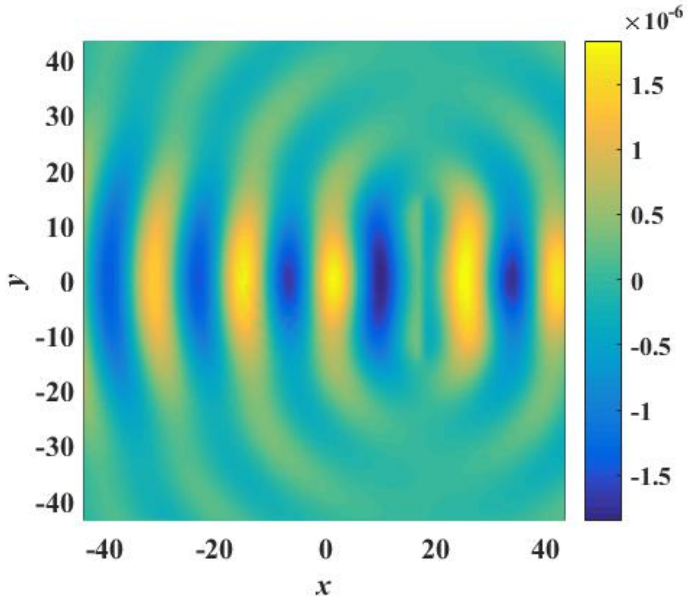

(units for *x*-*y* axis: *mm*)

(c)

3.5.3. Comparing analytical result with FEA result under line load

The scenarios of theoretical solution and FEA solution obtained in COMSOL are compared in this Section.

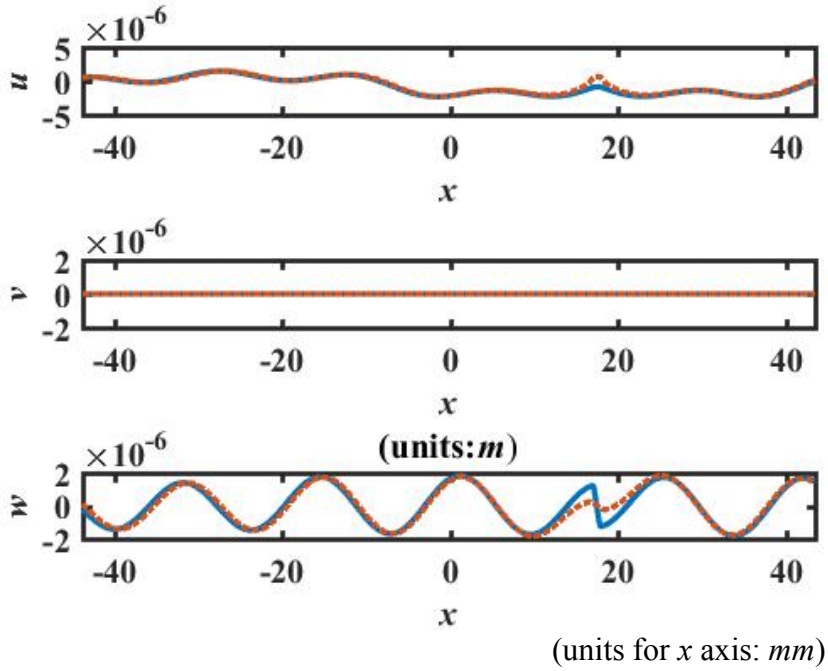

Figure 3.12 Comparing displacement under point load on along 0^o (line I) for theoretical solution and FEA solution under line load. Solid blue line: analytical solution; Dotted red line: COMSOL solution

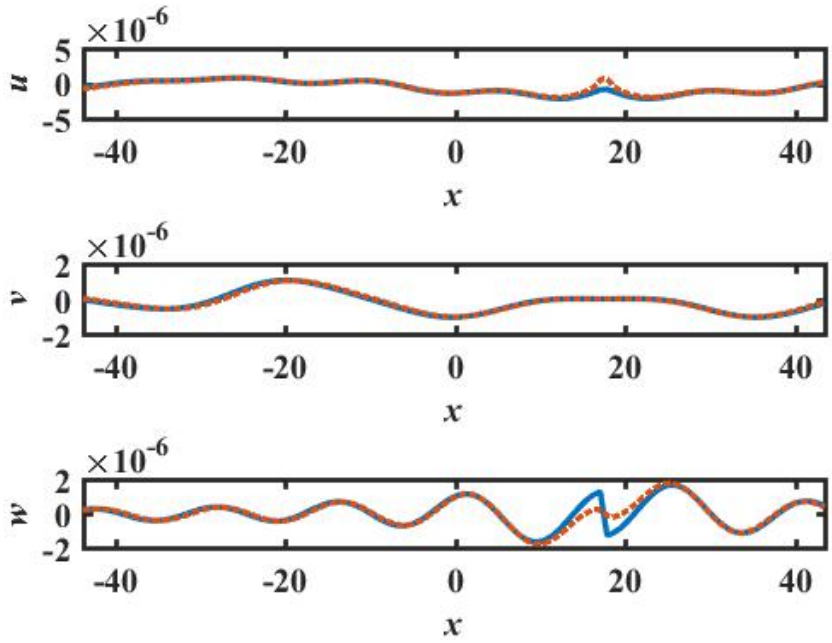

(units for *x* axis: *mm*)

Figure 3.13 Comparing displacement under point load on along atan(1/2) (line II) for theoretical solution and FEA solution under line load. Solid blue line: analytical solution; Dotted red line: COMSOL solution

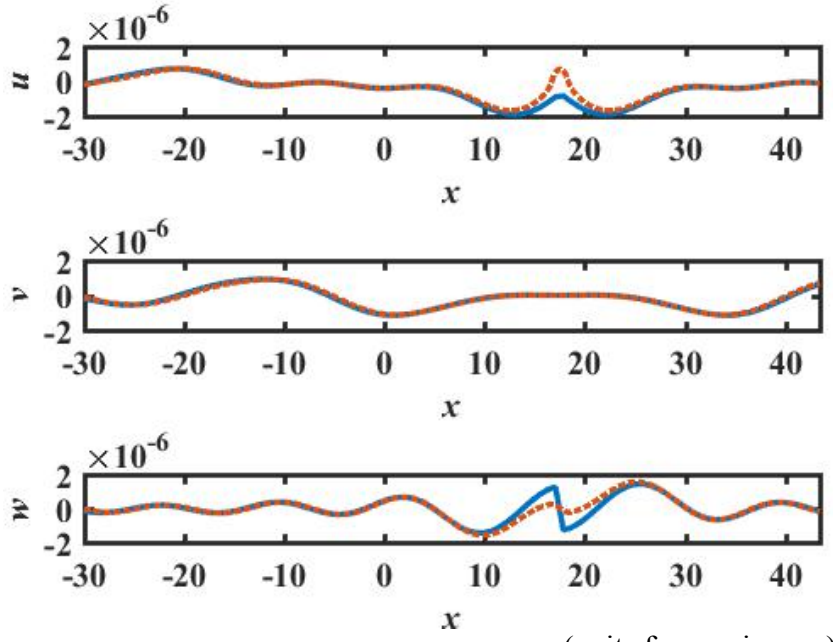

(units for *x* axis: *mm*)

Figure 3.14 Comparing displacement under point load on along 45° (line III) for theoretical solution and FEA solution under line load. Solid blue line: analytical solution; Dotted red line: COMSOL solution

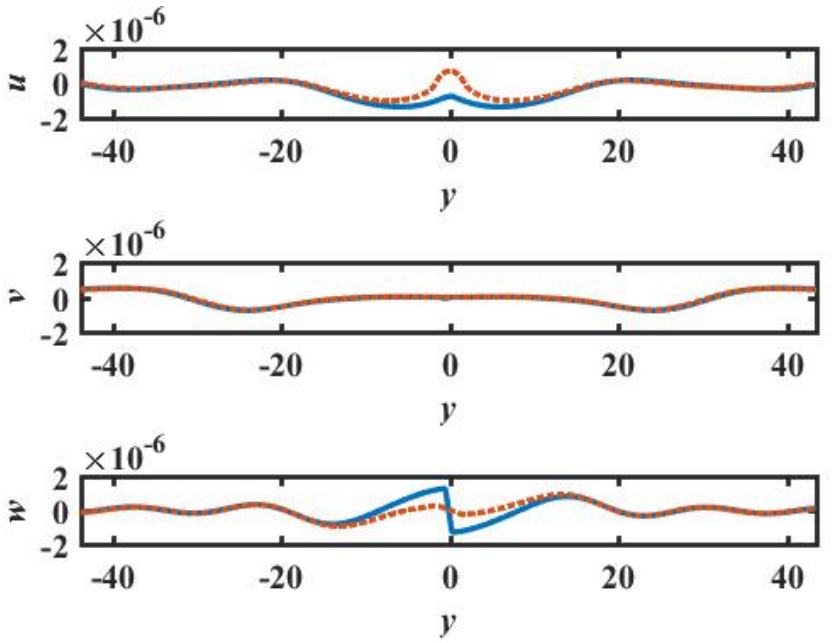

(units for horizontal axis: *mm*)

Figure 3.15 Comparing displacement under point load on along atan(2) (line IV) for theoretical solution and FEA solution under line load. Solid blue line: analytical solution; Dotted red line: COMSOL solution

It can be seen that displacement match pretty well along these four monitoring lines. The difference mainly resides on the area near the origin, where the force is applied. This is because in the theoretical solution, only propagating waves are concerned, while in the COMSOL results, besides propagating waves, there is also non-propagating waves near the force-applying position.

3.6 Verification of theoretical model for propagating plate wave under surface load along +*x* direction

After the verification of the theoretical solution for plate propagating wave under line load, Section 4.6 is going to extend the analytical solution to surface load and the solution will be verified by comparing to FEA result obtained in COMSOL.

3.6.1 Theoretical result for propagating plate wave under surface load

The following study is conducted at frequency $f = 100\,kHz$. Same as the line load case, for the infinite plate, the size of the rectangular area under observation is set to be $p_w \times p_l$, where $p_w = \max WL \cdot 1.6 = 87.52\,mm$ and $p_l = \max WL \cdot 1.6 = 87.52\,mm$. The thickness of the aluminum plate is 3.2 *mm*.

The *x*-*y* plane is set to be the middle layer of the plate. A surface load along +*x* direction are applied on the plate upper surface:

$$f_x = x^3 y^2 \times 10^{21} N/m^2 \quad \text{at} \quad -a_w/2 < x < a_w/2, -a_l/2 < y < a_l/2$$

where

$$a_w = 4\ mm, \quad a_l = 8\ mm$$

The results for displacement elements are calculated in Matlab, as shown below.

Figure 3.16 Theoretical result of (a) displacement *u* (b) displacement *v* (c) displacement *w* under surface load

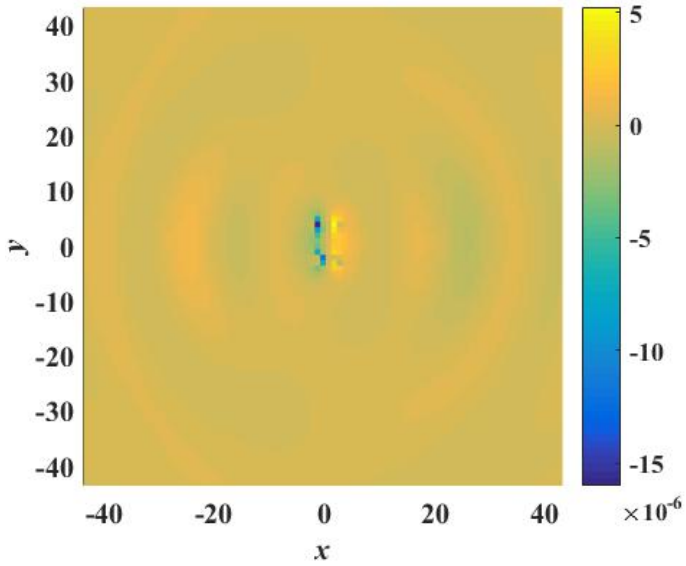

(units for *x*-*y* axis: *mm*)

(a)

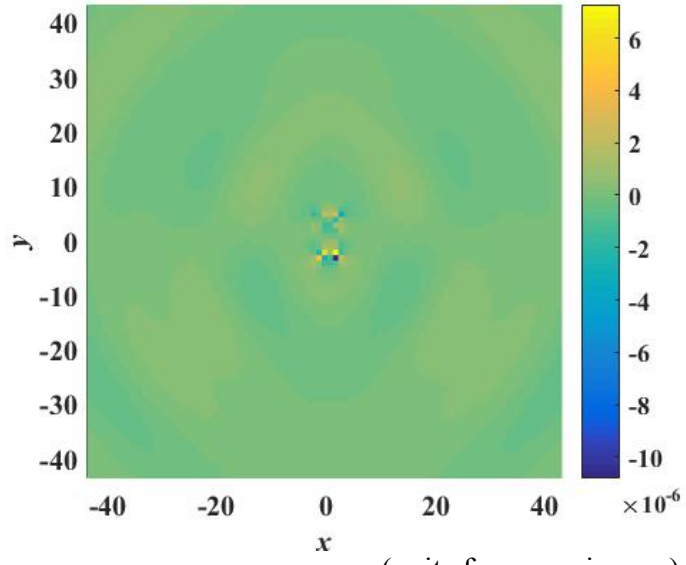

(units for *x*-*y* axis: *mm*)

(b)

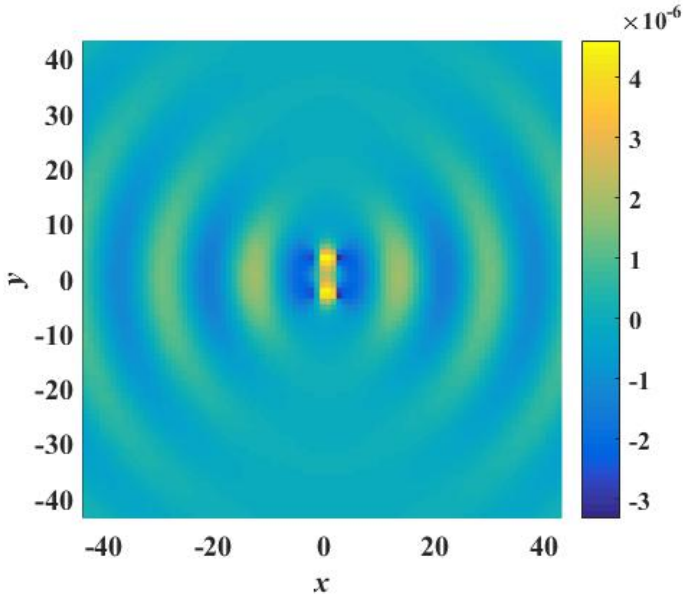

(units for *x*-*y* axis: *mm*)

(c)

In order to verify the theoretical result, FEA is conducted in the software COMSOL.

3.6.2 FEA result for propagating plate wave under surface load

The width of the PML is 1/2 of the maximum wavelength at the given frequency. From Section 4.5, it was concluded from parametric sweep study that when the PML scaling factor is set as 2 and the PML scaling curvature parameter is set as 3, no reflection is shown. Thus in this surface load study, the PML parameters are set to be the SF = 2, SCP = 3 as well.

The maximum size of elements on the plate and PML are 1/16 of the minimum wavelength, while the element size on the area where surface load is applied is even smaller (1/40 of minimum wavelength) than that of the plate.

The displacement components on plate upper surface are:

Figure 3.17 COMSOL result for plate (a) displacement *u* (b) displacement *v* (c) displacement *w* under surface loading

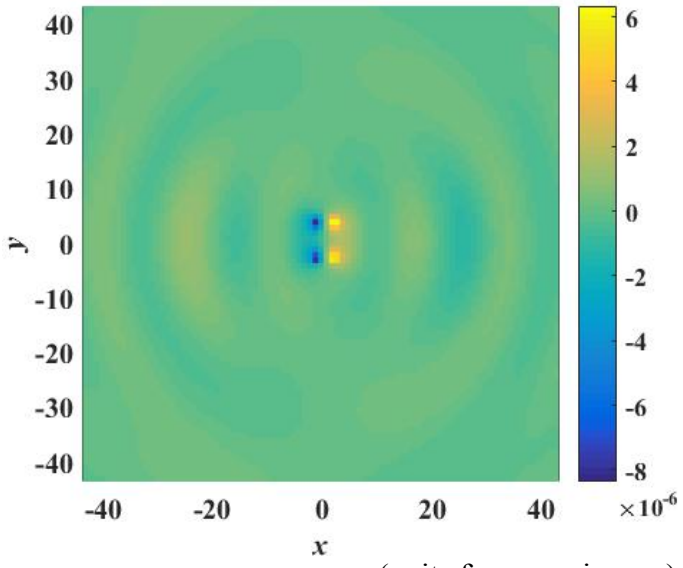

(units for *x*-*y* axis: *mm*)

(a)

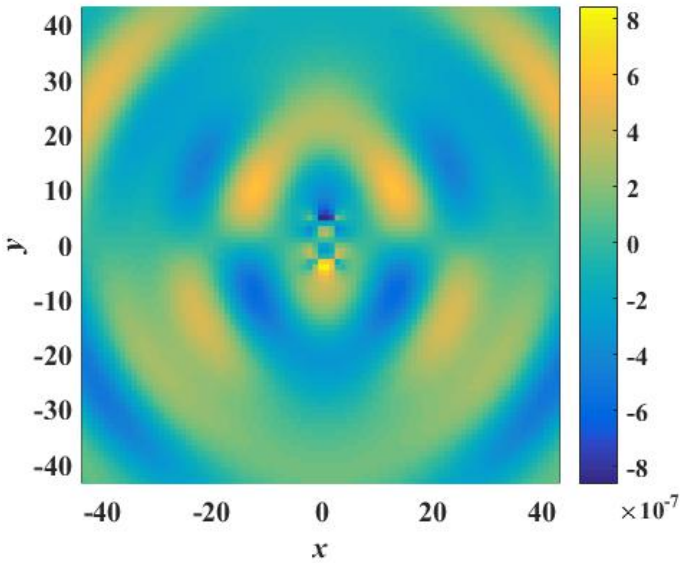

(units for *x*-*y* axis: *mm*)

(b)

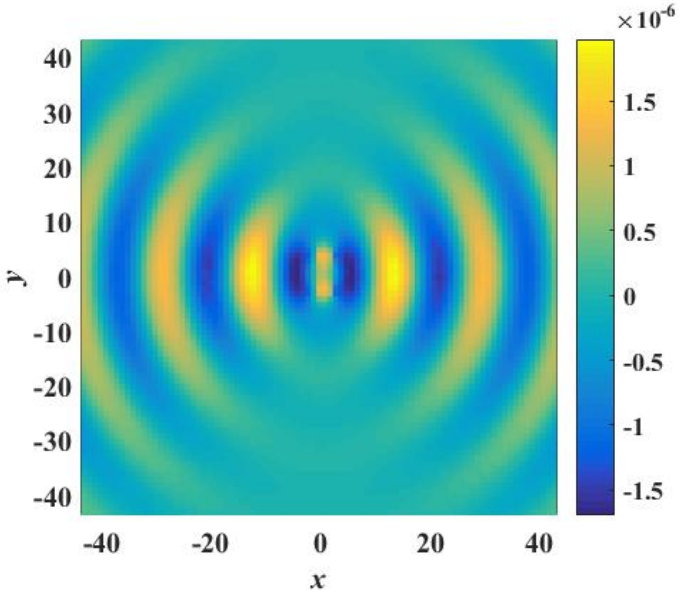

(units for *x*-*y* axis: *mm*)

(c)

3.6.3. Comparing analytical result with FEA result under surface loading

On the four monitoring lines, the theoretical result obtained in Matlab is compared with FEA result obtained in COMSOL, as shown below:

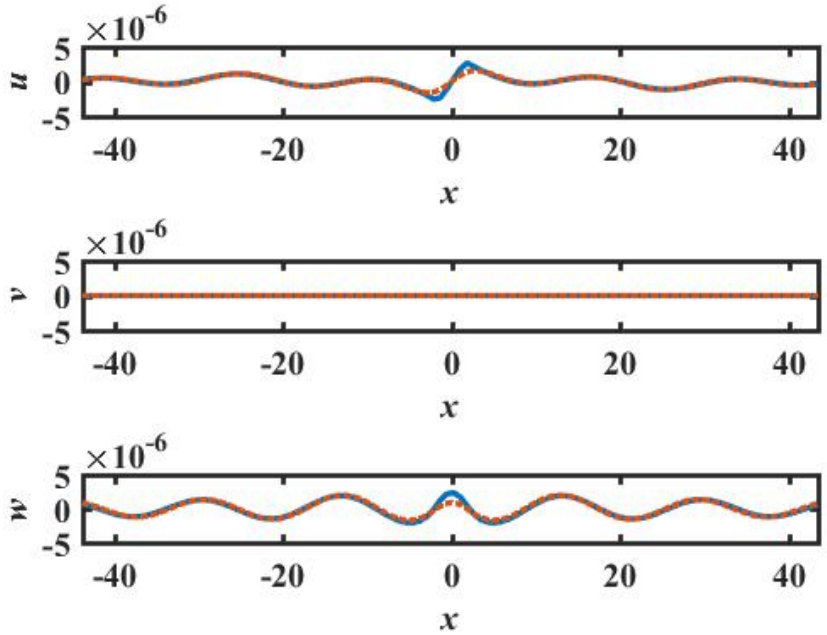

(units for *x* axis: *mm*)

Figure 3.18 Comparing displacement under point load on along 0° (line I) for theoretical solution and FEA solution under line load. Solid blue line: analytical solution; Dotted red line: COMSOL solution

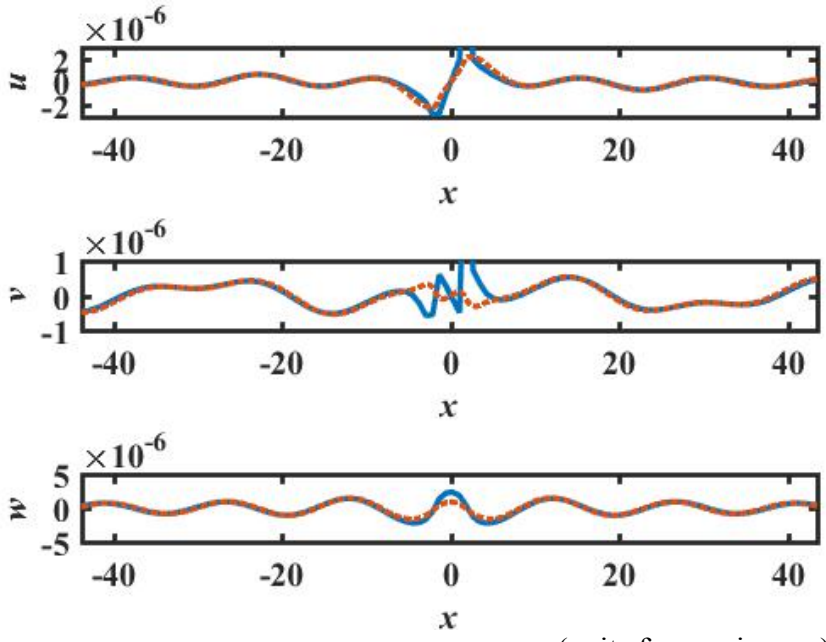

(units for *x* axis: *mm*)

Figure 3.19 Comparing displacement under point load on along atan(1/2) (line II) for theoretical solution and FEA solution under line load. Solid blue line: analytical solution; Dotted red line: COMSOL solution

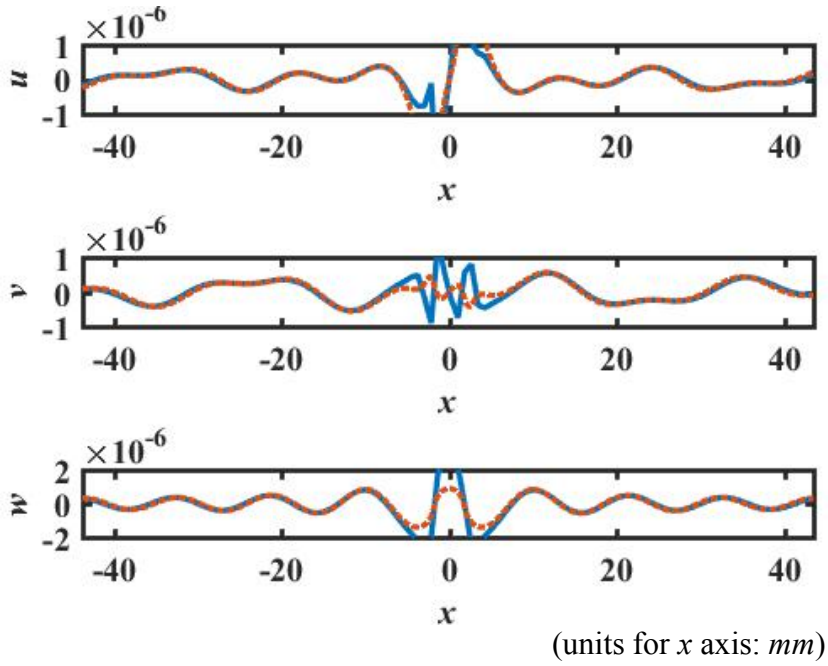

Figure 3.20 Comparing displacement under point load on along 45^{o} (line III) for theoretical solution and FEA solution under line load. Solid blue line: analytical solution; Dotted red line: COMSOL solution

It can be seen that displacement match pretty well along these monitoring lines. The difference mainly resides on the area near the origin, where the force is applied. This is because in the theoretical solution, only propagating waves are concerned, while in the COMSOL results, besides propagating waves, there is also non-propagating waves near the force-applying position.

3.7 Elastodynamic reciprocity for point load along +*y* direction

The carrier wave approach proposed by Achenbach and Xu (1999) gives the forms of plate wave modes under loading in +*x* direction, as listed in Eq. (5.20) to Eq. (5.22). For plate wave modes under loading in a random direction α with respect to the +*x* axis, the Lamb wave forms can be expressed as:

$$u_r^n = V_S^n(z)\Phi'(k_n r)\cos(\theta-\alpha) \tag{3.21}$$

$$u_z^n = W_S^n(z)\Phi(k_n r)\cos(\theta-\alpha) \tag{3.22}$$

$$u_\theta^n = V_S^n(z)\left(\frac{-1}{k_n r}\right)\Phi(k_n r)\sin(\theta-\alpha) \tag{3.23}$$

Therefore, for a point load along +*y* direction, *i.e.*, $\alpha = \pi/2$, the Lamb wave forms can be expressed as

$$u_r^n = V_S^n(z)\Phi'(k_n r)\cos(\theta-\pi/2) = V_S^n(z)\Phi'(k_n r)\sin\theta \tag{3.24}$$

$$u_z^n = W_S^n(z)\Phi(k_n r)\cos(\theta-\pi/2) = W_S^n(z)\Phi(k_n r)\sin\theta \tag{3.25}$$

$$u_\theta^n = V_S^n(z)\left(\frac{-1}{k_n r}\right)\Phi(k_n r)\sin(\theta-\pi/2) = V_S^n(z)\left(\frac{-1}{k_n r}\right)\Phi(k_n r)\cos\theta \tag{3.26}$$

3.7.1. Determination of coefficients for harmonic vertical point load scenario

The region under consideration is $0 \le r \le b, -h \le z \le h, 0 \le \theta \le 2\pi$. Set state A as load Q applied at $z_0 = 0, r = 0, \theta = 0$ in y axis. State *B* is set to be a single symmetric Lamb-

wave mode comprising the outgoing and converging wave. The displacement in state B is expressed as:

$$u_r^n = (1/2)V_S^n(z)[\Phi'(k_n r) + \overline{\Phi}'(k_n r)]\sin\theta,$$
$$u_\theta^n = -(1/2)V_S^n(z)(k_n r)^{-1}[\Phi(k_n r) + \overline{\Phi}(k_n r)]\cos\theta,$$
$$u_z^n = (1/2)W_S^n(z)[\Phi(k_n r) + \overline{\Phi}(k_n r)]\sin\theta.$$

In this scenario, the left hand side of reciprocity theorem becomes $Qu_r^n(0,0,0) = (1/2)QV_S^n(0)$. Substituting the displacement and stress into the right hand side (RHS) of the reciprocity theorem, the coefficient of each wave mode can be determined.

3.7.2. Determination of coefficients for harmonic horizontal point load along +y direction

Symmetric Lamb wave modes: *Determination of* A_n^S

When a horizontal load is applied at the position $z = h, r = 0, \theta = 0$, which can be split into a symmetric and antisymmetric loads. State A is thus set to be the symmetric part of the load. State B is set to be a single symmetric Lamb-wave mode comprising the outgoing and converging wave. Substituting displacement and stress components of the two states into the reciprocity theorem, yields

$$A_n^S = \frac{k_n}{4i}\frac{QV_S^n(z_0)}{I_{nn}^S} \tag{3.27}$$

Antisymmetric Lamb wave modes: *Determination of* A_n^A

Similarly, the coefficient for antisymmetric Lamb wave modes can be obtained:

$$A_n^A = \frac{k_n}{4i}\frac{QV_A^n(z_0)}{I_{nn}^A} \tag{3.28}$$

Symmetric SH wave modes: *Determination of* B_n^S

Set state A as symmetric loading with displacements shown in Figure 3.2 and state B as a single symmetric SH wave consisting of the outgoing and converging waves and using reciprocity, yields

$$B_n^S = \frac{1}{4i}\frac{Q}{J_{nn}} \quad \text{for} \quad n = 0,2,4,\cdots \tag{3.29}$$

where J_{nn} is listed in the Appendix.

Antisymmetric SH wave modes: *Determination of* B_m^A

Set state A as antisymmetric loading with displacements shown in Figure 3.2 and state B as a single antisymmetric SH mode comprising the outgoing and converging waves and using reciprocity, yields

$$B_n^A = \frac{1}{4i}\frac{Q}{J_{nn}} \quad \text{for} \quad n = 1,3,5,\cdots \tag{3.30}$$

Though the coefficients for each wave mode under point load in +y direction is the same as under point load in +x direction, the difference lies in the expression of carrier wave, where the terms of $\cos\theta$ becomes $\sin\theta$; the terms of $\sin\theta$ becomes $\cos\theta$.

CHAPTER 4

Non-propagating (evanescent) plate waves

Chapter 4 discusses the plate wave under point force excitation. The results in the previous chapter are for propagating waves with real wave number. In this chapter, the evanescent plate wave, which is of imaginary or complex wave number, under a point load force excitation is obtained. It was known that the amplitude of evanescent wave decays with respect to displacement. Thus, for far-field displacement analysis, which is needed in sensor response scrutiny, evanescent wave can be neglected. However, when solving for the interfacial stress coefficients, the displacement on the contact surface of the PZT actuator and bonding plate need to be equaled. On the contact surface, evanescent waves need to be taken into consideration since the location of interest is close to the point of force application. In this chapter, the evanescent wave propagation induced by point load is investigated first. Then, the surface stress scenario can be solved by simply integrating the point load solution over the contact area.

4.1 Introduction of evanescent waves

The dispersion relation gives the relation between frequency ω and wave number k. In correspond to any real-valued ω, infinite number of wave number k can be calculated numerically. Each wave number k represents a wave mode in the plate. The value of wave number k can be real, imaginary or complex.

(1) If the wave number is a real valued wave number k , the corresponding wave is either propagating Lamb wave mode or propagating *SH* wave mode.

(2) If a wave mode has a purely imaginary wave number k , the corresponding standing waves (or evanescent waves) will have an amplitudes decaying in the x_1x_2 plane.

(3) If a wave mode has a complex wave number k , the corresponding standing waves (or evanescent waves) will be the modulation of a propagating sinusoidal variation with an exponential decaying function.

For small valued wave number k ($\omega = 0^+$), there is one real valued wave number for symmetric and antisymmetric mode, representing S_0 and mode A_0 respectively, which are the lowest symmetric and antisymmetric modes. All other wave number k are either imaginary or complex.

Another thing to note is that with the increment of imaginary part in wave number, the corresponding wave will have a faster decaying rate. For example, since A_1 Lamb wave mode has the minimum wave number imaginary part compared to other evanescent wave modes at the same frequency, the A_1 Lamb wave will be the mode which decays the slowest among all other evanescent wave modes.

4.2 theoretical solution for amplitude of evanescent wave modes under point load along +*x* direction

4.2.1 Complex reciprocity theorem

For elastic solid subjected to a body, the equation of motion and strain-displacement relation is shown below:

$$\begin{cases} \nabla \cdot \boldsymbol{\sigma} = \rho \dfrac{\partial^2 u}{\partial t^2} - \mathbf{f} \\ \nabla \mathbf{u} = \boldsymbol{\varepsilon} \end{cases} \tag{4.1}$$

In the above equation, ρ is the volume density; $\boldsymbol{\sigma}$ and $\boldsymbol{\varepsilon}$ are the stress and strain tensor respectively; $\mathbf{u}$ is the displacement vector; $\mathbf{f}$ is the body force.

Consider two wavefields A and B with body forces $\mathbf{f}_A^*, \mathbf{f}_B$, displacements $\mathbf{u}_A^*, \mathbf{u}_B$, velocities $\mathbf{v}_A^*, \mathbf{v}_B$ and stresses $\boldsymbol{\sigma}_A^*, \boldsymbol{\sigma}_B$, where * denotes complex conjugate. Substituting these values into Eq. (4.1), the equation of motion and strain-displacement relation for these two fields are expressed as follows:

$$\begin{cases} \nabla \cdot \boldsymbol{\sigma}_A^* = \rho \dfrac{\partial \mathbf{v}_A^*}{\partial t} - \mathbf{f}_A^* \\ \nabla \mathbf{v}_A^* = \dfrac{\partial \boldsymbol{\varepsilon}_A^*}{\partial t} \end{cases} \tag{4.2}$$

$$\begin{cases} \nabla \cdot \boldsymbol{\sigma}_B = \rho \dfrac{\partial \mathbf{v}_B}{\partial t} - \mathbf{f}_B \\ \nabla \mathbf{v}_B = \dfrac{\partial \boldsymbol{\varepsilon}_B}{\partial t} \end{cases} \tag{4.3}$$

Multiplying Eq. (4.2-1) with velocity in wavefield B $\mathbf{v}_B$ and multiplying Eq. (4.2-2) with stress in wave filed B $\boldsymbol{\sigma}_B$, yields

$$\begin{cases} \mathbf{v}_B \cdot (\nabla \cdot \boldsymbol{\sigma}_A^*) = \rho \mathbf{v}_B \cdot \dfrac{\partial \mathbf{v}_A^*}{\partial t} - \mathbf{v}_B \cdot \mathbf{f}_A^* \\ \boldsymbol{\sigma}_B \cdot \nabla \mathbf{v}_A^* = \boldsymbol{\sigma}_B \cdot \dfrac{\partial \boldsymbol{\varepsilon}_A^*}{\partial t} \end{cases} \tag{4.4}$$

Multiplying Eq. (4.3-1) with velocity in wavefield A $\mathbf{v}_A^*$ and multiplying Eq. (4.2-2) with stress in wave filed B $\boldsymbol{\sigma}_A^*$, yields

$$\begin{cases} \mathbf{v}_A^* \cdot (\nabla \cdot \boldsymbol{\sigma}_B) = \rho \mathbf{v}_A^* \cdot \dfrac{\partial \mathbf{v}_B}{\partial t} - \mathbf{v}_A^* \cdot \mathbf{f}_B \\ \boldsymbol{\sigma}_A^* \cdot \nabla \mathbf{v}_B = \boldsymbol{\sigma}_A^* \cdot \dfrac{\partial \boldsymbol{\varepsilon}_B}{\partial t} \end{cases} \tag{4.5}$$

Summing up Eq. (4.4-1), Eq. (4.4-2), Eq. (4.5-1) and Eq. (4.5-2) yields

$$\begin{aligned} &\mathbf{v}_B \cdot (\nabla \cdot \boldsymbol{\sigma}_A^*) + \boldsymbol{\sigma}_B \cdot \nabla \mathbf{v}_A^* + \mathbf{v}_A^* \cdot (\nabla \cdot \boldsymbol{\sigma}_B) + \boldsymbol{\sigma}_A^* \cdot \nabla \mathbf{v}_B \\ &= \rho \mathbf{v}_B \cdot \frac{\partial \mathbf{v}_A^*}{\partial t} - \mathbf{v}_B \cdot \mathbf{f}_A^* + \boldsymbol{\sigma}_B \cdot \frac{\partial \boldsymbol{\varepsilon}_A^*}{\partial t} + \rho \mathbf{v}_A^* \cdot \frac{\partial \mathbf{v}_B}{\partial t} - \mathbf{v}_A^* \cdot \mathbf{f}_B + \boldsymbol{\sigma}_A^* \cdot \frac{\partial \boldsymbol{\varepsilon}_B}{\partial t} \end{aligned} \tag{4.6}$$

The divergent of tensor product has the following identities:

$$\begin{aligned} \nabla \cdot (\mathbf{v}_B \cdot \boldsymbol{\sigma}_A^*) &= \mathbf{v}_B \cdot (\nabla \cdot \boldsymbol{\sigma}_A^*) + \boldsymbol{\sigma}_A^* \cdot \nabla \mathbf{v}_B \\ \nabla \cdot (\mathbf{v}_A^* \cdot \boldsymbol{\sigma}_B) &= \mathbf{v}_A^* \cdot (\nabla \cdot \boldsymbol{\sigma}_B) + \boldsymbol{\sigma}_B \cdot \nabla \mathbf{v}_A^* \end{aligned} \tag{4.7}$$

Using Eq. (4.7), Eq. (4.6) becomes

$$\begin{aligned} &\nabla \cdot (\mathbf{v}_B \cdot \boldsymbol{\sigma}_A^*) + \nabla \cdot (\mathbf{v}_A^* \cdot \boldsymbol{\sigma}_B) \\ &= \rho \mathbf{v}_B \cdot \frac{\partial \mathbf{v}_A^*}{\partial t} + \rho \mathbf{v}_A^* \cdot \frac{\partial \mathbf{v}_B}{\partial t} + \boldsymbol{\sigma}_B \cdot \frac{\partial \boldsymbol{\varepsilon}_A^*}{\partial t} + \boldsymbol{\sigma}_A^* \cdot \frac{\partial \boldsymbol{\varepsilon}_B}{\partial t} - \mathbf{v}_A^* \cdot \mathbf{f}_B - \mathbf{v}_B \cdot \mathbf{f}_A^* \end{aligned} \tag{4.8}$$

The Hook's law in tensor notion is given by

$$\begin{aligned}\boldsymbol{\sigma} &= \mathbf{C} : \boldsymbol{\varepsilon} \\ \boldsymbol{\varepsilon} &= \mathbf{S} : \boldsymbol{\sigma}\end{aligned} \tag{4.9}$$

In the above equations, $\mathbf{C}$ and $\mathbf{S}$ represent the fourth-order stiffness tensor and compliance tensor respectively.

From the Hook's law in Eq. (4.9), the following equation can be obtained:

$$\boldsymbol{\sigma}_A^* : \frac{\partial \boldsymbol{\varepsilon}_B}{\partial t} + \boldsymbol{\sigma}_B : \frac{\partial \boldsymbol{\varepsilon}_A^*}{\partial t} = \boldsymbol{\sigma}_A^* : \mathbf{S} : \frac{\partial \boldsymbol{\sigma}_B}{\partial t} + \boldsymbol{\sigma}_B : \mathbf{S} : \frac{\partial \boldsymbol{\sigma}_A^*}{\partial t} \tag{4.10}$$

Since compliance matrix $\mathbf{S}$ is symmetric and real, the following equation can be obtained:

$$\boldsymbol{\sigma}_A^* : \mathbf{S} : \frac{\partial \boldsymbol{\sigma}_B}{\partial t} = \frac{\partial \boldsymbol{\sigma}_B}{\partial t} : \mathbf{S} : \boldsymbol{\sigma}_A^* \tag{4.11}$$

Substituting Eq. (4.11) into Eq. (4.10), yields

$$\boldsymbol{\sigma}_A^* : \frac{\partial \boldsymbol{\varepsilon}_B}{\partial t} + \boldsymbol{\sigma}_B : \frac{\partial \boldsymbol{\varepsilon}_A^*}{\partial t} = \frac{\partial \boldsymbol{\sigma}_B}{\partial t} : \mathbf{S} : \boldsymbol{\sigma}_A^* + \boldsymbol{\sigma}_B : \mathbf{S} : \frac{\partial \boldsymbol{\sigma}_A^*}{\partial t} \tag{4.12}$$

Substituting Eq. (4.12) into Eq. (4.8), yields

$$\begin{aligned}&\nabla \cdot (\mathbf{v}_B \cdot \boldsymbol{\sigma}_A^*) + \nabla \cdot (\mathbf{v}_A^* \cdot \boldsymbol{\sigma}_B) \\ &= \rho \mathbf{v}_B \cdot \frac{\partial \mathbf{v}_A^*}{\partial t} + \rho \mathbf{v}_A^* \cdot \frac{\partial \mathbf{v}_B}{\partial t} + \frac{\partial \boldsymbol{\sigma}_B}{\partial t} : \mathbf{S} : \boldsymbol{\sigma}_A^* + \boldsymbol{\sigma}_B : \mathbf{S} : \frac{\partial \boldsymbol{\sigma}_A^*}{\partial t} - \mathbf{v}_A^* \cdot \mathbf{f}_B - \mathbf{v}_B \cdot \mathbf{f}_A^*\end{aligned} \tag{4.13}$$

Eq. (4.13) can be simplified as

$$\nabla \cdot (\mathbf{v}_B \cdot \boldsymbol{\sigma}_A^* + \mathbf{v}_A^* \cdot \boldsymbol{\sigma}_B) = \frac{\partial}{\partial t}(\rho \mathbf{v}_A^* \mathbf{v}_B + \boldsymbol{\sigma}_B \cdot \varepsilon_A^*) - \mathbf{v}_A^* \cdot \mathbf{f}_B - \mathbf{v}_B \cdot \mathbf{f}_A^* \tag{4.14}$$

For steady state time harmonic wavefield, the reciprocity theorem can be expressed as

$$\nabla \cdot (\mathbf{v}_B \cdot \boldsymbol{\sigma}_A^* + \mathbf{v}_A^* \cdot \boldsymbol{\sigma}_B) = -(\mathbf{v}_A^* \cdot \mathbf{f}_B + \mathbf{v}_B \cdot \mathbf{f}_A^*) \tag{4.15a}$$

Since $v = \dot{u} = -i\omega u, v^* = (\dot{u})^* = (-i\omega u)^* = (-i)^*(\omega)^*(u)^* = i\omega u^*$, the above reciprocity can also be written using displacement:

$$i\omega\nabla \cdot (-\mathbf{u}_B \cdot \boldsymbol{\sigma}_A^* + \mathbf{u}_A^* \cdot \boldsymbol{\sigma}_B) = -i\omega(\mathbf{u}_A^* \cdot \mathbf{f}_B - \mathbf{u}_B \cdot \mathbf{f}_A^*) \tag{4.15b}$$

Eq. (4.15) is the **differential form of complex reciprocity theorem**. By integrating Eq. (4.15) over a region V with boundary S , the **integral form of complex reciprocity theorem** can be obtained as below:

$$\int_S (\mathbf{v}_B \cdot \boldsymbol{\sigma}_A^* + \mathbf{v}_A^* \cdot \boldsymbol{\sigma}_B)\mathbf{n}dS = -\int_V (\mathbf{v}_A^* \cdot \mathbf{f}_B + \mathbf{v}_B \cdot \mathbf{f}_A^*)dV \tag{4.16a}$$

or

$$i\omega\int_S (-\mathbf{u}_B \cdot \boldsymbol{\sigma}_A^* + \mathbf{u}_A^* \cdot \boldsymbol{\sigma}_B)\mathbf{n}dS = -i\omega\int_V (\mathbf{u}_A^* \cdot \mathbf{f}_B - \mathbf{u}_B \cdot \mathbf{f}_A^*)dV$$

In the above equations, $\mathbf{n}$ is a unit outward normal vector.

Multiplying both sides of the above equation with i/ω, yields

$$\int_S (\mathbf{u}_B \cdot \boldsymbol{\sigma}_A^* - \mathbf{u}_A^* \cdot \boldsymbol{\sigma}_B)\mathbf{n}dS = \int_V (\mathbf{u}_A^* \cdot \mathbf{f}_B - \mathbf{u}_B \cdot \mathbf{f}_A^*)dV \tag{4.16b}$$

4.2.2 Use of the complex reciprocity theorem

As discussed in the previous Section, the complex reciprocity theorem relating two time-harmonic states with superscripts A and B is:

$$\int_V (f_i^{A^*} u_i^B - f_i^B u_i^{A^*}) dV = \int_S (u_i^{A^*} \sigma_{ij}^B - u_i^B \sigma_{ij}^{A^*}) n_j dS \tag{4.17}$$

In the above equations, f_i^A and f_i^B are body forces; S is the boundary for region V; n_j are the outward normal components.

In an annular domain $|z| \le h,\ \ 0 \le r \le b,\ \ 0 \le \theta \le 2\pi$, the reciprocity theorem can be applied to two symmetric evanescent Lamb wave modes with no body forces. The wave numbers for the two symmetric evanescent Lamb wave modes m and n are k_m and k_n respectively. Since both modes do not have body forces, the left hand side of Eq. (4.17) is 0. The right hand side of Eq. (4.17) can be expressed as

$$Q_{m^*n}(b) = 0 \tag{4.18}$$

where

$$\begin{aligned} Q_{m^*n}(b) &= b\int_0^{2\pi}\int_{-h}^{h} \left\{ u_i^{m^*} \sigma_{ij}^n - u_i^n \sigma_{ij}^{m^*} \right\} n_j \, d\theta dz \\ &= b\int_0^{2\pi}\int_{-h}^{h} \Bigg\{ \underbrace{\left[u_r^{m^*} \sigma_{rr}^n - u_r^n \sigma_{rr}^{m^*} \right]}_{I} \\ &\qquad + \underbrace{\left[u_z^{m^*} \sigma_{rz}^n - u_z^n \sigma_{rz}^{m^*} \right]}_{II} \\ &\qquad + \underbrace{\left[u_\theta^{m^*} \sigma_{r\theta}^n - u_\theta^n \sigma_{r\theta}^{m^*} \right]}_{III} \Bigg\} d\theta dz \end{aligned} \tag{4.19}$$

As can be seen, in Eq. (4.19), the right hand side is divided into three sections, represented by I, II, III respectively.

As discussed in Chapter 4, the displacement and stress for an outgoing symmetric Lamb-wave mode can be written using carrier wave approach (Achenbach and Xu, 1999):

$$u_r^n = V_S^n(z)\Phi'(k_n r)\cos\theta \tag{4.20}$$

$$u_z^n = W_S^n(z)\Phi(k_n r)\cos\theta \tag{4.21}$$

$$u_\theta^n = V_S^n(z)\left(\frac{-1}{k_n r}\right)\Phi(k_n r)\sin\theta \tag{4.22}$$

$$\sigma_{rz}^n = -\Sigma_{rz}^{Sn}(z)\Phi'(k_n r)\cos\theta \tag{4.23}$$

$$\sigma_{zz}^n = \Sigma_{rz}^{Sn}(z)\Phi(k_n r)\cos\theta \tag{4.24}$$

$$\begin{aligned}\sigma_{rr}^n = {} & \Sigma_{rr}^{Sn}(z)\Phi(k_n r)\cos\theta - \overline{\Sigma}_{rr}^{Sn}(z) \\ & \times\left[\frac{1}{r}\Phi'(k_n r) - \frac{1}{k_n r^2}\Phi(k_n r)\right]\cos\theta\end{aligned} \tag{4.25}$$

$$\sigma_{\theta z}^n = \Sigma_{\theta z}^{Sn}(z)\left(\frac{-1}{k_n r}\right)\Phi(k_n r)\sin\theta \tag{4.26}$$

$$\sigma_{r\theta}^n = \Sigma_{r\theta}^{Sn}(z)\left[-\frac{1}{r}\Phi'(k_n r) + \frac{1}{k_n r^2}\Phi(k_n r)\right]\sin\theta \tag{4.27}$$

where the terms related to z are expressed as below:

$$V_S^n(z) = s_1\cos(pz) + s_2\cos(qz) \tag{4.28a}$$

$$W_S^n(z) = s_3 \sin(pz) + s_4 \sin(qz) \tag{4.28b}$$

$$\Sigma_{rz}^{Sn}(z) = \mu\left[s_5 \sin(pz) + s_6 \sin(qz)\right] \tag{4.28c}$$

$$\Sigma_{zz}^{Sn}(z) = \mu\left[s_7 \cos(pz) + s_8 \cos(qz)\right] \tag{4.28d}$$

$$\Sigma_{rr}^{Sn}(z) = \mu\left[s_9 \cos(pz) + s_{10} \cos(qz)\right] \tag{4.28e}$$

$$\overline{\Sigma}_{rr}^{Sn}(z) = \mu\left[s_{11} \cos(pz) + s_{12} \cos(qz)\right] \tag{4.28f}$$

$$\Sigma_{r\theta}^{Sn}(z) = \overline{\Sigma}_{rr}^{Sn}(z) \tag{4.28g}$$

$$\Sigma_{\theta z}^{Sn}(z) = -\Sigma_{rz}^{Sn}(z) \tag{4.28g}$$

where

$$s_1 = 2\cos(qh) \tag{4.29a}$$

$$s_2 = -\left[(k_n^2 - q^2)/k_n^2\right]\cos(ph) \tag{4.29b}$$

$$s_3 = -2(p/k_n)\cos(qh) \tag{4.29c}$$

$$s_4 = -\left[(k_n^2 - q^2)/(qk_n)\right]\cos(ph) \tag{4.29d}$$

$$s_5 = 4p\cos(qh) \tag{4.29e}$$

$$s_6 = \left[(k_n^2 - q^2)^2/(qk_n^2)\right]\cos(ph) \tag{4.29f}$$

$$s_7 = \left[2(k_n^2 - q^2)/k_n\right]\cos(qh) \tag{4.29g}$$

$$s_9 = \left[2(2p^2 - k_n^2 - q^2) / k_n \right] \cos(qh) \tag{4.29h}$$

$$s_{10} = \left[2(k_n^2 - q^2) / k_n \right] \cos(ph) \tag{4.29i}$$

$$s_{11} = 4\cos(qh) \tag{4.29j}$$

$$s_{12} = -\left[2(k_n^2 - q^2) / k_n^2 \right] \cos(ph) \tag{4.29k}$$

In these expressions

$$p^2 = \frac{\omega^2}{c_L^2} - k_n^2, \quad c_L^2 = \frac{\lambda + 2\mu}{\rho} \tag{4.30a}$$

$$q^2 = \frac{\omega^2}{c_T^2} - k_n^2, \quad c_T^2 = \frac{\mu}{\rho} \tag{4.30b}$$

Substituting Eq. (4.20)-Eq. (4.27) to Eq. (4.19) and considering $(1/k_n)^* = k_n^* / |k_n|^2$ and $\overline{\Sigma}_{rr}^{Sn}(z) = \Sigma_{r\theta}^{Sn}(z) = 2\mu V_S^n(z)$, the first term in Eq. (4.19) is evaluated as:

$$
\begin{aligned}
I &= u_r^{m*}\sigma_{rr}^{n} - u_r^{n}\sigma_{rr}^{m*} \\
&= \left[V_S^{m*}(z)\Phi'^{*}(k_m r)\cos\theta\right]\left\{\Sigma_{rr}^{Sn}(z)\Phi(k_n r)\cos\theta - \underline{\bar{\Sigma}_{rr}^{Sn}(z)}\times\left[\frac{1}{r}\Phi'(k_n r) - \frac{1}{k_n r^2}\Phi(k_n r)\right]\cos\theta\right\} \\
&\quad - \left[V_S^{n}(z)\Phi'(k_n r)\cos\theta\right]\left\{\Sigma_{rr}^{Sm*}(z)\Phi^{*}(k_m r)\cos\theta - \underline{\bar{\Sigma}_{rr}^{Sm*}(z)}\times\left[\frac{1}{r}\Phi'^{*}(k_m r) - \frac{k_m}{|k_m|^2 r^2}\Phi^{*}(k_m r)\right]\cos\theta\right\} \\
&\quad \bar{\Sigma}_{rr}^{Sn}(z)=2\mu V_S^{n}(z) \\
&= \left[V_S^{m*}(z)\Phi'^{*}(k_m r)\cos\theta\right]\left\{\Sigma_{rr}^{Sn}(z)\Phi(k_n r)\cos\theta - \underline{2\mu V_S^{n}(z)}\times\left[\frac{1}{r}\Phi'(k_n r) - \frac{1}{k_n r^2}\Phi(k_n r)\right]\cos\theta\right\} \\
&\quad - \left[V_S^{n}(z)\Phi'(k_n r)\cos\theta\right]\left\{\Sigma_{rr}^{Sm*}(z)\Phi^{*}(k_m r)\cos\theta - \underline{\underline{2\mu V_S^{m*}(z)}}\times\left[\frac{1}{r}\Phi'^{*}(k_m r) - \frac{k_m}{|k_m|^2 r^2}\Phi^{*}(k_m r)\right]\cos\theta\right\} \\
&= \cos^2\theta\left[V_S^{m*}(z)\Phi'^{*}(k_m r)\Sigma_{rr}^{Sn}(z)\Phi(k_n r) - V_S^{n}(z)\Phi'(k_n r)\Sigma_{rr}^{Sm*}(z)\Phi^{*}(k_m r)\right] \\
&\quad + 2\mu V_S^{m*}(z)V_S^{n}(z)\cos^2\theta\left[\cancel{-\frac{1}{r}\Phi'(k_n r)\Phi'^{*}(k_m r)} + \frac{1}{k_n r^2}\Phi(k_n r)\Phi'^{*}(k_m r)\right. \\
&\qquad \left. + \cancel{\frac{1}{r}\Phi'(k_n r)\Phi'^{*}(k_m r)} - \frac{k_m}{|k_m|^2 r^2}\Phi'(k_n r)\Phi^{*}(k_m r)\right] \\
&= \cos^2\theta\left[V_S^{m*}(z)\Phi'^{*}(k_m r)\Sigma_{rr}^{Sn}(z)\Phi(k_n r) - V_S^{n}(z)\Phi'(k_n r)\Sigma_{rr}^{Sm*}(z)\Phi^{*}(k_m r)\right] \\
&\quad + 2\mu V_S^{m*}(z)V_S^{n}(z)\cos^2\theta\left[\frac{1}{k_n r^2}\Phi(k_n r)\Phi'^{*}(k_m r) - \frac{k_m}{|k_m|^2 r^2}\Phi'(k_n r)\Phi^{*}(k_m r)\right]
\end{aligned}
\tag{4.31}
$$

The second term in Eq. (4.19) is evaluated as:

$$
\begin{aligned}
II &= u_z^{m*}\sigma_{rz}^{n} - u_z^{n}\sigma_{rz}^{m*} \\
&= \left[W_S^{m*}(z)\Phi^{*}(k_m r)\cos\theta\right]\left[-\Sigma_{rz}^{Sn}(z)\Phi'(k_n r)\cos\theta\right] \\
&\quad - \left[W_S^{n}(z)\Phi(k_n r)\cos\theta\right]\left[-\Sigma_{rz}^{Sm*}(z)\Phi'^{*}(k_m r)\cos\theta\right] \\
&= \cos^2\theta\left[-W_S^{m*}(z)\Sigma_{rz}^{Sn}(z)\Phi^{*}(k_m r)\Phi'(k_n r)\right. \\
&\qquad \left. + W_S^{n}(z)\Sigma_{rz}^{Sm*}(z)\Phi(k_n r)\Phi'^{*}(k_m r)\right]
\end{aligned}
\tag{4.32}
$$

The third term in Eq. (4.19) is evaluated as:

$$
\begin{aligned}
III &= u_\theta^{m*}\sigma_{r\theta}^{n} - u_\theta^{n}\sigma_{r\theta}^{m*} \\
&= \left[V_S^{m*}(z)\left(\frac{-k_m}{|k_m|^2 r} \right)\Phi^*(k_m r)\sin\theta \right]\left\{ \underline{\Sigma_{r\theta}^{Sn}(z)}\left[-\frac{1}{r}\Phi'(k_n r) + \frac{1}{k_n r^2}\Phi(k_n r) \right]\sin\theta \right\} \\
&\quad - \left[V_S^{n}(z)\left(\frac{-1}{k_n r} \right)\Phi(k_n r)\sin\theta \right]\left\{ \underline{\underline{\Sigma_{r\theta}^{Sm*}(z)}}\left[-\frac{1}{r}\Phi'^*(k_m r) + \left(\frac{k_m}{|k_m|^2 r^2} \right)\Phi^*(k_m r) \right]\sin\theta \right\} \\
&\overset{\Sigma_{r\theta}^{Sn}(z)=2\mu V_S^{n}(z)}{=} \left[V_S^{m*}(z)\left(\frac{-k_m}{|k_m|^2 r} \right)\Phi^*(k_m r)\sin\theta \right]\left\{ \underline{2\mu V_S^{n}(z)}\left[-\frac{1}{r}\Phi'(k_n r) + \frac{1}{k_n r^2}\Phi(k_n r) \right]\sin\theta \right\} \\
&\quad - \left[V_S^{n}(z)\left(\frac{-1}{k_n r} \right)\Phi(k_n r)\sin\theta \right]\left\{ \underline{\underline{2\mu V_S^{m*}(z)}}\left[-\frac{1}{r}\Phi'^*(k_m r) + \left(\frac{k_m}{|k_m|^2 r^2} \right)\Phi^*(k_m r) \right]\sin\theta \right\} \\
&= 2\mu V_S^{n}(z)V_S^{m*}(z)\sin^2\theta \left[\left(\frac{k_m}{|k_m|^2 r^2} \right)\Phi^*(k_m r)\Phi'(k_n r) + \cancel{\left(\frac{-k_m}{|k_m|^2 k_n r^3} \right)\Phi^*(k_m r)\Phi(k_n r)} \right. \\
&\qquad \left. - \frac{1}{k_n r}\Phi(k_n r)\Phi'^*(k_m r) + \cancel{\left(\frac{k_m}{k_n |k_m|^2 r^3} \right)\Phi(k_n r)\Phi^*(k_m r)} \right] \\
&= 2\mu V_S^{n}(z)V_S^{m*}(z)\sin^2\theta \left[\left(\frac{k_m}{|k_m|^2 r^2} \right)\Phi^*(k_m r)\Phi'(k_n r) - \frac{1}{k_n r}\Phi(k_n r)\Phi'^*(k_m r) \right]
\end{aligned}
$$

(4.33)

The integration of the terms involving θ is:

$$
\begin{aligned}
\int_0^{2\pi} \sin^2\theta d\theta &= \pi \\
\int_0^{2\pi} \cos^2\theta d\theta &= \pi
\end{aligned}
\tag{4.34}
$$

Substituting Eq. (4.31)-Eq. (4.34) into Eq. (4.18) and Eq. (4.19) yields

$$
\begin{aligned}
Q_{m^*n}(b) = b\pi \int_{-h}^{h} \Big\{ & V_S^{m^*}(z)\Phi'^{*}(k_m r)\Sigma_{rr}^{Sn}(z)\Phi(k_n r) - V_S^{n}(z)\Phi'(k_n r)\Sigma_{rr}^{Sm^*}(z)\Phi^{*}(k_m r) \\
& + 2\mu V_S^{m^*}(z)V_S^{n}(z)\left[\frac{1}{k_n r^2}\Phi(k_n r)\Phi'^{*}(k_m r) - \frac{k_m}{|k_m|^2 r^2}\Phi'(k_n r)\Phi^{*}(k_m r) \right] \\
& - W_S^{m^*}(z)\Sigma_{rz}^{Sn}(z)\Phi^{*}(k_m r)\Phi'(k_n r) \\
& + W_S^{n}(z)\Sigma_{rz}^{Sm^*}(z)\Phi(k_n r)\Phi'^{*}(k_m r) \\
& + 2\mu V_S^{n}(z)V_S^{m^*}(z)\left[\frac{k_m}{|k_m|^2 r^2}\Phi'(k_n r)\Phi^{*}(k_m r) - \frac{1}{k_n r}\Phi(k_n r)\Phi'^{*}(k_m r) \right] \Big\} dz \Big|_{r=b} \\
= b\pi \int_{-h}^{h} \Big[& V_S^{m^*}(z)\Sigma_{rr}^{Sn}(z)\Phi'^{*}(k_m r)\Phi(k_n r) - V_S^{n}(z)\Sigma_{rr}^{Sm^*}(z)\Phi'(k_n r)\Phi^{*}(k_m r) \\
& - W_S^{m^*}(z)\Sigma_{rz}^{Sn}(z)\Phi^{*}(k_m r)\Phi'(k_n r) + W_S^{n}(z)\Sigma_{rz}^{Sm^*}(z)\Phi(k_n r)\Phi'^{*}(k_m r) \Big] dz \Big|_{r=b} \\
= b\pi \int_{-h}^{h} \Big[& V_S^{m^*}(z)\Sigma_{rr}^{Sn}(z)\underline{\Phi'^{*}(k_m b)\Phi(k_n b)} - V_S^{n}(z)\Sigma_{rr}^{Sm^*}(z)\underline{\underline{\Phi'(k_n b)\Phi^{*}(k_m b)}} \\
& - W_S^{m^*}(z)\Sigma_{rz}^{Sn}(z)\underline{\underline{\Phi^{*}(k_m b)\Phi'(k_n b)}} + W_S^{n}(z)\Sigma_{rz}^{Sm^*}(z)\underline{\Phi(k_n b)\Phi'^{*}(k_m b)} \Big] dz
\end{aligned}
$$

(4.35)

By defining the following terms as

$$
\begin{aligned}
I_{nm^*}^{S} &= \int_{-h}^{h} \left[\Sigma_{rr}^{Sn}(z)V_S^{m^*}(z) + \Sigma_{rz}^{Sm^*}(z)W_S^{n}(z) \right] dz \\
I_{m^*n}^{S} &= \int_{-h}^{h} \left[\Sigma_{rr}^{Sm^*}(z)V_S^{n}(z) + \Sigma_{rz}^{Sn}(z)W_S^{m^*}(z) \right] dz
\end{aligned}
\qquad (4.36)
$$

Eq. (4.35) yields

$$
Q_{m^*n}(b) = b\pi \left[I_{nm^*}^{S}\Phi'^{*}(k_m b)\Phi(k_n b) - I_{m^*n}^{S}\Phi'(k_n b)\Phi^{*}(k_m b) \right] \qquad (4.37)
$$

By further substituting Eq. (4.37) into Eq. (4.18) yields

$$
I_{nm^*}^{S}\Phi'^{*}(k_m b)\Phi(k_n b) - I_{m^*n}^{S}\Phi'(k_n b)\Phi^{*}(k_m b) = 0 \qquad (4.38)
$$

Eq. (4.38) must satisfy for arbitrary values of b.

When $m^* = n$, $k_m^* = k_n$, Eq. (4.38) becomes

$$I_{nn}^{S}\underbrace{\left[\Phi'(k_n b)\Phi(k_n b)-\Phi'(k_n b)\Phi(k_n b)\right]}_{\equiv 0}=0 \tag{4.39}$$

Eq. (4.39) is always valid since the terms in the square brackets cancel each other.

When $m^{*}\neq n$, $k_m^{*}\neq k_n$, Eq. (4.38) is possible only if $I_{nm*}^{S}\equiv I_{m*n}^{S}\equiv 0$. Therefore we have

$$I_{nm*}^{S}\equiv I_{m*n}^{S}\equiv 0 \qquad \text{for} \qquad k_n\neq k_m^{*} \tag{4.40}$$

4.2.3 Determination of coefficients for evanescent waves

The coefficients of A_{m*}^{S} for evanescent wave mode can be solved by using reciprocity theorem. The domain is also chosen as an annular domain $|z|\le h,\ \ 0\le r\le b,\ \ 0\le\theta\le 2\pi$.

State A : A single evanescent symmetric Lamb wave mode with wave number k_m generated by point load Q applied at $r=0,\theta=0,z=0$.

State B : A single evanescent symmetric Lamb wave mode consisting of an outgoing and converging wave, with wave number k_n. The displacement components of state B are:

$$u_r^n=V_S^n(z)\left[\Phi'(k_n r)+\overline{\Phi}'(k_n r)\right]\cos\theta \tag{4.41}$$

$$u_z^n=W_S^n(z)\left[\Phi(k_n r)+\overline{\Phi}(k_n r)\right]\cos\theta \tag{4.42}$$

$$u_\theta^n=V_S^n(z)\left(\frac{-1}{k_n r}\right)\left[\Phi(k_n r)+\overline{\Phi}(k_n r)\right]\sin\theta \tag{4.43}$$

The left hand side of the reciprocity theorem in Eq. (4.17) is

$$Qu_r^n(0,0,0) = QV_S^n(0)\left[\Phi'(0) + \overline{\Phi}'(0)\right]\cos 0 \tag{4.44}$$

Recall that

$$\begin{aligned}\Phi(k_n r) &= H_1^{(2)}(k_n r)\\ \overline{\Phi}(k_n r) &= H_1^{(1)}(k_n r)\end{aligned} \tag{4.45}$$

The notation of $\Phi'(k_n r)$ is used for the derivative with respect to the argument $\Phi'(\xi) = d\Phi / d\xi$. Thus the derivation in Eq. (4.44) is

$$\begin{aligned}\Phi'(k_n r) &= \frac{1}{2}\left[H_0^{(2)}(k_n r) - H_2^{(2)}(k_n r)\right]\\ \overline{\Phi}'(k_n r) &= \frac{1}{2}\left[H_0^{(1)}(k_n r) - H_2^{(1)}(k_n r)\right]\end{aligned} \tag{4.46}$$

Substituting Eq. (4.46) into Eq. (4.44) yields

$$Qu_r^n(0,0,0) = Q\frac{1}{2}V_S^n(0)\left[H_0^{(2)}(0) - H_2^{(2)}(0) + H_0^{(1)}(0) - H_2^{(1)}(0)\right] \tag{4.47}$$

When the argument is 0, the Hankel function in the square brackets $H_0^{(2)}(x) - H_2^{(2)}(x) + H_0^{(1)}(x) - H_2^{(1)}(x)$ in Eq. (4.47) is equal to 2. Thus Eq. (4.47) becomes

$$Qu_r^n(0,0,0) = QV_S^n(0) \tag{4.48}$$

The right hand side of the reciprocity theorem in Eq. (4.17) can be evaluated in a similar manner as in Section 4.3.

Thus the reciprocity theorem for the states A and B defined in this Section can be expressed as

$$QV_S^n(0) = A_m^{S*}\left[Q_{m*n}^S(b) + T_{m*n}^S(b)\right] \tag{4.48}$$

In Eq. (4.48), $Q_{m*n}^S(b)$ is defined in Eq. (4.37) and $T_{m*n}^S(b)$ can be expressed as

$$T_{m*n}(b) = b\pi\left[I_{nm*}^S\Phi'^*(k_m b)\overline{\Phi}(k_n b) - I_{m*n}^S\overline{\Phi}'(k_n b)\Phi^*(k_m b)\right] \tag{4.49}$$

Eq. (4.18) indicates that $Q_{m*n}^S(b) = 0$ for both $k_n = k_m^*$ and $k_n \neq k_m^*$. Because Eq. (4.40) shows $I_{m*n}^S = I_{nm*}^S = 0$ when $k_n \neq k_m^*$, therefore $T_{m*n}^S(b)$ vanishes for $k_n \neq k_m^*$ as well. Therefore Eq. (4.48) can be simplified to:

$$QV_S^n(0) = A_n^S T_{nn}^S(b) \tag{4.50}$$

From Eq. (4.49), $T_{nn}^S(b)$ can be solved as:

$$T_{nn}(b) = b\pi I_{nn}^S\left[\Phi'(k_n b)\overline{\Phi}(k_n b) - \overline{\Phi}'(k_n b)\Phi(k_n b)\right] \tag{4.51}$$

Substituting Eq. (4.51) into Eq. (4.50) yields

$$QV_S^n(0) = A_n^S b\pi I_{nn}^S\left[\Phi'(k_n b)\overline{\Phi}(k_n b) - \overline{\Phi}'(k_n b)\Phi(k_n b)\right] \tag{4.52}$$

Substituting Eqs. (4.45) into Eq. (4.52) yields

$$QV_S^n(0) = A_n^S b\pi I_{nn}^S\left[H_1^{(2)}'(k_n b)H_1^{(1)}(k_n b) - H_1^{(1)}'(k_n b)H_1^{(2)}(k_n b)\right] \tag{4.53}$$

From page 198 of the book by McLachlan (1955), one identity of Hankel function is mentioned

$$\frac{d}{dx}H_\nu^{(1)}(x)H_\nu^{(2)}(x) - H_\nu^{(1)}(x)\frac{d}{dx}H_\nu^{(2)}(x) = -\frac{4i}{\pi x} \tag{4.54}$$

for all ν and $x \neq 0$

Since no wave number is equal to zero for non-zero frequency, thus Eq. (4.54) is always valid. Substituting Eq. (4.54) into Eq. (4.53) yields

$$QV_S^n(0) = A_n^S \cancel{\pi b} I_{nn}^S \frac{4i}{\cancel{\pi b} k_n} \tag{4.55}$$

Solving Eq. (4.55), the coefficient for evanescent wave mode is

$$A_n^S = \frac{k_n}{4i} \frac{QV_S^n(0)}{I_{nn}^S} \tag{4.56}$$

From Eq. (4.36), I_{nn}^S can be calculated as

$$\begin{aligned} I_{nn}^S &= \int_{-h}^{h} \left[V_S^n(z) \Sigma_{rr}^{Sn}(z) + W_S^n(z) \Sigma_{rz}^{Sn}(z) \right] dz \\ &= \mu \left[c_1^S \cos^2(ph) + c_2^S \cos^2(qh) \right] \end{aligned} \tag{4.57}$$

The constants of c_1^S and c_2^S are

$$c_1^S = \frac{(k_n^2 - q^2)(k_n^2 + q^2)}{2q^3 k_n^3} \left[2qh(k_n^2 - q^2) - (k_n^2 + 7q^2)\sin(2qh) \right], \tag{4.58}$$

$$c_2^S = \frac{k_n^2 + q^2}{pk_n^3} \left[4k_n^2 ph + 2(k_n^2 - 2p^2)\sin(2ph) \right]. \tag{4.59}$$

Similarly, the evanescent antisymmetric Lamb wave mode coefficient can be obtained as

$$A_n^A = \frac{k_n}{4i} \frac{QV_A^n(0)}{I_{nn}^A} \tag{4.60}$$

The evanescent symmetric *SH* wave mode coefficient can be obtained as

$$B_n^S = \frac{1}{4i}\frac{Q}{J_{nn}} \quad \text{for} \quad n = 0, 2, 4, \cdots \tag{4.61}$$

The evanescent antisymmetric *SH* wave mode coefficient can be obtained as

$$B_n^A = \frac{1}{4i}\frac{Q}{J_{nn}} \quad \text{for} \quad n = 1, 3, 5, \cdots \tag{4.62}$$

When the point load is applied at $r = 0, \theta = 0, z = z_0$, the coefficients of the wave modes can be obtained in a similar manner as below

$$A_n^S = \frac{k_n}{4i}\frac{QV_S^n(z_0)}{I_{nn}^S} \tag{4.63}$$

$$A_n^A = \frac{k_n}{4i}\frac{QV_A^n(z_0)}{I_{nn}^A} \tag{4.64}$$

$$B_n^S = \frac{1}{4i}\frac{\cos(n\pi z_0 / h)}{J_{nn}}Q \quad \text{for} \quad n = 0, 2, 4, \cdots \tag{4.65}$$

$$B_n^A = \frac{1}{4i}\frac{\sin(n\pi z_0 / h)}{J_{nn}}Q \quad \text{for} \quad n = 1, 3, 5, \cdots \tag{4.66}$$

When the point load is applied at the plate upper surface at $r = 0, \theta = 0, z = h$, the coefficients of the wave modes can be obtained in a similar manner as below

$$A_n^S = \frac{k_n}{4i}\frac{QV_S^n(h)}{I_{nn}^S} \tag{4.63}$$

$$A_n^A = \frac{k_n}{4i}\frac{QV_A^n(h)}{I_{nn}^A} \tag{4.64}$$

$$B_n^S = \frac{1}{4i}\frac{\cos(n\pi/2)}{J_{nn}}Q \quad \text{for} \quad n = 0,2,4,\cdots \tag{4.65}$$

$$B_n^A = \frac{1}{4i}\frac{\sin(n\pi/2)}{J_{nn}}Q \quad \text{for} \quad n = 1,3,5,\cdots \tag{4.66}$$

4.3. Verification of theoretical solution for evanescent wave modes for load along +*x* direction - Example One

In order to verify the theoretical solution for evanescent wave modes obtained in this chapter, it is verified by comparing the displacement in the near field with FEA results obtained in COMSOL. The surface load is of polynomial terms.

4.3.1. FEA result for plate wave (including evanescent waves) under surface load in the near field

The following study is conducted at frequency $f = 100\,kHz$. Same as the line load case, for the infinite plate, the size of the rectangular area under observation is set to be $p_w \times p_l$, where $p_w = \max WL \cdot 0.5 = 27.35\,mm$ and $p_l = \max WL \cdot 0.5 = 27.35\,mm$. The thickness of the aluminum plate is 3.2 *mm*.

The *x*-*y* plane is set to be the middle layer of the plate. A surface load along +*x* direction is applied on the plate upper surface:

$$f_x = x^3 y^2 \times 10^{21}\ N/m^2 \quad \text{at} \quad -a_w/2 < x < a_w/2, -a_l/2 < y < a_l/2$$

where

$$a_w = 4\ mm, \quad a_l = 8\ mm$$

The width of the PML is 1/2 of the maximum wavelength at the given frequency. The PML scaling factor is set as 2 and the PML scaling curvature parameter is set as 3.

In the FEA study, the plate can be set to be small, because the displacement in the near field, *i.e.*, the area where force is applied is under consideration since we are looking at evanescent waves in this section. By reducing the plate size, the calculation time in COMSOL can be reduced.

The maximum size of elements on the plate and PML are 1/16 of the minimum wavelength, while the element size on the area where surface load is applied is even smaller (1/80 of minimum wavelength) than that of the plate.

The results for displacement in COMSOL are plotted below:

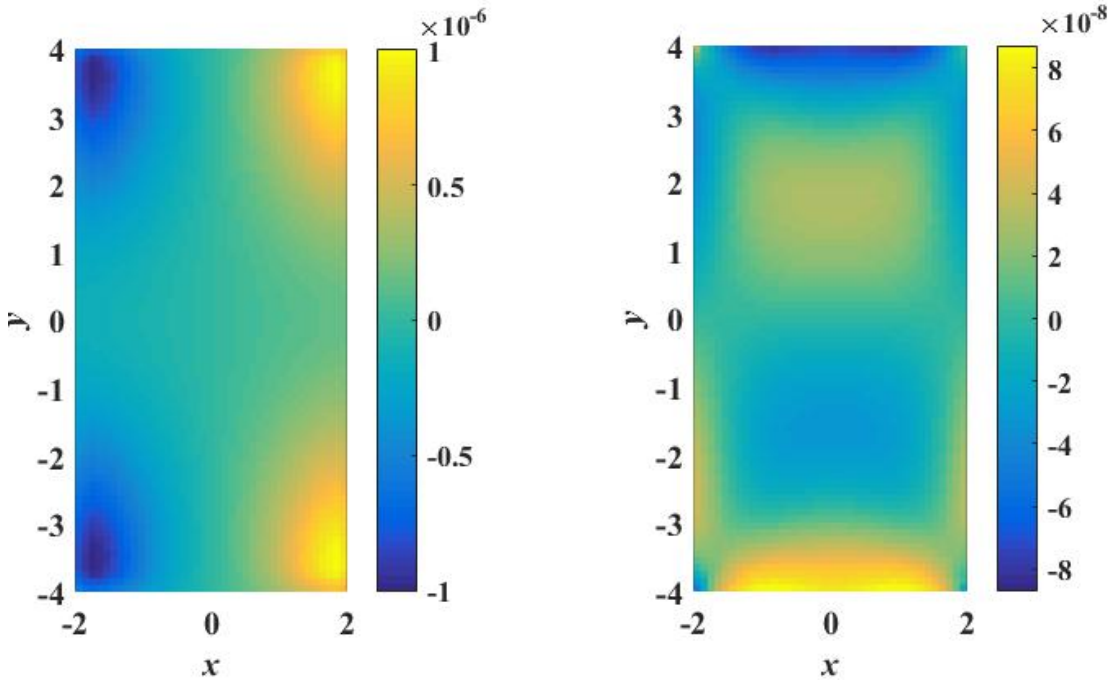

(units for *x*-*y* axis: *mm*) (units for *x*-*y* axis: *mm*)

(a) (b)

Figure 4.1. (a) displacement *u* and (b) displacement *v* on force applying area obtained in COMSOL for polynomial load

4.3.2 Comparing theoretical resulted plotted in Matlab with FEA result for plate wave under surface load in the near field - on the entire force-applying area

There are numerous evanescent wave modes at any given frequency, their amplitudes decay exponentially along the wave propagation direction. In last chapter, it was verified that the theoretical results for propagating waves in the far field matches very well FEA results for point load, line load and surface load. However, in the near field, if only theoretical propagating waves are taken into consideration, the displacement field will be very different

from FEA solution. If evanescent wavefields are added to the solution, the theoretical results should match the FEA results.

In this Section, four different studies are conducted:

(1) Scenario 1: Only considering propagating wavefields in the near field

(2) Scenario 2: Considering both propagating wavefields and evanescent Lamb $A_1, S_1 / S_2$ wave modes and shear horizontal SH_1, SH_2 wave modes.

(3) Scenario 3: Considering both propagating wavefields and evanescent Lamb $A_1, S_1 / S_2, A_2 / A_3, S_3 / S_4$ wave modes and shear horizontal SH_1, SH_2, SH_3, SH_4 wave modes.

(4) Scenario 4: Considering both propagating wavefields and evanescent Lamb wave $A_1, S_1 / S_2, A_2 / A_3, S_3 / S_4, A_4$ modes and shear horizontal $SH_1, SH_2, SH_3, SH_4, SH_5$ wave modes.

4.3.2.1 Scenario 1: Only considering propagating wavefields in the near field

If only propagating wave modes are considered, the results are shown below:

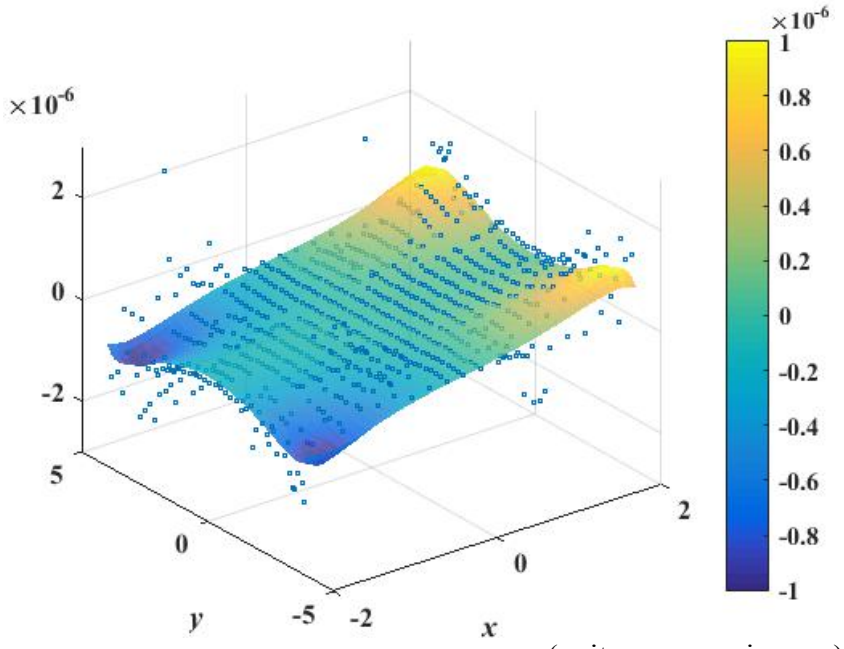

(units on *x*-*y* axis: mm)

(a)

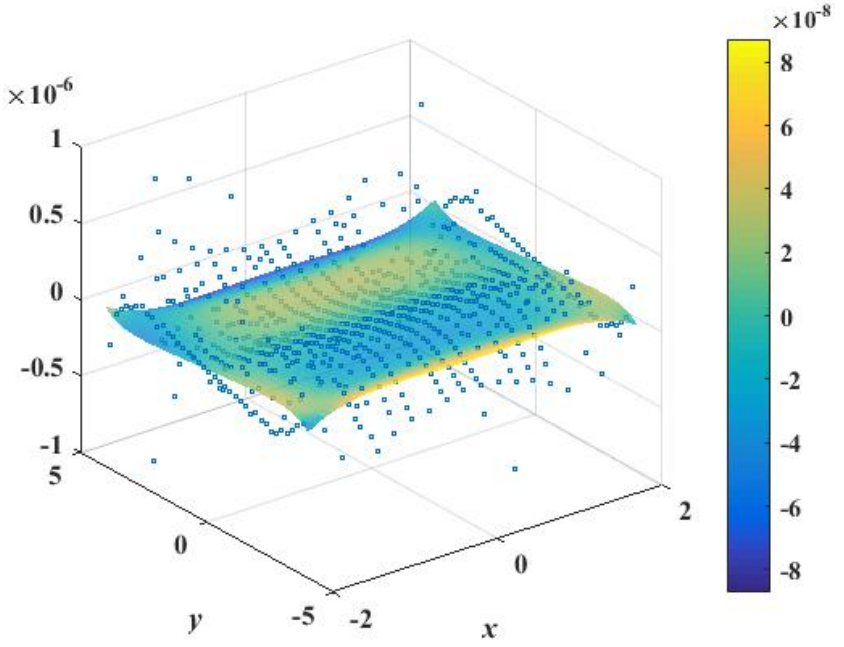

(units on *x*-*y* axis: *mm*)

(b)

Figure 4.2 Comparing (a) displacement *u* and (b) displacement *v* for theoretical solution (only propagating wave modes, colored surface) with FEA solution (blue dots)

In the above two figures, the surface is the theoretical solution with only propagating wave modes and the blue dots are the COMSOL solution. As can be seen, these two solutions deviates from each a lot. The reason why the theoretical solution is not smooth is due to the singularities of the wave modes at the force applying position.

4.3.2.2 Scenario 2: Considering both propagating wavefields and evanescent Lamb $A_1, \mathrm{S}_1 / S_2$ wave modes and shear horizontal SH_1, SH_2 wave modes

When considering both propagating waves and evanescent Lamb $A_1, \mathrm{S}_1 / S_2$ (Lamb S_1 / S_2 modes have the same pure imaginary wavenumber) wave modes and shear horizontal SH_1, SH_2 wave modes in the theoretical solution, the displacement on the force-applying surface for theoretical solution and COMSOL solution are compared here:

Figure 4.3 Comparing (a) displacement *u* and (b) displacement *v* for theoretical solution (both propagating waves and evanescent Lamb $A_1, S_1 / S_2$ wave modes and shear horizontal SH_1, SH_2 wave modes, colored surface) with FEA solution (blue dots)

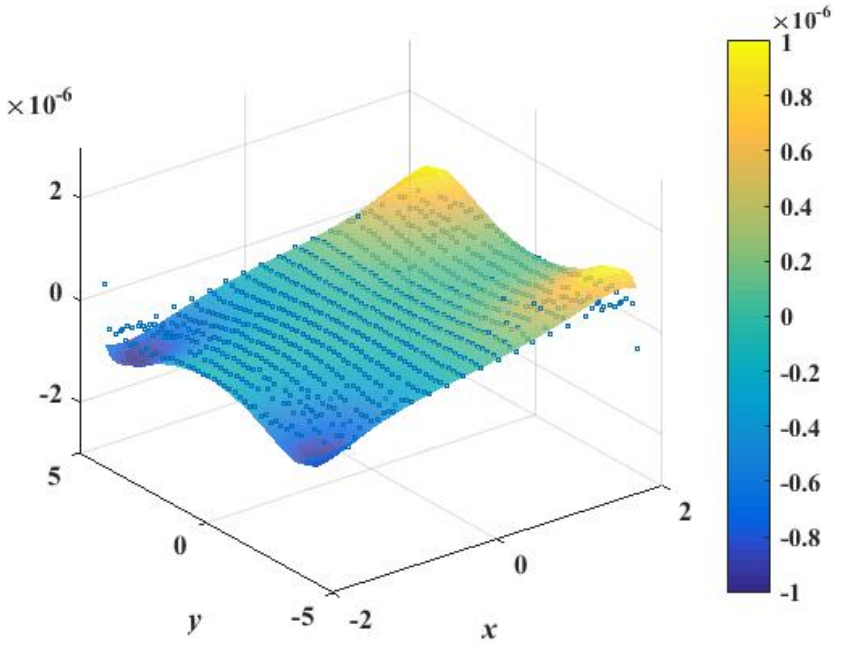

(units on *x*-*y* axis: *mm*)

(a)

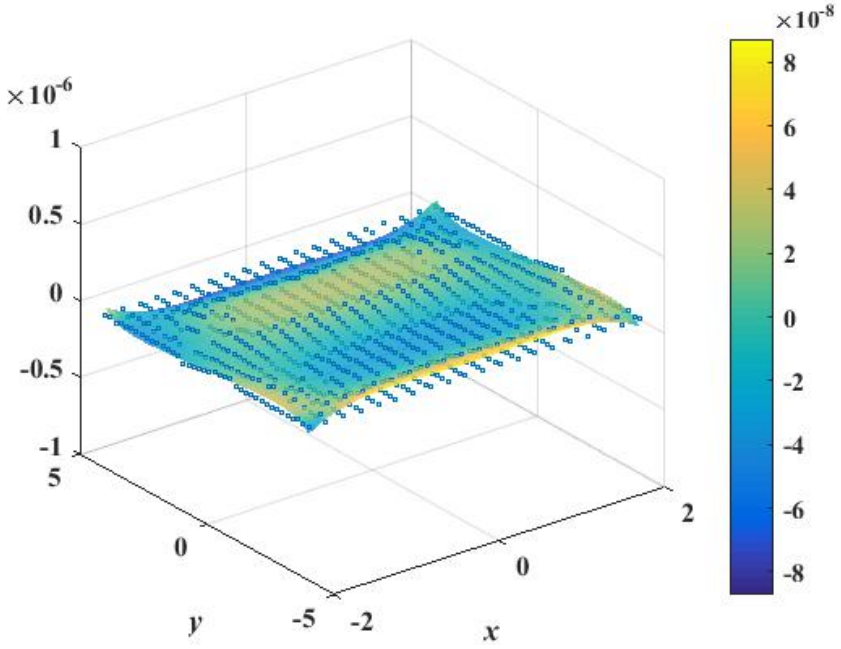

(units on *x*-*y* axis: *mm*)

(b)

When considering propagating waves and evanescent Lamb $A_1, \mathrm{S}_1 / S_2$ wave modes and shear horizontal SH_1, SH_2 wave modes, the displacement in the near field on the force-applying area already have the same shape as FEA results in COMSOL. Compared to the figures in Section 4.3.2.1 for scenario 1, adding these five evanescent wave modes is a huge improvement. This also verifies the correctness of the theoretical solution for evanescent wave modes.

As discussed earlier, there are infinite evanescent wave modes at the given frequency of $f = 100\, kHz$, in order to see how many evanescent wave modes need to be taken into consideration, scenarios 3 and 4 are carried out.

4.3.2.3 Scenario 3: Considering both propagating wavefields and evanescent Lamb $A_1, \mathrm{S}_1 / S_2, A_2 / A_3, \mathrm{S}_3 / S_4$ wave modes and shear horizontal SH_1, SH_2, SH_3, SH_4 wave modes

Compared to scenario 2, scenario 3 added six more evanescent wave modes: evanescent Lamb $A_2 / A_3, \mathrm{S}_3 / S_4$ wave modes and shear horizontal SH_3, SH_4 wave modes.

The displacement on the force-applying surface for both theoretical solution and COMSOL solution are compared here:

Figure 4.4 Comparing (a) displacement *u* and (b) displacement *v* for theoretical solution (both propagating waves and evanescent Lamb $A_1, \mathrm{S}_1 / S_2, A_2 / A_3, \mathrm{S}_3 / S_4$ wave modes and shear horizontal SH_1, SH_2, SH_3, SH_4 wave modes, colored surface) with FEA solution (blue dots)

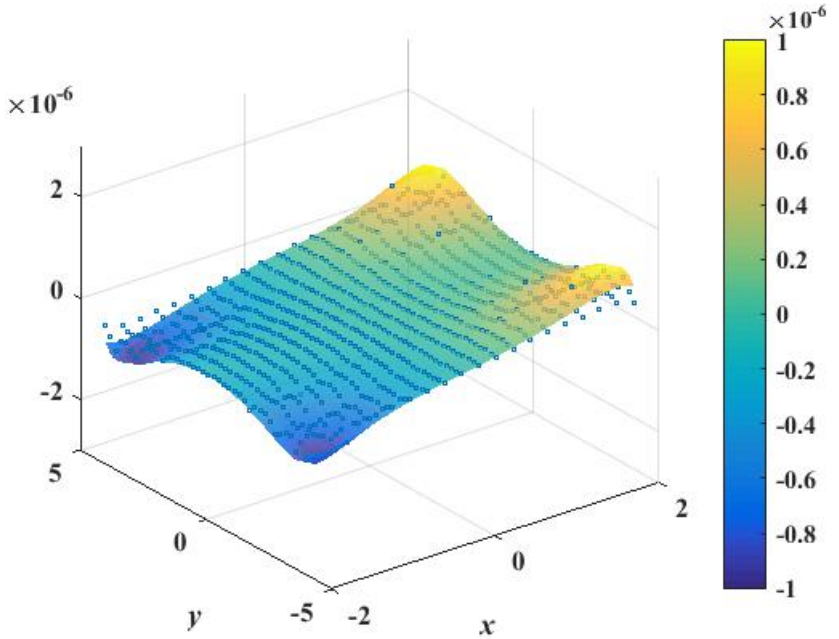

(units on *x*-*y* axis: *mm*)

(a)

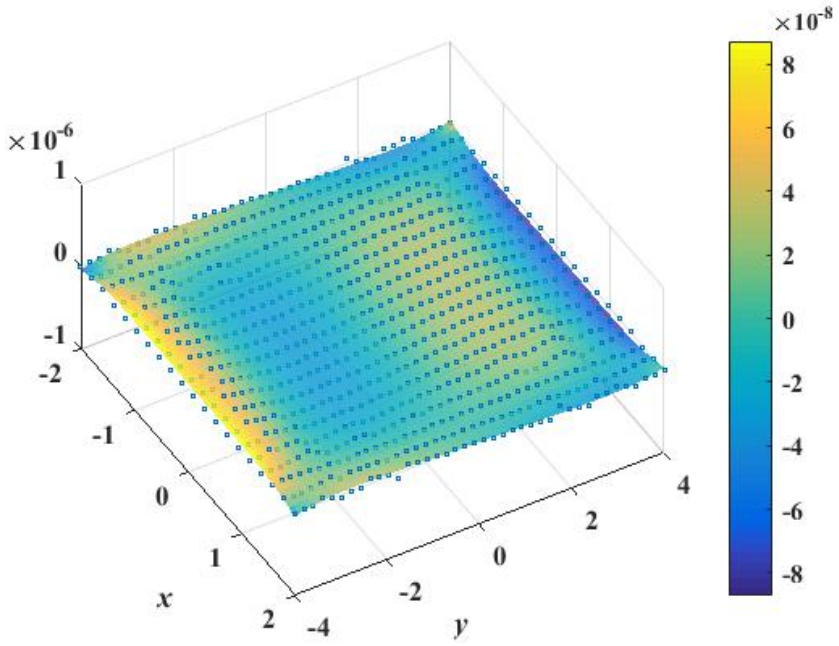

(units on *x*-*y* axis: *mm*)

(b)

4.3.2.4 Scenario 4: Considering both propagating wavefields and evanescent Lamb wave A_1- A_3, S_1- S_4 modes and shear horizontal SH_1 - SH_5 wave modes

Compared to scenario 3, scenario 4 added more evanescent wave modes: evanescent Lamb wave A_4 modes and shear horizontal SH_5 wave modes.

The displacement on the force-applying surface for both theoretical solution and COMSOL solution are compared here:

Figure 4.5 Comparing (a) displacement *u* and (b) displacement *v* for theoretical solution (both propagating waves and evanescent Lamb wave $A_1, \mathrm{S}_1 / S_2, A_2 / A_3, \mathrm{S}_3 / S_4, A_4$ modes and shear horizontal $SH_1, SH_2, SH_3, SH_4, SH_5$ wave modes, colored surface) with FEA solution (blue dots)

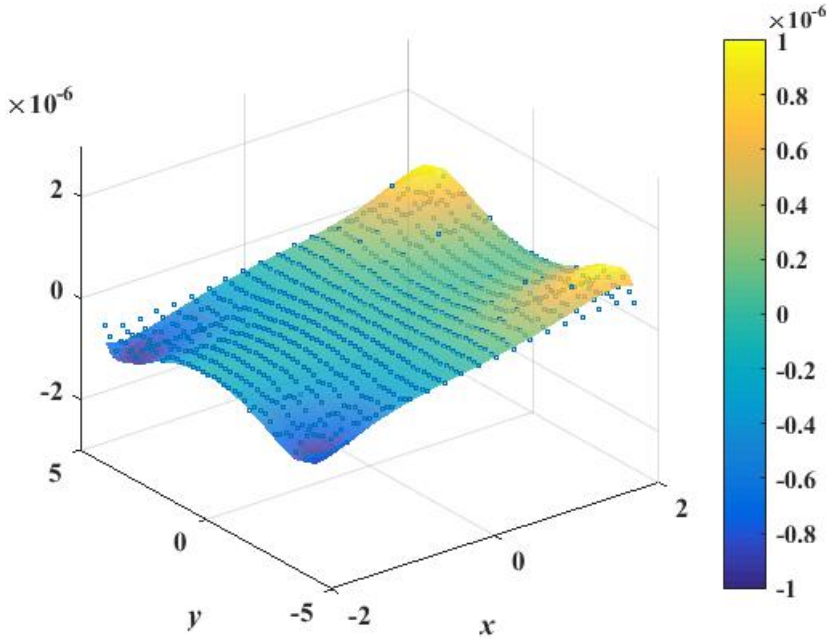

(units on *x*-*y* axis: *mm*)

(a)

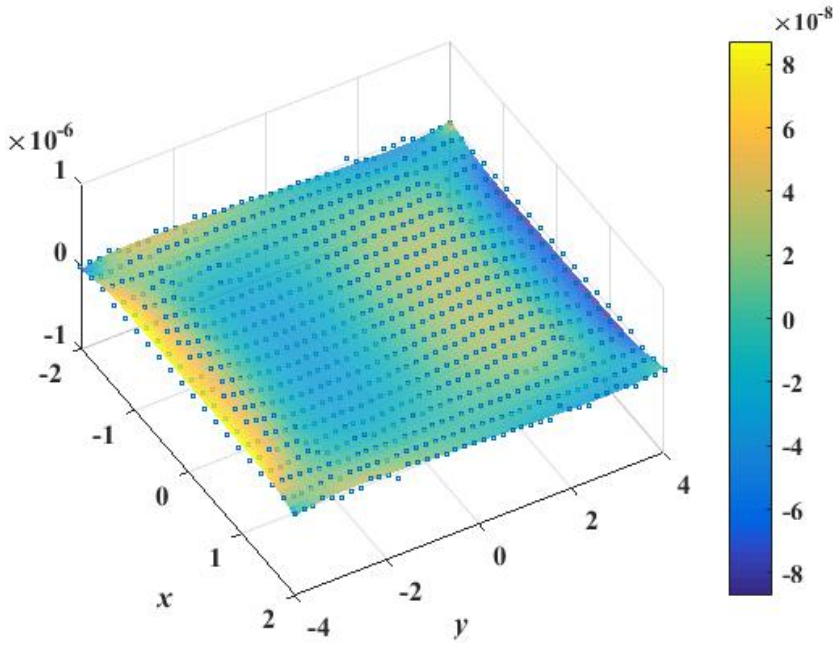

(units on *x*-*y* axis: *mm*)

(b)

When comparing scenario 4 with scenario 3, though more evanescent waves (Lamb wave A_4 mode and shear horizontal SH_5 wave mode) are added, the displacements in these two cases are almost the same. This indicates that the amplitudes of any more evanescent wave modes can be ignored at this given frequency ($f = 100\,kHz$). Only evanescent Lamb $A_1, S_1 / S_2, A_2 / A_3, S_3 / S_4$ wave modes and shear horizontal SH_1, SH_2, SH_3, SH_4 wave modes need to be taken into consideration at $f = 100\,kHz$.

The reason why displacement *u* magnitude is way larger than displacement *v* is because the surface loading is along the *x* direction.

It can be seen from the above figures that the theoretical result and the FEA result matches pretty well on the monitoring lines. This verifies the theoretical solution for evanescent wave mode coefficients.

4.4. Verification of theoretical solution for evanescent wave modes for load along +*x* direction - Example Two

In the second example, a surface load of 3-D Gaussian distribution is applied over a square area of $a_w \times a_w$ on plate upper surface. The size of a_w is set to be 1/5 of the minimum wavelength, which is 3.2 *mm*. This results a concentrated load, but no pure singularities, if the Gaussian is larger than a few mesh elements.

In COMSOL, the Gaussian function is applied on the plate upper surface over a small square region. The three-dimensional Gaussian function is defined by

$$Gaussian(x,y) = Ae^{-\frac{x^2}{a_w^2}-\frac{y^2}{a_w^2}}$$

where A is defined as 1×10^9 in this case.

4.4.1. COMSOL result for Gaussian surface loading in the near field

The size of the plate is 3 times of $a_w \times a_w$ along both x and y axis. The height of the plate is 3.2 *mm*. The width of the perfect matched layer is set to be half of the maximum wavelength. PML scaling factor is set to be 2 and PML scaling curvature parameter is set to be 3.

The mesh size of the plate is set to be 1/80 of minimum wavelength at the force applying area. The mesh size is set to be 1/20 of the minimum wavelength.

In-plane displacement result obtained in COMSOL is:

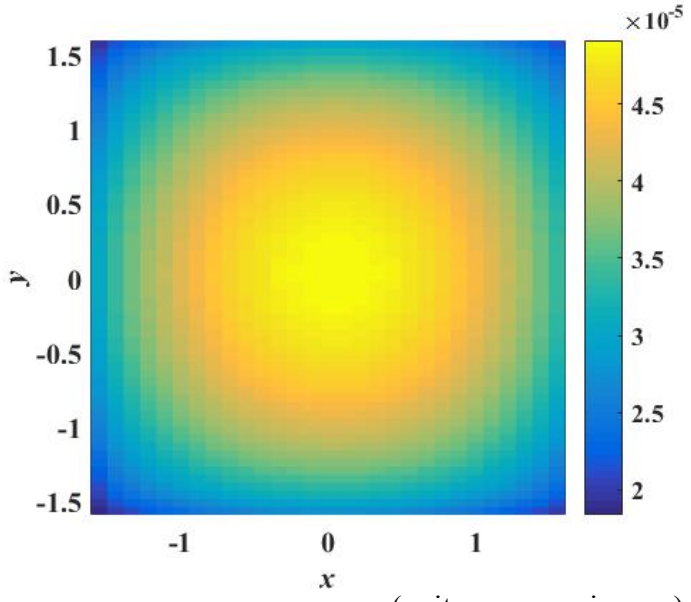

(units on *x*-*y* axis: *mm*)

(a)

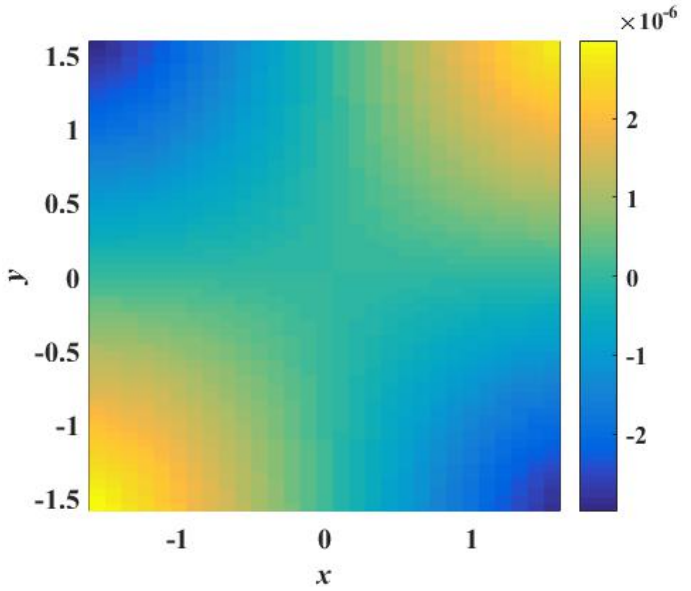

(units on *x*-*y* axis: *mm*)

(b)

Figure 4.6 (a) displacement *u* and (b) displacement *v* on plate upper surface force applying area under Gaussian load in COMSOL

4.4.2. Numerical result for plate wave (including evanescent waves) under Gaussian surface load

4.4.2.1. Determine the number of modes needed at the current forcing scenario

In Section 5.4, several scenarios were brought up in order to study the number of modes needed to for that specific loading and frequency, which can be quite cumbersome. In this example, in order to study how many modes are needed for the loading scenario, the amplitude of each wave mode under Gaussian loading is shown in the Table 4.1 below:

Table 4.1 Order of magnitude for displacement component of each wave mode under Gaussian load in the force applying area

Wave mode	Order of magnitude [m]
A_0	10^{-4}
A_1	10^{-4}
A_2 / A_3	10^{-7}
A_4	10^{-8}
S_0	10^{-3}
S_1 / S_2	10^{-7}
S_3 / S_4	10^{-7}
SH_0	10^{-3}
SH_1	10^{-4}
SH_2	10^{-6}
SH_3	10^{-6}
SH_4	10^{-6}
SH_5	10^{-6}
SH_6	10^{-7}

The dominating term are in the order of 1×10^{-3}, if considering all the terms with an amplitude larger than 1×10^{-6}, then the wave modes which need to be taken into consideration consists of: A_0, A_1, S_0, SH_0- SH_5.

The mesh size for the force applying area in Matlab is chosen to be 1/60 of minimum wavelength. The in-plane displacement under Gaussian load is compared with COMSOL result below:

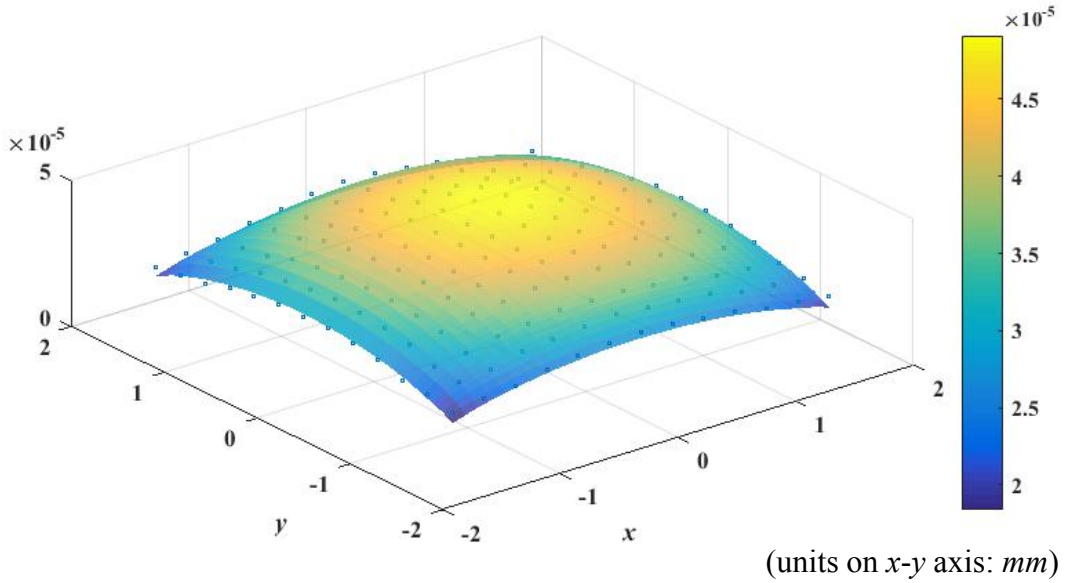

(units on *x*-*y* axis: *mm*)

(a)

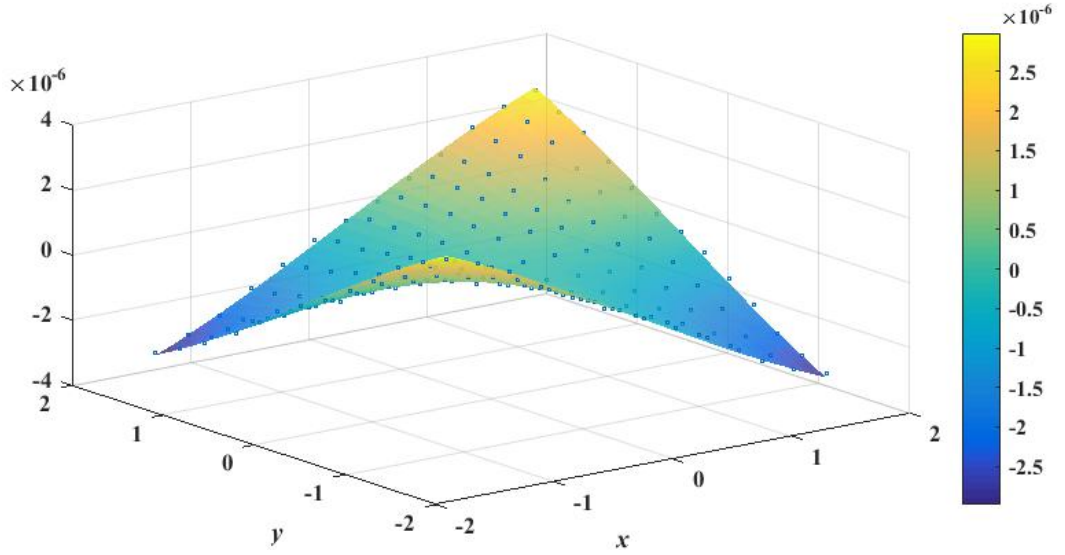

(units on *x*-*y* axis: *mm*)

(b)

Figure 4.7 Comparing analytical result (blue dots) for plate (a) displacement *u* (b) displacement *v* under Gaussian load in near field with FEA results (colored surface)

As can be seen, the analytical result matches pretty with the COMSOL result. This further verifies the correctness of the analytical derivation for evanescent wave displacement.

4.5 Theoretical solution for amplitude of evanescent wave modes under point load along +*y* direction

4.5.1 Use of the complex reciprocity theorem

As shown by Eq. (4.17), the complex reciprocity theorem relating two time-harmonic states with superscripts *A* and *B* is

$$\int_V (f_i^{A*} u_i^B - f_i^B u_i^{A*}) dV = \int_S (u_i^{A*} \sigma_{ij}^B - u_i^B \sigma_{ij}^{A*}) n_j dS$$

In the above equations, f_i^A and f_i^B are body forces; S is the boundary for region V; n_j are the outward normal components.

In an annular domain $|z| \le h,\ \ 0 \le r \le b,\ \ 0 \le \theta \le 2\pi$, the reciprocity theorem can be applied to two symmetric evanescent Lamb wave modes with no body forces. The wave numbers for the two symmetric evanescent Lamb wave modes m and n are k_m and k_n respectively. Since both modes do not have body forces, the left hand side of Eq. (4.17) is 0. The right hand side of Eq. (4.17) can be expressed as

$$Q_{m*n}(b) = 0 \qquad (4.67)$$

where

$$
\begin{aligned}
Q_{m^*n}(b) &= b\int_0^{2\pi}\int_{-h}^{h}\left\{u_i^{m^*}\sigma_{ij}^{n}-u_i^{n}\sigma_{ij}^{m^*}\right\}n_j\,d\theta dz \\
&= b\int_0^{2\pi}\int_{-h}^{h}\Bigg\{\underbrace{\left[u_r^{m^*}\sigma_{rr}^{n}-u_r^{n}\sigma_{rr}^{m^*}\right]}_{I} \\
&\qquad +\underbrace{\left[u_z^{m^*}\sigma_{rz}^{n}-u_z^{n}\sigma_{rz}^{m^*}\right]}_{II} \\
&\qquad +\underbrace{\left[u_\theta^{m^*}\sigma_{r\theta}^{n}-u_\theta^{n}\sigma_{r\theta}^{m^*}\right]}_{III}\Bigg\}d\theta dz
\end{aligned}
\tag{4.68}
$$

As can be seen, in Eq. (4.68), the right hand side is divided into three sections, represented by I, II, III respectively.

The carrier wave approach proposed by Achenbach and Xu (1999) gives the forms of plate wave modes under loading in +*x* direction, as listed in Eq. (4.20) to Eq. (4.22). For plate wave modes under loading in a random direction α with respect to the +*x* axis, the Lamb wave forms can be expressed as

$$u_r^n = V_S^n(z)\Phi'(k_n r)\cos(\theta-\alpha) \tag{4.69}$$

$$u_z^n = W_S^n(z)\Phi(k_n r)\cos(\theta-\alpha) \tag{4.70}$$

$$u_\theta^n = V_S^n(z)\left(\frac{-1}{k_n r}\right)\Phi(k_n r)\sin(\theta-\alpha) \tag{4.71}$$

Therefore, for a point load along +*y* direction, *i.e.* $\alpha = \pi/2$, the Lamb wave forms can be expressed as

$$u_r^n = V_S^n(z)\Phi'(k_n r)\cos(\theta - \pi/2) = V_S^n(z)\Phi'(k_n r)\sin\theta \tag{4.72}$$

$$u_z^n = W_S^n(z)\Phi(k_n r)\cos(\theta - \pi/2) = W_S^n(z)\Phi(k_n r)\sin\theta \tag{4.73}$$

$$u_\theta^n = V_S^n(z)\left(\frac{-1}{k_n r}\right)\Phi(k_n r)\sin(\theta - \pi/2) = V_S^n(z)\left(\frac{-1}{k_n r}\right)\Phi(k_n r)\cos\theta \tag{4.74}$$

The corresponding stress components under loading in +*y* direction are

$$u_z^n = W_S^n(z)\Phi(k_n r)\sin\theta \tag{4.75}$$

$$u_\theta^n = V_S^n(z)\left(\frac{-1}{k_n r}\right)\Phi(k_n r)\cos\theta \tag{4.76}$$

$$\sigma_{rz}^n = -\Sigma_{rz}^{Sn}(z)\Phi'(k_n r)\sin\theta \tag{4.77}$$

$$\sigma_{zz}^n = \Sigma_{rz}^{Sn}(z)\Phi(k_n r)\sin\theta \tag{4.78}$$

$$\begin{aligned}\sigma_{rr}^n = {} & \Sigma_{rr}^{Sn}(z)\Phi(k_n r)\cos\theta - \overline{\Sigma}_{rr}^{Sn}(z) \\ & \times\left[\frac{1}{r}\Phi'(k_n r) - \frac{1}{k_n r^2}\Phi(k_n r)\right]\sin\theta\end{aligned} \tag{4.79}$$

$$\sigma_{\theta z}^n = \Sigma_{\theta z}^{Sn}(z)\left(\frac{-1}{k_n r}\right)\Phi(k_n r)\cos\theta \tag{4.80}$$

$$\sigma_{r\theta}^n = \Sigma_{r\theta}^{Sn}(z)\left[-\frac{1}{r}\Phi'(k_n r) + \frac{1}{k_n r^2}\Phi(k_n r)\right]\cos\theta \tag{4.81}$$

where the terms related to z are expressed as in Eq. (4.28).

Substituting Eq. (4.72)-Eq. (4.81) to Eq. (4.68) and considering $(1/k_n)^* = k_n^*/|k_n|^2$ and $\bar{\Sigma}_{rr}^{Sn}(z) = \Sigma_{r\theta}^{Sn}(z) = 2\mu V_S^n(z)$, the first term in Eq. (4.68) is evaluated as

$$
\begin{aligned}
I &= u_r^{m*}\sigma_{rr}^n - u_r^n\sigma_{rr}^{m*} \\
&= \left[V_S^{m*}(z)\Phi'^*(k_m r)\sin\theta\right]\left\{\Sigma_{rr}^{Sn}(z)\Phi(k_n r)\sin\theta - \underline{\bar{\Sigma}_{rr}^{Sn}(z)}\times\left[\frac{1}{r}\Phi'(k_n r) - \frac{1}{k_n r^2}\Phi(k_n r)\right]\sin\theta\right\} \\
&\quad - \left[V_S^n(z)\Phi'(k_n r)\sin\theta\right]\left\{\Sigma_{rr}^{Sm*}(z)\Phi^*(k_m r)\sin\theta - \underline{\underline{\bar{\Sigma}_{rr}^{Sm*}(z)}}\times\left[\frac{1}{r}\Phi'^*(k_m r) - \frac{k_m^*}{|k_m|^2 r^2}\Phi^*(k_m r)\right]\sin\theta\right\} \\
&\overset{\bar{\Sigma}_{rr}^{Sn}(z)=2\mu V_S^n(z)}{=} \left[V_S^{m*}(z)\Phi'^*(k_m r)\sin\theta\right]\left\{\Sigma_{rr}^{Sn}(z)\Phi(k_n r)\sin\theta - \underline{2\mu V_S^n(z)}\times\left[\frac{1}{r}\Phi'(k_n r) - \frac{1}{k_n r^2}\Phi(k_n r)\right]\sin\theta\right\} \\
&\quad - \left[V_S^n(z)\Phi'(k_n r)\sin\theta\right]\left\{\Sigma_{rr}^{Sm*}(z)\Phi^*(k_m r)\sin\theta - \underline{\underline{2\mu V_S^{m*}(z)}}\times\left[\frac{1}{r}\Phi'^*(k_m r) - \frac{k_m^*}{|k_m|^2 r^2}\Phi^*(k_m r)\right]\sin\theta\right\} \\
&= \sin^2\theta\left[V_S^{m*}(z)\Phi'^*(k_m r)\Sigma_{rr}^{Sn}(z)\Phi(k_n r) - V_S^n(z)\Phi'(k_n r)\Sigma_{rr}^{Sm*}(z)\Phi^*(k_m r)\right] \\
&\quad + 2\mu V_S^{m*}(z)V_S^n(z)\sin^2\theta\left[\cancel{-\frac{1}{r}\Phi'(k_n r)\Phi'^*(k_m r)} + \frac{1}{k_n r^2}\Phi(k_n r)\Phi'^*(k_m r)\right. \\
&\qquad \left. + \cancel{\frac{1}{r}\Phi'(k_n r)\Phi'^*(k_m r)} - \frac{k_m^*}{|k_m|^2 r^2}\Phi'(k_n r)\Phi^*(k_m r)\right] \\
&= \sin^2\theta\left[V_S^{m*}(z)\Phi'^*(k_m r)\Sigma_{rr}^{Sn}(z)\Phi(k_n r) - V_S^n(z)\Phi'(k_n r)\Sigma_{rr}^{Sm*}(z)\Phi^*(k_m r)\right] \\
&\quad + 2\mu V_S^{m*}(z)V_S^n(z)\sin^2\theta\left[\frac{1}{k_n r^2}\Phi(k_n r)\Phi'^*(k_m r) - \frac{k_m^*}{|k_m|^2 r^2}\Phi'(k_n r)\Phi^*(k_m r)\right]
\end{aligned}
\tag{4.82}
$$

The second term in Eq. (4.68) is evaluated as

$$
\begin{aligned}
II &= u_z^{m*}\sigma_{rz}^{n} - u_z^{n}\sigma_{rz}^{m*} \\
&= \left[W_S^{m*}(z)\Phi^*(k_m r)\sin\theta\right]\left[-\Sigma_{rz}^{Sn}(z)\Phi'(k_n r)\sin\theta\right] \\
&\quad -\left[W_S^{n}(z)\Phi(k_n r)\sin\theta\right]\left[-\Sigma_{rz}^{Sm*}(z)\Phi'^*(k_m r)\sin\theta\right] \\
&= \sin^2\theta\left[-W_S^{m*}(z)\Sigma_{rz}^{Sn}(z)\Phi^*(k_m r)\Phi'(k_n r)\right. \\
&\qquad \left. +W_S^{n}(z)\Sigma_{rz}^{Sm*}(z)\Phi(k_n r)\Phi'^*(k_m r)\right]
\end{aligned}
\tag{4.83}
$$

The third term in Eq. (4.68) is evaluated as

$$
\begin{aligned}
III &= u_\theta^{m*}\sigma_{r\theta}^{n} - u_\theta^{n}\sigma_{r\theta}^{m*} \\
&= \left[V_S^{m*}(z)\left(\frac{-k_m^*}{|k_m|^2 r}\right)\Phi^*(k_m r)\cos\theta\right]\left\{\underline{\Sigma_{r\theta}^{Sn}(z)}\left[-\frac{1}{r}\Phi'(k_n r)+\frac{1}{k_n r^2}\Phi(k_n r)\right]\cos\theta\right\} \\
&\quad -\left[V_S^{n}(z)\left(\frac{-1}{k_n r}\right)\Phi(k_n r)\cos\theta\right]\left\{\underline{\underline{\Sigma_{r\theta}^{Sm*}(z)}}\left[-\frac{1}{r}\Phi'^*(k_m r)+\left(\frac{k_m^*}{|k_m|^2 r^2}\right)\Phi^*(k_m r)\right]\cos\theta\right\} \\
&\overset{\Sigma_{r\theta}^{Sn}(z)=2\mu V_S^{n}(z)}{=} \left[V_S^{m*}(z)\left(\frac{-k_m^*}{|k_m|^2 r}\right)\Phi^*(k_m r)\cos\theta\right]\left\{\underline{2\mu V_S^{n}(z)}\left[-\frac{1}{r}\Phi'(k_n r)+\frac{1}{k_n r^2}\Phi(k_n r)\right]\cos\theta\right\} \\
&\quad -\left[V_S^{n}(z)\left(\frac{-1}{k_n r}\right)\Phi(k_n r)\cos\theta\right]\left\{\underline{\underline{2\mu V_S^{m*}(z)}}\left[-\frac{1}{r}\Phi'^*(k_m r)+\left(\frac{k_m^*}{|k_m|^2 r^2}\right)\Phi^*(k_m r)\right]\cos\theta\right\} \\
&= 2\mu V_S^{n}(z)V_S^{m*}(z)\cos^2\theta\left[\left(\frac{k_m^*}{|k_m|^2 r^2}\right)\Phi^*(k_m r)\Phi'(k_n r)+\cancel{\left(\frac{-k_m^*}{|k_m|^2 k_n r^3}\right)\Phi^*(k_m r)\Phi(k_n r)}\right. \\
&\qquad \left.-\frac{1}{k_n r}\Phi(k_n r)\Phi'^*(k_m r)+\cancel{\left(\frac{k_m^*}{k_n|k_m|^2 r^3}\right)\Phi(k_n r)\Phi^*(k_m r)}\right] \\
&= 2\mu V_S^{n}(z)V_S^{m*}(z)\cos^2\theta\left[\left(\frac{k_m^*}{|k_m|^2 r^2}\right)\Phi^*(k_m r)\Phi'(k_n r)-\frac{1}{k_n r}\Phi(k_n r)\Phi'^*(k_m r)\right]
\end{aligned}
\tag{4.84}
$$

The integration of the terms involving θ is

$$\int_0^{2\pi} \sin^2\theta d\theta = \pi$$
$$\int_0^{2\pi} \cos^2\theta d\theta = \pi \tag{4.85}$$

Substituting Eq. (4.82)-Eq. (4.85) into Eq. (4.67) and Eq. (4.68) yields

$$\begin{aligned}
Q_{m^*n}(b) = b\pi\int_{-h}^{h}\Big\{ & V_S^{m^*}(z)\Phi'^{*}(k_m r)\Sigma_{rr}^{Sn}(z)\Phi(k_n r) - V_S^{n}(z)\Phi'(k_n r)\Sigma_{rr}^{Sm^*}(z)\Phi^{*}(k_m r) \\
& + 2\mu V_S^{m^*}(z)V_S^{n}(z)\left[\cancel{\frac{1}{k_n r^2}\Phi(k_n r)\Phi'^{*}(k_m r)} - \cancel{\frac{k_m^*}{|k_m|^2 r^2}\Phi'(k_n r)\Phi^{*}(k_m r)}\right] \\
& - W_S^{m^*}(z)\Sigma_{rz}^{Sn}(z)\Phi^{*}(k_m r)\Phi'(k_n r) \\
& + W_S^{n}(z)\Sigma_{rz}^{Sm^*}(z)\Phi(k_n r)\Phi'^{*}(k_m r) \\
& + 2\mu V_S^{n}(z)V_S^{m^*}(z)\left[\cancel{\frac{k_m^*}{|k_m|^2 r^2}\Phi'(k_n r)\Phi^{*}(k_m r)} - \cancel{\frac{1}{k_n r}\Phi(k_n r)\Phi'^{*}(k_m r)}\right]\Big\} dz\Big|_{r=b} \\
= b\pi\int_{-h}^{h}\Big[& V_S^{m^*}(z)\Sigma_{rr}^{Sn}(z)\Phi'^{*}(k_m r)\Phi(k_n r) - V_S^{n}(z)\Sigma_{rr}^{Sm^*}(z)\Phi'(k_n r)\Phi^{*}(k_m r) \\
& - W_S^{m^*}(z)\Sigma_{rz}^{Sn}(z)\Phi^{*}(k_m r)\Phi'(k_n r) + W_S^{n}(z)\Sigma_{rz}^{Sm^*}(z)\Phi(k_n r)\Phi'^{*}(k_m r)\Big] dz\Big|_{r=b} \\
= b\pi\int_{-h}^{h}\Big[& V_S^{m^*}(z)\Sigma_{rr}^{Sn}(z)\underline{\Phi'^{*}(k_m b)\Phi(k_n b)} - V_S^{n}(z)\Sigma_{rr}^{Sm^*}(z)\underline{\underline{\Phi'(k_n b)\Phi^{*}(k_m b)}} \\
& - W_S^{m^*}(z)\Sigma_{rz}^{Sn}(z)\underline{\underline{\Phi^{*}(k_m b)\Phi'(k_n b)}} + W_S^{n}(z)\Sigma_{rz}^{Sm^*}(z)\underline{\Phi(k_n b)\Phi'^{*}(k_m b)}\Big] dz
\end{aligned} \tag{4.86}$$

Eq. (4.86) is the same as Eq. (4.35), therefore this deduction will end up with the same conclusion as Eq. (4.40)

$$I_{nm^*}^{S} \equiv 0 \qquad \text{for} \qquad k_n \neq k_m^*$$

4.5.2 Determination of coefficients for evanescent waves

The coefficients of A_{m*}^{S} for evanescent wave mode can be solved by using reciprocity theorem. The domain is also chosen as an annular domain $|z| \le h,\ \ 0 \le r \le b,\ \ 0 \le \theta \le 2\pi$.

State A : A single evanescent symmetric Lamb wave mode with wave number k_m generated by point load Q applied at $r = 0, \theta = 0, z = 0$.

State B : A single evanescent symmetric Lamb wave mode consisting of an outgoing and converging wave, with wave number k_n. The displacement components of state B are

$$u_r^n = V_S^n(z)\left[\Phi'(k_n r) + \overline{\Phi}'(k_n r)\right]\sin\theta \tag{4.87}$$

$$u_z^n = W_S^n(z)\left[\Phi(k_n r) + \overline{\Phi}(k_n r)\right]\sin\theta \tag{4.88}$$

$$u_\theta^n = V_S^n(z)\left(\frac{-1}{k_n r}\right)\left[\Phi(k_n r) + \overline{\Phi}(k_n r)\right]\cos\theta \tag{4.89}$$

The left hand side of the reciprocity theorem in Eq. (4.17) is

$$\begin{aligned} Qu_r^n(0,\pi/2,0) &= QV_S^n(0)\left[\Phi'(0) + \overline{\Phi}'(0)\right]\sin(\pi/2) \\ &= QV_S^n(0)\left[\Phi'(0) + \overline{\Phi}'(0)\right] \end{aligned} \tag{4.90}$$

As discussed in Section 4.2.3, the term in the square bracket in Eq. (4.90) is equal to 1. Therefore, Eq. (4.90) becomes

$$Qu_r^n(0,\pi/2,0) = QV_S^n(0) \tag{4.91}$$

Eq. (4.91) is the same as Eq. (4.47). Thus the coefficients for evanescent wave mode induced by point load in $+y$ direction will be the same as point load in $+x$ direction.

The coefficient for evanescent wave mode is

$$A_n^S = \frac{k_n}{4i} \frac{QV_S^n(0)}{I_{nn}^S} \tag{4.92}$$

Similarly, the evanescent antisymmetric Lamb wave mode coefficient can be obtained as

$$A_n^A = \frac{k_n}{4i} \frac{QV_A^n(0)}{I_{nn}^A} \tag{4.93}$$

The evanescent symmetric *SH* wave mode coefficient can be obtained as

$$B_n^S = \frac{1}{4i} \frac{Q}{J_{nn}} \quad \text{for} \quad n = 0, 2, 4, \cdots \tag{4.94}$$

The evanescent antisymmetric *SH* wave mode coefficient can be obtained as

$$B_n^A = \frac{1}{4i} \frac{Q}{J_{nn}} \quad \text{for} \quad n = 1, 3, 5, \cdots \tag{4.95}$$

When the point load is applied at $r = 0, \theta = 0, z = z_0$, the coefficients of the wave modes can be obtained in a similar manner as below

$$A_n^S = \frac{k_n}{4i} \frac{QV_S^n(z_0)}{I_{nn}^S} \tag{4.96}$$

$$A_n^A = \frac{k_n}{4i} \frac{QV_A^n(z_0)}{I_{nn}^A} \tag{4.97}$$

$$B_n^S = \frac{1}{4i}\frac{\cos(n\pi z_0 / h)}{J_{nn}}Q \quad \text{for} \quad n = 0,2,4,\cdots \tag{4.98}$$

$$B_n^A = \frac{1}{4i}\frac{\sin(n\pi z_0 / h)}{J_{nn}}Q \quad \text{for} \quad n = 1,3,5,\cdots \tag{4.99}$$

When the point load is applied at the plate upper surface at $r = 0, \theta = 0, z = h$, the coefficients of the wave modes can be obtained in a similar manner as below

$$A_n^S = \frac{k_n}{4i}\frac{QV_S^n(h)}{I_{nn}^S} \tag{4.100}$$

$$A_n^A = \frac{k_n}{4i}\frac{QV_A^n(h)}{I_{nn}^A} \tag{4.101}$$

$$B_n^S = \frac{1}{4i}\frac{\cos(n\pi / 2)}{J_{nn}}Q \quad \text{for} \quad n = 0,2,4,\cdots \tag{4.102}$$

$$B_n^A = \frac{1}{4i}\frac{\sin(n\pi / 2)}{J_{nn}}Q \quad \text{for} \quad n = 1,3,5,\cdots \tag{4.103}$$

Though the coefficients for each wave mode under point load in +*y* direction is the same as under point load in +*x* direction, the difference lies in the expression of carrier wave, where the terms of $\cos\theta$ becomes $\sin\theta$; the terms of $\sin\theta$ becomes $\cos\theta$.

CHAPTER 5

Theoretical Model of Rectangular Actuator Vibration

5.1 Equation of motion (EOM) for the actuator

A rectangular PZT actuator with height h_a, length a (length along x axis) and width b (length along y axis) is bonded on the surface of a homogeneous, isotropic linear elastic plate. The poling direction is assumed to be along the z direction. Only the steady state wave propagation response of the system will be studied. The field variables of displacement, stress, strain and electric fields will involve a time factor $\exp(-i\omega t)$. For convenience, the time factor will be omitted in the following illustration and only the amplitude of the variables will be shown.

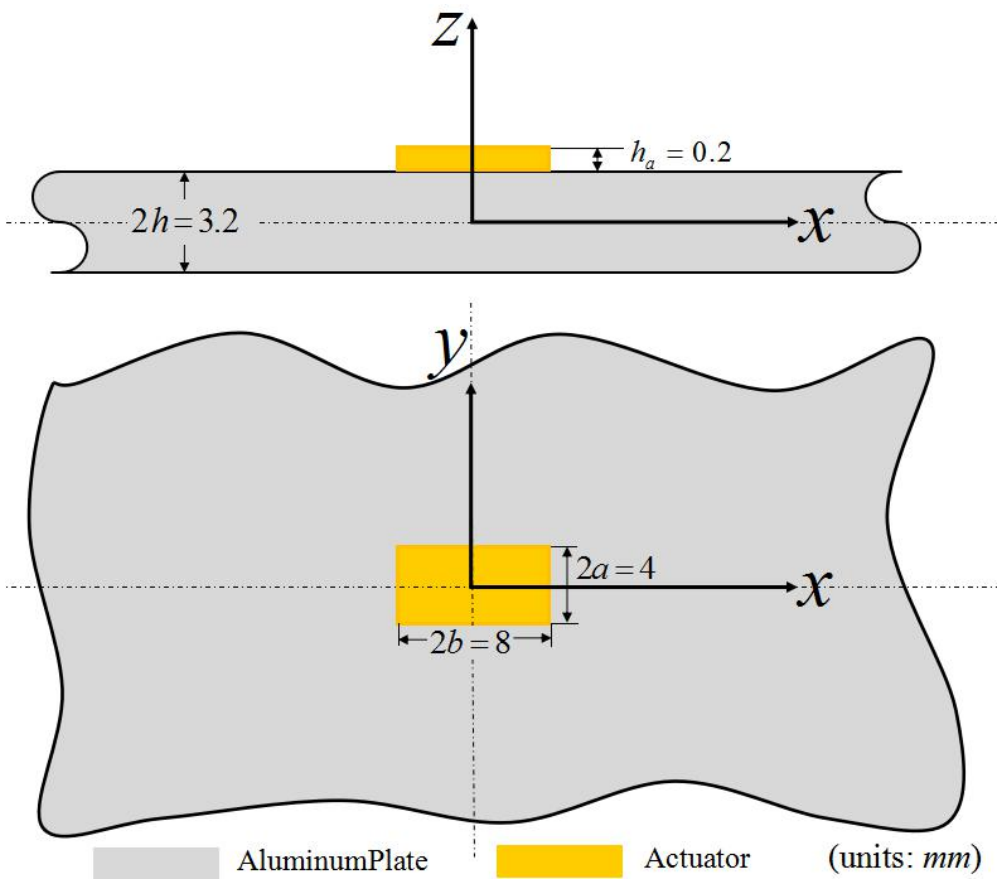

Figure 5.1 Configuration of actuator bonded on surface of aluminum plate

The PZT actuator will extend in both x and y direction when an electric field is applied on the upper surface of the actuator and the contact surface is grounded. The resulting deformation on the actuator will also cause deformation on the host structure. Because the height of the actuator is small compared to its width and length, the PZT actuator will be modeled as a plan stress model. When the loading frequency is relatively high, the typical wavelength will be smaller compared to the length and width of the actuator. The effect of actuator and plate on each other can be replaced by shear stress acting on the

contact surface. The stress is concentrated on the four peripheries and decreases dramatically towards the center of the actuator.

In order to find the stress distribution expression that best represents the actual circumstance, finite element analysis (FEA) in COMSOL is conducted. The material property of the aluminum plate is listed in the Table 5.1 below.

Table 5.1 Material properties of the host structure used in COMSOL for FEA

Material properties	Host plate structure (aluminum)
Mass density ($kg \cdot m^{-3}$)	2700
Young's modulus (GPa)	70
Poisson's ratio	0.33

The material properties for the piezoelectric actuator are listed below.

Table 5.2 Material properties of the PZT actuator used in COMSOL for FEA

Material properties	PZT actuator (PZT-5H)
Mass density ($kg \cdot m^{-3}$)	7750
Elastic constants (Pa)	$\boldsymbol{c}^{E} = \begin{bmatrix} 1.20346e+011 & 7.51791e+010 & 7.50901e+010 & 0 & 0 & 0 \\ 7.51791e+010 & 1.20346e+011 & 8.46702e10 & 0 & 0 & 0 \\ 7.50901e+010 & 7.50901e+010 & 1.10867e+011 & 0 & 0 & 0 \\ 0 & 0 & 0 & 2.10526e+010 & 0 & 0 \\ 0 & 0 & 0 & 0 & 2.10526e+010 & 0 \\ 0 & 0 & 0 & 0 & 0 & 2.25734e+010 \end{bmatrix}$
Piezoelectric stress matrix (C / m^2)	$\boldsymbol{e} = \begin{bmatrix} 0 & 0 & 0 & 0 & 12.2947 & 0 \\ 0 & 0 & 0 & 12.2947 & 0 & 0 \\ -5.35116 & -5.35116 & 15.7835 & 0 & 0 & 0 \end{bmatrix}$
Electric relative permittivity	$\frac{\boldsymbol{\epsilon}_T}{\epsilon_0} = \begin{bmatrix} 919.1 & 0 & 0 \\ 0 & 919.1 & 0 \\ 0 & 0 & 919.1 \end{bmatrix}$, $\epsilon_0 = 8.854 \times 10^{-12}$

The geometry of the system is listed below.

Table 5.3 Geometry of the system

Material type	PZT actuator (PZT-5H)	Aluminum plate
Height (along z direction)	0.2 mm	3.2 mm
Length (along x direction)	4 mm	∞
Width (along y direction)	8 mm	∞

The infinite plate can be modeled using perfect matched layer (PML), which is an artificial absorbing layer for wave equations. While applying a harmonic voltage (100 V at 100 kHz) on the upper surface of a horizontally isotropic PZT actuator, the stress distribution

on the contact surface of the PZT actuator and the plate are calculated in COMSOL and is shown below.

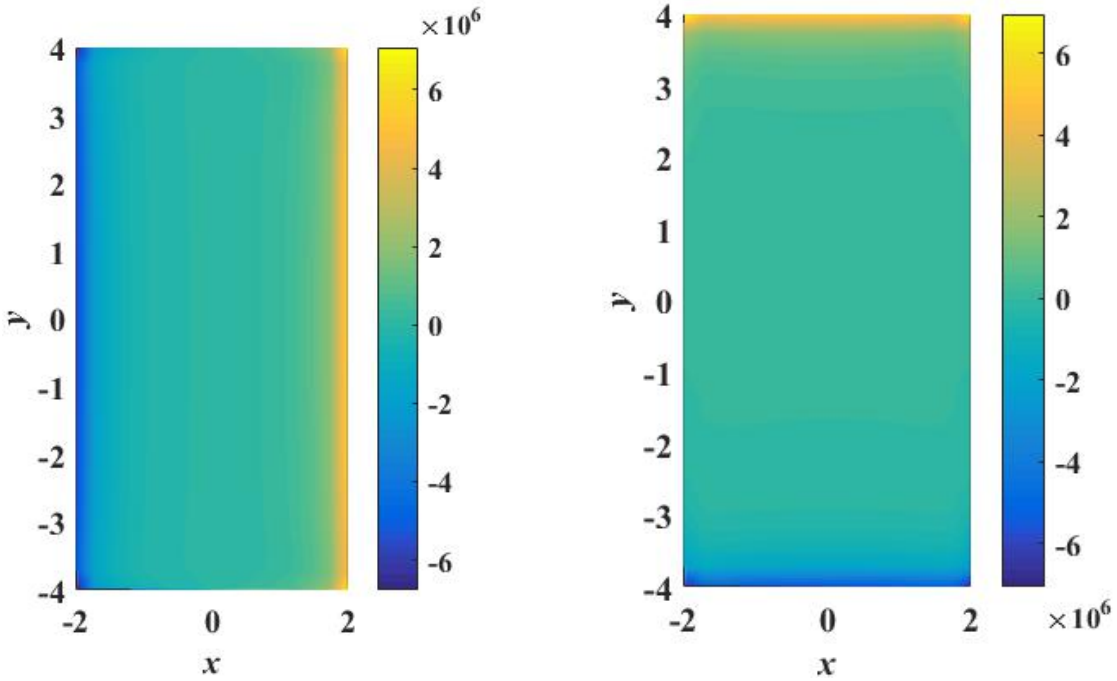

(units for *x*-*y* axis: *mm*) (units for *x*-*y* axis: *mm*)

(a) (b)

Figure 5.2 Stress components (a) τ_{xz} (b) τ_{yz} on the contact surface

As can be seen, τ_{xz} is concentrated at edges $x = \pm a$ while τ_{yz} is concentrated at edges $y = \pm b$. This kind of distribution can be expressed using Chebyshev polynomials:

$$\tau_{xz} = \frac{1}{\sqrt{1-(x/a)^2}} \sum_{i=0}^{N-1} \sum_{j=0}^{N-1} a_{ij} T_i(x/a) T_j(y/b)$$

$$\tau_{yz} = \frac{1}{\sqrt{1-(y/b)^2}} \sum_{i=0}^{N-1} \sum_{j=0}^{N-1} b_{ij} T_i(x/a) T_j(y/b)$$

where $T_i(x/l_a)$ and $T_j(y/w_a)$ are Chebyshev polynomials of the first kind with order *i* and *j*, respectively, $N-1$ is the highest order Chebyshev polynomial in the expansion, and (a_{ij}, b_{ij}) are the Chebyshev coefficients in the expansion to be determined. Eq. (2.1) indicates the shear stresses (τ_{zx}, τ_{zy}) have square-root singularity $1/\sqrt{1-(x/l_a)^2}$ and $1/\sqrt{1-(y/w_a)^2}$ at the peripheries of the actuator, respectively.

In practicality, they can be approximated by taking the summation of the first several terms instead of infinite terms. Here, the first few terms of Chebyshev polynomials of the first kind are shown below:

$$
\begin{aligned}
T_0(x) &= 1 \\
T_1(x) &= x \\
T_2(x) &= 2x^2 - 1 \\
T_3(x) &= 4x^3 - 3x \\
T_4(x) &= 8x^4 - 8x^2 + 1 \\
T_5(x) &= 16x^5 - 20x^3 + 5x
\end{aligned}
$$

The first six Chebyshev polynomials are shown in the figure below.

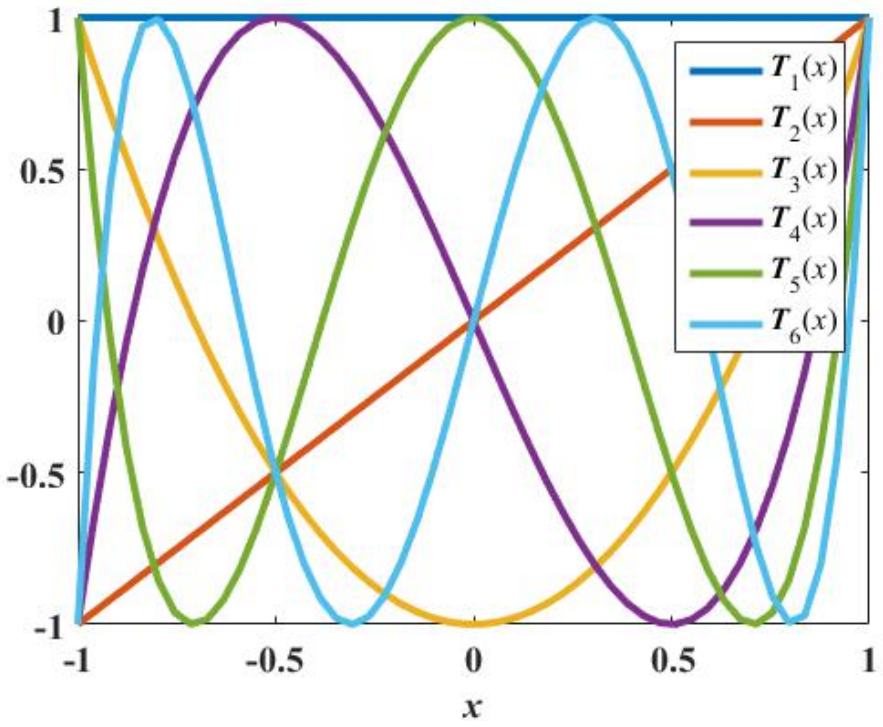

Figure 5.3 First six Chebyshev polynomials

As can be seen from Eq. (2.6), $T_{2n}(x)$ terms are symmetric with respect to the y axis and $T_{2n+1}(x)$ terms are antisymmetric with respect to the y axis (for n being integers). Due to the symmetry of the stress distribution, the stress expression can be reduced to:

$$\tau_{zx}\Big|_{actuator} = \begin{cases} \sum_{i=0}^{N-1}\sum_{j=0}^{N-1} a_{ij} T_{2i+1}(x/a) T_{2j}(y/b) \dfrac{1}{\sqrt{1-(x/a)^2}}, & |x|<a, |y|<b \\ 0 & \text{otherwise} \end{cases}$$

$$\tau_{zy}\Big|_{actuator} = \begin{cases} \sum_{i=0}^{N-1}\sum_{j=0}^{N-1} b_{ij} T_{2i}(x/a) T_{2j+1}(y/b) \dfrac{1}{\sqrt{1-(y/b)^2}}, & |x|<a, |y|<b \\ 0 & \text{otherwise} \end{cases}$$

The expression of stress in the above equations is quite complicated. In order to facilitate the following derivation and computation time, the Chebyshev stress expression is thus simplified:

(1) Reducing the defendant coordinates:

The stress components τ_{xz}, τ_{yz} data from COMSOL result are plotted in Figure 5.2. As can be seen, stress τ_{xz} is mainly dependent on x coordinate; whereas stress τ_{yz} is mainly dependent on y coordinate. Therefore, the stress expression can be reduced to:

$$\tau_{xz}\Big|_{actuator} = \frac{1}{\sqrt{1-(x/a)^2}}\left[a_{10}T_1(x/a) + a_{30}T_3(x/a)\right]$$

$$\tau_{yz}\Big|_{actuator} = \frac{1}{\sqrt{1-(y/b)^2}}\left[b_{01}T_1(y/b) + b_{03}T_3(y/b)\right]$$

Substituting the Chebyshev expression term into the above equations yields

$$\tau_{xz}\Big|_{actuator} = \frac{1}{\sqrt{1-(x/a)^2}}\left\{a_{10}(x/a)+a_{30}\left[4(x/a)^3-3(x/a)\right]\right\}$$
$$= \frac{1}{\sqrt{1-(x/a)^2}}\left\{4a_{30}(x/a)^3+\left(a_{10}-3a_{30}\right)(x/a)\right\}$$
$$\tau_{yz}\Big|_{actuator} = \frac{1}{\sqrt{1-(y/b)^2}}\left\{b_{01}(y/b)+b_{03}\left[4(y/b)^3-3(y/b)\right]\right\}$$
$$= \frac{1}{\sqrt{1-(y/b)^2}}\left\{4b_{03}(y/b)^3+\left(b_{01}-3b_{03}\right)(y/b)\right\}$$

(2) Simplify the square root term:

The Taylor expansion of the square root term at 0 is:

$$\frac{1}{\sqrt{1-(x/l_a)^2}} = 1+\frac{x^2}{2a^2}+O(x^4)$$
$$\frac{1}{\sqrt{1-(y/w_a)^2}} = 1+\frac{y^2}{2b^2}+O(y)^4$$

Substituting the Taylor expansion into the above stress expression yields

$$\tau_{xz}\Big|_{actuator} = a_1x+a_2x^3$$
$$\tau_{yz}\Big|_{actuator} = b_1y+b_2y^3 \qquad (5.1)$$

It can be verified in Matlab in the next session that using these four terms are sufficient to represent the stress distribution between the actuator and the plate.

This will introduce 4 coefficients: a_1, a_2, b_1, b_2 . These four coefficients will be determined using the displacement continuity of the plate and actuator at the contact surface.

For a random small element (volume of which is $h_a dxdy$) on the actuator, the force acting on the contact surface of the plate and actuator can be approximated as applied to the central surface (the surface of the actuator with half thickness) of the actuator element since the thickness of actuator is small compared to that of the plate. The moment generated by moving the force from contact surface to central surface is trivial. The force acting on the central surface is the body force expressed below:

$$\begin{aligned} dF_{bodyX} &= \tau_{xz}\big|_{actuator} \cdot dArea = \tau_{xz}\big|_{actuator} dxdy \\ dF_{bodyY} &= \tau_{yz}\big|_{actuator} \cdot dArea = \tau_{yz}\big|_{actuator} dxdy \end{aligned} \tag{5.2}$$

where τ is the stress distribution acting on the plate on the contact surface. The minus sign is due to Newton's third law of motion. The stress equations of motion:

$$\sigma_{ji,j} + \frac{F_{body}}{Volume} = \rho_a \ddot{u}_i \tag{5.3}$$

Since all the time-harmonic terms have $e^{-i\omega t}$ term, the above equation of motion becomes

$$\sigma_{ji,j} + \frac{F_{body}}{Volume} + \rho_a \omega^2 u_i = 0 \tag{5.4}$$

where σ_{ij} and u_i are the components of mechanical stress and displacement; ρ_a is the mass density, $Volume$ is the volume of the element ($h_a dxdy$).

The charge equation of electrostatics:

$$D_{i,i} = 0 \tag{5.5}$$

where D_i are the components of electric displacement.

The strain-mechanical displacement relations:

$$\varepsilon_{ij} = (u_{i,j} + u_{j,i})/2 \tag{5.6}$$

where ε_{ij} are the components of strain.

The electric field-electric potential relations:

$$E_k = -\varphi_{,k} \tag{5.7}$$

where E_k are the components of electric field and φ is electric potential. The maximum positive electric field is limited by the breakdown of the dielectric, whereas the maximum negative electric field is limited by the piezoelectric depoling (Sirohi and Chopra, 1998).

The linear piezoelectric constitutive relations: (IEEE, 1987):

$$\begin{aligned} &\text{converse piezoelectric effect:} \quad \sigma_{ij} = c^E_{ijkl}\varepsilon_{kl} - e_{kij}E_k \\ &\text{direct piezoelectric effect:} \quad D_i = e_{ikl}\varepsilon_{kl} + \epsilon^{\varepsilon}_{ik}E_k \end{aligned} \tag{5.8}$$

where $c^E_{ijkl}, e_{kij}, \epsilon^{\varepsilon}_{ik}$ are the elastic, piezoelectric and dielectric constants respectively. The superscripts E, ε denote the properties are under conditions of constant elastic field and constant strain respectively. Using contracted notations of c^E_{ijkl}, e_{kij} and $\epsilon^{\varepsilon}_{ik}$ can be expressed as

$$e_{ip} = d_{iq}c^E_{qp}, \quad \overset{\varepsilon}{ij} = \overset{\sigma}{ij} - d_{ip}c^E_{pq}d_{qj} \tag{5.9}$$

where i or $j = 1,2,3$ and p or $q = 1,2,3,4,5,6$. d_{ip} is the matrix for the piezoelectric strain constants d_{ijk}. Superscript σ denotes the properties are under conditions for constant stress.

For transversely isotropic or hexagonal piezoelectric materials poled in the thickness z direction (Meitzler *et al*., 1973), the matrices of the elastic, piezoelectric and dielectric constants are

$$c_{qp}^{E} = \begin{bmatrix} c_{11} & c_{12} & c_{13} & 0 & 0 & 0 \\ c_{12} & c_{11} & c_{13} & 0 & 0 & 0 \\ c_{13} & c_{13} & c_{33} & 0 & 0 & 0 \\ 0 & 0 & 0 & c_{44} & 0 & 0 \\ 0 & 0 & 0 & 0 & c_{44} & 0 \\ 0 & 0 & 0 & 0 & 0 & c_{66} \end{bmatrix}, c_{66} = (c_{11} - c_{12})/2 \tag{5.10}$$

$$e_{ip} = \begin{bmatrix} 0 & 0 & 0 & 0 & e_{15} & 0 \\ 0 & 0 & 0 & e_{15} & 0 & 0 \\ e_{31} & e_{31} & e_{33} & 0 & 0 & 0 \end{bmatrix} \tag{5.11}$$

$$d_{ip} = \begin{bmatrix} 0 & 0 & 0 & 0 & d_{15} & 0 \\ 0 & 0 & 0 & d_{15} & 0 & 0 \\ d_{31} & d_{31} & d_{33} & 0 & 0 & 0 \end{bmatrix} \tag{5.12}$$

$$\overset{S}{ij} = \begin{bmatrix} \epsilon_{11} & 0 & 0 \\ 0 & {}_{11} & 0 \\ 0 & 0 & \epsilon_{33} \end{bmatrix} \tag{5.13}$$

Take piezoelectric constant d_{31} as an example, a negative value of d_{31} would indicate that a positive electric field in the polarization direction would render a compressive strain on the PZT surface.

Substituting Eq. (5.10) to Eq. (5.13) into the constitutive equations in Eq. (5.8) yields

$$\begin{aligned}
\sigma_x &= c_{11}^E \varepsilon_x + c_{12}^E \varepsilon_y + c_{13}^E \varepsilon_z - e_{31} E_z \\
\sigma_y &= c_{12}^E \varepsilon_x + c_{11}^E \varepsilon_y + c_{13}^E \varepsilon_z - e_{31} E_z \\
\sigma_z &= c_{13}^E (\varepsilon_x + \varepsilon_y) + c_{33}^E \varepsilon_z - e_{33} E_z \\
\tau_{xz} &= c_{44}^E \gamma_{xz} - e_{15} E_x \\
\tau_{yz} &= c_{44}^E \gamma_{yz} - e_{15} E_y \\
\tau_{xy} &= \frac{1}{2}(c_{11}^E - c_{12}^E)\gamma_{xy} \\
D_x &= \varepsilon_{11}^S E_x + e_{15} \gamma_{xz} \\
D_y &= \varepsilon_{11}^S E_y + e_{15} \gamma_{yz} \\
D_z &= \varepsilon_{33}^S E_z + e_{31}(\varepsilon_x + \varepsilon_y) + e_{33} \varepsilon_z
\end{aligned} \tag{5.14}$$

For the conducting surfaces of the piezoelectric plate, $\varphi_{,x} = \varphi_{,y} = 0$ and external electric field

$$E_x = E_y = 0, E_z = -\varphi_{,z} = -\frac{V_{in}(t)}{h} \tag{5.15}$$

Since the thickness of the actuator h_a is much smaller than its lateral dimensions, the vibration of the actuator plate can be considered as two-dimensional by taking the average of the displacement and stress over the thickness:

$$
\begin{aligned}
\overline{u}_x &= \frac{1}{h_a}\int_{-h_a/2}^{h_a/2} u_x dz \\
\overline{u}_y &= \frac{1}{h_a}\int_{-h_a/2}^{h_a/2} u_y dz \\
\overline{u}_z &= \frac{1}{h_a}\int_{-h_a/2}^{h_a/2} u_z dz \\
\overline{\sigma}_x &= \frac{1}{h_a}\int_{-h_a/2}^{h_a/2} \sigma_x dz \\
\overline{\sigma}_y &= \frac{1}{h_a}\int_{-h_a/2}^{h_a/2} \sigma_y dz \\
\overline{\tau}_{xy} &= \frac{1}{h_a}\int_{-h_a/2}^{h_a/2} \tau_{xy} dz
\end{aligned}
\tag{5.16}
$$

For simplicity, the average sign (upper bar) will be omitted in the later context. Substituting Eq. (5.14) into Eq. (5.16) yields:

$$
\begin{aligned}
\sigma_x &= c_{11}^E u_{,x} + c_{12}^E v_{,y} + c_{13}^E \frac{u_z^+ - u_z^-}{h_a} + e_{31}^p \frac{V_{in}}{h_a} \\
\sigma_y &= c_{12}^E u_{,x} + c_{11}^E v_{,y} + c_{13}^E \frac{u_z^+ - u_z^-}{h_a} + e_{31}^p \frac{V_{in}}{h_a} \\
\tau_{xy} &= \frac{c_{11}^E - c_{12}^E}{2}(u_{,y} + v_{,x})
\end{aligned}
\tag{5.17}
$$

where u_z^+, u_z^- denote the displacement u_z at $z = \pm h_a / 2$ respectively.

Since the piezoelectric plate is thin, it can be assumed to be under plane stress state. In which the stress field is

$$
\sigma_z = \tau_{yz} = \tau_{xz} = 0 \tag{5.18}
$$

Integrating Eq. (5.14-3) and using Eq. (5.18) yields

$$\sigma_z = 0 = c_{13}^E (u_{,x} + v_{,y}) + c_{33}^E \frac{u_z^+ - u_z^-}{h_a} + e_{33} \frac{V}{h_a} \tag{5.19}$$

Re-arranging terms in Eq. (5.19), yields

$$\frac{u_z^+ - u_z^-}{h_a} = -\frac{c_{13}^E}{c_{33}^E}(u_{,x} + v_{,y}) - \frac{e_{33}}{c_{33}^E}\frac{V}{h_a} \tag{5.20}$$

Substituting Eq. (5.20) into Eq. (5.17) yields

$$\sigma_z = c_{11}^E u_{,x} + c_{12}^E v_{,y} + c_{13}^E \left(-\frac{c_{13}^E}{c_{33}^E}(u_{,x} + v_{,y}) - \frac{e_{33}}{c_{33}^E}\frac{V}{h_a} \right) + e_{31}^p \frac{V_{in}}{h_a}$$

$$\sigma_y = c_{12}^E u_{,x} + c_{11}^E v_{,y} + c_{13}^E \left(-\frac{c_{13}^E}{c_{33}^E}(u_{,x} + v_{,y}) - \frac{e_{33}}{c_{33}^E}\frac{V}{h_a} \right) + e_{31}^p \frac{V_{in}}{h_a}$$

$$\tau_{xy} = \frac{c_{11}^E - c_{12}^E}{2}(u_{,y} + v_{,x})$$

Re-arranging terms in the above equations yields

$$\begin{aligned} \sigma_x &= 2Gu_{,x} + (c_{12}^E + cc_{13}^E)\bar{\theta} + e_{31}^p \frac{V_{in}}{h_a} \\ \sigma_y &= 2Gv_{,y} + (c_{12}^E + cc_{13}^E)\bar{\theta} + e_{31}^p \frac{V_{in}}{h_a} \\ \tau_{xy} &= G(u_{,y} + v_{,x}) \end{aligned} \tag{5.21}$$

where

$$\begin{aligned} G &= \frac{c_{11}^E - c_{12}^E}{2} \\ \bar{\theta} &= u_{,x} + v_{,y} \\ c &= -\frac{c_{13}^E}{c_{33}^E} \\ e_{31}^p &= e_{31} + e_{33} \end{aligned} \tag{5.22}$$

Using Eq. (5.3), the equation of motion for the actuator can be expressed as

$$\begin{aligned}\frac{\partial \sigma_x}{\partial x}+\frac{\partial \tau_{xy}}{\partial y}+\rho_a \omega^2 u+\frac{\tau_{zx}\big|_{\text{actuator body force}}}{h_a}=0\\ \frac{\partial \sigma_y}{\partial y}+\frac{\partial \tau_{xy}}{\partial x}+\rho_a \omega^2 v+\frac{\tau_{zy}\big|_{\text{actuator body force}}}{h_a}=0\end{aligned} \tag{5.23}$$

where all the stress, displacement terms in the above equation are averaged terms.

Substituting Eq. (5.21) and Eq. (5.22) into Eq. (5.23) yields

$$\begin{aligned}\nabla^2 u+\frac{m}{m-2}\frac{\partial \bar{\theta}}{\partial x}+\frac{\rho_a}{G}\omega^2 u+\frac{\tau_{zx}\big|_{\text{actuator body force}}}{Gh_a}=0\\ \nabla^2 v+\frac{m}{m-2}\frac{\partial \bar{\theta}}{\partial y}+\frac{\rho_a}{G}\omega^2 v+\frac{\tau_{zy}\big|_{\text{actuator body force}}}{Gh_a}=0\end{aligned} \tag{5.24}$$

where

$$\begin{aligned}\nabla^2 &= \frac{\partial}{\partial x^2}+\frac{\partial}{\partial y^2}\\ m &= \frac{c_{11}^E+cc_{13}^E}{c_{12}^E+cc_{13}^E}+1\end{aligned} \tag{5.25}$$

5.2 General solution for PZT actuator EOM

The EOM for PZT actuator shown in Eq. (5.24) are two in-homogeneous partial differential equations (PDE). The solutions for these two PDEs consist of the general solution from the homogeneous form of the PDE and the particular solution of the PDE. The general solution is the free vibration term and the particular solution is the forced vibration term due to body forces τ_{xz}, τ_{yz}.

According to the superposition method proposed by Gorman (2004), the **free vibration** of in-plane displacement of the PZT thin film can be expressed as a summation of four terms:

symmetric-symmetric (*SS*);

antisymmetric- antisymmetric (*AA*);

symmetric-antisymmetric (*SA*);

antisymmetric- symmetric (*AS*).

The expression of in-plane displacement is:

$$\begin{aligned} u &= u_{SS}(x,y) + u_{AA}(x,y) + u_{SA}(x,y) + u_{AS}(x,y) \\ v &= v_{SS}(x,y) + v_{AA}(x,y) + v_{SA}(x,y) + v_{AS}(x,y) \end{aligned} \tag{5.26}$$

Each first subscript, *S* or *A*, indicates if the displacement is symmetric or antisymmetric with respect to *x* axis. Each second subscript, *S* or *A*, indicates if the displacement is symmetric or antisymmetric with respect to *y* axis. For example, u_{SA} means the displacement is symmetric with respect to x axis and antisymmetric with respect to y axis, *i.e.*,

$$u_{SA}(x,y) = u_{SA}(-x,y) = -u_{SA}(x,-y) = -u_{SA}(-x,-y)$$

From the EOM in Eq. (5.20), displacements u, v are coupled. If *u* is symmetric with respect to a certain axis, *v* will be antisymmetric with that same axis; and vice versa. Thus, the notation for *v* subscripts is different from that of u. The subscript always denotes symmetry condition of *u* component of the displacement.

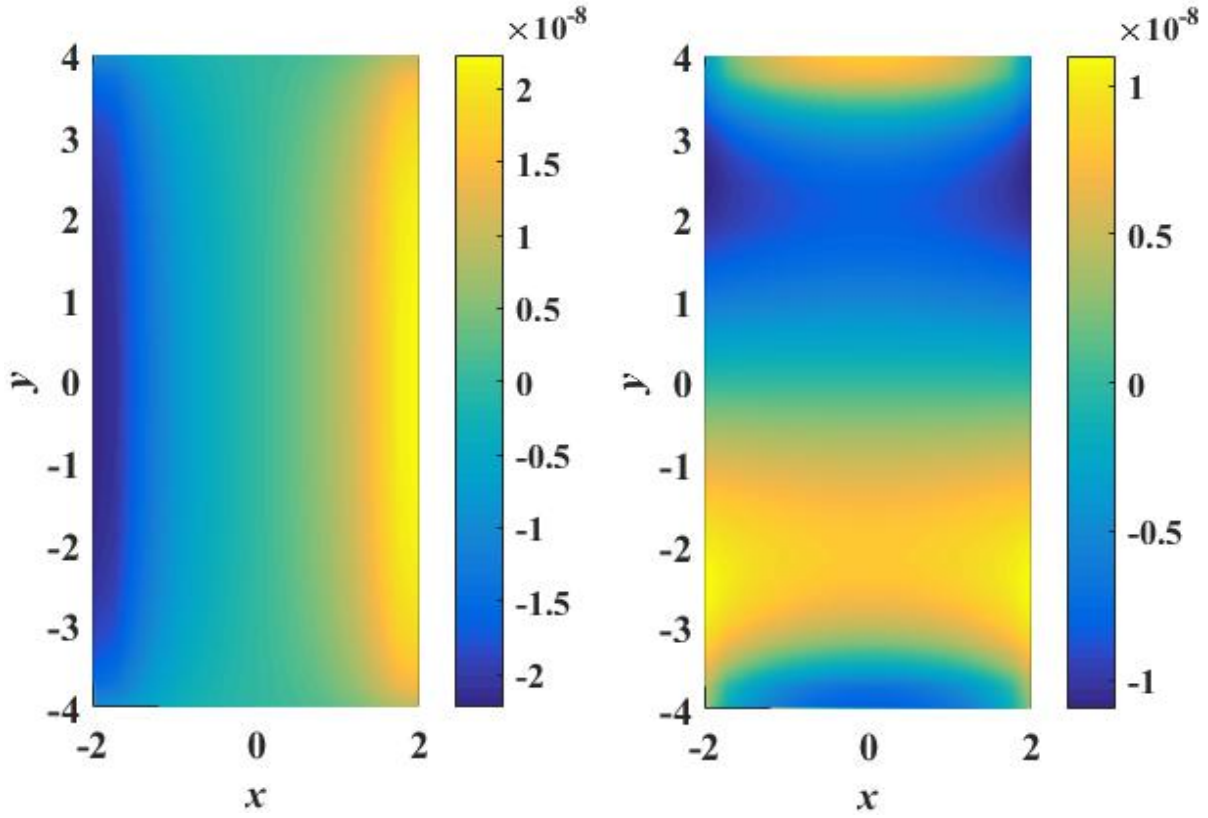

(units for *x*-*y* axis: *mm*) (units for *x*-*y* axis: *mm*)

(a) (b)

Figure 5.4 COMSOL result for actuator (a) displacement *u* component and (b) displacement *v* component on the contact surface

In the current case, due to the symmetry of the body force, the displacement *u* component is symmetric along *x* axis and symmetric along *y* axis; the displacement *v* component is symmetric along *x* axis and symmetric along *x* axis (as can be seen in the figures above). The expression for in-plane displacement can thus be reduced to:

$$\begin{aligned} u &= u_{SS}(x,y) = u_1 + u_2 \\ v &= v_{SS}(x,y) = v_1 + v_2 \end{aligned} \tag{5.27}$$

where

$$u_1 = \sum_{n=0}^{\infty} U_n(y)\sin(\alpha_n x)$$
$$v_1 = \sum_{n=0}^{\infty} V_n(y)\cos(\alpha_n x) \tag{5.28}$$

$$u_2 = \sum_{k=0}^{\infty} U_k(x)\cos(\beta_k y)$$
$$v_2 = \sum_{k=0}^{\infty} V_k(x)\sin(\beta_k y) \tag{5.29}$$

The left superscript of U, V indicates whether it is related to x (superscript 1) or y (superscript 2).

For S-S mode,

$$\alpha_n = \frac{n\pi}{a}, \beta_k = \frac{k\pi}{b} \tag{5.30}$$

5.2.1. Determining $U_n(y)$ and $V_n(y)$.

The homogeneous form for Eq. (5.24) is:

$$\nabla^2 u + \frac{m}{m-2}\frac{\partial\bar{\theta}}{\partial x} + \frac{\rho_a}{G}\omega^2 u = 0$$
$$\nabla^2 v + \frac{m}{m-2}\frac{\partial\bar{\theta}}{\partial y} + \frac{\rho_a}{G}\omega^2 v = 0 \tag{5.31}$$

which can be expanded to

$$\begin{aligned}
&\frac{2m-2}{m-2}\frac{\partial^2 u}{\partial x^2}+\frac{\partial^2 u}{\partial y^2}+\frac{m}{m-2}\frac{\partial^2 v}{\partial x\partial y}+\frac{\rho_a}{G}\omega^2 u=0\\
&\frac{\partial^2 v}{\partial x^2}+\frac{2m-2}{m-2}\frac{\partial^2 v}{\partial y^2}+\frac{m}{m-2}\frac{\partial^2 u}{\partial x\partial y}+\frac{\rho_a}{G}\omega^2 v=0
\end{aligned} \tag{5.32}$$

Substituting Eq. (5.28) into Eq. (5.32) yields

$$\begin{aligned}
&-\frac{2m-2}{m-2}\sum_{n=1}^{\infty}\ {\alpha_n}^2 U_n(y)\sin(\alpha_n x)+\sum_{n=1}^{\infty}\ U_n''(y)\sin(\alpha_n x)\\
&-\frac{m}{m-2}\sum_{n=1}^{\infty}\ \alpha_n V_n'(y)\sin(\alpha_n x)+\frac{\rho_a}{G}\omega^2\sum_{n=1}^{\infty}\ U_n(y)\sin(\alpha_n x)=0\\
&-\sum_{n=1}^{\infty}\ {\alpha_n}^2 V_n(y)\cos(\alpha_n x)+\frac{2m-2}{m-2}\sum_{n=1}^{\infty}\ V_n''(y)\cos(\alpha_n x)\\
&-\frac{m}{m-2}\sum_{n=1}^{\infty}\ \alpha_n U_n'(y)\cos(\alpha_n x)+\frac{\rho_a}{G}\omega^2\sum_{n=1}^{\infty}\ V_n(y)\cos(\alpha_n x)=0
\end{aligned} \tag{5.33}$$

Eq. (5.33) yields

$$\begin{aligned}
&U_n''(y)+b_{n1}V_n'(y)+c_{n1}U_n(y)=0\\
&a_{n2}V_n''(y)+b_{n2}U_n'(y)+c_{n2}V_n(y)=0
\end{aligned} \tag{5.34}$$

where

$$\begin{aligned}
b_{n1}&=-\frac{m}{m-2}\alpha_n\\
c_{n1}&=\left(\frac{\rho_a}{G}\omega^2-\frac{2m-2}{m-2}{\alpha_n}^2\right)\\
a_{n2}&=\frac{2m-2}{m-2}\\
b_{n2}&=-\frac{m}{m-2}\alpha_n\\
c_{n2}&=\frac{\rho_a}{G}\omega^2-{\alpha_n}^2
\end{aligned} \tag{5.35}$$

(1) when *n*=0

When n =0, α_n =0, it leads to $b_{n1} = b_{n2} = 0$. Eq. (5.34-2) becomes:

$$V_n''(y) + \lambda_1^2 V_n(y) = 0 \tag{5.36}$$

where

$$\lambda_1^2 = \frac{\rho_a \omega^2 (m-2)}{G(2m-2)}$$

Since $V_n(y)$ is antisymmetric with respect to y axis, the solution for Eq. (5.36) is:

$$V_0(y) = A_0 \sin(\lambda_1 y) \tag{5.37}$$

When n = 0, Eq. (5.34-1) becomes:

$$U_n''(y) + \lambda_2^2 U_n(y) = 0 \tag{5.38}$$

where

$$\lambda_2^2 = \frac{\rho_a}{G}\omega^2$$

Since $U_n(y)$ is symmetric with respect to y axis, the solution for Eq. (5.36) is:

$$U_0(y) = B_0 \cos(\lambda_2 y) \tag{5.39}$$

The stress free boundary condition requires that

$$\tau_{xy}\Big|_{y=b} = 0 \tag{5.40}$$

Substituting Eq. (5.21) into Eq. (5.40) yields

$$\left(u_{,y} + v_{,x}\right)\Big|_{y=b} = 0 \tag{5.41}$$

Substituting Eq. (5.28) into Eq. (5.40) yields

$$\sum_{n=0}^{\infty} U_n'(b)\sin(\alpha_n x) - \sum_{n=0}^{\infty} \alpha_n V_n(b)\sin(\alpha_n x) = 0 \tag{5.42}$$

which leads to

$$U_n'(b) - \alpha_n V_n(b) = 0 \tag{5.43}$$

When $n = 0$, $\alpha_n = 0$. Thus Eq. (5.43) becomes

$$U_0'(b) = 0 \tag{5.44}$$

Substituting the expression of $U_0(y)$ into Eq. (5.43) yields

$$B_0 = 0 \tag{5.45}$$

Therefore

$$\begin{aligned} V_0(y) &= A_0 \sin(\lambda_1 y) \\ U_0(y) &= 0 \end{aligned} \tag{5.46}$$

(2) When $n > 0$

Differentiating Eq. (5.34-1) with respect to y yields

$$U_n'''(y) + b_{n1} V_n''(y) + c_{n1} U_n'(y) = 0 \tag{5.47}$$

From Eq. (5.34-2), the derivative of $U_n'(y)$ can be expressed using $V_n''(y), V_n(y)$

$$U_n'(y) = -\frac{1}{b_{n2}}\left[a_{n2} V_n''(y) + c_{n2} V_n(y) \right] \tag{5.48}$$

Taking derivative of both sides of Eq. (5.48) with respect to y twice, yields

$$U_n'''(y) = -\frac{1}{b_{n2}}\left[a_{n2} V_n^{iv}(y) + c_{n2} V_n''(y) \right] \tag{5.49}$$

Substituting Eq. (5.48) and Eq. (5.49) into Eq. (5.47) yields

$$-\frac{a_{n2}}{b_{n2}} V_n^{iv}(y) + \left(-\frac{c_{n2}}{b_{n2}} + b_{n1} - \frac{c_{n1} a_{n2}}{b_{n2}} \right) V_n''(y) - \frac{c_{n1} c_{n2}}{b_{n2}} V_n(y) = 0$$

Multiplying both sides of the above equation by $-b_{n2} / a_{n2}$, yields

$$V_n^{iv}(y) + b V_n''(y) + c V_n(y) = 0 \tag{5.50}$$

where

$$\begin{aligned} b &= \frac{c_{n2}}{a_{n2}} - \frac{b_{n1} b_{n2}}{a_{n2}} + c_{n1} \\ c &= \frac{c_{n1} c_{n2}}{a_{n2}} \end{aligned} \tag{5.51}$$

For the differential equation (5.50), denoting the square of the roots of the characteristic equation associated with it as ε^2, therefore

$$(\varepsilon^2)^2 + b\varepsilon^2 + c = 0 \tag{5.52}$$

The roots for ε^2 are denoted as ${\varepsilon_1}^2, {\varepsilon_2}^2$,

$$Root1 = {\varepsilon_1}^2 = \frac{-b + \sqrt{b^2 - 4c}}{2}, \quad Root2 = {\varepsilon_2}^2 = \frac{-b - \sqrt{b^2 - 4c}}{2} \tag{5.53}$$

For the given material (PZT-5A), for $n > 1$, Root1 > 0 and Root2 > 0. Therefore, the solution of Eq. (5.50) is

$$V_n(y) = A_n \sinh(\vartheta_n y) + B_n \cosh(\vartheta_n y) + C_n \sinh(\gamma_n y) + D_n \cosh(\gamma_n y)$$

where

$$\vartheta_n = \sqrt{Root1}$$
$$\gamma_n = \sqrt{Root2}$$

Since $V_n(y)$ is antisymmetric along y axis, it would be

$$V_n(y) = A_n \sinh(\vartheta_n y) + C_n \sinh(\gamma_n y) \tag{5.54}$$

From Eq. (5.34-1),

$$U_n(y) = -\frac{1}{c_{n1}}\left[U_n''(y) + b_{n1} V_n'(y)\right] \tag{5.55}$$

From Eq. (5.34-2),

$$U_n'(y) = -\frac{1}{b_{n2}}\left[a_{n2}V_n''(y) + c_{n2}V_n(y)\right]$$

Taking derivative of both sides of the above equation with respect to y yields

$$U_n''(y) = -\frac{1}{b_{n2}}\left[a_{n2}V_n'''(y) + c_{n2}V_n'(y)\right] \tag{5.56}$$

Substituting Eq. (5.56) into Eq. (5.55) yields

$$U_n(y) = \frac{a_{n2}}{c_{n1}b_{n2}}V_n'''(y) + \frac{c_{n2} - b_{n1}b_{n2}}{c_{n1}b_{n2}}V_n'(y) \tag{5.57}$$

Taking derivative of the expression of $V_n(y)$ in Eq. (5.54) yields

$$\begin{aligned} V_n'(y) &= A_n\vartheta_n\cosh(\vartheta_n y) + C_n\gamma_n\cosh(\gamma_n y) \\ V_n'''(y) &= A_n\vartheta_n^{\,3}\cosh(\vartheta_n y) + C_n\gamma_n^{\,3}\cosh(\gamma_n y) \end{aligned} \tag{5.58}$$

Substituting Eq. (5.58) into Eq. (5.57) yields

$$U_n(y) = A_n\varpi_{1n}\cosh(\vartheta_n y) + C_n\varpi_{2n}\cosh(\gamma_n y) \tag{5.59}$$

where

$$\begin{aligned} \varpi_{1n} &= \frac{a_{n2}}{c_{n1}b_{n2}}\vartheta_n^{\,3} + \frac{c_{n2} - b_{n1}b_{n2}}{c_{n1}b_{n2}}\vartheta_n \\ \varpi_{2n} &= \frac{a_{n2}}{c_{n1}b_{n2}}\gamma_n^{\,3} + \frac{c_{n2} - b_{n1}b_{n2}}{c_{n1}b_{n2}}\gamma_n \end{aligned} \tag{5.60}$$

The stress free boundary condition $\tau_{xy}\big|_{y=b} = 0$ leads to Eq. (5.42):

$$\sum_{n=1}^{\infty} U_n'(b)\sin(\alpha_n x) - \sum_{n=1}^{\infty} \alpha_n V_n(b)\sin(\alpha_n x) = 0$$

and Eq. (5.43):

$$U_n'(b) - \alpha_n V_n(b) = 0$$

Substituting Eq. (5.54) and Eq. (5.59) into Eq. (5.43) yields

$$(\varpi_{1n}\vartheta_n - \alpha_n)A_n \sinh(\vartheta_n b) + (\varpi_{2n}\gamma_n - \alpha_n)C_n \sinh(\gamma_n b) = 0$$

Thus

$$C_n = \mu_1 A_n \tag{5.61}$$

where

$$\mu_1 = -\frac{(\varpi_{1n}\vartheta_n - \alpha_n)\sinh(\vartheta_n b)}{(\varpi_{2n}\gamma_n - \alpha_n)\sinh(\gamma_n b)} \tag{5.62}$$

Substituting Eq. (5.61) into the expressions of $V_n(y), U_n(y)$ in Eq. (5.54) and Eq. (5.59) yields

$$\begin{aligned} U_n(y) &= A_n\left[\varpi_{1n}\cosh(\vartheta_n y) + \mu_1\varpi_{2n}\cosh(\gamma_n y)\right], n > 1 \\ V_n(y) &= A_n\left[\sinh(\vartheta_n y) + \mu_1\sinh(\gamma_n y)\right], n > 1 \end{aligned} \tag{5.63}$$

To sum up, the expression for $U_n(y), V_n(y)$ is

$$\begin{aligned} V_0(y) &= A_0\sin(\lambda_1 y) \\ U_0(y) &= 0 \\ U_n(y) &= A_n\left[\varpi_{1n}\cosh(\vartheta_n y) + \mu_1\varpi_{2n}\cosh(\gamma_n y)\right], n > 0 \\ V_n(y) &= A_n\left[\sinh(\vartheta_n y) + \mu_1\sinh(\gamma_n y)\right], n > 0 \end{aligned} \tag{5.64}$$

5.2.2. Determining $U_n(x)$ and $V_n(x)$.

Substituting expressions of u_2, v_2 in Eq. (5.29) into Eq. (5.32) yields

$$\begin{aligned}
&\frac{2m-2}{m-2}\sum_{k=1}^{\infty} U_k''(x)\cos(\beta_k y) - \sum_{k=1}^{\infty} U_k(x)\beta_k{}^2\cos(\beta_k y) \\
&+\frac{m}{m-2}\sum_{k=1}^{\infty} \beta_k V_k'(x)\cos(\beta_k y) + \frac{\rho_a}{G}\omega^2\sum_{k=1}^{\infty} U_k(x)\cos(\beta_k y) = 0 \\
&\sum_{k=1}^{\infty} V_k''(x)\sin(\beta_k y) - \frac{2m-2}{m-2}\sum_{k=1}^{\infty} \beta_k{}^2 V_k(x)\sin(\beta_k y) \\
&-\frac{m}{m-2}\sum_{k=1}^{\infty} \beta_k U_k'(x)\sin(\beta_k y) + \frac{\rho_a}{G}\omega^2\sum_{k=1}^{\infty} V_k(x)\sin(\beta_k y) = 0
\end{aligned} \tag{5.65}$$

Eq. (5.65) yields

$$\begin{aligned}
&a_{k1}U_k''(x) + b_{k1}V_k'(x) + c_{k1}U_k(x) = 0 \\
&V_k''(x) + b_{k2}U_k'(x) + c_{k2}V_k(x) = 0
\end{aligned} \tag{5.66}$$

where

$$\begin{aligned}
a_{k1} &= \frac{2m-2}{m-2} \\
b_{k1} &= \frac{m}{m-2}\beta_k \\
c_{k1} &= \frac{\rho_a}{G}\omega^2 - \beta_k{}^2 \\
b_{k2} &= -\frac{m}{m-2}\beta_k \\
c_{k2} &= \frac{\rho_a}{G}\omega^2 - \frac{2m-2}{m-2}\beta_k{}^2
\end{aligned} \tag{5.67}$$

(1) when $k = 0$

When k =0, β_k =0, it leads to $b_{k1} = b_{k2} = 0$. Eq. (5.66-2) becomes

$$V_k''(x) + \lambda_2^2 V_k(x) = 0 \tag{5.68}$$

where

$$\lambda_2^2 = \frac{\rho_a}{G}\omega^2$$

Since $V_k(x)$ is symmetric with respect to *x* axis, the solution for Eq. (5.68) is

$$V_0(x) = C_0 \cos(\lambda_2 x) \tag{5.69}$$

When $k = 0$, Eq. (5.66-1) becomes

$$U_k''(x) + \lambda_1^2 U_k(x) = 0 \tag{5.70}$$

where

$$\lambda_1^2 = \frac{\rho_a \omega^2 (m-2)}{G(2m-2)}$$

Since $U_k(x)$ is antisymmetric with respect to *x* axis, the solution for Eq. (5.70) is

$$U_0(x) = D_0 \sin(\lambda_1 x) \tag{5.71}$$

The stress free boundary condition requires that

$$\tau_{xy}\Big|_{x=a} = 0$$

Substituting Eq. (5.21) into the above equation yields

$$\left(u_{,y}+v_{,x}\right)\Big|_{x=a}=0$$

Substituting Eq. (5.29) into the above equation yields

$$-\sum_{k=0}^{\infty} U_k(a)\beta_k \sin(\beta_k y)+\sum_{k=0}^{\infty} V_k'(a)\sin(\beta_k y)=0 \tag{5.72}$$

which leads to

$$-U_k(a)\beta_k+V_k'(a)=0 \tag{5.73}$$

When $n=0$, $\beta_k=0$. Thus Eq. (5.73) becomes

$$V_0'(a)=0 \tag{5.74}$$

Substituting the expression of $V_0(x)$ in Eq. (5.69) into Eq. (5.74) yields

$$C_0=0 \tag{5.75}$$

Therefore

$$\begin{aligned} U_0(x) &= D_0 \sin(\lambda_1 x) \\ V_0(x) &= 0 \end{aligned} \tag{5.76}$$

(2) When $k > 0$

Differentiating Eq. (5.66-1) with respect to x yields

$$a_{k1}U_k'''(x) + b_{k1}V_k''(x) + c_{k1}U_k'(x) = 0 \tag{5.77}$$

From Eq. (5.66-2), the derivative of $U_k'(x)$ can be expressed using $V_k''(x), V_k(x)$

$$U_k'(x) = -\frac{1}{b_{k2}}\left[V_k''(x) + c_{k2}V_k(x)\right] \tag{5.78}$$

Taking derivative of both sides of Eq. (5.78) with respect to x twice yields

$$U_k'''(x) = -\frac{1}{b_{k2}}\left[V_k^{iv}(x) + c_{k2}V_k''(x)\right] \tag{5.79}$$

Substituting Eq. (5.78) and Eq. (5.79) into Eq. (5.77) yields

$$-\frac{a_{k1}}{b_{k2}}V_k^{iv}(x) + \left(-\frac{a_{k1}c_{k2}}{b_{k2}} + b_{k1} - \frac{c_{k1}}{b_{k2}}\right)V_k''(x) - \frac{c_{k1}c_{k2}}{b_{k2}}V_k(x) = 0$$

Multiplying both sides of the above equation by $-b_{k2} / a_{k1}$, yields

$$V_k^{iv}(x) + \bar{b}V_k''(x) + \bar{c}V_k(x) = 0 \tag{5.80}$$

where

$$\begin{aligned} \bar{b} &= c_{k2} - \frac{b_{k1}b_{k2}}{a_{k1}} + \frac{c_{k1}}{a_{k1}} \\ \bar{c} &= \frac{c_{k1}c_{k2}}{a_{k1}} \end{aligned} \tag{5.81}$$

For the differential equation (5.80), denoting the square of the roots of the characteristic equation associated with it as $\bar{\varepsilon}^2$, therefore

$$(\bar{\varepsilon}^2)^2 + \bar{b}\bar{\varepsilon}^2 + \bar{c} = 0 \tag{5.82}$$

The roots for $\bar{\varepsilon}^2$ are denoted as $\bar{\varepsilon}_1^2, \bar{\varepsilon}_2^2$,

$$Root3 = \bar{\varepsilon}_1^2 = \frac{-\bar{b} + \sqrt{\bar{b}^2 - 4\bar{c}}}{2}, \quad Root4 = \bar{\varepsilon}_2^2 = \frac{-\bar{b} - \sqrt{\bar{b}^2 - 4\bar{c}}}{2} \tag{5.83}$$

For the given material (PZT-5A), for $k > 1$, Root3 > 0 and Root4 > 0. Therefore, the solution of Eq. (5.80) is

$$V_k(x) = E_k \sinh(\bar{\vartheta}_k x) + F_k \cosh(\bar{\vartheta}_k x) + G_k \sinh(\bar{\gamma}_k x) + H_k \cosh(\bar{\gamma}_k x)$$

where

$$\bar{\vartheta}_k = \sqrt{Root3}$$
$$\bar{\gamma}_k = \sqrt{Root4}$$

Since $V_k(x)$ is symmetric along y axis, it would be

$$V_k(x) = F_k \cosh(\bar{\vartheta}_k x) + H_k \cosh(\bar{\gamma}_k x) \tag{5.84}$$

From Eq. (5.66-1),

$$U_k(x) = -\frac{1}{c_{k1}}\left[a_{k1} U_k''(x) + b_{k1} V_k'(x)\right] \tag{5.85}$$

From Eq. (5.66-2),

$$U_k'(x) = -\frac{1}{b_{k2}}\left[V_k''(x) + c_{k2}V_k(x)\right]$$

Taking derivative of both sides of the above equation with respect to x yields

$$U_k''(x) = -\frac{1}{b_{k2}}\left[V_k'''(x) + c_{k2}V_k'(x)\right] \tag{5.86}$$

Substituting Eq. (5.86) into Eq. (5.85) yields

$$U_k(x) = \frac{a_{k1}}{c_{k1}b_{k2}}V_k'''(x) - \left(\frac{b_{k1}}{c_{k1}} - \frac{a_{k1}c_{k2}}{c_{k1}b_{k2}}\right)V_k'(x) \tag{5.87}$$

Taking derivative of the expression of $V_k(x)$ in Eq. (5.84) yields

$$\begin{aligned} V_k'(x) &= F_k\bar{\vartheta}_k \sinh(\bar{\vartheta}_k x) + H_k\bar{\gamma}_k \sinh(\bar{\gamma}_k x) \\ V_k'''(x) &= F_k\bar{\vartheta}_k^{\,3} \sinh(\bar{\vartheta}_k x) + H_k\bar{\gamma}_k^{\,3} \sinh(\bar{\gamma}_k x) \end{aligned} \tag{5.88}$$

Substituting Eq. (5.88) into Eq. (5.87) yields

$$U_k(x) = F_k\varpi_{1k} \sinh(\bar{\vartheta}_k x) + H_k\varpi_{2k} \sinh(\bar{\gamma}_k x) \tag{5.89}$$

where

$$\begin{aligned} \varpi_{1k} &= \frac{a_{k1}}{c_{k1}b_{k2}}\bar{\vartheta}_k^{\,3} - \left(\frac{b_{k1}}{c_{k1}} - \frac{a_{k1}c_{k2}}{c_{k1}b_{k2}}\right)\bar{\vartheta}_k \\ \varpi_{2k} &= \frac{a_{k1}}{c_{k1}b_{k2}}\bar{\gamma}_k^{\,3} - \left(\frac{b_{k1}}{c_{k1}} - \frac{a_{k1}c_{k2}}{c_{k1}b_{k2}}\right)\bar{\gamma}_k \end{aligned} \tag{5.90}$$

The stress free boundary condition $\tau_{xy}\big|_{x=a} = 0$ requires that is expressed in Eq. (5.72)

$$-\sum_{k=0}^{\infty} U_k(a)\beta_k \sin(\beta_k y) + \sum_{k=0}^{\infty} V_k'(a)\sin(\beta_k y) = 0$$

and Eq. (5.73)

$$-U_k(a)\beta_k + V_k'(a) = 0$$

Substituting Eq. (5.84) and Eq. (5.89) into Eq. (5.73) yields

$$(-\varpi_{1k}\beta_k + \overline{\vartheta}_k)F_k \sinh(\overline{\vartheta}_k a) + (-\varpi_{2k}\beta_k + \overline{\gamma}_k)H_k \sinh(\overline{\gamma}_k a) = 0$$

Thus

$$H_k = \mu_2 F_k \tag{5.91}$$

where

$$\mu_2 = -\frac{(-\varpi_{1k}\beta_k + \overline{\vartheta}_k)\sinh(\overline{\vartheta}_k a)}{(-\varpi_{2k}\beta_k + \overline{\gamma}_k)\sinh(\overline{\gamma}_k a)} \tag{5.92}$$

Substituting Eq. (5.61) into the expressions of $V_n(y), U_n(y)$ in Eq. (5.84) and Eq. (5.89) yields

$$\begin{aligned} U_k(x) &= F_k\left[\varpi_{1k}\sinh(\overline{\vartheta}_k x) + \mu_2\varpi_{2k}\sinh(\overline{\gamma}_k x)\right] \\ V_k(x) &= F_k\left[\cosh(\overline{\vartheta}_k x) + \mu_2\cosh(\overline{\gamma}_k x)\right] \end{aligned} \tag{5.93}$$

To sum up, $U_k(x), V_k(x)$ are

$$
\begin{aligned}
&U_0(x) = D_0 \sin(\lambda_1 x) \\
&V_0(x) = 0 \\
&U_k(x) = F_k \left[\varpi_{1k} \sinh(\bar{\vartheta}_k x) + \mu_2 \varpi_{2k} \sinh(\bar{\gamma}_k x) \right], k > 1 \\
&V_k(x) = F_k \left[\cosh(\bar{\vartheta}_k x) + \mu_{2k} \cosh(\bar{\gamma}_k x) \right], k > 1
\end{aligned}
\tag{5.94}
$$

Substituting Eq. (5.64) and Eq. (5.94) into Eq. (5.27) yields

$$
\begin{aligned}
u_{general} &= \sum_{n=0}^{\infty} U_n(y) \sin(\alpha_n x) + \sum_{k=0}^{\infty} U_k(x) \cos(\beta_k y) \\
v_{general} &= \sum_{n=0}^{\infty} V_n(y) \cos(\alpha_n x) + \sum_{k=0}^{\infty} V_k(x) \sin(\beta_k y)
\end{aligned}
\tag{5.95}
$$

where

$$
\begin{aligned}
&U_0(x) = D_0 \sin(\lambda_1 x) \\
&V_0(x) = 0 \\
&U_k(x) = F_k \left[\varpi_{1k} \sinh(\bar{\vartheta}_k x) + \mu_2 \varpi_{2k} \sinh(\bar{\gamma}_k x) \right], k > 0 \\
&V_k(x) = F_k \left[\cosh(\bar{\vartheta}_k x) + \mu_{2k} \cosh(\bar{\gamma}_k x) \right], k > 0
\end{aligned}
\tag{5.96}
$$

$$
\begin{aligned}
&V_0(y) = A_0 \sin(\lambda_1 y) \\
&U_0(y) = 0 \\
&U_n(y) = A_n \left[\varpi_{1n} \cosh(\vartheta_n y) + \mu_1 \varpi_{2n} \cosh(\gamma_n y) \right], n > 0 \\
&V_n(y) = A_n \left[\sinh(\vartheta_n y) + \mu_1 \sinh(\gamma_n y) \right], n > 0
\end{aligned}
\tag{5.97}
$$

For the unification of the symbols, the D_0 in Eq. (5.96-1) will be denoted as F_0 from now on.

5.3 Particular solution for PZT actuator EOM

Re-arranging terms in Eq. (5.24) yields

$$\left(1+\frac{m}{m-2}\right)\frac{\partial^2 u}{\partial x^2}+\frac{\partial^2 u}{\partial y^2}+\frac{m}{m-2}\frac{\partial^2 v}{\partial x\partial y}+\frac{\rho_a}{G}\omega^2 u=-\frac{\tau_{zx}\big|_{\text{actuator body force}}}{Gh_a}$$
$$\frac{\partial^2 v}{\partial x^2}+\left(1+\frac{m}{m-2}\right)\frac{\partial^2 v}{\partial y^2}+\frac{m}{m-2}\frac{\partial^2 u}{\partial x\partial y}+\frac{\rho_a}{G}\omega^2 v=-\frac{\tau_{zy}\big|_{\text{actuator body force}}}{Gh_a} \quad (5.98)$$

where

$$m=\frac{c_{11}^E+cc_{13}^E}{c_{12}^E+cc_{13}^E}+1$$

Substituting Eq. (5.1) into Eq. (5.98) yields

$$\left(1+\frac{m}{m-2}\right)\frac{\partial^2 u}{\partial x^2}+\frac{\partial^2 u}{\partial y^2}+\frac{m}{m-2}\frac{\partial^2 v}{\partial x\partial y}+\frac{\rho_a}{G}\omega^2 u=-\frac{a_1x+a_2x^3}{Gh_a}$$
$$\frac{\partial^2 v}{\partial x^2}+\left(1+\frac{m}{m-2}\right)\frac{\partial^2 v}{\partial y^2}+\frac{m}{m-2}\frac{\partial^2 u}{\partial x\partial y}+\frac{\rho_a}{G}\omega^2 v=-\frac{b_1y+b_2y^3}{Gh_a} \quad (5.99)$$

3.3.1 Particular solution for PZT actuator displacement *u*

Assuming that the particular solution for displacement u, v are related to x, y only. Thus the EOM in Eq. (5.99) can be reduced as

$$\left(1+\frac{m}{m-2}\right)\frac{\partial^2 u}{\partial x^2}+\frac{\rho_a}{G}\omega^2 u=-\frac{a_1x+a_2x^3}{Gh_a}$$
$$\left(1+\frac{m}{m-2}\right)\frac{\partial^2 v}{\partial y^2}+\frac{\rho_a}{G}\omega^2 v=-\frac{b_1y+b_2y^3}{Gh_a} \quad (5.100)$$

Writing the particular solution of Eq. (5.100-1) as

$$u_{\text{particular}}=u_{\text{particular}}(x)$$

The solution for Eq. (5.35-1) is

$$u_{\text{particular}} = \frac{(-12a_2G + 12a_2Gm + 2a_1\rho\omega^2 - a_1m\rho\omega^2)x + (2a_2\rho\omega^2 - a_2m\rho\omega^2)x^3}{ha(-2+m)\rho^2\omega^4} + C[1]\cos\left[\frac{\sqrt{-2+m}\sqrt{\rho}\omega}{\sqrt{2}\sqrt{G}\sqrt{-1+m}}x\right] + C[2]\sin\left[\frac{\sqrt{-2+m}\sqrt{\rho}\omega}{\sqrt{2}\sqrt{G}\sqrt{-1+m}}x\right] \quad (5.101)$$

where $C[1], C[2]$ are four random coefficients to be determined by boundary conditions.

Since *u* is symmetric along *x* axis, $C[1] = 0$. For simplicity, *C*[2] is also defined as 0, thus

$$u_{\text{particular}} = \frac{\left[12a_2G(-1+m) + a_1\rho\omega^2(2-m)\right]x + a_2\rho\omega^2(2-m)x^3}{h_a(-2+m)\rho^2\omega^4} \quad (5.102)$$

which also satisfy Considering that $u(x=0) = 0$. It is worth noting that the *C*[2] term has the same form the first term in the general solution.

3.3.2 Particular solution for PZT actuator displacement *v*

Writing the particular solution of Eq. (5.100-2) as

$$v_{\text{particular}} = v_{\text{particular}}(y) \quad (5.103)$$

The solution for Eq. (5.100-2) is

$$v_{\text{particular}} = \frac{(-12b_2G + 12b_2Gm + 2b_1\rho\omega^2 - b_1m\rho\omega^2)y + (2b_2\rho\omega^2 - b_2m\rho\omega^2)y^3}{h_a(-2+m)\rho^2\omega^4} + C[3]\cos\left[\frac{\sqrt{-2+m}\sqrt{\rho}\omega}{\sqrt{2}\sqrt{G}\sqrt{-1+m}}y\right] + C[4]\sin\left[\frac{\sqrt{-2+m}\sqrt{\rho}\omega}{\sqrt{2}\sqrt{G}\sqrt{-1+m}}y\right] \quad (5.104)$$

where $C[3], C[4]$ are four random coefficients to be determined by boundary conditions.

Since v is symmetric along y axis, $C[3] = 0$. For simplicity, C[4] is also defined as 0. Thus

$$v_{\text{particular}} = \frac{\left[12b_2G(-1+m) + b_1\rho\omega^2(2-m)\right]y + b_2\rho\omega^2(2-m)y^3}{h_a(-2+m)\rho^2\omega^4} \quad (5.105)$$

which also satisfy $v(y=0) = 0$. It is worth noting that the C[4] term has the same form the first term in the general solution.

5.4 Determining the coefficients in total solution for PZT actuator displacement using boundary conditions

The total solution would be the summation of general solution and particular solution

$$\begin{aligned} u &= u_{\text{general}} + u_{\text{particular}} \\ v &= v_{\text{general}} + v_{\text{particular}} \end{aligned} \quad (5.106)$$

Eq. (5.21) gives the relation between stress and displacement. Since

$$2G + c_{12}^E + cc_{13}^E = c_{11}^E - c_{12}^E + c_{12}^E + cc_{13}^E = c_{11}^E + cc_{13}^E$$

Eq. (5.21) can be re-written as

$$\begin{aligned}\sigma_z &= c_{11}^p u_{,x} + c_{12}^p v_{,y} + e_{31}^p \frac{V_{in}}{h_a} \\ \sigma_y &= c_{12}^p u_{,x} + c_{11}^p v_{,y} + e_{31}^p \frac{V_{in}}{h_a} \\ \tau_{xy} &= G(u_{,y} + v_{,x})\end{aligned} \tag{5.107}$$

where

$$\begin{aligned}c_{11}^p &= c_{11}^E + cc_{13}^E \\ c_{12}^p &= c_{12}^E + cc_{13}^E\end{aligned} \tag{5.108}$$

Since the displacement consists of general solution and particular solution, Eq. (5.107) can be expanded as

$$\begin{aligned}\sigma_x &= c_{11}^p (u_{\text{general},x} + u_{\text{particular},x}) + c_{12}^p (v_{\text{general},y} + v_{\text{particular},y}) + e_{31}^p \frac{V_{in}}{h_a} \\ &= c_{11}^p u_{\text{general},x} + c_{12}^p v_{\text{general},y} \\ &\quad + c_{11}^p u_{\text{particular},x} + c_{12}^p v_{\text{particular},y} + e_{31}^p \frac{V_{in}}{h_a} \\ \sigma_y &= c_{12}^p (u_{\text{general},x} + u_{\text{particular},x}) + c_{11}^p (v_{\text{general},y} + v_{\text{particular},y}) + e_{31}^p \frac{V_{in}}{h_a} \\ &= c_{12}^p u_{\text{general},x} + c_{11}^p v_{\text{general},y} \\ &\quad + c_{12}^p u_{\text{particular},x} + c_{11}^p v_{\text{particular},y} + e_{31}^p \frac{V_{in}}{h_a} \\ \tau_{xy} &= G(u_{\text{general},y} + u_{\text{particular},y} + v_{\text{general},x} + v_{\text{particular},x}) \\ &= G(u_{\text{general},y} + v_{\text{general},x}) + G(u_{\text{particular},y} + v_{\text{particular},x})\end{aligned} \tag{5.109}$$

Substituting Eq. (5.95), Eq. (5.102) and Eq. (5.105) into Eq. (5.109) yields

$$\sigma_x =$$

$$c_{11}^p\left[\sum_{n=0}^{\infty}\alpha_n U_n(y)\cos(\alpha_n x)+\sum_{k=0}^{\infty}U_k'(x)\cos(\beta_k y)\right]$$
$$+c_{12}^p\left[\sum_{n=0}^{\infty}V_n'(y)\cos(\alpha_n x)+\sum_{k=0}^{\infty}\beta_k V_k(x)\cos(\beta_k y)\right] \qquad (5.110)$$
$$+c_{11}^p\frac{\left[12a_2G(-1+m)+a_1\rho\omega^2(2-m)\right]+3a_2\rho\omega^2(2-m)x^2}{ha\left(-2+m\right)\rho^2\omega^4}$$
$$+c_{12}^p\frac{\left[12b_2G(-1+m)+b_1\rho\omega^2(2-m)\right]+3b_2\rho\omega^2(2-m)y^2}{h_a\left(-2+m\right)\rho^2\omega^4}+e_{31}^p\frac{V_{in}}{h_a}=0$$

$$\sigma_y =$$

$$c_{12}^p\left[\sum_{n=0}^{\infty}\alpha_n U_n(y)\cos(\alpha_n x)+\sum_{k=0}^{\infty}U_k'(x)\cos(\beta_k y)\right]$$
$$+c_{11}^p\left[\sum_{n=0}^{\infty}V_n'(y)\cos(\alpha_n x)+\sum_{k=0}^{\infty}\beta_k V_k(x)\cos(\beta_k y)\right] \qquad (5.111)$$
$$+c_{12}^p\frac{\left[12a_2G(-1+m)+a_1\rho\omega^2(2-m)\right]+3a_2\rho\omega^2(2-m)x^2}{ha\left(-2+m\right)\rho^2\omega^4}$$
$$+c_{11}^p\frac{\left[12b_2G(-1+m)+b_1\rho\omega^2(2-m)\right]+3b_2\rho\omega^2(2-m)y^2}{h_a\left(-2+m\right)\rho^2\omega^4}+e_{31}^p\frac{V_{in}}{h_a}=0$$

$$\tau_{xy} =$$

$$G\left[\sum_{n=0}^{\infty}U_n'(y)\sin(\alpha_n x)-\sum_{k=0}^{\infty}\beta_k U_k(x)\sin(\beta_k y)\right. \qquad (5.112)$$
$$\left.-\sum_{n=0}^{\infty}\alpha_n V_n(y)\sin(\alpha_n x)+\sum_{k=0}^{\infty}V_k'(x)\sin(\beta_k y)\right]=0$$

Substituting Eq. (5.96) and Eq. (5.97) into the above stress expressions yields

$$
\begin{aligned}
\sigma_x = \\
& c_{11}^p \left[F_0 \lambda_1 \cos(\lambda_1 x) \right] \\
& + c_{11}^p \left[\sum_{n=1}^{\infty} \alpha_n A_n \left[\varpi_{1n} \cosh(\vartheta_n y) + \mu_1 \varpi_{2n} \cosh(\gamma_n y) \right] \cos(\alpha_n x) \right] \\
& + c_{11}^p \left[\sum_{k=1}^{\infty} F_k \left[\varpi_{1k} \overline{\vartheta} \cosh(\overline{\vartheta}_k x) + \mu_2 \varpi_{2k} \overline{\gamma}_k \cosh(\overline{\gamma}_k x) \right] \cos(\beta_k y) \right] \\
& + c_{12}^p \left[A_0 \lambda_1 \cos(\lambda_1 y) \right] \\
& + c_{12}^p \left[\sum_{n=1}^{\infty} A_n \left[\vartheta_n \cosh(\vartheta_n y) + \mu_1 \gamma_n \cosh(\gamma_n y) \right] \cos(\alpha_n x) \right] \\
& + c_{12}^p \left[\sum_{k=1}^{\infty} \beta_k F_k \left[\cosh(\overline{\vartheta}_k x) + \mu_2 \cosh(\overline{\gamma}_k x) \right] \cos(\beta_k y) \right] \\
& + c_{11}^p \frac{\left[12 a_2 G(-1+m) + a_1 \rho \omega^2 (2-m) \right] + 3 a_2 \rho \omega^2 (2-m) x^2}{ha\left(-2+m\right) \rho^2 \omega^4} \\
& + c_{12}^p \frac{\left[12 b_2 G(-1+m) + b_1 \rho \omega^2 (2-m) \right] + 3 b_2 \rho \omega^2 (2-m) y^2}{h_a \left(-2+m\right) \rho^2 \omega^4} + e_{31}^p \frac{V_{in}}{h_a} = 0
\end{aligned}
\tag{5.113}
$$

$$
\begin{aligned}
\sigma_y = \\
& c_{12}^p \left[F_0 \lambda_1 \cos(\lambda_1 x) \right] \\
& + c_{12}^p \left[\sum_{n=1}^{\infty} \alpha_n A_n \left[\varpi_{1n} \cosh(\vartheta_n y) + \mu_1 \varpi_{2n} \cosh(\gamma_n y) \right] \cos(\alpha_n x) \right] \\
& + c_{12}^p \left[\sum_{k=1}^{\infty} F_k \left[\varpi_{1k} \overline{\vartheta} \cosh(\overline{\vartheta}_k x) + \mu_2 \varpi_{2k} \overline{\gamma}_k \cosh(\overline{\gamma}_k x) \right] \cos(\beta_k y) \right] \\
& + c_{11}^p \left[A_0 \lambda_1 \cos(\lambda_1 y) \right] \\
& + c_{11}^p \left[\sum_{n=1}^{\infty} A_n \left[\vartheta_n \cosh(\vartheta_n y) + \mu_1 \gamma_n \cosh(\gamma_n y) \right] \cos(\alpha_n x) \right] \\
& + c_{11}^p \left[\sum_{k=1}^{\infty} \beta_k F_k \left[\cosh(\overline{\vartheta}_k x) + \mu_2 \cosh(\overline{\gamma}_k x) \right] \cos(\beta_k y) \right] \\
& + c_{12}^p \frac{\left[12 a_2 G(-1+m) + a_1 \rho \omega^2 (2-m) \right] + 3 a_2 \rho \omega^2 (2-m) x^2}{ha\left(-2+m\right) \rho^2 \omega^4} \\
& + c_{11}^p \frac{\left[12 b_2 G(-1+m) + b_1 \rho \omega^2 (2-m) \right] + 3 b_2 \rho \omega^2 (2-m) y^2}{h_a \left(-2+m\right) \rho^2 \omega^4} + e_{31}^p \frac{V_{in}}{h_a} = 0
\end{aligned}
\tag{5.114}
$$

$$\tau_{xy} =$$

$$G\Bigg[\sum_{n=1}^{\infty} A_n\left[\varpi_{1n}\vartheta_n \sinh(\vartheta_n y)+\mu_1\varpi_{2n}\gamma_n \sinh(\gamma_n y)\right]\sin(\alpha_n x)$$

$$-\sum_{k=1}^{\infty} \beta_k F_k\left[\varpi_{1k}\sinh(\overline{\vartheta}_k x)+\mu_2\varpi_{2k}\sinh(\overline{\gamma}_k x)\right]\sin(\beta_k y) \qquad (5.115)$$

$$-\sum_{n=1}^{\infty} \alpha_n A_n\left[\sinh(\vartheta_n y)+\mu_1\sinh(\gamma_n y)\right]\sin(\alpha_n x)$$

$$+\sum_{k=1}^{\infty} F_k\left[\overline{\vartheta}\sinh(\overline{\vartheta}_k x)+\mu_2\overline{\gamma}_k\sinh(\overline{\gamma}_k x)\right]\sin(\beta_k y)\Bigg]=0$$

Combining terms with the same coefficients, the above stress distributions can be rewritten as

$$\sigma_x =$$

$$A_0 c_{12}^p\lambda_1\cos(\lambda_1 y)+F_0 c_{11}^p\lambda_1\cos(\lambda_1 x)$$

$$+\sum_{n=1}^{\infty}\left\{A_n\cos(\alpha_n x)\left[c_{11}^p\alpha_n\left(\varpi_{1n}\cosh(\vartheta_n y)+\mu_1\varpi_{2n}\cosh(\gamma_n y)\right)+c_{12}^p\left(\vartheta_n\cosh(\vartheta_n y)+\mu_1\gamma_n\cosh(\gamma_n y)\right)\right]\right\}$$

$$+\sum_{k=1}^{\infty}\left\{F_k\cos(\beta_k y)\left[c_{11}^p\left(\varpi_{1k}\overline{\vartheta}\cosh(\overline{\vartheta}_k x)+\mu_2\varpi_{2k}\overline{\gamma}_k\cosh(\overline{\gamma}_k x)\right)+c_{12}^p\beta_k\left(\cosh(\overline{\vartheta}_k x)+\mu_2\cosh(\overline{\gamma}_k x)\right)\right]\right\}$$

$$+c_{11}^p\frac{\left[12a_2G(-1+m)+a_1\rho\omega^2(2-m)\right]+3a_2\rho\omega^2(2-m)x^2}{ha\left(-2+m\right)\rho^2\omega^4}$$

$$+c_{12}^p\frac{\left[12b_2G(-1+m)+b_1\rho\omega^2(2-m)\right]+3b_2\rho\omega^2(2-m)y^2}{h_a\left(-2+m\right)\rho^2\omega^4}+e_{31}^p\frac{V_{in}}{h_a}=0$$

(5.116)

$$
\begin{aligned}
\sigma_y = \\
&A_0 c_{11}^p \lambda_1 \cos(\lambda_1 y) + F_0 c_{12}^p \lambda_1 \cos(\lambda_1 x) \\
&+ \sum_{n=1}^{\infty} \left\{ A_n \cos(\alpha_n x) \left[c_{12}^p \alpha_n \left(\varpi_{1n} \cosh(\vartheta_n y) + \mu_1 \varpi_{2n} \cosh(\gamma_n y) \right) + c_{11}^p \left(\vartheta_n \cosh(\vartheta_n y) + \mu_1 \gamma_n \cosh(\gamma_n y) \right) \right] \right\} \\
&+ \sum_{k=1}^{\infty} \left\{ F_k \cos(\beta_k y) \left[c_{12}^p \left(\varpi_{1k} \overline{\vartheta} \cosh(\overline{\vartheta}_k x) + \mu_2 \varpi_{2k} \overline{\gamma}_k \cosh(\overline{\gamma}_k x) \right) + c_{11}^p \beta_k \left(\cosh(\overline{\vartheta}_k x) + \mu_2 \cosh(\overline{\gamma}_k x) \right) \right] \right\} \\
&+ c_{12}^p \frac{\left[12 a_2 G(-1+m) + a_1 \rho \omega^2 (2-m) \right] + 3 a_2 \rho \omega^2 (2-m) x^2}{ha\left(-2+m\right)\rho^2 \omega^4} \\
&+ c_{11}^p \frac{\left[12 b_2 G(-1+m) + b_1 \rho \omega^2 (2-m) \right] + 3 b_2 \rho \omega^2 (2-m) y^2}{h_a \left(-2+m\right)\rho^2 \omega^4} + e_{31}^p \frac{V_{in}}{h_a} = 0
\end{aligned}
\tag{5.117}
$$

$$
\begin{aligned}
\tau_{xy} = \\
&G \sum_{n=1}^{\infty} A_n \sin(\alpha_n x) \left[\left(\varpi_{1n} \vartheta_n \sinh(\vartheta_n y) + \mu_1 \varpi_{2n} \gamma_n \sinh(\gamma_n y) \right) - \alpha_n \left(\sinh(\vartheta_n y) + \mu_1 \sinh(\gamma_n y) \right) \right] \\
&- G \sum_{k=1}^{\infty} F_k \sin(\beta_k y) \left[\beta_k \left(\varpi_{1k} \sinh(\overline{\vartheta}_k x) + \mu_2 \varpi_{2k} \sinh(\overline{\gamma}_k x) \right) + \left(\overline{\vartheta} \sinh(\overline{\vartheta}_k x) + \mu_2 \overline{\gamma}_k \sinh(\overline{\gamma}_k x) \right) \right] = 0
\end{aligned}
\tag{5.118}
$$

Boundary condition is set to be traction free at the four peripheries

$$
\begin{cases}
\sigma_x^a = 0 \quad \text{at} \quad x = \pm a \\
\sigma_y^a = 0 \quad \text{at} \quad y = \pm b \\
\tau_{xy}^a = 0 \quad \text{at} \quad x = \pm a \quad \textit{and} \quad y = \pm b
\end{cases}
\tag{5.119}
$$

From the expression of τ_{xy} in Eq. (5.118), the boundary condition in Eq. (5.119-3) is automatically satisfied.

The strong boundary conditions are transformed to weak boundary conditions as:

$$h_a \int_{y=-b}^{b} \sigma_x^a \Big|_{x=a} = 0$$
$$h_a \int_{y=-b}^{b} \sigma_x^a \Big|_{x=-a} = 0$$
$$h_a \int_{x=-a}^{a} \sigma_y^a \Big|_{y=b} = 0$$
$$h_a \int_{x=-a}^{a} \sigma_y^a \Big|_{y=-b} = 0$$

Since σ_x is symmetric along y axis and σ_y is symmetric along x axis, the above boundary conditions are reduced to

$$\begin{aligned} h_a \int_{y=-b}^{b} \sigma_x^a \Big|_{x=a} &= 0 \\ h_a \int_{x=-a}^{a} \sigma_y^a \Big|_{y=b} &= 0 \end{aligned} \tag{5.120}$$

The stresses at the boundaries are

$$\begin{aligned} &\sigma_x \big|_{x=a} = \\ &A_0 c_{12}^p \lambda_1 \cos(\lambda_1 y) + F_0 c_{11}^p \lambda_1 \cos(\lambda_1 a) \\ &+ \sum_{n=1}^{\infty} \left\{ A_n \cos(\alpha_n a) \left[c_{11}^p \alpha_n \left(\varpi_{1n} \cosh(\vartheta_n y) + \mu_1 \varpi_{2n} \cosh(\gamma_n y) \right) + c_{12}^p \left(\vartheta_n \cosh(\vartheta_n y) + \mu_1 \gamma_n \cosh(\gamma_n y) \right) \right] \right\} \\ &+ \sum_{k=1}^{\infty} \left\{ F_k \cos(\beta_k y) \left[c_{11}^p \left(\varpi_{1k} \overline{\vartheta} \cosh(\overline{\vartheta}_k a) + \mu_2 \varpi_{2k} \overline{\gamma}_k \cosh(\overline{\gamma}_k a) \right) + c_{12}^p \beta_k \left(\cosh(\overline{\vartheta}_k a) + \mu_2 \cosh(\overline{\gamma}_k a) \right) \right] \right\} \\ &+ c_{11}^p \frac{\left[12 a_2 G(-1+m) + a_1 \rho \omega^2 (2-m) \right] + 3 a_2 \rho \omega^2 (2-m) a^2}{ha\left(-2+m\right) \rho^2 \omega^4} \\ &+ c_{12}^p \frac{\left[12 b_2 G(-1+m) + b_1 \rho \omega^2 (2-m) \right] + 3 b_2 \rho \omega^2 (2-m) y^2}{h_a \left(-2+m\right) \rho^2 \omega^4} + e_{31}^p \frac{V_{in}}{h_a} \end{aligned}$$

(5.121)

$$\sigma_y\Big|_{y=b} =$$

$$A_0 c_{11}^p \lambda_1 \cos(\lambda_1 b) + F_0 c_{12}^p \lambda_1 \cos(\lambda_1 x)$$

$$+\sum_{n=1}^{\infty} \left\{ A_n \cos(\alpha_n x) \left[c_{12}^p \alpha_n \left(\varpi_{1n} \cosh(\vartheta_n b) + \mu_1 \varpi_{2n} \cosh(\gamma_n b) \right) + c_{11}^p \left(\vartheta_n \cosh(\vartheta_n b) + \mu_1 \gamma_n \cosh(\gamma_n b) \right) \right] \right\}$$

$$+\sum_{k=1}^{\infty} \left\{ F_k \cos(\beta_k b) \left[c_{12}^p \left(\varpi_{1k} \overline{\vartheta} \cosh(\overline{\vartheta}_k x) + \mu_2 \varpi_{2k} \overline{\gamma}_k \cosh(\overline{\gamma}_k x) \right) + c_{11}^p \beta_k \left(\cosh(\overline{\vartheta}_k x) + \mu_2 \cosh(\overline{\gamma}_k x) \right) \right] \right\}$$

$$+ c_{12}^p \frac{\left[12 a_2 G(-1+m) + a_1 \rho \omega^2 (2-m) \right] + 3 a_2 \rho \omega^2 (2-m) x^2}{ha\left(-2+m\right)\rho^2 \omega^4}$$

$$+ c_{11}^p \frac{\left[12 b_2 G(-1+m) + b_1 \rho \omega^2 (2-m) \right] + 3 b_2 \rho \omega^2 (2-m) b^2}{h_a \left(-2+m\right)\rho^2 \omega^4} + e_{31}^p \frac{V_{in}}{h_a}$$

(5.122)

Substituting Eq. (5.121) and Eq. (5.122) into Eq. (5.120) yields

$$h_a \int_{y=-b}^{b} \sigma_x^a \Big|_{x=a}$$

$$= h_a A_0 2\sin(b\lambda_1) c_{12}^p + h_a F_0 2b c_{11}^p \lambda_1 \cos(\lambda_1 a)$$

$$+ h_a \sum_{n=1}^{\infty} \left\{ A_n \cos(\alpha_n a) \left[(c_{11}^p \alpha_n \varpi_{1n} + c_{12}^p \vartheta_n) \frac{2\sinh(b\vartheta_n)}{\vartheta_n} + (c_{11}^p \alpha_n \mu_1 \varpi_{2n} + c_{12}^p \mu_1 \gamma_n) \frac{2\sinh(b\gamma_n)}{\gamma_n} \right] \right\}$$

$$+ h_a \sum_{k=1}^{\infty} \left\{ F_k \frac{2\sin(b\beta_k)}{\beta_k} \left[(c_{11}^p \varpi_{1k} \overline{\vartheta} + c_{12}^p \beta_k) \cosh(\overline{\vartheta}_k a) + (c_{11}^p \mu_2 \varpi_{2k} \overline{\gamma}_k + c_{12}^p \beta_k \mu_2) \cosh(\overline{\gamma}_k a) \right] \right\}$$

$$+ 2h_a b c_{11}^p \frac{\left[12 a_2 G(-1+m) + a_1 \rho \omega^2 (2-m) \right] + 3 a_2 \rho \omega^2 (2-m) a^2}{ha\left(-2+m\right)\rho^2 \omega^4}$$

$$+ h_a c_{12}^p \frac{2b\left[12 b_2 G(-1+m) + b_1 \rho \omega^2 (2-m) \right] + 2b^3 b_2 \rho \omega^2 (2-m)}{h_a \left(-2+m\right)\rho^2 \omega^4} + 2h_a b e_{31}^p \frac{V_{in}}{h_a} = 0$$

(5.123)

$$
\begin{aligned}
&h_a \int_{x=-a}^{a} \sigma_y^a \Big|_{y=b} \\
&= h_a A_0 2ac_{11}^p \lambda_1 \cos(\lambda_1 b) + h_a F_0 c_{12}^p 2\sin(a\lambda_1) \\
&+ h_a \sum_{n=1}^{\infty} \left\{ A_n \frac{2\sin(a\alpha_n)}{\alpha_n} \left[(c_{12}^p \alpha_n \varpi_{1n} + c_{11}^p \vartheta_n) \cosh(\vartheta_n b) + (c_{12}^p \alpha_n \mu_1 \varpi_{2n} + c_{11}^p \mu_1 \gamma_n \cosh(\gamma_n b) \right] \right\} \\
&+ h_a \sum_{k=1}^{\infty} \left\{ F_k \cos(\beta_k b) \left[(c_{12}^p \varpi_{1k} \overline{\vartheta} + c_{11}^p \beta_k) \frac{2\sinh(a\overline{\vartheta}_k)}{\overline{\vartheta}_k} + (c_{12}^p \mu_2 \varpi_{2k} \overline{\gamma}_k + c_{11}^p \beta_k \mu_2) \frac{2\sinh(a\overline{\gamma}_k)}{\overline{\gamma}_k} \right] \right\} \\
&+ h_a c_{12}^p \frac{2a\left[12a_2 G(-1+m) + a_1 \rho\omega^2 (2-m)\right] + 2a^3 a_2 \rho\omega^2 (2-m)}{ha\left(-2+m\right)\rho^2\omega^4} \\
&+ h_a c_{11}^p 2a \frac{\left[12b_2 G(-1+m) + b_1 \rho\omega^2 (2-m)\right] + 3b_2 \rho\omega^2 (2-m)b^2}{h_a\left(-2+m\right)\rho^2\omega^4} + 2h_a a e_{31}^p \frac{V_{in}}{h_a} = 0
\end{aligned}
\tag{5.124}
$$

5.4.1 If only considering the first term in the general solution and the particular solution

If only considering the first term in general solution and the particular solution, Eq. (5.123) and Eq. (5.124) becomes

$$
\begin{aligned}
&h_a \int_{y=-b}^{b} \sigma_x^a \Big|_{x=a} \\
&= h_a A_0 2\sin(b\lambda_1) c_{12}^p + h_a F_0 2bc_{11}^p \lambda_1 \cos(\lambda_1 a) \\
&+ 2h_a b c_{11}^p \frac{\left[12a_2 G(-1+m) + a_1 \rho\omega^2 (2-m)\right] + 3a_2 \rho\omega^2 (2-m)a^2}{ha\left(-2+m\right)\rho^2\omega^4} \\
&+ h_a c_{12}^p \frac{2b\left[12b_2 G(-1+m) + b_1 \rho\omega^2 (2-m)\right] + 2b^3 b_2 \rho\omega^2 (2-m)}{h_a\left(-2+m\right)\rho^2\omega^4} + 2h_a b e_{31}^p \frac{V_{in}}{h_a} = 0
\end{aligned}
\tag{5.125}
$$

$$
\begin{aligned}
&h_a \int_{x=-a}^{a} \sigma_y^a \Big|_{y=b} \\
&= h_a A_0 \, 2ac_{11}^p \lambda_1 \cos(\lambda_1 b) + F_0 h_a c_{12}^p 2\sin(a\lambda_1) \\
&+ h_a c_{12}^p \frac{2a\left[12a_2 G(-1+m) + a_1 \rho\omega^2 (2-m)\right] + 2a^3 a_2 \rho\omega^2 (2-m)}{ha\left(-2+m\right)\rho^2\omega^4} \\
&+ h_a c_{11}^p 2a \frac{\left[12b_2 G(-1+m) + b_1 \rho\omega^2 (2-m)\right] + 3b_2 \rho\omega^2 (2-m) b^2}{h_a\left(-2+m\right)\rho^2\omega^4} + 2ah_a e_{31}^p \frac{V_{in}}{h_a} = 0
\end{aligned}
\tag{5.126}
$$

Solving Eq. (5.125) and Eq. (5.126) for A_0, F_0 yields

$$
\begin{aligned}
A_0 = {} & \frac{1}{h_a\left(-2+m\right)\rho^2\omega^4\left[abc_{11}^{P2}\lambda_1{}^2\cos(a\lambda_1)\cos(b\lambda_1) - c_{12}^{p\,2}\sin(a\lambda_1)\sin(b\lambda_1)\right]} \times \\
& \Big\{abc_{11}^P\lambda_1\Big[a_2c_{12}^p\left(-12G\left(-1+m\right)+a^2\left(-2+m\right)\rho\omega^2\right) - \\
& 3b_2c_{11}^P\left(4G\left(-1+m\right)-b^2\left(-2+m\right)\rho\omega^2\right)+\left(-2+m\right)\rho\omega^2\left(b_1c_{11}^P+a_1c_{12}^p-e_{31}^pV_{in}\rho\omega^2\right)\Big]\cos(a\lambda_1) - \\
& c12p\Big[b^3b_2c_{12}^p\left(-2+m\right)\rho\omega^2 - ae_{31}^p\left(-2+m\right)V\rho^2\omega^4 - 3a_2bc_{11}^P\left(4G\left(-1+m\right)-a^2\left(-2+m\right)\rho\omega^2\right)+ \\
& b\left(-12b_2c_{12}^pG\left(-1+m\right)+\left(a_1c_{11}^P+b_1c_{12}^p\right)\left(-2+m\right)\rho\omega^2\right)\Big]\sin(a\lambda_1)\Big) \\
F_0 = {} & \frac{1}{h_a\left(-2+m\right)\rho^2\omega^4\left(abc_{11}^{P2}\lambda_1{}^2\cos(b\lambda_1)\cot(a\lambda_1) - c12p^2\sin(b\lambda_1)\right)} \times \\
& \Big\{a\csc(a\lambda_1)\Big[-c_{11}^P\lambda_1(-b^3b_2c_{12}^p\left(-2+m\right)\rho\omega^2 + ae_{31}^p\left(-2+m\right)V\rho^2\omega^4 \\
& + 3a2bc_{11}^P\left(4G\left(-1+m\right)-a^2\left(-2+m\right)\rho\omega^2\right)+ \\
& b\left(12b_2c_{12}^pG\left(-1+m\right)-\left(a1c_{11}^P+b1c_{12}^p\right)\left(-2+m\right)\rho\omega^2\right))\cos(b\lambda_1)+ \\
& c_{12}^p(a_2c_{12}^p\left(12G\left(-1+m\right)-a^2\left(-2+m\right)\rho\omega^2\right)+3b_2c_{11}^P\left(4G\left(-1+m\right)-b^2\left(-2+m\right)\rho\omega^2\right)+ \\
& \left(-2+m\right)\rho\omega^2\left(-b_1c_{11}^P-a_1c_{12}^p+e_{31}^pV_{in}\rho\omega^2\right))\sin(b\lambda_1)\Big]\Big\}
\end{aligned}
\tag{5.127}
$$

5.4.2 If only considering the first two term in the general solution and the particular solution

In order to solve for A_0, F_0, A_n, F_k from the boundary conditions, Eq. (5.121) and Eq. (5.122) are divided into two parts separately and each part is set to be zero

$$\begin{aligned}
&\sigma_{x1}\big|_{x=a} = \\
&A_0 c_{12}^p \lambda_1 \cos(\lambda_1 y) + F_0 c_{11}^p \lambda_1 \cos(\lambda_1 a) \\
&+ c_{11}^p \frac{\left[12a_2 G(-1+m) + a_1 \rho\omega^2 (2-m)\right] + 3a_2 \rho\omega^2 (2-m)a^2}{ha\left(-2+m\right)\rho^2\omega^4} \\
&+ c_{12}^p \frac{\left[12b_2 G(-1+m) + b_1 \rho\omega^2 (2-m)\right] + 3b_2 \rho\omega^2 (2-m)y^2}{h_a\left(-2+m\right)\rho^2\omega^4} + e_{31}^p \frac{V_{in}}{h_a}
\end{aligned} \tag{5.128}$$

$$\begin{aligned}
&\sigma_{x2}\big|_{x=a} = \\
&+ \sum_{n=1}^{\infty} \left\{ A_n \cos(\alpha_n a)\left[c_{11}^p \alpha_n \left(\varpi_{1n} \cosh(\vartheta_n y) + \mu_1 \varpi_{2n} \cosh(\gamma_n y) \right) + c_{12}^p \left(\vartheta_n \cosh(\vartheta_n y) + \mu_1 \gamma_n \cosh(\gamma_n y) \right) \right] \right\} \\
&+ \sum_{k=1}^{\infty} \left\{ F_k \cos(\beta_k y)\left[c_{11}^p \left(\varpi_{1k} \overline{\vartheta} \cosh(\overline{\vartheta}_k a) + \mu_2 \varpi_{2k} \overline{\gamma}_k \cosh(\overline{\gamma}_k a) \right) + c_{12}^p \beta_k \left(\cosh(\overline{\vartheta}_k a) + \mu_2 \cosh(\overline{\gamma}_k a) \right) \right] \right\}
\end{aligned} \tag{5.129}$$

$$\begin{aligned}
&\sigma_{y1}\big|_{y=b} = \\
&A_0 c_{11}^p \lambda_1 \cos(\lambda_1 b) + F_0 c_{12}^p \lambda_1 \cos(\lambda_1 x) \\
&+ c_{12}^p \frac{\left[12a_2 G(-1+m) + a_1 \rho\omega^2 (2-m)\right] + 3a_2 \rho\omega^2 (2-m)x^2}{ha\left(-2+m\right)\rho^2\omega^4} \\
&+ c_{11}^p \frac{\left[12b_2 G(-1+m) + b_1 \rho\omega^2 (2-m)\right] + 3b_2 \rho\omega^2 (2-m)b^2}{h_a\left(-2+m\right)\rho^2\omega^4} + e_{31}^p \frac{V_{in}}{h_a}
\end{aligned} \tag{5.130}$$

$$\sigma_{y2}\Big|_{y=b} =$$
$$+\sum_{n=1}^{\infty}\ \left\{A_n\cos(\alpha_n x)\left[c_{12}^{p}\alpha_n\left(\varpi_{1n}\cosh(\vartheta_n b)+\mu_1\varpi_{2n}\cosh(\gamma_n b)\right)+c_{11}^{p}\left(\vartheta_n\cosh(\vartheta_n b)+\mu_1\gamma_n\cosh(\gamma_n b)\right)\right]\right\}$$
$$+\sum_{k=1}^{\infty}\ \left\{F_k\cos(\beta_k b)\left[c_{12}^{p}\left(\varpi_{1k}\overline{\vartheta}\cosh(\overline{\vartheta}_k x)+\mu_2\varpi_{2k}\overline{\gamma}_k\cosh(\overline{\gamma}_k x)\right)+c_{11}^{p}\beta_k\left(\cosh(\overline{\vartheta}_k x)+\mu_2\cosh(\overline{\gamma}_k x)\right)\right]\right\}$$

(5.131)

Eq. (5.128) and Eq. (5.130) are stresses from the particular displacement solution and the first term in general solution. The weak form of boundary conditions for the stresses given in Eq. (5.128) and Eq. (5.130) can be expressed in Eq. (5.125) and Eq. (5.126), from which A_0, F_0 can be solved.

Eq. (5.129) and Eq. (5.131) are stresses from the general solution besides the first term. The weak form of the stress free boundary conditions from the stresses given in Eq. (5.129) and Eq. (5.131) are expressed below:

$$h_a\int_{y=-b}^{b}\sigma_{x2}\Big|_{x=a}$$
$$=h_a\sum_{n=1}^{\infty}\ \left\{A_n\cos(\alpha_n a)\left[(c_{11}^{p}\alpha_n\varpi_{1n}+c_{12}^{p}\vartheta_n)\frac{2\sinh(b\vartheta_n)}{\vartheta_n}+(c_{11}^{p}\alpha_n\mu_1\varpi_{2n}+c_{12}^{p}\mu_1\gamma_n)\frac{2\sinh(b\gamma_n)}{\gamma_n}\right]\right\}$$
$$+h_a\sum_{k=1}^{\infty}\ \left\{F_k\frac{2\sin(b\beta_k)}{\beta_k}\left[(c_{11}^{p}\varpi_{1k}\overline{\vartheta}+c_{12}^{p}\beta_k)\cosh(\overline{\vartheta}_k a)+(c_{11}^{p}\mu_2\varpi_{2k}\overline{\gamma}_k+c_{12}^{p}\beta_k\mu_2)\cosh(\overline{\gamma}_k a)\right]\right\}$$

(5.132)

$$h_a \int_{x=-a}^{a} \sigma_{y2}\Big|_{y=b}$$

$$= h_a \sum_{n=1}^{\infty} \left\{ A_n \frac{2\sin(a\alpha_n)}{\alpha_n} \left[(c_{12}^p \alpha_n \varpi_{1n} + c_{11}^p \vartheta_n) \cosh(\vartheta_n b) + (c_{12}^p \alpha_n \mu_1 \varpi_{2n} + c_{11}^p \mu_1 \gamma_n \cosh(\gamma_n b) \right] \right\}$$

$$+ h_a \sum_{k=1}^{\infty} \left\{ F_k \cos(\beta_k b) \left[(c_{12}^p \varpi_{1k} \overline{\vartheta} + c_{11}^p \beta_k) \frac{2\sinh(a\overline{\vartheta}_k)}{\overline{\vartheta}_k} + (c_{12}^p \mu_2 \varpi_{2k} \overline{\gamma}_k + c_{11}^p \beta_k \mu_2) \frac{2\sinh(a\overline{\gamma}_k)}{\overline{\gamma}_k} \right] \right\}$$

(5.133)

In order to solve for A_n, F_k from the above two equations, the method of 'least square' is used, which is explained as below.

Define a function $LS(A_n, F_k)$ as:

$$LS(A_n, F_k) = \left(\int_{x=-a}^{a} \sigma_{x2}\Big|_{y=b} \right)^2 + \left(\int_{x=-a}^{a} \sigma_{y2}\Big|_{y=b} \right)^2 \tag{5.134}$$

Where $\int_{x=-a}^{a} \sigma_{x2}\Big|_{y=b}, \int_{x=-a}^{a} \sigma_{y2}\Big|_{y=b}$ are given in Eq. (132) and Eq. (133).

The derivative of $LS(A_n, F_k)$ with respect to A_n, F_k is set to zero in order to have the value of $\int_{x=-a}^{a} \sigma_{x2}\Big|_{y=b}, \int_{x=-a}^{a} \sigma_{y2}\Big|_{y=b}$ closest to 0. The list of equations is:

$$
\begin{aligned}
&\frac{\partial}{\partial A_1} LS(A_n, F_k) = 0 \\
&\frac{\partial}{\partial A_1} LS(A_n, F_k) = 0 \\
&\qquad \vdots \\
&\frac{\partial}{\partial A_n} LS(A_n, F_k) = 0 \\
&\frac{\partial}{\partial F_1} LS(A_n, F_k) = 0 \\
&\frac{\partial}{\partial F_1} LS(A_n, F_k) = 0 \\
&\qquad \vdots \\
&\frac{\partial}{\partial F_k} LS(A_n, F_k) = 0
\end{aligned}
\tag{5.135}
$$

5.5. Verification of the theoretical model for PZT actuator displacement

5.5.1 If only considering the first term in the general solution and the particular solution

In this Section, the coefficients in the total solutions are calculated for the given stress coefficients (see Eq. (5.1) for stress expression)

$$
\begin{aligned}
a_1 &= -8.3660 \times 10^8; \\
a_2 &= \ \ 8.1920 \times 10^{14}; \\
b_1 &= -4.7180 \times 10^8; \\
b_2 &= \ \ 8.5670 \times 10^{13}.
\end{aligned}
$$

For the given material properties and the given frequency, A_0, F_0 are

$$A_0 = -9.3192 \times 10^{-5};$$
$$F_0 = -8.7520 \times 10^{-4}.$$

By comparing Eq. (5.96) with Eq. (5.101), the first term in general solution is actually the same term as the omitted form in the particular solution. Same conclusion can be drawn by comparing Eq. (5.97) with Eq. (5.104). Thus if only considering the first term in general solution and the particular solution, it is the same as just considering the particular solution.

5.5.2 If only considering the first two term in the general solution and the particular solution

If the second term in the general solutions is considered, the solution of A_1, F_0, A_1, F_1 is

$$\begin{aligned} A_0 &= -9.3192 \times 10^{-5}; \\ F_0 &= -8.7520 \times 10^{-4}; \\ A_1 &= -1.2740 \times 10^{-9}; \\ F_1 &= \ 5.8553 \times 10^{-8}. \end{aligned} \tag{5.136}$$

5.5.3 If only considering the first three term in the general solution and the particular solution

If the first three terms in the general solutions are considered, the solution of A_n, F_k is

$$
\begin{aligned}
A_0 &= -9.3192\times10^{-5};\\
F_0 &= -8.7520\times10^{-4};\\
A_1 &= -1.4449\times10^{-9};\\
F_1 &= \ \ 5.8580\times10^{-8};\\
A_2 &= -4.1067\times10^{-12};\\
F_2 &= -4.3356\times10^{-8}.
\end{aligned}
\tag{5.137}
$$

As can be seen from Eq. (5.137), the coefficients decrease dramatically as n, k increases. Thus it can be conducted that the solution is already converged and the first two or three terms in the general solution is sufficient to express the displacement of the piezoelectric actuator.

5.6 Verification on why shear stresses are the best parameters to describe connection between PZT actuator and bonded plate

In order to compare the plate response under (1) surface bonded piezoelectric actuator; (2) replacing the actuator with line loads on the peripheries of the rectangular actuator; (3) replacing the actuator with shear stress τ_{xz} and τ_{yz} on the contact surface; (4) replacing the actuator with prescribed displacement u, v, w on the contact surface, the displacement and strain on plate upper surface along five monitoring lines are compared. The five monitoring lines are listed below:

Monitoring line I: along x axis;

Monitoring line II: along $\tan^{-1}(1/2)$ with respect to x axis;

Monitoring line III: along $\tan^{-1}1.1$ with respect to x axis;

Monitoring line IV: along $\tan^{-1} 2$ with respect to x axis;

Monitoring line V: along y axis.

The velocity components, displacement components and strain components on the monitoring lines are compared below.

5.6.1. Comparison of results along line I

The displacement components on the monitoring line I are shown below. The Displacement v is not shown because it all vanishes along line I.

Figure 5.5 (a) Displacement *u* (*m*) (b) displacement *w* (*m*) along *x* axis (*mm*)

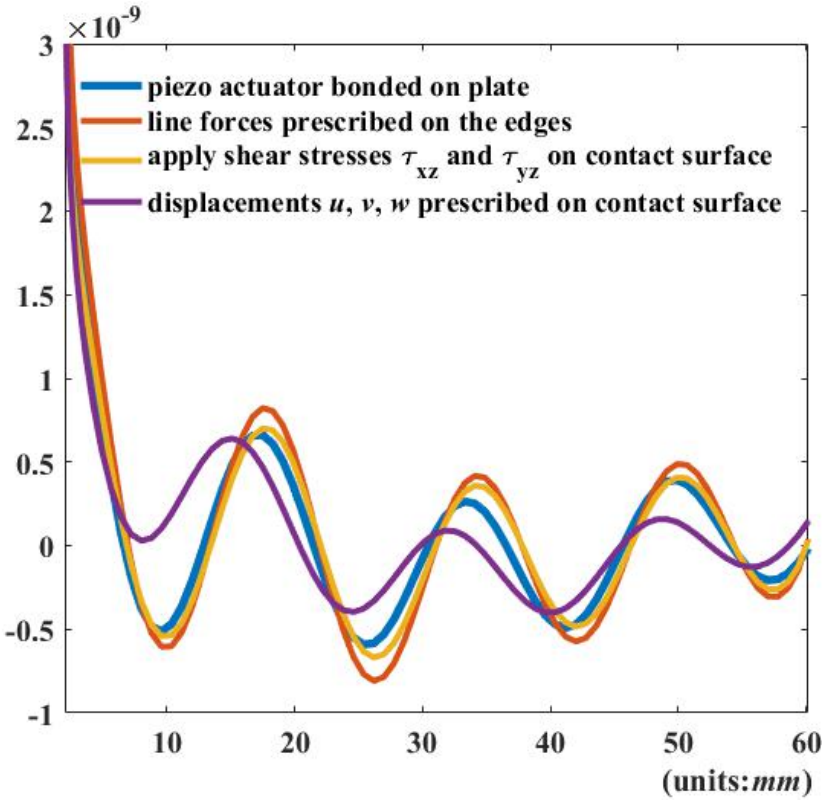
×10^-9
3
2.5
2
1.5
1
0.5
0
-0.5
-1
10
20
30
40
50
60
(units:mm)
piezo actuator bonded on plate
line forces prescribed on the edges
apply shear stresses τxz and τyz on contact surface
displacements u, v, w prescribed on contact surface

(a)

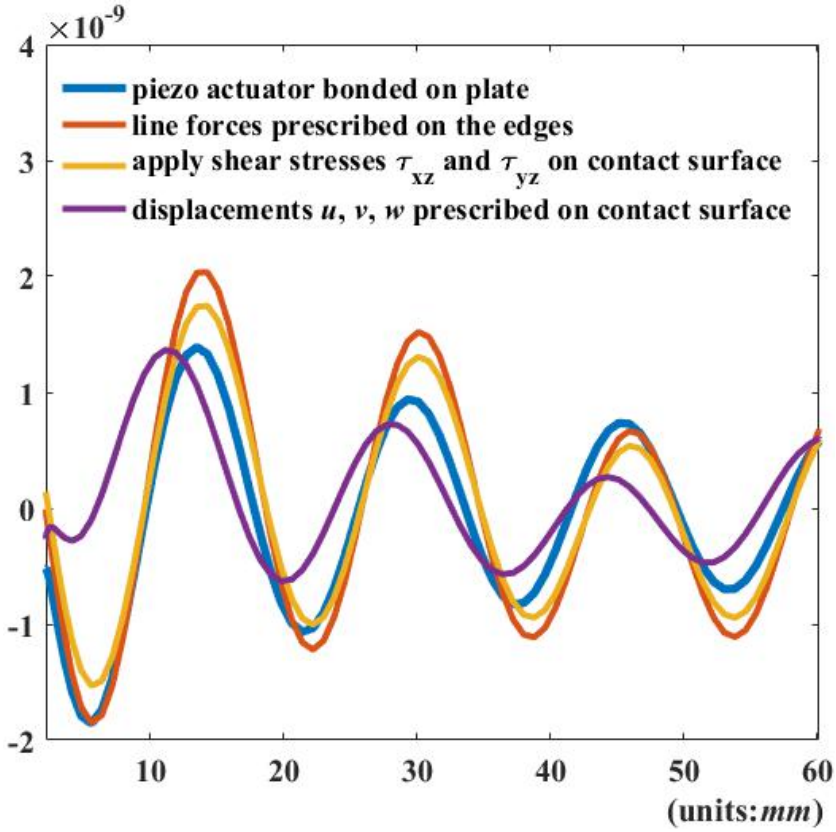
×10^-9
4
3
2
1
0
-1
-2
piezo actuator bonded on plate
line forces prescribed on the edges
apply shear stresses τxz and τyz on contact surface
displacements u, v, w prescribed on contact surface
10
20
30
40
50
60
(units:mm)

(b)

It can be seen that when only line load is applied, the plate has similar response compared with when an actuator is bonded on the plate upper surface in areas away from the actuator. However, in the area close to where the actuator is bonded, the plate response under line load is very different from when an actuator is bonded. This is because only applying line load on the peripheries would introduce a stress concentration at the peripheries. Besides, it can be seen that applying line load and applying shear stress renders almost identical results besides the areas near the actuator. Similar results can be seen on other monitoring lines.

In this thesis, the amplitudes of the stresses on contact surface is determined by matching the displacement of actuator and plate on the peripheries. Thus, it can be seen that applying shear stress would render a way better approximation compared with only applying line load.

5.6.7. Conclusions

In this Section, comparison of the plate response under four different excitation is conducted.

(1) surface bonded actuator;

(2) replacing the actuator with line loads on the peripheries of the rectangular actuator;

(3) replacing the actuator with shear stress τ_{zx} and τ_{zy} on the contact surface;

(4) replacing the actuator with prescribed displacement *u*, *v*, *w* on the contact surface.

The following conclusions can be drawn from the results obtained above:

(A) (3) represents the actuator the best compared to the other methods considered here.

(C) The plate response for '(2) replacing the actuator with line loads on the peripheries of the rectangular actuator;' is close to (3).

(D) (2) also represents the actuator with good approximations through (3) are slightly more accurate.

(A) '(4) replacing the actuator with prescribed displacement u, v, w on the contact surface' still renders the same waveform of plate response, but the deviation of it from the actuator scenario is relatively larger compared to other scenarios.

CHAPTER 6

Validation of Theoretical Model

6.1 Determination of polynomial coefficients for inter-facial shear stress

6.1.1 Review of PZT displacement under inter-facial shear stress and applied voltage

As discussed in Chapter 3, the polynomials used to approximate the inter-facial shear stress are:

$$\begin{aligned} \tau_{xz} &= a_1 x + a_2 x^3 \\ \tau_{yz} &= b_1 y + b_2 y^3 \end{aligned} \tag{6.1}$$

This will introduce 4 coefficients: a_1, a_2, b_1, b_2.

In chapter 3, the displacement of PZT actuator vibration is obtained by substituting Fourier series into equation of motion and using traction free boundary conditions. The expression of PZT displacement when considering only the first term of Fourier series is listed in Eq. (2.51) and Eq. (2.52), which is listed here:

$$\begin{aligned} u^a(x,y,\omega) &= A_{11} \sin\frac{\pi x}{a} \cos\frac{\pi y}{b}, \\ v^a(x,y,\omega) &= B_{11} \cos\frac{\pi x}{a} \sin\frac{\pi y}{b} \end{aligned} \tag{6.2}$$

where

$$A_{11}=-\frac{4\begin{pmatrix}-a^2\left(c_{12}^p+c_{66}\right)\pi^2\left(4b^2b_1\pi^2+4e_{31}^pE_zh_a\pi^4+3b^4b_2\left(-8+\pi^2\right)\right)\\+\left(4a^2a_1\pi^2+4e_{31}^pE_zh_a\pi^4+3a^4a_2\left(-8+\pi^2\right)\right)\left(b^2c_{66}\pi^2+a^2\left(c_{11}^p\pi^2-b^2\rho\omega^2\right)\right)\end{pmatrix}}{ah_a\pi^5\left(\left(c_{12}^p+c_{66}\right)^2\pi^4-a^2b^2\left(\frac{c_{11}^p\pi^2}{b^2}+\frac{c_{66}\pi^2}{a^2}-\rho\omega^2\right)\left(\frac{c_{11}^p\pi^2}{a^2}+\frac{c_{66}\pi^2}{b^2}-\rho\omega^2\right)\right)}$$

$$B_{11}=-\frac{4a^2b\begin{Bmatrix}-4a^2c_{66}e_{31}^pE_zh_a\pi^6-3b^6b_2\left(-8+\pi^2\right)\left(c_{11}^p\pi^2-a^2\rho\omega^2\right)\\+b^4\pi^2\left(-4b_1c_{11}^p\pi^2+a^2\left(-3b_2c_{66}\left(-8+\pi^2\right)+4b_1\rho\omega^2\right)\right)\\+b^2\pi^2\begin{bmatrix}4\left(-c_{11}^p+c_{12}^p+c_{66}\right)e_{31}^pE_zh_a\pi^4+3a^4a_2\left(c_{12}^p+c_{66}\right)\left(-8+\pi^2\right)\\+4a^2\pi^2\left(-b_1c_{66}+a_1\left(c_{12}^p+c_{66}\right)+e_{31}^pE_zh_a\rho\omega^2\right)\end{bmatrix}\end{Bmatrix}}{h_a\pi^5\begin{pmatrix}b^4c_{11}^pc_{66}\pi^4+a^4\left(c_{11}^p\pi^2-b^2\rho\omega^2\right)\left(c_{66}\pi^2-b^2\rho\omega^2\right)\\-a^2b^2\pi^2\left(-c_{11}^{p\,2}\pi^2+c_{12}^{p\,2}\pi^2+2c_{12}^pc_{66}\pi^2+b^2c_{11}^p\rho\omega^2+b^2c_{66}\rho\omega^2\right)\end{pmatrix}} \tag{6.3}$$

For the given material properties for PZT-5A and an applied voltage of 100*kHz* at $f=100kHz$, A_{11},B_{11} can be obtained in Matlab as:

$$\begin{aligned}A_{11}&=3.072\times10^{-16}a_1+6.984\times10^{-22}a_2-4.118\times10^{-16}b_1-3.744\times10^{-21}b_2-4.043\times10^{-11}\\B_{11}&=1.232\times10^{-15}a_1-4.681\times10^{-22}a_2-2.059\times10^{-16}b_1+1.121\times10^{-20}b_2-2.023\times10^{-11}\end{aligned} \tag{6.4}$$

6.1.2 Review of plate displacement under inter-facial shear stress

Under inter-facial shear stress loading, the plate will generate propagating and evanescent Lamb wave and *SH* waves. At $f=100kHz$, the propagating wave modes includes: A_0,S_0,SH_0. As discussed in hapter 5, for evanescent wave modes, only evanescent Lamb

$A_1, S_1 / S_2, A_2 / A_3, S_3 / S_4$ wave modes and shear horizontal SH_1, SH_2, SH_3, SH_4 wave modes. need to be taken into consideration at $f = 100kHz$.

The displacement form of wave modes under point load are given by carrier wave. The amplitudes of each mode are obtained by reciprocity theorem. The wave mode displacement under surface load is obtained by integrating the plate displacement under a point load over the entire contact surface.

6.1.3 Determining coefficients using displacement continuity

As can be seen in Eq. (6.1), the expression of inter-facial shear stress introduces four coefficients: a_1, a_2, b_1, b_2. In order to find the value of these four coefficients, displacement continuity on four points on the contact surface is used. Due to the symmetry of displacement, all the points are chosen in the first quadrant.

Case 1: Choosing 1 point in first quadrant:

Since the displacement is larger on the edges of the contact surface, the point is chosen to be towards the edge of the contact surface. The *x*-*y* coordinates of this point is $(1.96mm, 3.92mm)$. The location of the point is shown below:

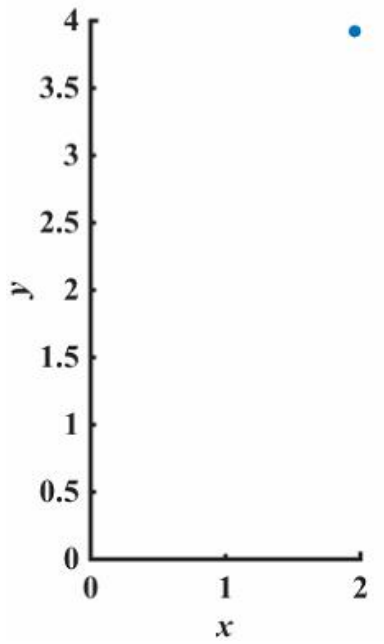

(units: *mm*)

Figure 6.1 The location of the 1 point chosen in first quadrant

By matching the displacement of actuator and plate on this point, the four coefficients can be obtained by using least square method:

$$
\begin{aligned}
LS &= (u_{plate}\big|_{at\ point\ n} - u_{pzt}\big|_{at\ point\ n})^2 + (v_{plate}\big|_{at\ point\ n} - v_{pzt}\big|_{at\ point\ n})^2 \\
&\frac{\partial}{\partial a_1} LS = 0 \\
&\frac{\partial}{\partial a_2} LS = 0 \\
&\frac{\partial}{\partial b_1} LS = 0 \\
&\frac{\partial}{\partial b_2} LS = 0
\end{aligned}
\tag{6.5}
$$

The displacements u, v at this point on the plate and on the PZT actuator can be calculated. Using Eq. (6.6) and the displacements listed in the above four tables, the results for the coefficients are obtained as:

$$
\begin{aligned}
a_1 &= -5.4054\times10^{8} \\
a_2 &= \ \ 5.8757\times10^{14} \\
b_1 &= \ \ 1.6619\times10^{8} \\
b_2 &= \ \ 1.4261\times10^{13}
\end{aligned}
\tag{6.6}
$$

Thus the analytical inter-facial shear stress is:

$$
\begin{aligned}
\tau_{xz} &= -5.4054\times10^{8}\,x + 5.8757\times10^{14}\,x^3 \\
\tau_{yz} &= \ \ 1.6619\times10^{8}\,y + 1.4261\times10^{13}\,y^3
\end{aligned}
\tag{6.7}
$$

The analytical inter-facial shear stress obtained from displacement continuity can be compared with the COMSOL result when a PZT actuator is mounted on the surface of the plate:

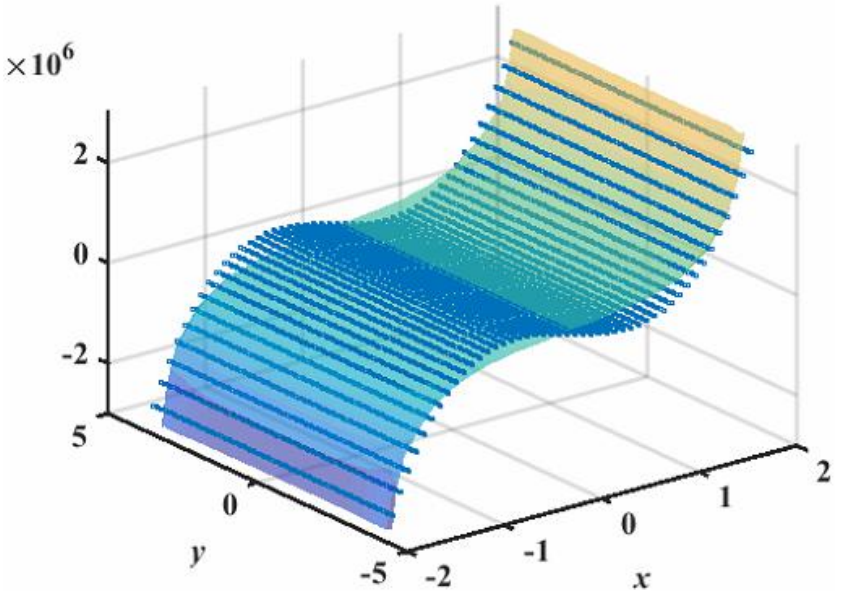

(units for *x*-*y* axis: *mm*)

(a)

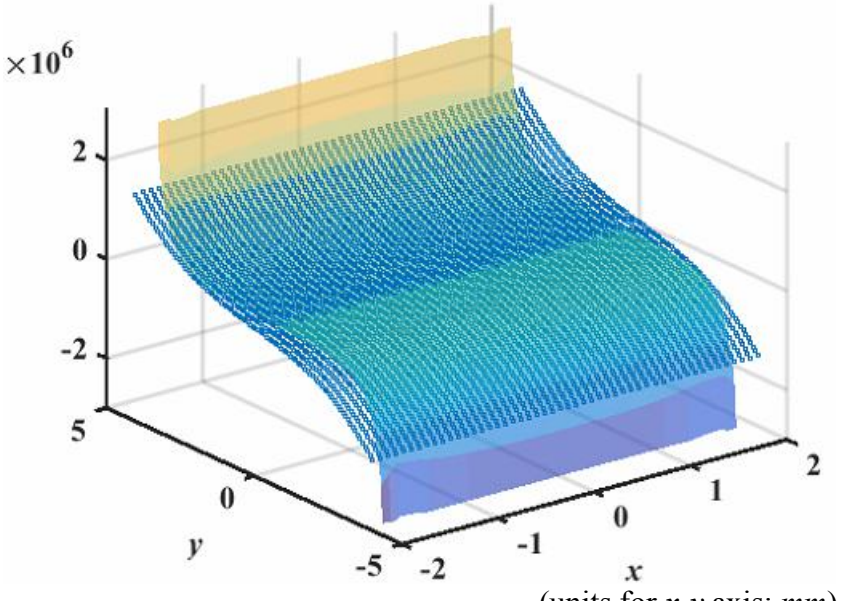

(units for *x*-*y* axis: *mm*)

(b)

Figure 6.2 Comparison of analytical (blue points) inter-facial shear stress (a) τ_{xz} and (b) τ_{yz} obtained from displacement continuity at 1 point with FEA result (colored surface)

From the above result, it can be seen that the stress τ_{xz} term matches well, but τ_{yz} term does not match well towards the edges. Thus more, points are needed for a more accurate match.

Case 2: Choosing 3×3 point in first quadrant:

The 3×3 points are evenly distributed over the entire first quadrant, as shown below:

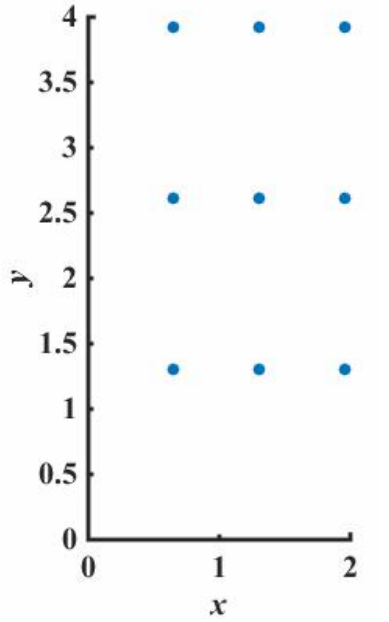

(units: *mm*)

Figure 6.3 The location of the 3×3 points chosen in first quadrant

The coordinates of the 3×3 points are:

Table 6.1 Coordinates of the 3×3 points used to calculate shear stress coefficients

x coordinates (*mm*)	*y* coordinates (*mm*)
0.6533	1.3067
0.6533	2.6133
0.6533	3.9200

1.3067	1.3067
1.3067	2.6133
1.3067	3.9200
1.9600	1.3067
1.9600	2.6133
1.9600	3.9200

Similarly, by matching the displacement of actuator and plate on these 3×3 points, the four coefficients can be obtained by using least square method.

Using the displacements at the nine points, the results for the coefficients are obtained as:

$$\begin{aligned} a_1 &= \ 3.2484\times10^{8} \\ a_2 &= \ 1.9488\times10^{14} \\ b_1 &= -5.2439\times10^{8} \\ b_2 &= \ 8.5942\times10^{13} \end{aligned} \tag{6.8}$$

Thus the analytical inter-facial shear stress is:

$$\begin{aligned} \tau_{xz} &= \ 3.2484\times10^{8}\,x + 1.9488\times10^{14}\,x^{3} \\ \tau_{yz} &= -5.2439\times10^{8}\,y + 8.5942\times10^{13}\,y^{3} \end{aligned} \tag{6.9}$$

The analytical inter-facial shear stress obtained from displacement continuity can be compared with the COMSOL result when a PZT actuator is mounted on the surface of the plate:

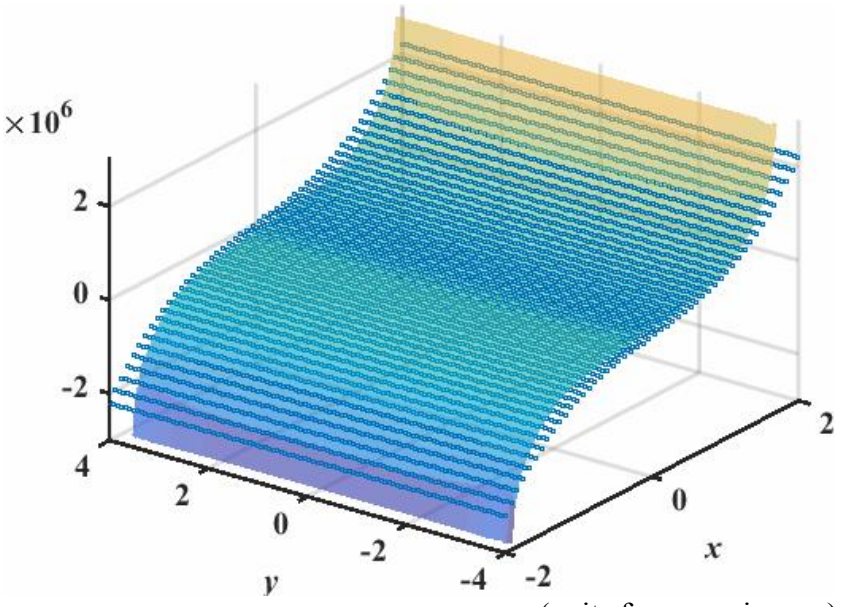

(units for *x*-*y* axis: *mm*)

(a)

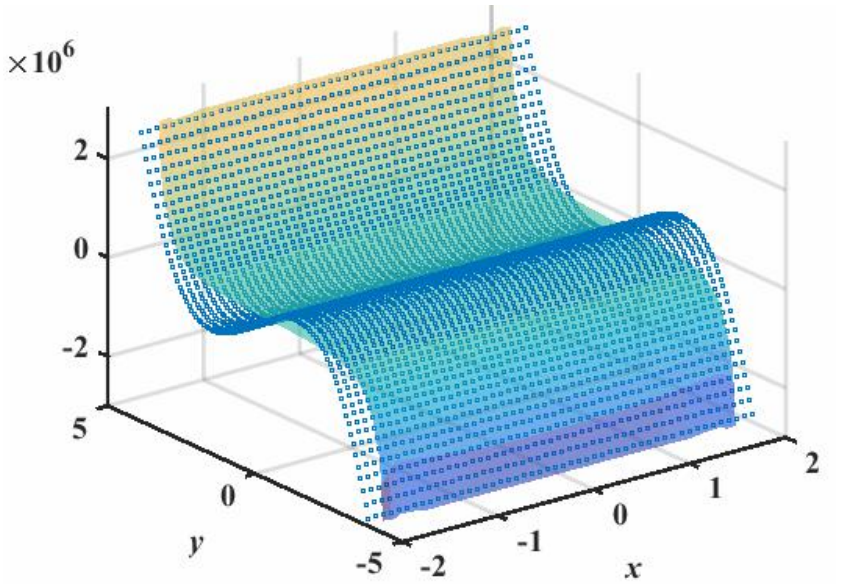

(units for *x*-*y* axis: *mm*)

(b)

Figure 6.4 Comparison of analytical (blue points) inter-facial shear stress (a) τ_{xz} and (b) τ_{yz} obtained from displacement continuity at 3×3 points with FEA result (colored surface)

Comparing with the first case, the 3×3 points case renders better match for τ_{yz}. This shows that the more point chosen to compare the displacement, the better match for inter-facial stress will render.

Case 3: Choosing 4×4 point in first quadrant:

The 4×4 points are evenly distributed over the entire first quadrant, as shown below:

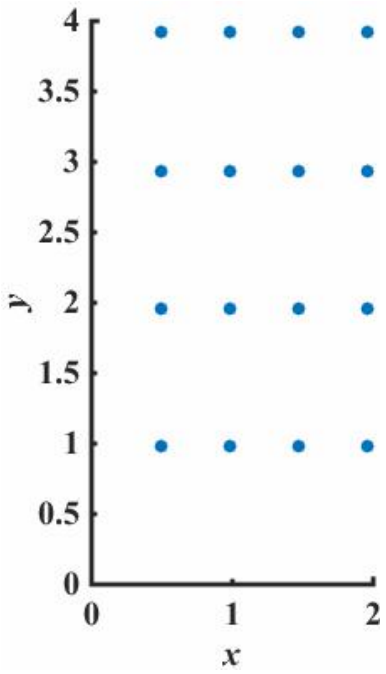

(units: *mm*)

Figure 6.5 The location of the 4×4 points chosen in first quadrant

The coordinates of the 4×4 points are:

Table 6.2 Coordinates of the 4×4 points used to calculate shear stress coefficients

x coordinates (*mm*)	*y* coordinates (*mm*)
0.4900	0.9800
0.4900	1.9600
0.4900	2.9400
0.4900	3.9200
0.9800	0.9800
0.9800	1.9600
0.9800	2.9400
0.9800	3.9200
1.4700	0.9800
1.4700	1.9600
1.4700	2.9400
1.4700	3.9200
1.9600	0.9800
1.9600	1.9600
1.9600	2.9400
1.9600	3.9200

Similarly, by matching the displacement of actuator and plate on these 4×4 points, the four coefficients can be obtained by using least square method.

Using the displacements at the 4×4 points, the results for the coefficients are obtained as:

$$\begin{aligned} a_1 &= 2.5663\times10^{8} \\ a_2 &= 2.2316\times10^{14} \\ b_1 &= -4.3038\times10^{8} \\ b_2 &= 7.5475\times10^{13} \end{aligned} \tag{6.10}$$

Thus the analytical inter-facial shear stress is:

$$\begin{aligned} \tau_{xz} &= \quad 2.5663\times10^{8}x + 2.2316\times10^{14}x^{3} \\ \tau_{yz} &= -4.3038\times10^{8}y + 7.5475\times10^{13}y^{3} \end{aligned} \tag{6.11}$$

The analytical inter-facial shear stress obtained from displacement continuity can be compared with the COMSOL result when a PZT actuator is mounted on the surface of the plate:

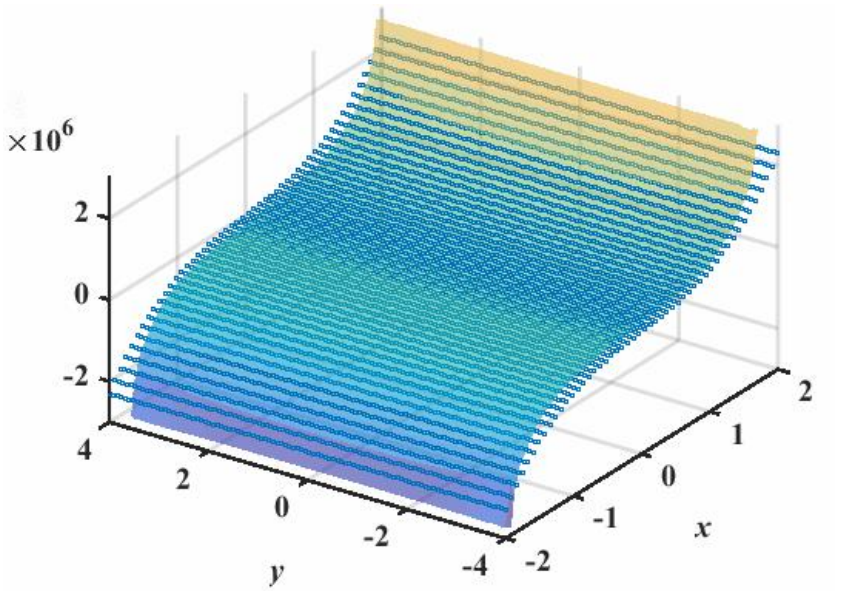

(units for *x*-*y* axis: *mm*)

(a)

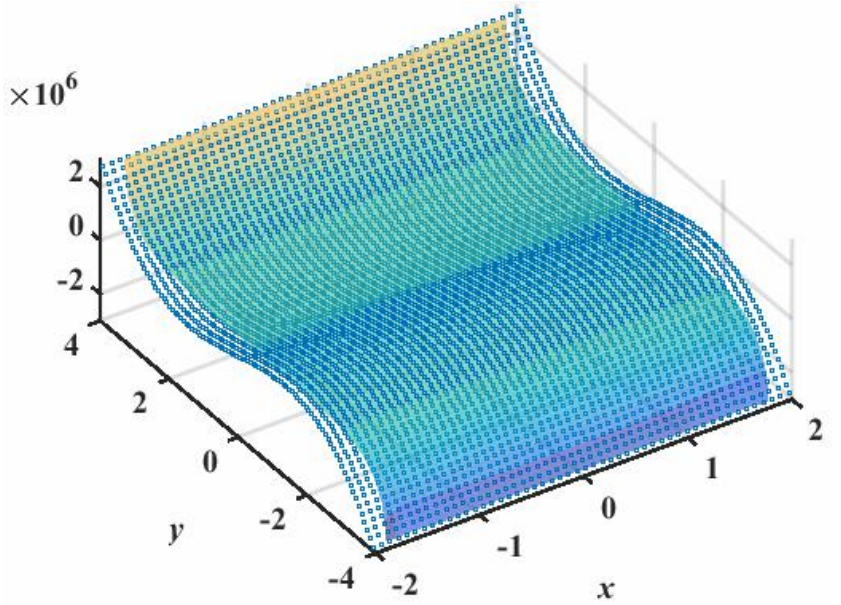

(units for *x*-*y* axis: *mm*)

(b)

Figure 6.6 Comparison of analytical (blue points) inter-facial shear stress (a) τ_{xz} and (b) τ_{yz} obtained from displacement continuity at 4×4 points with FEA result (colored surface)

Comparing with the 3×3 case, the 4×4 points case renders better match for both stress components . This again verifies that the more point chosen to compare the displacement, the better match for inter-facial stress will render.

Case 4: Choosing 7×7 point in first quadrant:

The **7×7** points are evenly distributed over the entire first quadrant, as shown below:

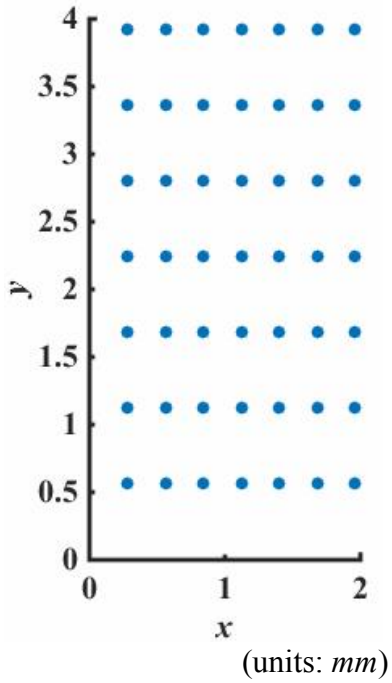

(units: *mm*)

Figure 6.7 The location of the 7×7 points chosen in first quadrant

The coordinates of the 7×7 points are:

Table 6.3 Coordinates of the 7×7 points used to calculate shear stress coefficients

x coordinates (*mm*)	*y* coordinates (*mm*)
0.2800	0.5600
0.2800	1.1200
0.2800	1.6800
0.2800	2.2400
0.2800	2.8000
0.2800	3.3600
0.2800	3.9200
0.5600	0.5600
0.5600	1.1200
0.5600	1.6800
0.5600	2.2400
0.5600	2.8000
0.5600	3.3600
0.5600	3.9200
0.8400	0.5600
0.8400	1.1200
0.8400	1.6800
0.8400	2.2400
0.8400	2.8000
0.8400	3.3600
0.8400	3.9200
1.1200	0.5600
1.1200	1.1200
1.1200	1.6800
1.1200	2.2400
1.1200	2.8000
1.1200	3.3600
1.1200	3.9200
1.4000	0.5600
1.4000	1.1200
1.4000	1.6800
1.4000	2.2400
1.4000	2.8000
1.4000	3.3600
1.4000	3.9200
1.6800	0.5600
1.6800	1.1200
1.6800	1.6800
1.6800	2.2400
1.6800	2.8000

Table 6.3 Continued

x coordinates (mm)	y coordinates (mm)
1.6800	3.3600
1.6800	3.9200
1.9600	0.5600
1.9600	1.1200
1.9600	1.6800
1.9600	2.2400
1.9600	2.8000
1.9600	3.3600
1.9600	3.9200

Similarly, by matching the displacement of actuator and plate on these 7×7 points, the four coefficients can be obtained by using least square method.

Using the displacements at the 7×7 points, the results for the coefficients are obtained as:

$$\begin{aligned} a_1 &= 5.8292\times10^{8} \\ a_2 &= 3.1635\times10^{14} \\ b_1 &= -3.7996\times10^{8} \\ b_2 &= 6.9548\times10^{13} \end{aligned} \tag{6.12}$$

Thus the analytical inter-facial shear stress is:

$$\begin{aligned} \tau_{xz} &= 5.8292\times10^{8}x + 3.1635\times10^{14}x^3 \\ \tau_{yz} &= -3.7996\times10^{8}y + 6.9548\times10^{13}y^3 \end{aligned} \tag{6.13}$$

The analytical inter-facial shear stress obtained from displacement continuity can be compared with the COMSOL result when a PZT actuator is mounted on the surface of the plate:

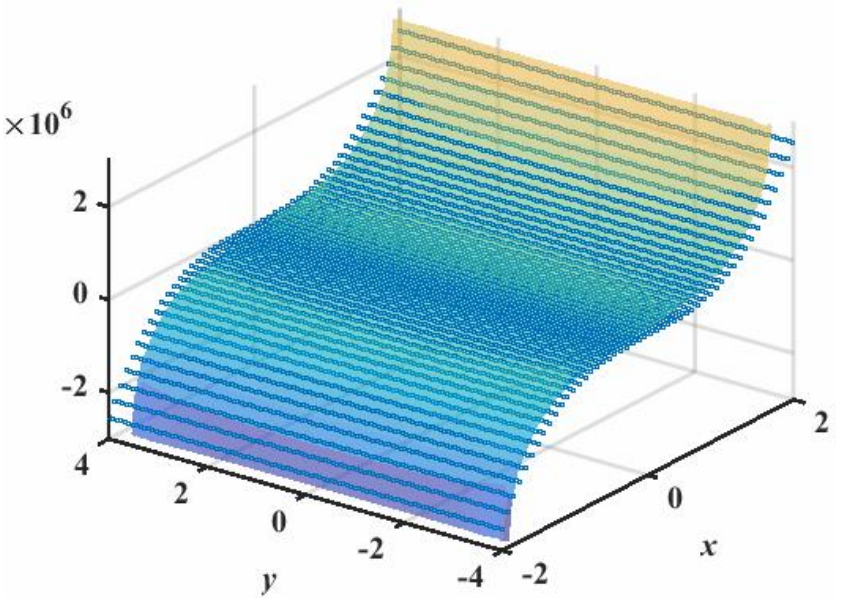

(units for *x*-*y* axis: mm)

(a)

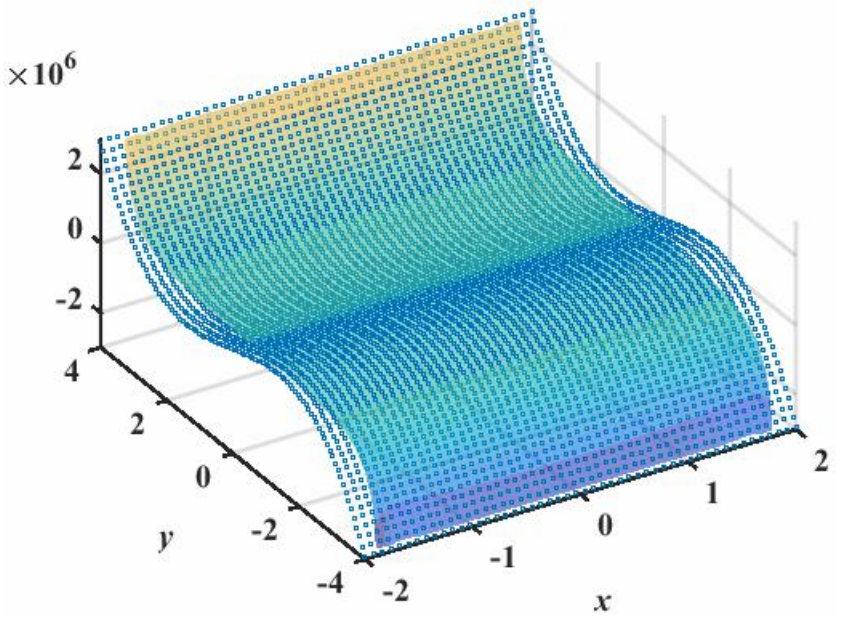

(units for *x*-*y* axis: mm)

(b)

Figure 6.8 Comparison of analytical (blue points) inter-facial shear stress (a) τ_{xz} and (b) τ_{yz} obtained from displacement continuity at 7×7 points with FEA result (colored surface)

Comparing with the 4×4 case, the 7×7 points case renders almost similar result when comparing inter-facial stress with FEA result. This shows that the 4×4 case, in which 16 evenly distributed points are chosen in the first quadrant, leads to an acceptable result.

6.2 Validation of theoretical plate wave with FEA results

The following study is conducted at frequency $f = 100kHz$. The thickness of the aluminum plate is 3.2mm. The *x*-*y* plane is set to be the middle layer of the plate. The width of the PML is 1/2 of the maximum wavelength at the given frequency. The PML parameters are set to be the SF = 2, SCP = 3 as well.

In order to have a comparison of the plate displacement in COMSOL with the plate displacement with the give stress function in Eq. (6.13), four monitoring lines are chosen, as listed below:

Line I: along *x* axis;

Line II: along atan(1/2) with respect to *x* axis;

Line III: along 45^{o} with respect to *x* axis;

Line IV: along atan(2) with respect to *x* axis.

The displacement on these four monitoring lines obtained by using the stress function with COMSOL results are compared below:

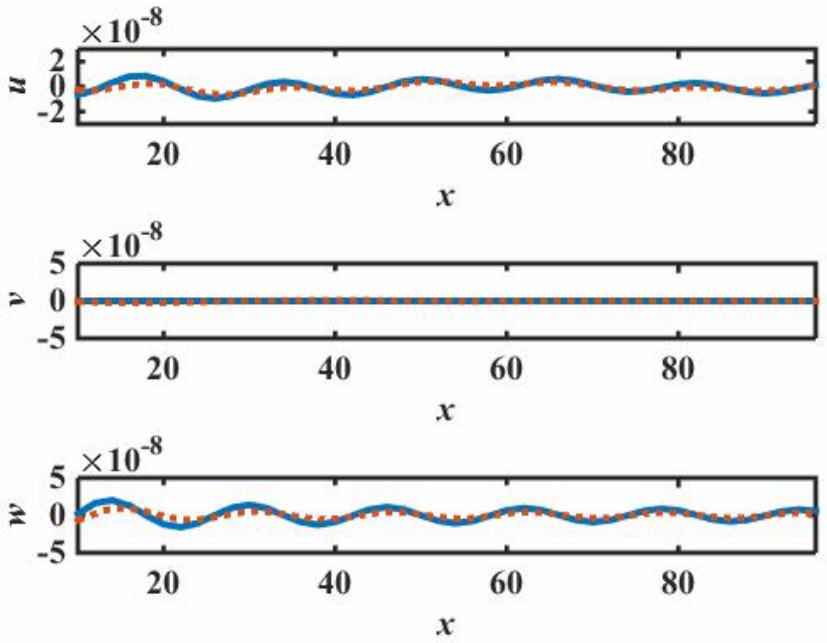

(units for *x* axis: *mm*)

Figure 6.9 Displacement comparison along *x* axis (line I); blue line: analytical solution based on shear stress coefficients obtained from displacement continuity, red dot: COMSOL result

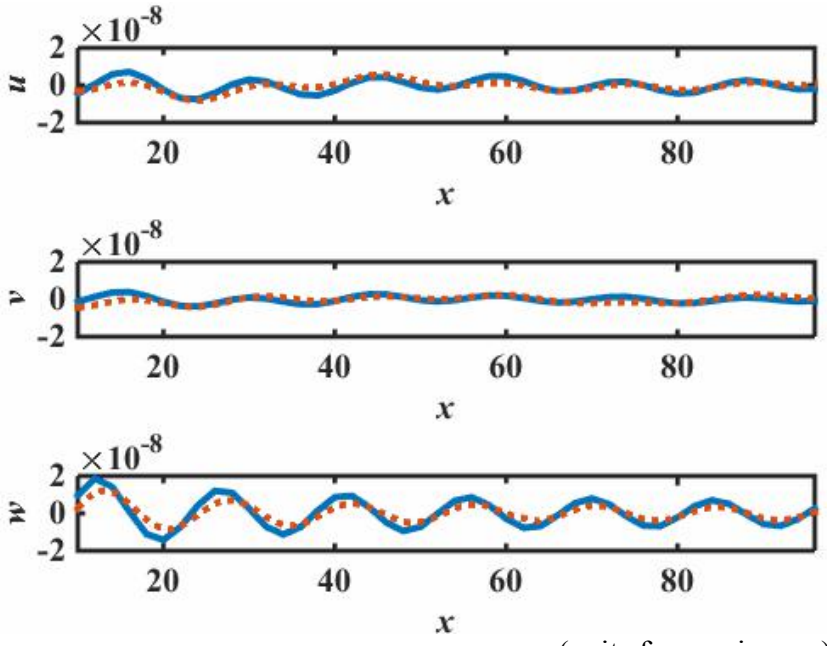

(units for *x* axis: *mm*)

Figure 6.10 Displacement comparison along atan(1/2) with respect to *x* axis (on line II); blue line: analytical solution based on shear stress coefficients obtained from displacement continuity, red dot: COMSOL result

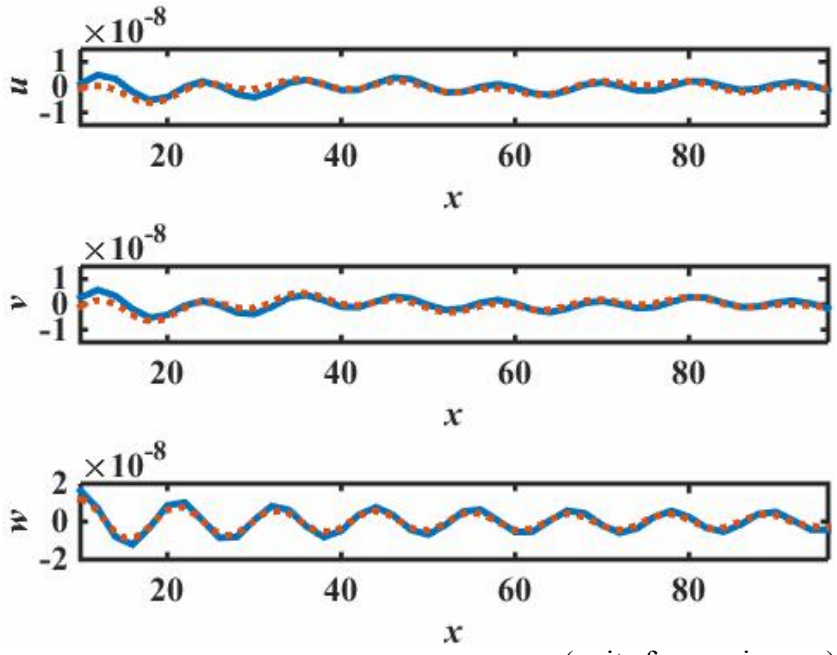

(units for *x* axis: *mm*)

Figure 6.11 Displacement comparison along 45^{o} with respect to *x* axis (on line III); blue line: analytical solution based on shear stress coefficients obtained from displacement continuity, red dot: COMSOL result

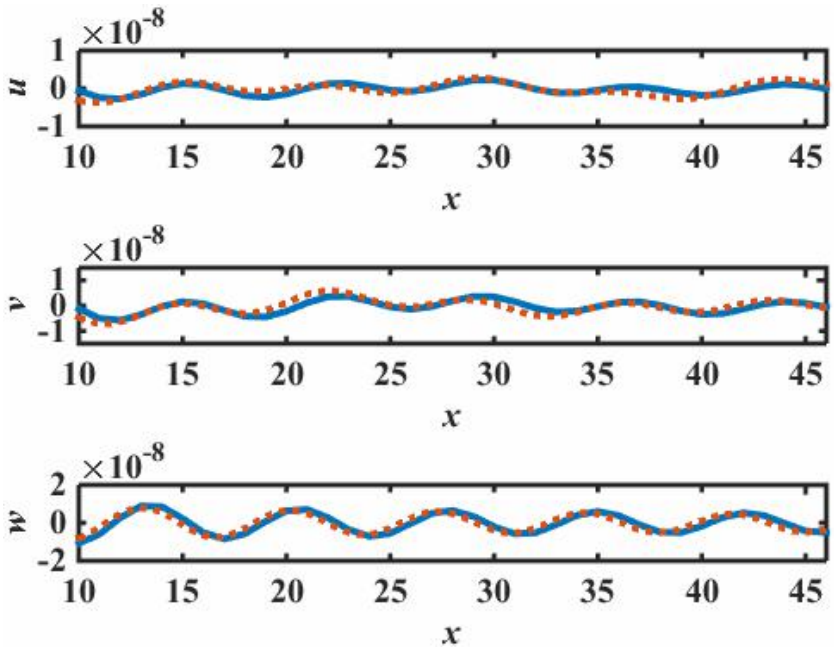

(units for *x* axis: *mm*)

Figure 6.12 Displacement comparison along atan(2) with respect to *x* axis (on line IV); blue line: analytical solution based on shear stress coefficients obtained from displacement continuity, red dot: COMSOL result

As can be seen, the analytical result matches pretty well with COMSOL result. This verifies the method of matching inter-facial displacement to obtain the stress coefficients.

CHAPTER 7

Sensor Response

7.1 Analytical model for sensor response - open circuit model

[Insert your main body text here. Organization and format depends on your style guide.]

Piezoelectric transducers directly convert the mechanical stress and strain energy into electrical energy, thus it can also be used for stress and strain sensing. The piezoelectric constitutive equations are

$$\begin{aligned} &\text{direct piezoelectric effect:} \quad D_i = d_{ikl}\sigma_{kl} + \epsilon_{ik}^{\sigma}\mathbb{E}_k \\ &\text{converse piezoelectric effect:} \quad \sigma_{ij} = c_{ijkl}^{E}\varepsilon_{kl} - e_{kij}\mathbb{E}_k \end{aligned} \tag{7.1}$$

where $c_{ijkl}^{E}, e_{kij}, \epsilon_{ik}^{\varepsilon}$ are the elastic, piezoelectric and dielectric constants (relative permittivity) respectively. The superscripts E, σ denote the properties are under conditions of constant elastic field and constant stress respectively.

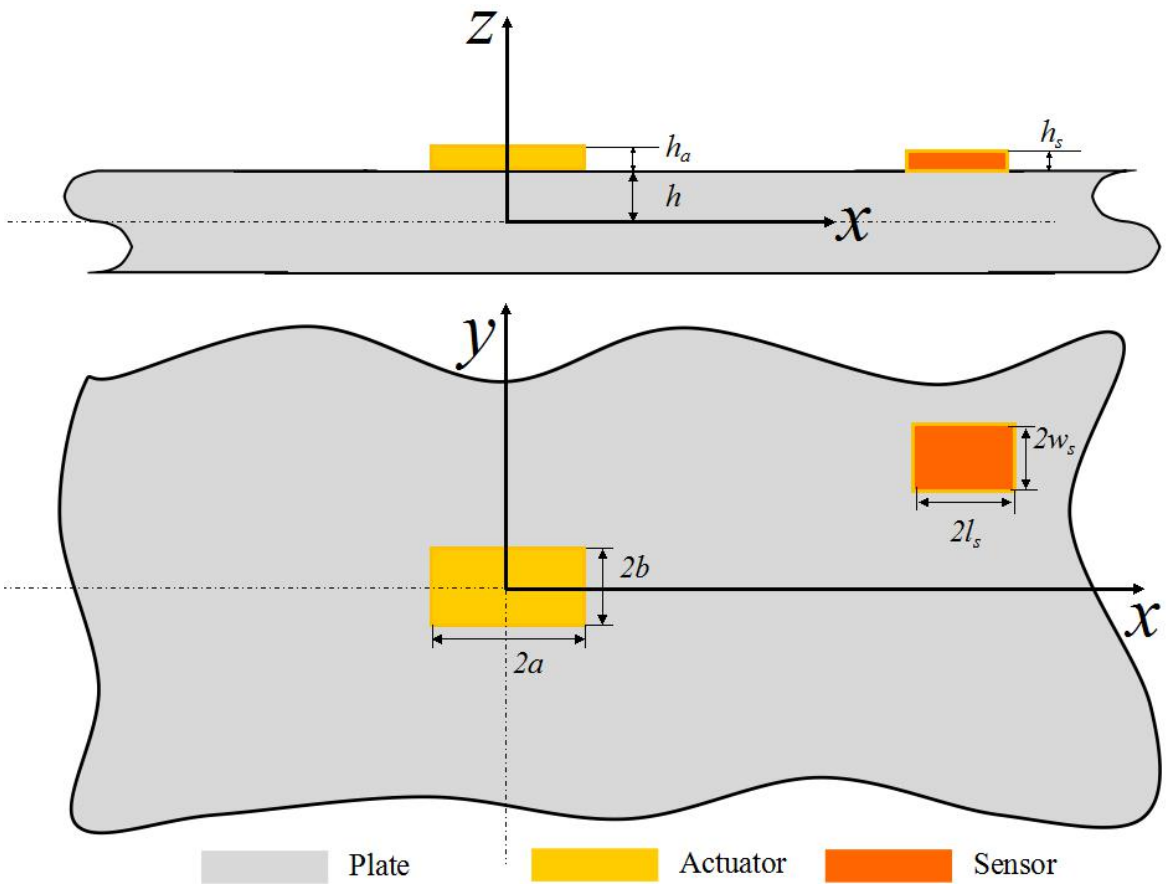

Figure 7.1 Side and top view of the actuator bonded on an aluminum plate of infinite length in x - y plane

Considering a thin, rectangular surface-bonded transverse isotropic piezoelectric sensor of 3-1 mode. The PZT sensor has a length $2l_s$ along x direction, a width $2w_s$ along y direction and a height h_s along z direction. For a PZT sensor which is thin enough, it can be seen as of ***plane stress*** condition, thus $\sigma_{13} = \sigma_{23} = \sigma_{33} = 0$ .The electric displacement field components $D_1 = D_2 = 0$. Substituting Eq. (7.1-2) into Eq. (7.1-1) yields

$$D_3 = d_{3ij}(c^E_{ijkl}\varepsilon_{kl} - e_{kij}E_k) + \epsilon^{\sigma}_{33}E_3 \tag{7.2}$$

Recalling that $e_{ip} = d_{iq} c^E_{qp}$, the above equation becomes

$$D_3 = d_{3ij}(c^E_{ijkl}\varepsilon_{kl} - d_{kmn}c^E_{mnij}E_k) + \epsilon^\sigma_{33}E_3$$

In matrix form, the above tensor form can be written as

$$D_3 = \begin{bmatrix} d_{31} & d_{32} & 0 \end{bmatrix} \begin{bmatrix} c^p_{11} & c^p_{12} & 0 \\ c^p_{12} & c^p_{11} & 0 \\ 0 & 0 & c_{66} \end{bmatrix} \left(\begin{bmatrix} \varepsilon_{11} \\ \varepsilon_{22} \\ \gamma_{12} \end{bmatrix} - E_3 \begin{bmatrix} d_{31} \\ d_{32} \\ 0 \end{bmatrix} \right) + \epsilon^\sigma_{33}E_3 \tag{7.3}$$

For transverse isotropic piezoelectric material, the piezoelectric constants $d_{31} = d_{32}$. Upon expanding, Eq. (7.3) becomes

$$D_3 = d_{31}(c^p_{11} + c^p_{12})(\varepsilon_{11} + \varepsilon_{22}) - [2d^2_{31}(c^p_{11} + c^p_{12}) - \epsilon^\sigma_{33}]E_3 \tag{7.4}$$

Considering the open-circuit boundary condition of the PZT sensor, the total charge over the electrode area is zero, thus

$$\iint D_3 dxdy = 0 \tag{7.5}$$

Substituting Eq. (7.4) into Eq. (7.5) yields

$$\iint \left\{ d_{31}(c^p_{11} + c^p_{12})(\varepsilon_{11} + \varepsilon_{22}) - [2d^2_{31}(c^p_{11} + c^p_{12}) - \epsilon^\sigma_{33}]E_3 \right\} dxdy = 0$$

which can be transformed to

$$\begin{aligned} \iint E_3 dxdy &= \iint \frac{d_{31}(c^p_{11} + c^p_{12})(\varepsilon_{11} + \varepsilon_{22})}{2d^2_{31}(c^p_{11} + c^p_{12}) - \epsilon^\sigma_{33}} dxdy \\ &= \frac{d_{31}(c^p_{11} + c^p_{12})}{2d^2_{31}(c^p_{11} + c^p_{12}) - \epsilon^\sigma_{33}} \iint (\varepsilon_{11} + \varepsilon_{22}) dxdy \end{aligned} \tag{7.6}$$

The voltage on the sensor is the integration of electric field over the entire volume:

$$V = -\frac{\iiint E_3 dxdydz}{4l_s w_s} \tag{7.7}$$

Substituting Eq. (7.6) into Eq. (7.7) yields

$$V = \frac{d_{31}(c_{11}^p + c_{12}^p)\iiint(\varepsilon_{11} + \varepsilon_{22})dxdydz}{4l_s w_s\left[\epsilon_{33}^\sigma - 2d_{31}^2(c_{11}^p + c_{12}^p)\right]} \tag{7.8}$$

If modeling the sensor as plane stress, the strain distribution overt the thickness direction will just be the same, thus Eq. (7.8) can be simplified to:

$$V = \frac{h_s d_{31}(c_{11}^p + c_{12}^p)\iint(\varepsilon_{11} + \varepsilon_{22})dxdy}{4l_s w_s\left[\epsilon_{33}^\sigma - 2d_{31}^2(c_{11}^p + c_{12}^p)\right]} \tag{7.9}$$

It can be seen from Eq. (7.8) that the resulting voltage is proportional to the strain rate. After substituting the strain field of Lamb wave and *SH* wave on plate into Eq. (7.9), the voltage response on the sensor can be obtained. It was assumed that the existence of the sensor does not significantly affect the strain field on plate.

7.2 Verification of open circuit model in COMSOL

In order to verify the equation used to solve voltage output in piezoelectric sensor expressed in Eq. (7.8), we conducted this study in COMSOL:

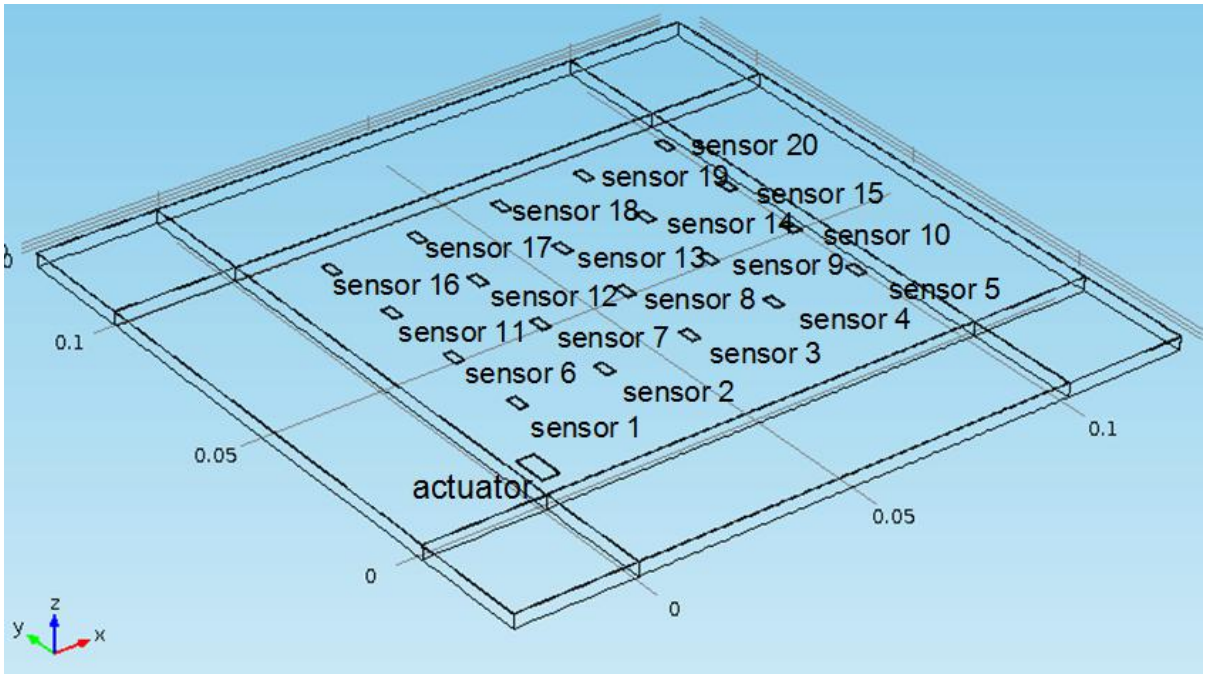

Figure 7.2 Configuration of 20 sensors on plate upper surface

In this Model, there is a PZT actuator (located at the left bottom corner in the above figure) and an array of 20 PZT sensors mounted on the upper surface of the aluminum plate. With a voltage input on the actuator the sensor voltage ouput and strain integration can be obtained. Based on the strain integration, using Eq. (7.8), the analytical voltage ouput can be obtained and compared with the COMSOL result of voltage. The result is listed here:

Table 7.1 Comparison of sensor result with FEA result

Sensor number	$x-y$ coordinates of sensor center	$\iiint(\varepsilon_{11}+\varepsilon_{22})dxdydz$	Analytical voltage based on Eq. (7.8)	COMSOL result for voltage output	Error between analytical voltage and COMSOL result
1	(10mm, 20mm)	-1.76642e-15	0.37	0.36	2.8772%
2	(30mm, 20mm)	-1.0404e-15	0.22	0.21	3.8744%
3	(50mm, 20mm)	-9.65957e-16	0.20	0.2	1.2641%
4	(70mm, 20mm)	-2.5716e-16	0.05	0.05	7.8353%
5	(90mm, 20mm)	7.88395e-16	-0.16	-0.16	3.3122%
6	(10mm, 40mm)	-6.8e-17	0.01	0.01	0%
7	(30mm, 40mm)	-6.5e-17	0.01	0.01	0%
8	(50mm, 40mm)	4.21491e-16	-0.0884	-0.09	-1.8086%
9	(70mm, 40mm)	1.28135e-16	-0.03	-0.03	0%
10	(90mm, 40mm)	-3.6617e-16	0.07	0.07	0%
11	(10mm, 60mm)	9.26058e-16	-0.1942	-0.19	2.1909%
12	(30mm, 60mm)	-6.27952e-16	0.1317	0.13	1.2770%
13	(50mm, 60mm)	6.89456e-16	-0.1446	-0.14	3.29%
14	(70mm, 60mm)	7.8324e-16	-0.1642	-0.16	2.6367%
15	(90mm, 60mm)	7.6061e-16	-0.1595	-0.16	-0.3288%
16	(10mm, 80mm)	1.16631e-16	-0.02	-0.02	0%
17	(30mm, 80mm)	-8.27671e-16	0.1735	0.17	2.0790%
18	(50mm, 80mm)	7.79605e-16	-0.1635	-0.16	2.1603%
19	(70mm, 80mm)	4.41765e-16	-0.0926	-0.09	2.9145%
20	(90mm, 80mm)	-1.50237e-16	0.03	0.03	0%

From this table, it can be seen that the equation used to calculate sensor output voltage is correct.

CHAPTER 8

Discussion and Conclusions

8.1 Review of the dissertation

This dissertation has developed a theoretical method for predicting the surface bonded PZT sensor output when a voltage is applied to surface bonded PZT actuator on an isotropic plate. The analytical solution is verified to with FEA result obtained in COMSOL. The approaches are threefold:

(1) Obtain analytical solution for rectangular PZT actuator response under prescribed harmonic/transient voltage;

(2) Obtain analytical solution for 3-D Lamb wave solution induced by surface bonded PZT actuator including propagating and evanescent waves;

(3) Obtain analytical solution for surface-bonded rectangular PZT sensor response.

The whole dissertation can be summarized as below:

In Chapter 1, the motivation of this research is discussed, then a literature review of previous methods used to model PZT actuator and plate wave is conducted.

In Chapter 2, a theoretical background of guided wave in plates is briefly discussed. Lamb wave and *SH* wave characterization and dispersion relation is discussed.

In Chapter 3, a theoretical model for propagating plate waves and its validation is shown. First, carrier wave approach is introduced to describe the general wave form for Lamb and *SH* waves. Then, elastodynamic reciprocity is used to determine the coefficients of

each wave mode under a single point load. The analytical derivation is verified by comparing the analytical result of plate wave under a point load, line load and surface load with FEA result respectively. The analytical results matches well with FEA results, which verifies the analytical derivation for propagating wave amplitude under point load on plate upper surface.

In Chapter 4, theoretical model for evanescent plate waves and its validation is shown. First, a brief introduction of evanescent waves is given. Then, based on complex reciprocity theorem, the coefficients for evanescent Lamb and *SH* wave modes are calculated. The theoretical solution for evanescent wave modes is verified by comparing the near field analytical plate displacement with FEA results under two different loading scenarios: a polynomial surface loading and a Gaussian surface loading. The comparison verifies the correctness of the theoretical derivation for evanescent plate wave amplitude under loading on plate upper surface.

In Chapter 5, theoretical model for rectangular actuator vibration is described. First, the equation of motion (EOM) for the surface bonded actuator with voltage input is given. The form of the EOM is a pair of inhomogeneous coupled partial differential equations. The general solution of the PZT actuator EOM is obtained using superposition methods. The particular solution of the EOM is also solved. Then, the coefficients in the total solution for PZT actuator displacement is determined using boundary conditions. The theoretical model for PZT actuator displacement is verified by comparing to FEA result.

In Chapter 6, the displacement continuity of PZT actuator and plate on the contact surface is used to determine the polynomial coefficients of inter-facial shear stresses. The result is also verified with FEA result.

In Chapter 7, the surface bonded sensor response is solved by means of open-circuit model.

8.2 Conclusions

The objective of this dissertation is to provide analytical solutions for the interaction between rectangular PZT actuator/sensor and plate through electro-mechanical coupling. The approaches are threefold:

(1) Obtain analytical solution for rectangular PZT actuator response under prescribed harmonic/transient voltage;

(2) Obtain analytical solution for 3-D Lamb wave solution induced by surface bonded PZT actuator including propagating and evanescent waves;

(3) Obtain analytical solution for surface-bonded rectangular PZT sensor response.

Three major contributions beyond previous work are achieved in this thesis:

(1) Previously, this problem has been addressed by determining the stress induced by actuator as a normalized value, thus the result for plate strain is also a normalized value instead of the actual value (Raghavana and Cesnik, 2004). Whereas in this thesis, since the

actual stress is obtained through displacement continuity, the plate strain can be obtained as the actual value.

(2) Besides, when considering plate displacement, previous endeavors only consider the propagating waves (Wang and Huang, 2001). However, it is proved in this thesis that evanescent waves must be taken into account when comparing the near-field plate displacement with PZT actuator displacement. The amplitudes of evanescent wave modes are calculated using complex reciprocity theorem.

(3) Previously, the problem is only analyzed in one-dimensional, which includes asymmetrical case for circular PZT actuator and plane strain case with infinitely long PZT beam. In this thesis, two dimensional PZT vibration problem is solved and three dimensional plate wave propagation is obtained.

REFERENCES

Achenbach, J. D. (1975). *Wave propagation in elastic solids*. Amsterdam ; New York: Elsevier. Retrieved from http://www2.lib.ncsu.edu/catalog/record/NCSU1673020

Achenbach, J. D. (1998). Lamb waves as thickness vibrations superimposed on a membrane carrier wave. *Journal of the Acoustical Society of America, 103*(5), 2283-6. doi:10.1121/1.422746

ANSYS, I. (2013). ANSYS mechanical APDL element reference.

Boukabache, H., Escriba, C., and Fourniols, J. -. (2014). Toward smart aerospace structures: Design of a piezoelectric sensor and its analog interface for flaw detection. *Sensors, 14*(11), 20543-61. doi:10.3390/s141120543

Chaudhry, Z., and Rogers, C. A. (1994). The pin-force model revisited. *Journal of Intelligent Material Systems and Structures, 5*(3), 347-54. doi:10.1177/1045389X9400500307

Crawley, E. F., and de Luis, J. (1987). Use of piezoelectric actuators as elements of intelligent structures. *AIAA Journal, 25*(10), 1373-85. doi:10.2514/3.9792

Dawe, D. J., and Roufaeil, O. L. (1980). Rayleigh-ritz vibration analysis of mindlin plates. *Journal of Sound and Vibration, 69*(3), 345-59. doi:10.1016/0022-460X(80)90477-0

di Scalea, F. L., Matt, H., and Bartoli, I. (2007). The response of rectangular piezoelectric sensors to rayleigh and lamb ultrasonic waves. *Journal of the Acoustical Society of America, 121*(1), 175-87. doi:10.1121/1.2400668

Duquenne, L., Moulin, E., Assaad, J., and Grondel, S. (2004). Transient modeling of lamb waves generated in viscoelastic materials by surface bonded piezoelectric transducers. *Journal of the Acoustical Society of America, 116*(1), 133-41. doi:10.1121/1.1760109

Gazis, D. C. (1958). Exact analysis of the plane-strain vibrations of thick-walled hollow cylinders. *The Journal of the Acoustical Society of America, 30*, 786-94.

Giurgiutiu, V. (2003). Lamb wave generation with piezoelectric wafer active sensors for structural health monitoring. Paper presented at the *Smart Structures and Integrated Systems, , 5056.* pp. 111-22. doi:10.1117/12.483492

Giurgiutiu, V. (2005). Tuned lamb wave excitation and detection with piezoelectric wafer active sensors for structural health monitoring. *Journal of Intelligent Material Systems and Structures, 16*(4), 291-305. doi:10.1177/1045389X05050106

Giurgiutiu, V. (2008). *Structural health monitoring with piezoelectric wafer active sensors*. Amsterdam ; Boston: Academic Press. Retrieved from http://www2.lib.ncsu.edu/catalog/record/NCSU2046168

Giurgiutiu, V. (2014). *Structural health monitoring with piezoelectric wafer active sensors electronic resource]*. Amsterdam: Academic Press, an imprint of Elsevier. Retrieved from http://www2.lib.ncsu.edu/catalog/record/NCSU3536579; Get an online version (NCSU only) (http://proxying.lib.ncsu.edu/index.php?url=http://www.sciencedirect.com/science/book/9780124186910)

Glushkov, E. V., Glushkova, N. V., Kvasha, O. V., and Lammering, R. (2010). Selective lamb mode excitation by piezoelectric coaxial ring actuators. *Smart Materials and Structures, 19*(3), 035018 (7 pp.). doi:10.1088/0964-1726/19/3/035018

Gonzalez, A. M., and Alemany, C. (1996). Determination of the frequency dependence of characteristic constants in lossy piezoelectric materials. Paper presented at the *International Workshop on New Magnetic Materials, , 29.* (9) pp. 2476-82. doi:10.1088/0022-3727/29/9/037

Gorman, D. J. (2004). Free in-plane vibration analysis of rectangular plates by the method of superposition. *Journal of Sound and Vibration, 272*(3-5), 831-51. doi:10.1016/S0022-460X(03)00421-8

Han, S., Palazotto, A. N., and Leakeas, C. L. (2009). Finite-element analysis of lamb wave propagation in a thin aluminum plate. *Journal of Aerospace Engineering, 22*(2), 185-97. doi:10.1061/(ASCE)0893-1321(2009)22:2(185)

Huang, G. L., Song, F., and Wang, X. D. (2010). Quantitative modeling of coupled piezo-elastodynamic behavior of piezoelectric actuators bonded to an elastic medium for structural health monitoring: A review. *Sensors, 10*, 3681.

Huang, G. L., and Sun, C. T. (2006). The dynamic behaviour of a piezoelectric actuator bonded to an anisotropic elastic medium. *International Journal of Solids and Structures, 43*(5), 1291-1307. doi:http://dx.doi.org/10.1016/j.ijsolstr.2005.03.010

Krushynska, A., Meleshko, V., Chien-Ching Ma, and Yu-Hsi Huang. (2011). Mode excitation efficiency for contour vibrations of piezoelectric resonators. *IEEE Transactions on Ultrasonics, Ferroelectrics and Frequency Control, 58*(10), 2222-38. doi:10.1109/TUFFC.2011.2072

Lamb, H. (1917). On waves in an elastic plate. *Proceedings of the Royal Society, 93*, 293-312.

Lin, X., and Yuan, F. G. (2001). Diagnostic lamb waves in an integrated piezoelectric sensor/actuator plate: Analytical and experimental studies. *Smart Materials and Structures, 10*(5), 907-13. doi:10.1088/0964-1726/10/5/307

Liu, W., and Giurgiutiu, V. (2007). Finite element simulation of piezoelectric wafer active sensors for structural health monitoring with coupled-filed elements. Paper presented at the *Sensors and Smart Structures Technologies for Civil, Mechanical, and Aerospace Systems 2007, , 6529*. pp. 65293R (13 pp.). doi:10.1117/12.715238

McLachlan, N. W. (. (1955). In Subhash K. Batra Collection (North Carolina State University). (Ed.), *Bessel functions for engineers* Oxford, Clarendon Press, 1955. Retrieved from http://www2.lib.ncsu.edu/catalog/record/NCSU222139

Moulin, E., Assaad, J., Delebarre, C., Kaczmarek, H., and Balageas, D. (1997). Piezoelectric transducer embedded in a composite plate: Application to lamb wave generation. *Journal of Applied Physics, 82*(5), 2049-55. doi:10.1063/1.366015

Moulin, E., Assaad, J., Delebarre, C., and Osmont, D. (2000). Modeling of lamb waves generated by integrated transducers in composite plates using a coupled finite element-normal modes expansion method. *Journal of the Acoustical Society of America, 107*(1), 87-94. doi:10.1121/1.428294

Nienwenhui, J. H., Neumann, J. J., J., Greve, D. W., and Oppenheim, I. J. (2005). Generation and detection of guided waves using PZT wafer transducers. *IEEE Transactions on Ultrasonics, Ferroelectrics and Frequency Control, 52*(11), 2103-11.

Raghavan, A., and Cesnik, C. E. S. (2004). Modeling of piezoelectric-based lamb-wave generation and sensing for structural health monitoring. Paper presented at the *Sensors and Smart Structures Technologies for Civil, Mechanical, and Aerospace Systems, , 5391*. (1) pp. 419-30. doi:10.1117/12.540269

Raghavan, A., and Cesnik, C. E. S. (2005). Finite-dimensional piezoelectric transducer modeling for guided wave based structural health monitoring. *Smart Materials and Structures, 14*(6), 1448-1461. doi:10.1088/0964-1726/14/6/037

Raghavan, A., and Cesnik, C. E. S. (2007). Modeling of guided-wave excitation by finite-dimensional piezoelectric transducers in composite plates. Paper presented at the *48th AIAA/ASME/ASCE/AHS/ASC Structures, Structural Dynamics, and Materials Conference, April 23, 2007 - April 26, , 1*. pp. 287-301.

Reissner, E. (1946). Analysis of shear lag in box beams by principle of minimum potential energy. *Brown University Quarterly of Applied Mathematics, 4*(3), 268-278.

Rose, J. L. (1999). *Ultrasonic waves in solid media*. Cambridge, U.K. ;New York: Cambridge University Press. Retrieved from http://www2.lib.ncsu.edu/catalog/record/UNCb3267038

Rose, L. R. F., and Wang, C. H. (2004). Mindlin plate theory for damage detection: Source solutions. *Journal of the Acoustical Society of America, 116*(1), 154-71. doi:10.1121/1.1739482

Santosa, F., and Pao, Y. (1989). Transient axially asymmetric response of an elastic plate. *Wave Motion, 11*(3), 271-295. doi:10.1016/0165-2125(89)90006-1

Scalea, L. D., and Salamone, S. (2008). Temperature effects in ultrasonic lamb wave structural health monitoring systems. *Journal of the Acoustical Society of America, 124*(1), 161-174. doi:10.1121/1.2932071

Sirohi, J., and Chopra, I. (1998). Fundamental behavior of piezoceramic sheet actuators. Paper presented at the *Smart Structures and Materials 1998: Smart Structures and Integrated Systems, , 3329*. (1-2) pp. 626-46. doi:10.1117/12.316932

Sohn, H., and Lee, S. J. (2010). Lamb wave tuning curve calibration for surface-bonded piezoelectric transducers. *Smart Materials and Structures, 19*(1) doi:10.1088/0964-1726/19/1/015007

Sohn, H., and Sang, J. L. (2010). Lamb wave tuning curve calibration for surface-bonded piezoelectric transducers. *Smart Materials and Structures, 19*(1), 015007 (12 pp.). doi:10.1088/0964-1726/19/1/015007

Troitsky, M. S. (1976). *Stiffened plates : Bending, stability, and vibrations*. Amsterdam ; New York; New York: Elsevier Scientific Pub. Co.; distributors for the U.S. and Canada, Elsevier/North-Holland. Retrieved from http://search.trln.org/search?id=DUKE000215226

Veidt, M., Liu, T., and Kitipornchai, S. (2001). Flexural waves transmitted by rectangular piezoceramic transducers. *Smart Materials and Structures, 10*(4), 681-8. doi:10.1088/0964-1726/10/4/311

Viktorov, I. A. (. (1967). *Rayleigh and lamb waves: Physical theory and applications* New York, Plenum Press, 1967. Retrieved from http://www2.lib.ncsu.edu/catalog/record/NCSU127002

Wang, X. D., and Huang, G. L. (2001). Wave propagation in electromechanical structures: Induced by surface-bonded piezoelectric actuators. *Journal of Intelligent Material Systems and Structures, 12*(2), 105-15. doi:10.1106/MHD5-ON62-24EH-8B9T

Wang, X. D., and Huang, G. L. (2002). Wave propagation induced by multiple piezoelectric actuators in electromechanical structures. *Transactions of the ASME.Journal of Pressure Vessel Technology, 124*(3), 311-18. doi:10.1115/1.1484115

Wang, X. D., and Huang, G. L. (2003). On the elastic wave propagation induced by a network of piezoelectric actuators. *Acta Mechanica, 160*(1-2), 1-18. doi:10.1007/s00707-002-0969-y

Wang, X. D., and Huang, G. L. (2006). The coupled dynamic behavior of piezoelectric sensors bonded to elastic media. *Journal of Intelligent Material Systems and Structures, 17*(10), 883-94. doi:10.1177/1045389X06061130

Wang, X. D., and Huang, G. L. (2006). Wave propagation generated by piezoelectric actuators attached to elastic substrates. *Acta Mechanica, 183*(3-4), 155-76. doi:10.1007/s00707-006-0313-z

Wang, X. D., and Meguid, S. A. (2000). On the electroelastic behaviour of a thin piezoelectric actuator attached to an infinite host structure. *International Journal of Solids and Structures, 37*(23), 3231-51. doi:10.1016/S0020-7683(99)00118-3

Wilcox, P. (2004). Modeling the excitation of lamb and *SH* waves by point and line sources. Paper presented at the *Review of Progress in Quantitative Nondestructive Evaluation,* (700) pp. 206-13. doi:10.1063/1.1711626

Yan, X., and Fuh-Gwo Yuan. (2015). Conversion of evanescent lamb waves into propagating waves via a narrow aperture edge. *Journal of the Acoustical Society of America, 137*(6), 3523-33. doi:10.1121/1.4921599

Yu, L., Bottai-Santoni, G., and Giurgiutiu, V. (2010). Shear lag solution for tuning ultrasonic piezoelectric wafer active sensors with applications to lamb wave array imaging. *International Journal of Engineering Science, 48*(10), 848-861. doi:10.1016/j.ijengsci.2010.05.007

Zhang, B., Zhang, J., and Fan, J. (2003). A coupled electromechanical analysis of a piezoelectric layer bonded to an elastic substrate: Part II, numerical solution and applications. *International Journal of Solids and Structures, 40*(24), 6799-6812. doi:10.1016/S0020-7683(03)00312-3

Zhang, J., Zhang, B., and Fan, J. (2003). A coupled electromechanical analysis of a piezoelectric layer bonded to an elastic substrate: Part I, development of governing equations. *International Journal of Solids and Structures, 40*(24), 6781-97. doi:10.1016/S0020-7683(03)00307-X

APPENDIX

Appendix A - Coefficients in carrier wave approach

For symmetric modes:

$$V_S^n(z) = s_1 \cos(pz) + s_2 \cos(qz)$$

$$W_S^n(z) = s_3 \sin(pz) + s_4 \sin(qz)$$

where

$$s_1 = 2\cos(qh)$$
$$s_2 = -[(k_n^2 - q^2)/k_n^2]\cos(ph)$$
$$s_3 = -2(p/k_n)\cos(qh)$$
$$s_4 = -[(k_n^2 - q^2)/qk_n]\cos(ph)$$

For antisymmetric modes:

$$V_A^n(z) = a_1 \sin(pz) + a_2 \sin(qz)$$

$$W_A^n(z) = a_3 \cos(pz) + a_4 \cos(qz)$$

where

$$a_1 = 2\sin(qh)$$
$$a_2 = -[(k_n^2 - q^2)/k_n^2]\sin(ph)$$
$$a_3 = -2(p/k_n)\sin(qh)$$
$$a_4 = [(k_n^2 - q^2)/qk_n]\sin(ph)$$

and

$$p^2 = \frac{\omega^2}{c_L^2} - k_n^2, \quad c_L^2 = \frac{\lambda + 2\mu}{\rho}$$
$$q^2 = \frac{\omega^2}{c_T^2} - k_n^2, \quad c_T^2 = \frac{\mu}{\rho}$$

$$I_{nn}^S = \mu[c_1^S \cos^2(ph) + c_2^S \cos^2(qh)]$$

where

$$c_1^S = \frac{(k_n^2 - q^2)(k_n^2 + q^2)}{2q^3 k_n^3}[2qh(k_n^2 - q^2) - (k_n^2 + 7q^2)\sin(2qh)]$$
$$c_2^S = \frac{k_n^2 + q^2}{pk_n^3}[4k_n^2 ph + 2(k_n^2 - 2p^2)\sin(2ph)]$$

$$I_{nn}^A = \mu[c_1^A \sin^2(ph) + c_2^A \sin^2(qh)]$$

where

$$c_1^A = \frac{(k_n^2 - q^2)(k_n^2 + q^2)}{2q^3 k_n^3}[2qh(k_n^2 - q^2) + (k_n^2 + 7q^2)\sin(2qh)]$$
$$c_2^A = \frac{k_n^2 + q^2}{pk_n^3}[4k_n^2 ph - 2(k_n^2 - 2p^2)\sin(2ph)]$$

$$J_{nn} = h$$